Convective Heat Transfer in a Rotating Annulus

King, Martin Peter

Award date:
2003

Awarding institution:
University of Bath

CONVECTIVE HEAT TRANSFER IN A ROTATING ANNULUS

Submitted by Martin Peter King
for the degree of
Doctor of Philosophy
of the University of Bath
2003

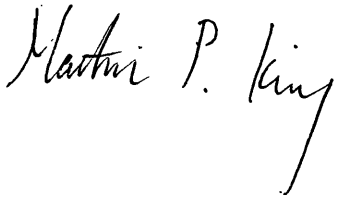

ProQuest LLC
789 East Eisenhower Parkway
P.O. Box 1346
Ann Arbor, MI 48106-1346

Contents

Acknowledgements

I am grateful to my supervisors, Dr M. Wilson and Prof. J.M. Owen. They were extremely patient with me and my short-comings. Dr Wilson was always willing in giving his time and advice. He also allowed me the freedom to study around different topics. I also value his corrections and suggestions that greatly improved the presentation of this thesis. Prof. Owen pointed me to the study of Rayleigh-Bénard convection, which provided the foundation for my computational results. It also led to the work, which I particularly enjoyed doing, presented in Chapters 3 and 7 of this thesis.

I would like to acknowledge Dr T. Lewis, who is the original developer of the computational codes without which many of my computations would not have been be possible. I also appreciate the occassional, but helpful, advice I received from Dr D.A.S. Rees. Some of the figures in the thesis were produced using programs written by Dr Rees.

I was very fortunate and privileged to receive financial support in the form of the Bath University Research Studentship. For this I am indebted to the University, and to my supervisors who assisted me in the application process.

I dedicate this thesis to my parents and sister. I thank my parents for their sacrifices and encouragement.

I am grateful to the fellowship of Widcombe Baptist Church in Bath. I will miss the sound biblical teaching I have received there. I also thank the many friends I have come to know in the U.K. for their love and prayers. I live in the constant knowledge that the Lord is gracious to me.

Finally, I thank you for picking up my thesis. I hope that my presentation is clear and you will find something of interest to you here. You are welcome to send comments to me at `m_p_king@yahoo.com`.

Convective heat transfer in a rotating annulus

Martin P. King

Submitted for the degree of Ph.D. of the University of Bath

2003

Summary

The free convection heat transfer in a sealed rotating annulus is investigated. The annulus has a heated outer cylinder and a cooled inner cylinder. Flow is induced by buoyancy in the centrifugal field and affected by the Coriolis force. In addition to fundamental understanding of free convection in rotating enclosures, the problem is specifically relevant to flow in compressors and turbine-discs of gas-turbines.

The heat transfer efficiency, characterised by Nusselt number-Rayleigh number scaling laws $Nu \sim Ra^{\gamma}$, is the main focus of the thesis. Both numerical simulations and simple phenomenological models with dimensional analyses have been employed to address the problem. The latter method is also used to study heat transfer in a cavity with axial throughflow.

It is found that the influence of rotational Reynolds number, which is associated with the Coriolis force, in reducing heat transfer is weak if the value of $\beta\Delta T$ cannot be varied over a large range. The Nusselt number is strongly dependent only on Rayleigh number. Simulations do not reproduce measured heat transfer results by Bohn *et al.* (1995) for rotating annuli, instead the results are closer to those for Rayleigh-Bénard convection. Rayleigh-Bénard convection is the stationary 'counterpart' of free convective flow in rotating annulus, and its understanding has enjoyed much progress in recent years (e.g. Grossmann & Lohse, 2000 & 2001). Results from Rayleigh-Bénard convection are applied carefully for comparisons with and interpretations of the computational results obtained in the current study. An explanation is also suggested in this context for the results of Bohn *et al.*

From the results obtained in the current study and in the literature, it is remarkable to note that scaling laws for apparently very different convective heat transfer situations (such as orientations and shapes of the enclosures, cavities or flat plates and even whether they are stationary or rotating) are not vastly different. The typical γ values, for example, vary between 1/5 and 1/2 inclusive. The orders of magnitude for heat transfer are similar; the effect is especially noticeable if a large range of Rayleigh number is considered.

Simple phenomenological models (inspired by Castaing *et al.*, 1989) and dimensional analyses are used to derive many scaling laws. This type of study enables a more unified understanding of the flow processes and parameters that give rise to the scaling laws for different convective flows.

For cavities with axial throughflow, different convection regimes with their corresponding scaling laws were also derived using similar theoretical models and dimensional considerations. The results are summarised in a regime diagram of Re_z vs. Ra_z delineating different types of convection and scaling laws.

Nomenclature

Listed here are the commonly used symbols in the text. A local meaning is given in the text where the symbol appears. [.] gives the dimension of a quantity, where M is the dimension for 'mass', L for 'length', T for 'time', Θ for 'temperature', and Q for 'heat energy'.

Dimensional quantities

a	radius of inner cylinder $[L]$
b	radius of outer cylinder $[L]$
c_p	specific heat capacity $[QM^{-1}\Theta^{-1}]$
d	separation between hot and cold walls $[L]$
g	gravitational acceleration $[LT^{-2}]$
h	heat transfer coefficient $[QT^{-1}L^{-2}\Theta^{-1}]$
k	thermal conductivity $[Q\Theta^{-1}T^{-1}L^{-1}]$
l	separation between adiabatic walls $[L]$
$\dot{Q}$	heat transfer rate $[QT^{-1}]$
$\dot{q}$	heat flux $[QL^{-2}T^{-1}]$
r_m	mean radius $(=\frac{a+b}{2})$ $[L]$
s or z_{max}	axial separation between discs $[L]$
T_c	temperature on cold surface $[\Theta]$
T_h	temperature on hot surface $[\Theta]$
T_i	temperature of fluid at inlet to cavity $[\Theta]$
t	time $[T]$
u, v, w	radial, tangential, & axial velocities repectively $[LT^{-1}]$
u_c	wind velocity in turbulent well-mixed region $[LT^{-1}]$
W	velocity of axial througflow $[LT^{-1}]$
w	width of an enclosure $[L]$

Greek letters

β	volumetric expansion coefficient $[\Theta^{-1}]$
δ_u	viscous/kinetic boundary-layer thickness $[L]$
δ_θ	thermal boundary-layer thickness $[L]$
Δd	radial clearance of annular inlet $[L]$
$\Delta r, \Delta z, \Delta\theta$	grid intervals in r, z, θ directions respectively.
ΔT	hot and cold surfaces temperature difference $(=T_h - T_c)$ $[\Theta]$
ΔT_{fluc}	temperature fluctuations for fluid in central region $[\Theta]$
Δt	timestep
γ	real number constant exponent in $Nu \sim Ra^\gamma$
κ	thermal diffusivity $(=\frac{k}{c_p\rho})$ $[L^2T^{-1}]$
μ	viscosity $[ML^{-1}T^{-1}]$
ν	kinematic viscosity $(=\mu/\rho)$ $[L^2T^{-1}]$
ρ	density $[ML^{-3}]$
ρ_0	reference density $[ML^{-3}]$

ϕ	rescaled streamfunction ($= \phi/r$) $[L^2T^{-1}]$
ψ	streamfunction $[L^3T^{-1}]$
Ω	angular speed $[T^{-1}]$
ω	vorticity $[T^{-1}]$
Dimensionless parameters	
Gr	Grashof number ($= Ra/Pr$)
l/d	aspect ratio of cavity or enclosure
Nu	Global Nusselt number ($= \frac{\dot{q}d}{k\Delta T}$)
Nu_z	Nusselt number for cavity with axial throughflow ($= \frac{\dot{q}s}{2k\Delta T}$)
Pr	Prandlt number ($= \nu/\kappa$)
Ra	Rayleigh number ($= \frac{g\beta\Delta T d^3}{\nu\kappa}$)
Ra_b	rotational Rayleigh number based on b ($= \frac{\Omega^2\beta\Delta T b^4}{\nu\kappa}$)
Ra_z	Rayleigh number for cavity with axial throughflow ($= \frac{b\Omega^2\beta\Delta T s^3}{8\nu\kappa}$ or $= \frac{g\beta\Delta T s^3}{8\nu\kappa}$)
Ra_ϕ	rotational Rayleigh number ($= \frac{r_m\Omega^2\beta\Delta T d^3}{\nu\kappa}$)
Re	Reynolds number ($= \frac{u_c d}{\nu}$)
Re_b	rotational Reynolds number based on b ($= \frac{\Omega b^2}{\nu}$)
Re_z	axial Reynolds number ($= \frac{W2\Delta d}{\nu}$ for annular inlet; $= \frac{W2a}{\nu}$ for circular inlet)
Re_ϕ	rotational Reynolds number ($= \frac{r_m\Omega d}{\nu}$)
r_i, r_o	dimensionless inner and outer radii respectively ($r_i = a/b$, $r_o = b/b = 1$)

Chapter 1

Introduction

The study of heat transfer in enclosures has direct industrial applications such as heat exchangers, heat transfer in turbo-machineries, indoor climate, double-glazed windows, etc. It can act as a 'launching pad' into studies of more complicated systems such as heat transfer within the oceans and the atmosphere. There are also pure scientific interests in the boundary-layers, turbulence, etc of convective flows.

This thesis primarily concerns the heat transfer efficiencies, which are expressed in Nusselt number against Rayleigh number correlations, for *sealed* stationary and *sealed* rotating annuli (i.e. free convection). Chapter 7, which is an exception, deals with heat transfer in a cavity with an inlet and an outlet of cooling air.

The annulus has a uniformly heated outer cylinder and a uniformly cooled inner cylinder. Hence, buoyancy is set up in a centrifugal field (analogous to gravity in a stationary enclosure); the flow is also affected by other rotational effects. If the annulus is sealed, only *free* convection exists; if there is a throughflow, *free*, or *mixed*, or *forced* convection can occur depending on the comparative strengths of buoyancy and the throughflow. Some of the cases studied in this thesis are relevant to the flows of corotating compressors and turbine discs in gas–turbine engines.

The main methodology used is computer simulation, but simple theoretical

models together with dimensional and scaling law analyses are also applied. Other published results for convective heat transfer in enclosures and flat plates are also used extensively for validations or comparisons, to interpret results obtained here, and to support reasonings from which the conclusions are made.

As explained in the thesis, there are similarities between free convection in a rotating annulus and Rayleigh-Bénard convection. There have been extensive theoretical, experimental and computational studies of the latter. For example, recently, Niemela *et al.*(2000) made measurements up to $Ra = 10^{17}$, and Grossmann & Lohse (2000 & 2001) derived various scaling laws comprehensively. In this thesis, the connections between heat transfer in Rayleigh-Bénard convection and free convection in rotating annuli are explored. Simple dimensional analysis and phenomenological models are used to re-derive some scaling laws for Rayleigh-Bénard convection.

There appears to be a relative lack of study for rotating annulus convection with radial heat flux at high Rayleigh number. Bohn *et al.*(1995) conducted measurements for rotating annuli up to $Ra_\phi = 10^{12}$. Lewis (1999) carried out numerical studies, but there was no systematic investigation of the heat transfer properties. However, there have been extensive laboratory and numerical studies of convection in a vertical (gravity is not negligible and it acts along the axis of rotation) rotating annuli for flow relevant to the 'geophysical' regimes (see, for example, the review by Read, 1992).

This thesis attempts to extend the understanding of the heat transfer and qualitative flow structures in sealed rotating annulus up to as high a Rayleigh number as possible using 2D and 3D unsteady computations. A study of heat transfer in a rotating annulus with axial throughflow is also carried out by the method of dimensional analysis and simple phenomenological models. It is an aim of the thesis to report the various scaling laws for heat transfer ($Nu \sim Ra^\gamma$) from the current

investigation and comparisons with published results.

The thesis also attempts to convey that the scaling laws for many apparently different convections are very similar, and the simple theoretical derivations used here can give a more unifying picture of the underlying processes involve in giving rise to these scaling laws.

1.1 The themes

The main questions that this thesis aims to address are:

(i) What are the relationships between Nusselt and Rayleigh numbers for the stationary and rotating annuli being considered here? Are there any discrepancies between results obtained here and those of other investigations, and if so, how can they be explained?

(ii) It is accepted widely that $Nu \sim Ra^{\gamma}$ for convective heat transfer of moderately high Rayleigh number and greater. Do the present investigations confirm (or refute) this relation; what are the values of γ both from previous investigations and from the current research? In what conditions (such as range of Prandtl number, Rayleigh number, etc) a certain value of γ applies?

(iii) How do the geometries and boundary conditions of the annuli affect these correlations?

(iv) What are the flow structures like?

(v) How capable are the computational codes?

1.2 The plan of the thesis

Chapter 1 Introduction: The current chapter.

Chapter 2 Literature review: Previous investigations provide foundations, frame-

work, and preliminary solutions for further investigations. Correlations for various stationary and rotating enclosures, and factors that affect heat transfer are reviewed.

Chapter 3 Dimensional and scaling analyses of Rayleigh-Bénard convection: The important dimensionless parameters for free convective heat transfer are derived. Different scaling-laws ($Nu \sim Ra^{\gamma}$) are calculated using simplified procedures; results from a theory of Grossmann & Lohse (2000, 2001) are used to show to what conditions a certain scaling law applies. An alternative explanation is suggested for the scaling laws obtained by sealed rotating annulus experiments.

Chapter 4 Two-dimensional (radial-tangential) computations: Results from computations of free convective flows in the radial-tangential plane (axially invariant) are presented. Cases for both a stationary annulus, that approximates Rayleigh-Bénard convection, and the corresponding rotating annulus are computed. Effects of radius ratio and rotation on the heat transfer are discussed. The Nusselt number against Rayleigh number correlations obtained from the computations are compared with other published results.

Chapter 5 Two-dimensional (radial-axial) computations: Results from axisymmetric computation of free convective flows in the radial-axial plane are presented. Investigations and analyses similar to those in Chapter 4 are conducted.

Chapter 6 Three-dimensional computations: Unsteady three-dimensional computations are performed. Investigations are performed on stationary annulus flow that approximates Rayleigh-Bénard convection, rotating annulus flow, and flow in an annulus with an insulating radial barrier. The flow structures are discussed. The effects of the rotation, dimensions of annuli, and the radial barrier to the heat transfer are investigated.

Chapter 7 Heat transfer in cavities with axial throughflow: Techniques and models similar to those used in Chapter 3 are applied here for heat transfer in cavi-

ties with throughflow of cooling air. The flow can be in the free, or mixed, or forced convection regime depending on the Reynolds and Rayleigh numbers. Correlations are derived and a schematic convection regime diagram (delineating different types of convection) is also presented.

Chapter 8 Conclusions and suggestions for future work: Summarising the main findings and conclusions of this thesis. A few ideas for future work are also suggested.

References

Appendix Unsteady flow in a rotating cavity with a stationary casing: This is a revised version of the 'Transfer Report' on work that was carried out in the first year of this Ph.D. study. It is included here for completeness and to show the versatility of the computational code which was also used for the study reported in Chapter 5. Here the boundary conditions are different to those in Chapter 5. All the walls are isothermal, the outer cylinder is stationary, while the discs and inner cylinder are corotating. A secondary flow is created by the presence of shear between the stationary casing and the rotating surfaces.

Figures

Chapter 2

Literature review

This chapter begins with a section on free convection in stationary sealed enclosures, and is followed by a section on rotating annuli. Correlations for Nusselt number with Rayleigh number are presented. It is shown that free convective heat transfer within stationary sealed enclosures is similar in magnitude regardless of the shapes, geometries, and orientations of the cavities. Though not exhaustive, the aim of this review is to 'set the scene' for this thesis by using some of the important results found in the literature.

2.1 Free convection in stationary enclosures

For reasons to be explained later in this chapter and repeated elsewhere in the thesis, free convective flow in stationary enclosures shares many similarities with that in rotating enclosures.

2.1.1 Rayleigh–Bénard convection(heat transfer in horizontal layers)

Flow between two parallel horizontal plates with uniform heating from the bottom plate and uniform cooling on the top plate is also called Rayleigh-Bénard convection (Figure 2.1). For flows obeying the Boussinesq approximation (Tritton,

1988, pp.188–196), there are two important dimensionless groups, the Rayleigh and Prandtl numbers defined respectively as

$$Ra = \frac{g\beta\Delta T d^3}{\nu\kappa}, \qquad Pr = \nu/\kappa.$$

The aspect ratio(l/d) is made very large by supposing a horizontally infinite layer. The Nusselt number, defined as the ratio of total heat flux to heat flux by conduction only, is used to characterise the heat transfer efficiency. Chapter 3 describes the derivation of these dimensionless groups and how Nusselt number can be related to Rayleigh and Prandtl numbers in scaling-laws.

For Rayleigh number below the critical value of 1708 (Tritton, p.360–362), the fluid is stationary, resulting in a conductive temperature profile and $Nu = 1$. This critical Rayleigh number is Prandtl number independent (Goldstein *et al.*, 1990). Above this critical value the fluid becomes unstable and convective flow occurs. The first mode of motion is usually that of two-dimensional steady convective rolls, then time-dependent, and finally turbulent flow as the Rayleigh number is increased further (Goldstein *et al.*, 1990). For Prandtl number less than about 5, the steady two-dimensional flow first becomes steady three-dimensional before the transitions to other regimes as the Rayleigh number increases. Krishnamurti (1970a, 1970b & 1973) made extensive experimental studies on the different transitions to unsteady flows. Here it is only noted that for $Pr \approx 1$, the flow becomes unsteady near $Ra = 10^4$. The transitions to turbulent flows occur at higher Rayleigh number as the Prandtl number is increased (Krishnamurti, 1970b). This is because a high Prandtl number fluid has high viscosity in relation to its conductivity.

In the late 1980's, it was discovered that non-periodic (chaotic) behaviour, which traditionally (such as by Krishnamurti) has been regarded as turbulence, is very different from fully developed turbulence (Heslot *et al.*, 1987). Fully developed

turbulence includes 'soft' and 'hard' turbulent regimes which are characterised by the Gaussian and exponential distributions, respectively, of the probability density of the temperature fluctuations at a point at the centre of the enclosure. Heslot *et al.*(1987) postulated that in the hard turbulence regime, oscillating boundary layers from which plumes detach abruptly leads to sharp temperature peaks; these plumes are localised objects. In soft turbulence the plumes are extended objects at the boundary between convective rolls. The physics of convective turbulence is beyond the scope of this thesis: refer to Heslot *et al.*(1987), Castaing *et al.*(1989), Niemela *et al.*(2000) and Siggia (1994) for more detailed explanations and measurements of soft and hard turbulence.

The main focus of this thesis is the relationship between Nusselt and Rayleigh numbers. For convecting flow, Nusselt number is greater than unity. Hollands *et al.*(1984) used an analytical conduction layer model and empirical adjustment to obtain the following relationship:

$$Nu = 1 + max\left\{(1 - 1708/Ra), 0\right\}\left[k_1 + 2(Ra^{1/3}/k_2)^{1-\ln(Ra^{1/3}/k_2)}\right]$$

$$+max\left\{((Ra/5830)^{1/3} - 1), 0\right\}, \qquad (2.1)$$

where $k_1 = 1.44/(1 + 0.018/Pr + 0.00136/Pr^2)$ and $k_2 = 75\exp(1.5Pr^{-1/2})$.

Figure 2.2 shows four results, for low to high Prandtl number fluids, obtained using the correlation above and plotted on log-log axes. Each line terminates at a Rayleigh number up to which the correlation has been verified by experiments for that Prandtl number (see Hollands, 1984). It may be seen from Figure 2.2 that the dependence of Nu on Pr is weak for $Pr \gtrsim 0.7$. This statement will be supported more clearly in chapter 3. *N.B. There are typographic errors in the original paper by Hollands (1984), the correct form of the correlation (which is equation 2.1) is quoted from Rohsenow et al.(1998), p.4.44.*

For turbulent Rayleigh-Bénard convection, there is evidence in experiments and theories (e.g. Castaing *et al.*(1989), Cioni *et al.*(1997), Niemela *et al.*(2000), Glazier *et al.*(1999) & Grossmann & Lohse(2000, 2001)) that a scaling law $Nu = CRa^{\gamma}$, where C and γ are constants, is able to correlate Nusselt number with Rayleigh number. Values of γ of $\frac{1}{2}$, $\frac{1}{3}$, $\frac{2}{7}$, $\frac{1}{4}$, $\frac{1}{5}$, etc. have been measured experimentally and/or derived theoretically. C is dependent on enclosure aspect ratio and usually can only be found from experiment (Wu & Libchaber, 1992 and Grossmann & Lohse, 2000). The value of γ is believed to be independent of the aspect ratio (Grossmann & Lohse, 2000), but dependent on the range of Rayleigh and Prandtl numbers.

Obviously, determining the numerical values of C and γ are important for practical applications. Chapter 3 presents derivations of different scaling laws. This thesis also reports values of C and γ, for stationary and rotating enclosures, determined from computational results obtained by the author.

Heat transfer across horizontal layers restricted in the horizontal directions (i.e aspect ratio $l/d \ll \infty$) are characterised by critical Rayleigh numbers (for onset of convection) larger than 1708. This is because either a conducting or an adiabatic side-wall can dampen the velocity and temperature perturbations in the fluid.

The recommended Nu vs. Ra correlation for such horizontally nonextensive enclosures (Hollands *et al.*,1984) is

$$Nu = 1 + max\left\{(1 - Ra_c/Ra), 0\right\}\left[k_1 + 2\left(\frac{Ra^{1/3}}{k_2}\right)^{1-\ln\left(Ra^{1/3}/k_2\right)}\right]$$

$$+max\left\{((Ra/5830)^{1/3} - 1), 0\right\}\left(1 - \exp\left[-0.95max\left\{((Ra/Ra_c)^{1/3} - 1), 0\right\}\right]\right), \tag{2.2}$$

where Ra_c is the critical Rayleigh number, k_1 and k_2 are as defined in Equation 2.1. Again, the correct form of the equation is quoted from Rohsenow *et al.*(1998,

p.4.50). The advantage of this inelegant correlation is that to obtain a relationship for Nu and Ra, all complexities, such as side-wall effects, are reduced to the determination of a critical Rayleigh number. Refer to, for example, Hollands *et al.*(1984), Catton & Edwards (1967), Catton (1972) and Rohsenow *et al.*(1998, pp.4.46–4.50) for determination of critical Rayleigh numbers and references therein on this topic. Equation (2.2) reduces to Equation (2.1) at $Ra_c = 1708$.

Figure 2.3 displays the Nu vs. Ra relationships for enclosures with either insulated or conducting side-walls for five different aspect ratios of 3, 2, 1, 0.5 and 0.25. The Prandtl number is 0.7. The critical Rayleigh numbers are obtained from tabulated data in Rohsenow *et al.*(1998, p.4.47). The correlations are then calculated using Equation (2.2).

Figure 2.3 shows that as the aspect ratio decreases, i.e the enclosures become 'taller', the critical Rayleigh number increases. This is true regardless of the thermal property of the side-walls. For the same aspect ratio, an enclosure with conducting side-walls has a higher critical Rayleigh number than that with insulated side-walls. Allowing heat to escape from the side-walls reduces Nusselt numbers; fluid fluctuations are weakened because the system is losing energy and heat transfer is reduced as a result.

Figure 2.3 also illustrates that both the enclosure aspect ratio and the side-wall thermal boundary conditions become irrelevant when the aspect ratio is increased to greater than about 0.5. With increasing aspect ratio, the correlations approximate asymptotically to that for an extensive horizontal layer. Also, it is noted that the side-wall effects and aspect ratio are irrelevant at Rayleigh numbers greater than about 10^7. It is also at $Ra > 10^7$ that hard turbulence sets in (Heslot *et al.*, 1987).

In Chapter 5 of this thesis, the conclusions in the above paragraph are used to interprete the computational results for some related non-extensive enclosures.

2.1.2 Heat transfer in enclosures with differentially heated side walls

This section discusses free convective heat transfer in enclosures with one of the vertical walls heated uniformly and the other cooled uniformly (Figure 2.4). This is also called a vertical enclosure (as opposed to a horizontal enclosure in Rayleigh-Bénard convection). The enclosure may also be inclined at any angle between 0^o (Rayleigh-Bénard convection) and 90^o (vertical enclosure).

A flow exists for any finite Rayleigh number in a vertical enclosure. For small Ra, the velocities are small and virtually parallel to the walls, therefore the contribution to the heat transfer is small and $Nu = 1$ for all practical purposes. These conditions are regarded as the conduction regime. The development of the flow beyond this regime as Ra increases depends on the aspect ratio l/d. For $l/d \gtrsim 40$, as Ra increases the flow goes through first conduction, then turbulent transition, and then turbulent boundary layer flow ; for $l/d \lesssim 40$, the corresponding regimes are conduction, then laminar boundary layer flow, then turbulent boundary layer flow (Rohsenow *et al.*, 1998, p.4.51). Gill (1966), Kutateladze *et al.*(1978) and Tritton (1988, p.37) give more details on the flow structures.

Dimensional analysis shows that $Nu = f(Ra, l/d)$. Shewen *et al.*(1996) presented the following correlation for $l/d \geq 40$ and $w/d \gtrsim 5$ (w is the width of the enclosure) to fit their experimental data:

$$Nu = \left[1 + \left(\frac{0.0665 Ra^{1/3}}{1 + (9000/Ra)^{1.4}}\right)^2\right]^{1/2}, \tag{2.3}$$

which was verified by experiments for $Pr \approx 0.7$ and $Ra < 10^6$. They noticed that the result is nearly independent of l/d for $l/d \geq 40$. This correlation is shown in Figure 2.5.

ElSherbiny *et al.*(1982) derived the following correlation for $5 < l/d < 40$ and

$w/d \gtrsim 5$ which has been verified up to $Ra = 2 \times 10^7$ for $Pr \approx 0.7$:

$$Nu = max\{Nu_l, Nu_{trans}, Nu_t\}, \tag{2.4}$$

where,

$$Nu_l = 0.242(Ra\ d/l)^{0.273}, \tag{2.5}$$

$$Nu_{trans} = \left[1 + \left\{\frac{0.104Ra^{0.293}}{1 + (6310/Ra)^{1.36}}\right\}^3\right]^{1/3}, \tag{2.6}$$

$$Nu_t = 0.0605Ra^{1/3}. \tag{2.7}$$

This correlation is shown in Figure 2.5 for three values of $l/d = (7, 10, 40)$.

Lastly, for cavities of $0.5 < l/d < 5$ and $w/d \gtrsim 5$, Kuyper *et al.*(1993) give the following correlations:

$$Nu = 0.171Ra^{0.282}, \quad for \ \ 10^4 < Ra < 10^8, \tag{2.8}$$

$$Nu = 0.050Ra^{0.341}, \quad for \ \ 10^8 < Ra < 10^{12}. \tag{2.9}$$

These relationships are also displayed in Figure 2.5.

From the graphs, it is observed that for $Ra \lesssim 10^5$, the Nusselt number decreases as the aspect ratio is increased. It is believed that the flows remain laminar for the range of Ra displayed in Figure 2.5, as a computational study by Bohn *et al.*(1994) suggests that the flow is probably still laminar at $Ra = 10^{11}$. For higher Rayleigh number, it can be argued that aspect ratio has only a weak influence on Nu compared to the influence Ra has on Nu. Although the correlations presented here are for $Pr \approx 0.7$ (air), there is evidence that Pr is insignificant if $Pr \gtrsim 0.7$ (Rohsenow *et al.*, 1998, p.4.54), just as in Rayleigh-Bénard convection.

For $l/d = 0.25$, Arnold *et al.*(1977) showed experimentally that Nu is unaffected when w/d is reduced from essentially infinity to 0.5. It is recalled from the previous section that this is the same value of aspect ratio above which the Nusselt

number dependence on aspect ratio is negligible for Rayleigh-Bénard convection.

Depending on the inclination of the enclosure, the flow can resemble that in the corresponding horizontal or vertical cavity; it rarely combines the characteristics of both (Rohsenow *et al.*, 1998, p.4.55). Consequently, Nu can be determined to a reasonable approximation from either the horizontal or the vertical correlation using simple inclination angle scalings. It is generally found that the value of Nu for an inclined layer lies between that for a horizontal layer and that for a vertical layer (ElSherbiny *et al.*, 1982). Since Nu from the horizontal and vertical layers are similar in order of magnitude, it can be argued that effect of inclination can be neglected (compared to the effect of Ra on Nu) for most practical purposes. The validity of this statement becomes stronger if a large order of magnitude for Rayleigh number is involved because heat transfer depends strongly on Ra and also the differences among different correlations become smaller at high Ra.

$\lg(Ra)$	Nu			
	vertical cavities		horizontal cylinder	R-B convection
	$0.5 < l/d < 5$	$l/d = 40$	$a/b = 0.5, b - a = 0.5$	
3.0	-	1.00	1.08	1.00
3.5	-	1.01	1.44	1.64
4.0	2.3	1.30	1.92	2.36
4.5	3.18	2.03	2.56	3.08
5.0	4.4	3.00	3.42	3.96
5.5	6.08	4.25	4.56	5.19
6.0	8.41	6.05	6.08	7.00
6.5	11.64	8.88	8.1	9.75
6.8	14.14	11.18	9.63	12.05
7.0	16.11	13.03	10.81	13.94
7.5	22.28	-	14.41	20.21
8.0	26.73	-	19.22	29.25
8.5	39.58	-	25.63	41.8
9.0	58.61	-	34.17	59.31

Table 2.1: Values of $\lg(Ra)$ and Nu for two vertical cavities (ElSherbiny *et al.*, 1982), a horizontal cylinder (Raithby & Hollands, 1975), and Rayleigh-Bénard convection (Hollands *et al.*, 1984).

Numerical values for Nu at some selected values of $\lg(Ra)$ for $0.5 < l/d < 5$

and $l/d = 40$ vertical enclosures are given in table 2.1. The differences in Nu between these two vertical enclosures are the maximum between any two vertical enclosures shown in Figure 2.5. Data from Rayleigh-Bénard convection (Hollands *et al.*, 1975) are also given for comparison.

2.1.3 Heat transfer in horizontal cylinders

For heat transfer between horizontal concentric cylinders, Raithby and Hollands (1975) obtained the following empirical correlation:

$$Nu = max \left\{ \frac{0.405 \ln (b/a) Ra^{1/4}}{(1 + (0.492/Pr)^{9/16})^{4/9} \left[(\frac{d}{2a})^{3/5} + (\frac{d}{2b})^{3/5} \right]^{5/4}}, 1 \right\}, \tag{2.10}$$

which is valid for $Ra \leq 8 \times 10^7$, $0.7 \leq Pr \leq 6000$, and $0.125 \leq a/b \leq 0.87$. Rayleigh number is defined as $Ra = g\beta\Delta T d^3/(\nu\kappa)$, where $d = b - a$.

For $Pr = 0.7$, $a/b = 0.5$, $b - a = 0.5$, Equation 2.10 gives

$$Nu = 0.192 Ra^{1/4}, \tag{2.11}$$

which has an identical gradient, and is not too dissimilar in magnitude, to laminar Rayleigh-Bénard convection, see Figure 2.6 and Table 2.1. The results deviate at higher Ra as Rayleigh-Bénard convection assumes $\gamma \approx 1/3$ gradient.

2.2 Convection in rotating annuli

Studies of free convective heat transfer within rotating annuli (co-rotating concentric cylinders) are relevant to understanding heat transfer conditions in gas-filled cavities between the discs in gas-turbine engines. In the radial heat flux configuration, an annular cavity with a uniformly heated outer and uniformly cooled inner cylindrical walls with adiabatic side-discs is used. In the axial heat flux arrangement, one of the side-discs is heated uniformly, the other cooled uniformly, and the cylindrical

walls are adiabatic. In either setup, and for a fixed fluid (so fixed Pr) and fixed cavity geometries ($2(b-a)/(b+a)$ and $2s/(b+a)$), Nusselt number is a function of rotational Rayleigh number and rotational Reynolds numbers ($Nu = f(Ra_\phi, Re_\phi)$).

Previous studies with high rotational Rayleigh numbers, in the range found in gas-turbine cavities, were carried out by Bohn *et al.*. Their works are described below.

2.2.1 Radial heat flux

Bohn *et al.*(1995) carried out experiments, for $10^7 \leq Ra_\phi \leq 10^{11}$, of free convective heat transfer in sealed air-filled rotating annuli, for three different annuli and with differential radial heating, as illustrated in Figure 2.7. They reported $Nu \propto Ra_\phi^\gamma$, with γ close to 0.2. Their results are shown in Figure 2.8. It is clear that the heat transfer in these experiments for rotating annuli is much lower than that for Rayleigh-Bénard convection.

	Cavity A	Cavity B	Cavity C
a, b, s[mm]	125, 355, 120	125, 240, 120	125, 240, 120
Correlations	$Nu = 0.246Ra_\phi^{0.228}$ $Re_\phi = 0.733Ra_\phi^{0.573}$	$Nu = 0.317Ra_\phi^{0.211}$ $Re_\phi = 1.441Ra_\phi^{0.557}$	$Nu = 0.365Ra_\phi^{0.213}$ $Re_\phi = 1.615Ra_\phi^{0.556}$

Table 2.2: Rotating cavities studied experimentally (Bohn *et al.*, 1995)

Table 2.2 summarises the cavity geometries used and the correlations obtained by Bohn *et al.*(1995), where the rotational Rayleigh and rotational Reynolds numbers are $Ra_\phi = \frac{(a+b)\Omega^2\Delta T d^3}{2\nu\kappa}$ and $Re_\phi = \frac{\Omega(a+b)d}{2\nu}$ respectively. Cavity C has eight equally-spaced radial separation walls, thus producing eight sealed sectors. The presence of these walls should decrease the radial component of the Coriolis force. Coriolis force is believed to be responsible for inhibiting heat transfer in a rotating system (Bohn *et al.*, 1994). However it is clear from the results that differences in geometry and the Coriolis force contribute only slightly to the reduction in Nu in

a rotating annulus when compared with the differences in Nu between Rayleigh-Bénard convection and these rotating annuli. A rotating annulus with radial (or axial) heat flux can approximate Rayleigh-Bénard convection (or that in a stationary vertical enclosure) by using a large $\frac{a+b}{2d}$ ratio, and an angular velocity Ω so that $\frac{(a+b)\Omega^2}{2}$ equates to gravity.

The rotational Reynolds number is associated with the Coriolis terms in the momentum equations. It will be explained in detail in Chapter 4 that even though Re_ϕ could not be held constant througout the experiments of Bohn *et al.*, this did not affect the Nu vs. Ra_ϕ correlations obtained (also true for the axial heat transfer case, Bohn *et al.*, 1996). This is because Ra_ϕ has a much stronger influence than Re_ϕ on Nu if both Ra_ϕ and Re_ϕ are varied over a similar range of orders of magnitude.

Bohn *et al.*(1996) performed computations with governing equations in which the density is calculated by the ideal gas law (rather than using the Boussinesq approximation). They were able to vary $\beta\Delta T$ (and thus Re_ϕ) over a wider range than possible in the experiments and then showed that the effect of Re_ϕ on Nu is stronger in axial heat transfer than in radial heat transfer. Therefore, in a radial heat transfer case it is more permissible to say that Nu depends strongly on Ra_ϕ, because: (i) Nu depends strongly on only Ra_ϕ in both the radial and axial heat transfer experiments. (ii) the effect of Re_ϕ on Nu is weaker in the radial heat transfer case than in the axial heat transfer case. This conclusion is valid for cases bound by the Boussinesq approximation and limited range of $\beta\Delta T$ (typical gas-turbine conditions are found to satisfy these restrictions). The computations for axial heat transfer by Bohn *et al.*(1996) show that Nu is affected by Re_ϕ if $\beta\Delta T$ (and thus Re_ϕ) can be varied over a wide range.

Owen & Wilson (2000) suggested that the flows may have remained laminar even at high Ra_ϕ since $\gamma \approx 0.2$ obtained by Bohn *et al.*(1995) is similar to $\gamma =$

0.25 for laminar Rayleigh-Bénard convection. The centrifugal force field, which decreases linearly (in $r\Omega^2$) from the outer to inner cylindrical walls, may stabilise the flow. Bohn *et al.* did not make observations of the flow structures or velocity measurements, therefore the above suggestion cannot be confirmed.

In the last section of Chapter 3, a recent theory (Grossmann & Lohse, 2000, 2001) is used to suggest how the conditions of the boundary layers are affected by rotation, and giving rise to $\gamma \approx 0.22$ as obtained in the Bohn *et al.*'s experiments. This analysis permits turbulent bulk flow (away from the boundary layers).

A steady-state, laminar computation carried out by Bohn *et al.*(1995) for cavity C gave Nu results which agreed with their own experiments. They also carried out an unsteady simulation and found that the flow showed no tendency to reach a steady state. The Nu value they obtained for a particular Ra_ϕ was greater in the unsteady than in the corresponding steady computation. Bohn & Gier (1998) carried out steady 2D and 3D turbulent simulations which produced almost 20% greater heat transfer than that in the experiment. Three-dimensionality in the computation has only a small impact on the overall heat transfer (again, this is because $s/d > 0.5$ and $Ra_\phi > 10^7$, so side-wall effects can be ignored). Thus, it was concluded in King & Wilson (2002) that the inclusion of unsteadiness and turbulence are responsible for the higher computed heat transfer than that from the rotating annulus experiments.

Lewis (1999) performed Linear Stability Theory analysis (LST), and Unsteady 2D and 3D non-linear computations of buoyancy-induced flow in a sealed rotating annulus. LST suggests that numerous solutions with different discrete number of cyclonic-anticyclonic pairs are stable for given defining parameters. Non-linear computations confirm these results. The rolls are also precessing relative to the rotating surfaces. The rate of roll precession is dependent on the disc separation–an in-

crease in precession rate with a decrease in the separation. Heat transfer data was computed but the results were not analysed in details by Lewis (1999). The computations in the current study are extensions to Lewis (1999) with a focus on heat transfer correlations and factors that influence them.

2.2.2 Axial heat flux

Bohn *et al.*(1994) and Bohn *et al.*(1996) studied computationally and experimentally a rotating annulus with imposed axial thermal gradient (Figure 2.9). Using a cavity with the same geometrical dimensions as cavity B in Table 2.2, Bohn *et al.*(1996) derived the following correlation from the experimental data in the range $2 \times 10^8 < Ra_\phi < 10^{10}$:

$$Nu = 0.346 Ra_\phi^{0.124}. \tag{2.12}$$

The relation is displayed in Figure 2.10. It is compared with relations for a stationary vertical cavity, rotating annulus B with radial heat flux, and Rayleigh-Bénard convection. It is seen that Nu is much lower than that for cavity B.

The fluid circulates around the wall in thin layers, and there is nearly no motion in the core region. The fluid moves radially inward on the hot disc, then at the inner cylindrical surface from the hot to the cold side-disc, then moves radially outward on the cold disc, and finally back towards the hot disc at the outer cylindrical wall (Figure 2.9). Since Nu vs. Ra relations in stationary vertical enclosures (which are analogous to rotating cavity with axial heat flux) are similar to that in Rayleigh-Bénard convection (see previous sections and Figure 2.10), the reason that Nu is low in a rotating cavity with axial heat flux cannot simply be because the bulk of the fluid in the core is not involved in convecting heat.

A more influential factor is the Coriolis force which damps the fluid motion on both the hot and cold walls, thus producing lower heat transfer than that in a

stationary vertical cavity. The flow remained axisymmetric until about $Ra_\phi = 10^9$ (Bohn *et al.*, 1996) and may be still laminar at $Ra_\phi = 10^{11}$ (Bohn *et al.*, 1994). At Ra_ϕ above 10^9 and large enough Re_ϕ, the flow becomes three-dimensional, although essentially still two-dimensional because the flow is confined to near-wall regions (note that axisymmetry and two-dimensionality are not the same thing). The heat transfer is more sensitive to Re_ϕ (and so Coriolis force) precisely because the fluid velocity is weak. Actually, it is not so clear *whether* the fluid velocity is weak because of the influential Coriolis force *or* the Coriolis force is influential because the fluid velocity is weak. Obviously, there is a balance to be reached when the flow is developing.

Chapter 3

Dimensional and scaling analyses of Rayleigh-Bénard convection

3.1 Introduction

It is beneficial to carry out dimensional and scaling analyses to reveal the relationships between important quantities for a problem before proceeding to solve the governing equations directly. In many cases simple correlations appear; even when they do not, insights can be gained into the problem concerned. Some of the methods or results presented here are found in the literature, and the rest are results obtained by the author using existing techniques.

In this chapter, correlations of the dimensionless groups governing the heat transfer in Rayleigh-Bénard convection are derived. The values of the exponents and coefficients in the correlations are then calculated using various theoretical models. A new explanation of heat transfer in sealed rotating annuli is also suggested.

3.2 Correlating equations

For a Rayleigh-Bénard convection problem,

$$h = f(\mu, \rho, k, c_p, g\beta, \Delta T, d, l, J), \tag{3.1}$$

where h is the heat transfer coefficient, d is the distance between the horizontal walls (i.e. the hot and cold walls), and l is the distance between the vertical walls (i.e. the adiabatic walls). If the viscous energy dissipation to the thermal balance is taken into account, the mechanical equivalent of heat, J, must be included (Barenblatt, 1996, p.59). The term $g\beta$ plays an important part in the buoyancy effect for free convection using the Boussinesq approximation. Its two components are gathered in one group because it is not desirable to have them appearing separately in different dimensionless groups. Variations with temperature in the viscosity, specific heat capacity, and thermal conductivity of the fluid have been neglected. The class of fundamental units used consists of L (Length), M (Mass), T (Time), Θ (Temperature) and Q (Heat energy). There are ten variables and five fundamental units. Then according to Buckingham's Π theorem, there are $10 - 5 = 5$ dimensionless groups. It is common to assume that Equation(3.1) can be written as the following polynomial,

$$h = A\mu^{a_1}\rho^{a_2}k^{a_3}c_p^{a_4}(g\beta)^{a_5}(\Delta T)^{a_6}d^{a_7}l^{a_8}J^{a_9} + B\mu^{b_1}\rho^{b_2}k^{b_3}c_p^{b_4}(g\beta)^{b_5}(\Delta T)^{b_6}d^{b_7}l^{b_8}J^{b_9} + ..., \tag{3.2}$$

where $A, B, ...$ and $a_i, b_i, ...$ are constants. Barenblatt (1996, pp.34–37) proves that the dimension function (derived unit) of every physical quantity must be a power-law monomial of the fundamental units (i.e. a derived unit is always in the form of $M^aL^bT^c...$ instead of, for example, with $\sin L \log M$ or $M \exp L$ which cannot exist). The assumption used to form equation (3.2) is an indirect consequence of this power-law monomial.

The units of the ten variables are tabulated in table 3.1; each number indicates the dimension of each fundamental unit for that quantity.

Five linear simultaneous equations will result for each term in Equation (3.2). Considering only the first term, since there are nine unknowns in five simultaneous

	mass	length	time	temperature	heat
h	0	-2	-1	-1	1
μ	1	-1	-1	0	0
ρ	1	-3	0	0	0
k	0	-1	-1	-1	1
c_p	-1	0	0	-1	1
βg	0	1	-2	-1	0
ΔT	0	0	0	1	0
d	0	1	0	0	0
l	0	1	0	0	0
J	1	2	-2	0	-1

Table 3.1: Dimensions of variables

equations, five solutions must be expressed in terms of four other arbitrarily chosen unknowns. The choice of these unknowns will affect the dimensionless groups obtained. The variables c_p, ΔT, l and J are selected because it is desirable for them to appear in separate groups and each in one group only. Since h must be dimensionally consistent, the following equations can be written,

$$0 = a_1 + a_2 - a_4 + a_9,$$

$$-2 = -a_1 - 3a_2 - a_3 + a_5 + a_7 + a_8 + 2a_9,$$

$$-1 = -a_1 - a_3 - 2a_5 - 2a_9,$$

$$-1 = -a_3 - a_4 - a_5 + a_6,$$

$$1 = a_3 + a_4 - a_9.$$

a_3, a_5, a_1, a_2 and a_7 are solved in terms of a_4, a_6, a_8 and a_9 which are the power indices of the quantities c_p, ΔT, l and J:

$$a_3 = 1 - a_4 + a_9,$$

$$a_5 = a_6 - a_9,$$

$$a_1 = a_4 - 2a_6 - a_9,$$

$$a_2 = 2a_6,$$

$$a_7 = -1 + 3a_6 - a_8 - a_9.$$

Similarly, all the b_i's will have the same forms. Equation (3.2) then becomes,

$$h = A\frac{k}{d}\left(\frac{c_p\mu}{k}\right)^{a_4}\left(\frac{\beta g\Delta T\rho^2 d^3}{\mu^2}\right)^{a_6}\left(\frac{l}{d}\right)^{a_8}\left(\frac{Jk}{g\beta\mu d}\right)^{a_9} +$$

$$B\frac{k}{d}\left(\frac{c_p\mu}{k}\right)^{b_4}\left(\frac{\beta g\Delta T\rho^2 d^3}{\mu^2}\right)^{b_6}\left(\frac{l}{d}\right)^{b_8}\left(\frac{Jk}{g\beta\mu d}\right)^{b_9} + \ldots$$

or

$$Nu = A(Pr)^{a_4}(Gr)^{a_6}\left(\frac{l}{d}\right)^{a_8}\left(\frac{Jk}{g\beta\mu d}\right)^{a_9} + B(Pr)^{b_4}(Gr)^{b_6}\left(\frac{l}{d}\right)^{b_8}\left(\frac{Jk}{g\beta\mu d}\right)^{b_9} + \ldots \tag{3.3}$$

The coefficients and the exponents can be found in a straight-forward way by experiments; however, pure theoretical or semi-empirical (i.e. theoretical methods combined with empirical results) models can also be used. Some of these methods will be discussed in the next section. If a particular dimensionless group has a weak influence, it can be incorporated into the constant coefficient. The strength of influence from a group may also reach a constant value in certain flow regimes.

The derivation above and thus Equation (3.3) is also valid for free convective heat transfer in a vertical enclosure (where the heat transfer is through the side-walls and the horizontal walls are insulated). In this setup, d (the separation of the hot and cold walls) is the horizontal extent of the enclosure, while l is the height of the enclosure (see Section 2.1.2).

By definition, $Gr = \frac{Ra}{Pr}$. Rayleigh number compares the ratio of potential energy (from buoyancy) to energy dissipated by viscosity. It is a well-known result of linear stability analysis that Rayleigh-Bénard convection between two rigid and perfect conductors has a critical Rayleigh number of 1708. This critical Rayleigh

number is for extensive horizontal layers, i.e. the effects of vertical side walls are negligible. Below this critical Rayleigh number the fluid is stagnant and a conduction temperature profile is the result; above it a regime of steady two-dimensional buoyancy-driven convection rolls sets in. Changes to other flow regimes, such as steady three-dimensional, unsteady, etc, will occur as Rayleigh number increases through other critical values (see Krishnamurti, 1970a, 1970b & 1973).

The fourth group on the right-hand-side of Equation (3.3), $Jk/g\beta\mu d$, gives an important insight and requires explanation. The characteristic length is estimated through $Jk/g\beta\mu$. For water, $J = 1Nm/J$ (assuming viscous dissipation is converted into heat energy completely), $k = 0.6W/mK$, $g = 9.8m/s^2$, $\beta = 2 \times 10^{-4}K^{-1}$ and $\mu = 1 \times 10^{-3}kg/ms$, giving $Jk/g\beta\mu \approx 3 \times 10^5 m$. For air, for which $k = 2.6 \times 10^{-2}W/mK$, $\beta = 3.4 \times 10^{-3}K^{-1}$ and $\mu = 1.8 \times 10^{-5}kg/ms$, $Jk/g\beta\mu \approx 16300m$. The point to note here is that the characteristic length is large and therefore convection layers can usually be regarded as thin. If the dimensionless group $Jk/g\beta\mu d$ is large, its effect can be neglected. This is because for different values of the horizontal layer thickness d, $Jk/g\beta\mu d$ always remains large and so its variation with d can be neglected. It is a common practice in dimensional analysis to ignore a very small or a very large dimensionless parameter, although this is always a major assumption (Barenblatt, 1996, p.60).

When modelling free convection within horizontal layers in laboratory experiments or computations with the *same* fluid, the following similarity condition must be met,

$$\Delta T_{(M)} = \Delta T_{(P)} \left(\frac{d_{(P)}}{d_{(M)}} \right)^3 , \tag{3.4}$$

where subscript (M) denotes a variable from the 'model', and subscript (P) denotes a variable from the 'prototype'. In general, the model is a smaller version of the prototype in which geometric and dynamic similarities must be satisfied. The above

condition arises from the fact that the Grashof numbers must be the same in the model and the prototype. It can be shown that the dimensionless group which involves heat flux $\dot{q}$ is $\frac{\dot{q}\beta g\rho^2 d^4}{\mu^3 c_p}$, therefore,

$$\dot{q}_{(M)} = \dot{q}_{(P)} \left(\frac{d_{(P)}}{d_{(M)}} \right)^4 . \tag{3.5}$$

For convection within very thick layers, where $Jk/g\beta\mu d$ cannot be neglected, we find that modelling with the same fluid is impossible as $d_{(M)} = d_{(P)}$ (a full-scale modelling!). In the study of convection in the earth mantle or stellar atmospheres, where the thicknesses can reach thousands of kilometers, more ingenious models have to be devised. Using fluids with different properties to the real fluid is one example. In most engineering systems, however, Equations (3.4) and (3.5) still hold since the convection layers can usually be considered thin.

If we restrict our study to one type of fluid (e.g. air) only and assuming that the horizontal layer is extensive so that the term containing l/d, the aspect ratio, can be eliminated, equation (3.3) can be further simplified to:

$$Nu = C_1 Ra^{a_6} + C_2 Ra^{b_6} + ..., \tag{3.6}$$

where C_1, C_2, ... and a_6, b_6, ... are constants.

Using exactly the same argument as above, the correlation of Nusselt number for free convection within a rotating annulus, with a hot outer cylinder and cold inner cylinder, has the same form as Equation (3.6). Ra is then substituted by Ra_ϕ, the rotational Rayleigh number. Note that rotational Reynolds number does not appear explicitly as it is a function of rotational Rayleigh number, $Ra_\phi = Re_\phi^2 Pr\beta\Delta T\frac{d}{r_m}$, where $r_m = (a+b)/2$ is the mean radius, $Ra_\phi = \frac{r_m\Omega^2\beta\Delta T d^3}{\nu\kappa}$ is the rotational Rayleigh number and $Re_\phi = \frac{r_m\Omega d}{\nu}$ is the rotational Reynolds number.

3.3 Scaling laws

After the values of the exponents in equations such as equation (3.3) are determined, either from experiments or theoretical models, the resulting correlations are known as scaling laws. Much work has been devoted to finding the exponents. The assumptions used in the theoretical models can be somewhat arbitrary and experiments are needed to provide validations. The topic is not without competing theories. Siggia (1994) provides a good review; Grossmann & Lohse (2000 & 2001) refer to many recent developments and present perhaps the most complete general theory for scalings in thermal convection so far; for very readable accounts refer to Kadanoff (2001) and Sommeria (1999).

Most studies concentrate on heat transfer at very high Rayleigh numbers within the turbulent regime because this is where disagreements appear among different researchers, and the behaviour of the flow is known least due to the lack of a complete turbulent theory. The most significant scalings are presented here.

3.3.1 The 1/2-scaling (Kraichnan, 1962)

Since $\dot{q} = h\Delta T$, Nusselt number can be written as

$$Nu = \frac{\dot{q}}{k\Delta T/d}.$$

At very high Ra, velocity and heat flux $\dot{q}$ are independent of viscosity and conductivity of the fluid. It is seen that $(RaPr)^{1/2} \propto 1/k$ and from the equation above $Nu \propto 1/k$. Therefore, in the scaling

$$Nu \propto (RaPr)^{1/2}, \tag{3.7}$$

any dependence of $\dot{q}$ on k is cancelled.

An alternative argument is that, at very high Rayleigh number, heat is trans-

ported by buoyant structures (for example thermal plumes, blobs and eddies) that move at free fall velocity. This means that viscous force is negligible compared to the inertial force, and the buoyant structures accelerate as free undamped particles subject to the buoyancy force produced by gravity (Glazier, 1999). The free fall velocity can be scaled as $(\beta g \Delta T d)^{1/2}$, which is proportional to $Ra^{1/2}$. Therefore heat flux and so Nusselt number can be scaled as $Nu \propto Ra^{1/2}$. This scaling above can be traced to Kraichnan (1962).

This regime is triggered by the laminar-turbulent transition in the boundary layer and is believed to be the 'ultimate state' of high Rayleigh number thermal convection. Although the critical Rayleigh number is difficult to predict, there is some evidence that the regime is expected at $Ra = 10^{14}$ (Chavanne *et al.*, 1997). Recently, Roche *et al.*(2001) measured this 1/2-scaling for the first time in history. The transition to this regime was at $Ra \approx 10^{12}$. It should be noted that an enclosure with ordered surface roughness on the interior walls was used. The roughness may have initiated the turbulent boundary layers. The roughness effect is not well understood and is currently still under investigations. Another experimental study (Du & Tong, 2000) found that heat transfer is increased significantly over a rough surface. However this experiment produced a more commonly observed 2/7-scaling, and only the amplitude (i.e. the coefficient in the correlation) is increased (by 76%). The result of Roche *et al.*(2001) is also used to support Chavanne *et al.*(1997) who claimed to have observed the transition to the 1/2-scaling. There is alternative theoretical evidence that the regime most probably exists at sufficiently high Rayleigh number and low Prandtl number (Grossmann & Lohse, 2000), see section 3.3.6 below.

3.3.2 The 1/3-scaling (Howard, 1966)

An alternative scaling uses the simple assumption that the heat flux $\dot{q}$ is independent of the enclosure height d. Because $Nu \propto \dot{q}d$ and $Ra \propto d^3$, so the scaling

$$Nu \propto Ra^{1/3} \tag{3.8}$$

eliminates the dependence of $\dot{q}$ on d. The assumption is supported by the observation (Gille, 1967) that in the bulk flow the fluid is well mixed and the time-averaged temperature is uniform. Therefore temperature gradients are confined to thin boundary layers, where velocity is influenced by wall effects. This results in a thermal conductance across each boundary layer, where the temperature drop is $\Delta T/2$. Thus the heat flux is independent of the cell height d. This scaling originated from Priestley (1954). It is fairly close to the exponent values of around 0.3 obtained in many experiments (the same comment from Sommeria, 1999 and Grossmann & Lohse, 2000).

Howard (1966) formalised the idea that the boundary layer is marginally stable. He assumed that there is a thermal boundary layer of thickness δ_θ outside which the temperature gradient is negligible and within which there is no fluid motion (Figure 3.1). Considering the bottom boundary (at the hot wall), from the solution for one-dimensional heat conduction,

$$T = T_c + \frac{\Delta T}{2}(1 + erfc(\frac{z}{2\sqrt{\kappa t}})),$$

$$\delta_\theta = \sqrt{\pi \kappa t}.$$

The thickness δ_θ should be small enough for the layer to be stable but will grow by thermal diffusion until time t_c when $\delta_\theta = \delta_c = \sqrt{\pi \kappa t_c}$ and then breaks down reducing δ_θ to zero. The whole process then repeats itself. The critical Rayleigh

number for break down of the boundary layer is,

$$Ra_c = \frac{\beta g \Delta T \delta_c^3}{2\kappa\nu}$$

$$\Rightarrow \delta_c = \left(\frac{2\kappa\nu}{\beta g \Delta T}\right)^{1/3} Ra_c^{1/3}$$

$$\Rightarrow \frac{\delta_c}{d} = \left(\frac{2Ra_c}{Ra}\right)^{1/3}.$$

The time-averaged heat flux is

$$\dot{q} = \frac{1}{t_c}\int_0^{t_c} \frac{k\Delta T}{2\sqrt{\pi\kappa t}} dt = \frac{k\Delta T}{\delta_c}.$$

Since $Nu = \frac{\dot{q}d}{k\Delta T}$,

$$Nu_{(Pr \gtrsim 1)} = \frac{d}{\delta_c} = \left(\frac{Ra}{2Ra_c}\right)^{1/3}.$$

A reasonable value of Ra_c is 1100 (Chandrasekhar,1961). Therefore,

$$Nu_{(Pr \gtrsim 1)} = 0.0769 Ra^{1/3}. \tag{3.9}$$

Note that there is no dimensional consideration and the value of the coefficient appears in the derivation. The correlation (3.9) is plotted in Figure 3.2. Its validity is limited to fluids of $Pr \gtrsim 1$ in order to support the assumption that there is negligible fluid motion inside the thermal boundary layer, which is only possible (if it is possible at all) if the thermal boundary layer is embedded within the kinetic boundary layer, i.e. for cases where Pr is greater than or approximately equal to unity. This model of a growing conduction layer cannot be adapted easily to low Prandtl number cases where the thermal boundary layer may grow into the 'advective' region of the flow. The scaling appears to be confirmed by the experiments of Ashkenazi & Steinberg (1999) and Lui & Xia (1998); see Table 3.2 below.

Using an analytical conduction layer model and empirical adjustment, Hol-

lands *et al.*(1975) were able to derive a correlation that predicts Nusselt number right from the subcritical Rayleigh number:

$$Nu_{(Pr\approx 0.7)} = 1 + 1.44max\left\{\left(1 - \frac{1708}{Ra}\right), 0\right\} + max\left\{\left(\frac{Ra}{5830}\right)^{1/3} - 1, 0\right\}. \quad (3.10)$$

This is plotted in Figure 3.2. Previously this correlation had been verified up to $Ra = 10^8$. Comparison with the result of Niemela *et al.*(2000) (see also Table 3.2 below) indicates that its prediction is fairly accurate even at very high Rayleigh number. Note that at very high Rayleigh number, Equation 3.10 gives a 1/3-scaling.

3.3.3 The 2/7-scaling

It is also found in many laboratory experiments (e.g. Castaing *et al.*(1989), Wu & Libchaber (1991), Shen *et al.*(1996), Chavanne *et al.*(1997), Cioni *et al.*(1997)) that a single term of Equation (3.6), $Nu \propto Ra^{\gamma}$, is sufficient, with $\gamma = 0.282 \pm 0.006 \approx \frac{2}{7}$ as the most robust exponent. A model which gives this scaling is thus needed. The following theoretical (or so-called phenomenological) model is inspired by Castaing *et al.*(1989). Here, the current author has simplified the derivation of the scaling, and at the same time obtained relationships that also include Pr.

Three flow regions of different widths (Figure 3.3) are identified: A central region occupying most of the enclosure which contains buoyant structures and has temperature fluctuations, ΔT_{fluc}, that enable heat flux equal to that across the boundary layers; a thin mixing layer where hot (or cold) fluid breaks from the stagnant thermal boundary layers and accelerates to speeds that allow the fluid to merge into the central region; an even thinner, aforementioned, thermal boundary layer (thickness δ_θ) where heat is transported by conduction only. Note that only the bottom horizontal wall is shown in Figure 3.3; the three zones described above are symmetrical about a horizontal axis through the centre of the enclosure. This

type of flow structure was observed in the experiment of Qiu & Tong (2001).

The central region is in essence the same as the model in Section 3.3.1 above in which viscosity and conductivity are negligible compared to turbulent mixing, and a typical velocity scale is,

$$u_c \sim (\beta g \Delta T_{fluc} d)^{1/2}. \tag{3.11}$$

The heat flux is scaled as,

$$\dot{q} \sim c_p \rho_0 u_c \Delta T_{fluc}. \tag{3.12}$$

By definition,

$$\dot{q} = \frac{Nuk\Delta T}{d} \sim \frac{k\Delta T}{\delta_\theta} \tag{3.13}$$

$$\Rightarrow Nu \sim \frac{d}{\delta_\theta}. \tag{3.14}$$

The thermal boundary layer may be nested within the viscous boundary layer or vice versa depending on the Prandtl number (Figures 3.3.a & 3.3.b). It will become clear that this has an effect on the scaling obtained. It can be shown that for the laminar kinetic boundary layer,

$$\delta_u \sim \frac{d}{Re^{1/2}}, \tag{3.15}$$

where $Re = u_c d/\nu$; u_c is the large-scale roll velocity in the central region (see Equation (3.11)). This velocity is sometimes referred to as 'wind of turbulence', which has been observed in many experiments including Qiu *et al.*(2000) and Niemela *et al.*(2001). It is the shear from this wind of turbulence that produces and stabilises both the thermal and the viscous boundary layers, even at high Rayleigh number (Lui & Xia, 1998).

First, we look at cases of moderate to high Prandtl number ($Pr \gtrsim 1$), i.e. the thermal boundary layer is nested within the kinetic boundary layer (Figure 3.3.a).

It is assumed that the conductive thermal boundary layer breaks into filaments of thickness similar to the original boundary layer thickness δ_θ (Figure 3.4.a). The filaments accelerate to u_c when the buoyancy force balances the viscous force,

$$\beta g \Delta T \rho_0 \delta_\theta \sim \mu \frac{u_c}{\delta_u}. \tag{3.16}$$

From order of magnitude analysis in the dominant terms of the thermal boudary layer equation (Grossmann & Lohse, 2001), it can be shown that when $\delta_u > \delta_\theta$,

$$Nu \sim Re^{1/2} Pr^{1/3}. \tag{3.17}$$

Combining Equations (3.11) to (3.17), we obtain

$$Nu_{(Pr \gtrsim 1)} \sim Ra^{2/7}. \tag{3.18}$$

Therefore the effect of Prandtl number on Nusselt number is negligible for this range of Prandtl numbers. Cioni *et al.*(1997) and Grossmann & Lohse (2000 & 2001) reached the same conclusion. Although Cioni *et al.*(1997) derived $Nu_{(Pr \gtrsim 1)} \sim Ra^{2/7} Pr^{-1/7}$, i.e. increasing Prandtl number reduces heat transfer, we stress here that the disagreement is small for most practical or comparison purposes and may be within experimental uncertainties (Grossmann & Lohse, 2000). Grossmann & Lohse (2001) showed that, over the entire range of Rayleigh numbers, Nusselt number is independent of the Prandtl number for very high Prandtl number regimes (see Section 3.3.6 for more details). Air ($Pr \approx 1.0$), helium ($Pr \approx 0.7$) and water ($Pr \approx 7.0$) are examples of fluids that satisfy the relationship (3.18). Using the value of the coefficient determined in Castaing *et al.*(1989), from an experiment with helium gas, Equation (3.18) becomes

$$Nu_{(Pr \gtrsim 1)} = (0.23 \pm 0.03) Ra^{2/7}. \tag{3.19}$$

Investigators	fluid(Pr)	Ra range	γ
Ashkenazi & Steinberg(1999)	$SF_6(1-93)$	10^9-10^{14}	0.30 ± 0.03
Lui & Xia(1998)	$H_2O(\approx 7)$	$2\times10^8-2\times10^{10}$	0.28 ± 0.06
Shen *et al.*(1996)	$H_2O(\approx 7)$	$8\times10^7-7\times10^9$	0.281 ± 0.015
Castaing *et al.*(1989)	$He(0.7-1)$	$\leq 10^{11}$	0.282 ± 0.006
Wu & Libchaber(1991)	$He(0.6-1.2)$	$4\times10^7-10^{12}$	0.285
Chavanne *et al.*(1997)	$He(0.6-0.73)$	$3\times10^7-10^{11}$	2/7
Niemela *et al.*(2000)	$He(\approx 0.7)$	10^6-10^{17}	0.309 ± 0.0043
Cioni *et al.*(1997)	$Hg(0.025)$	$5\times10^6-10^8$	0.26 ± 0.02
Cioni *et al.*(1997)	$Hg(0.025)$	$4\times10^8-2\times10^9$	0.20
Glazier *et al.*(1999)	$Hg(0.025)$	$2\times10^5-8\times10^{10}$	0.29 ± 0.01

Table 3.2: Exponents γ of the power law $Nu\sim Ra^{\gamma}$ from different experiments.

This relationship is plotted in Figure 3.2. The exponent is independent of the aspect ratio, (l/d), for aspect ratios greater than 1/2. However, the coefficients are dependent on aspect ratio (Wu & Libchaber, 1992). Equation (3.19) is valid for $l/d=1$. The exponent 2/7 compares very well with the exponents obtained by experiments of Shen *et al.*(1996), Castaing *et al.*(1989), Wu & Libchaber (1991) and Chavanne *et al.*(1997) among many others not reported here (see Table 3.2). The experiment by Niemela *et al.*(2000) is considered to be very reliable and with the largest range of Rayleigh number to date. Their exponent of 0.309 ± 0.0043 confirms neither the 1/3– nor the 2/7–scaling.

For low Prandtl number ($Pr\lesssim 1$) where the thermal boundary layer is thicker than the viscous boundary layer (Figure 3.4.b), Equation (3.16) is modified slightly:

$$\beta g\Delta T\rho_0\delta_u\sim\mu\frac{u_c}{\delta_u}. \tag{3.20}$$

This is because the part of the thermal boundary layer which is outside the viscous boundary layer cannot exist stably, therefore the detaching filament has a length scale of δ_u (instead of δ_θ for the moderate to high Prandtl number case above). Analysing the order of magnitude for terms in the thermal boundary layer equation

as before gives

$$Nu \sim Re^{1/2} Pr^{1/2}, \tag{3.21}$$

for $\delta_u < \delta_\theta$. Other relations remain unchanged, the following scaling is then obtained,

$$Nu_{(Pr \lesssim 1)} \sim Pr^{2/7} Ra^{2/7}. \tag{3.22}$$

This is the same scaling derived by Cioni *et al.*(1997). Assuming an aspect ratio $l/d = 10$, and using a more complicated derivation, they obtained the following correlation:

$$Nu_{(Pr \lesssim 1)} = 0.25 Pr^{2/7} Ra^{2/7}. \tag{3.23}$$

For mercury ($Pr = 0.025$),

$$Nu_{(Hg)} = 0.0871 Ra^{2/7}. \tag{3.24}$$

The following correlation was obtained from the experiment of Cioni *et al.*(1997) in a unity aspect ratio cell:

$$Nu_{(Hg)} = (0.140 \pm 0.005) Ra^{(0.26 \pm 0.02)}, \tag{3.25}$$

for $5 \times 10^6 < Ra < 5 \times 10^8$. Equation (3.24) is plotted in Figure 3.2. Refer to table 3.2 for other exponents for low Prandtl number fluid.

Glazier *et al.*(1999), see Table 3.2, obtained experimentally an exponent very close to, though probably not validating, 2/7. A unifying theory by Grossmann & Lohse (2000) explains disagreements, such as this, in the exponents of the correlation, as well as more glaring differences arising from different theoretical models and laboratory experiments.

3.3.4 The 1/4-scaling

Using the same Castaing *et al* model, yet another scaling will be derived. If it is assumed that the roll velocity u_c is proportional to the free-fall velocity (Xin & Xia, 1996) then,

$$u_c \sim (\beta g \Delta T d)^{1/2}. \tag{3.26}$$

Equations (3.14) to (3.17), and (3.26) are used to obtain

$$Nu_{(Pr \gtrsim 1)} \sim Pr^{-1/12} Ra^{1/4}. \tag{3.27}$$

The exact correlation has also been obtained by Grossmann & Lohse (2000). This is their regime I_u shown in Table 3.3. Nu is weakly dependent on Pr. Nu decreases with increasing Pr. This is because an increase in ν reduces convective heat transfer.

For $Pr \lesssim 1$, Equations (3.14), (3.15), (3.20), (3.21) and (3.26) are used to derive

$$Nu_{(Pr \lesssim 1)} \sim Pr^{1/4} Ra^{1/4}. \tag{3.28}$$

The exponent 1/4 for Pr is different from that derived by Grossmann & Lohse (which is 1/8), but the same relation has been obtained by other investigators (see Cioni *et al.*, 1997). The 1/4–regime is validated by the experiments of Lui & Xia (1998) and Cioni *et al.*(1997). This scaling is well-known in engineering literature. Grossmann & Lohse argue that it is this 1/4–regime that has been observed in most turbulent convection experiments, but usually the scaling is affected by scalings from neigbouring regimes (see Section 3.3.6).

3.3.5 Other scalings

Miscellaneous other scalings will be derived in this section, before Grossmann & Lohse's results are described in the next section. For convenience, certain relations

are repeated here: Roll velocity or wind of turbulence $u_c \sim (\beta g \Delta T_{fluc} d)^{1/2}$; heat flux $\dot{q} \sim c_p \rho_0 u_c \Delta T_{fluc}$; and Nusselt number $Nu = \frac{\dot{q} d}{k \Delta T}$. From these relations,

$$Re \sim Nu^{1/3} Ra^{1/3} Pr^{-2/3}. \tag{3.29}$$

Substituting (3.29) to Equations (3.17) and (3.21) respectively the following relations result:

$$Nu_{(Pr \gtrsim 1)} \sim Ra^{1/5}, \tag{3.30}$$

$$Nu_{(Pr \lesssim 1)} \sim Pr^{1/5} Ra^{1/5}. \tag{3.31}$$

This 1/5-scaling is observed in one of the experiments of Cioni *et al.*(1997), see Table 3.2. Grossmann & Lohse also derived the same scaling for their regime II.

Next, the Castaing *et al.* model is used again. Combining $\beta g \Delta T \rho_0 \delta_\theta \sim \mu u_c / \delta_u$ (3.16), $Nu \sim d/\delta_\theta$ (3.14), $\delta_u \sim d/Re^{1/2}$ (3.15) and $Re \sim Nu^{1/3} Ra^{1/3} Pr^{-2/3}$ (3.29) results in

$$Nu_{(Pr \gtrsim 1)} \sim Pr^{-1/9} Ra^{7/18}. \tag{3.32}$$

To the knowledge of this author, this 7/18–scaling has not been derived theoretically before. It is probably a combination of regimes I and III_u that are due to Grossmann & Lohse. This point will be discussed in more detail in the next section. This scaling may also be that observed by Chavanne *et al.*(1997).

For $Pr \lesssim 1$, combining $\beta g \Delta T \rho_0 \delta_u \sim \mu u_c / \delta_u$ (3.20), $\delta_u \sim d/Re^{1/2}$ (3.14)and $Re \sim Nu^{1/3} Ra^{1/3} Pr^{-2/3}$ (3.29) to obtain

$$Nu_{(Pr \lesssim 1)} \sim Pr^{1/2} Ra^{1/2}. \tag{3.33}$$

The 1/2-scaling from Section (3.3.1) is again derived. This applies to regimes II_l', IV_l, IV_l' and IV_u' of Grossmann & Lohse (see Table 3.3 and Figure 3.5). It should be noted here that the scaling is derived initially with $\delta_u \sim d/Re^{1/2}$ which applies to

a laminar kinetic boundary layer only, i.e. it is valid for regime IV_l. However, when the Rayleigh number is sufficiently high for the kinetic boundary layer to become turbulent, it can be argued that both the kinetic and thermal dissipation should be scaled as in the turbulent bulk. Thus regimes Regimes II_l', IV_l' and IV_u', which are the 'turbulent kinetic boundary layer' extensions of regimes II_l, IV_l and IV_u respectively at higher Rayleigh number, should acquire the scalings from the bulk-dominated regime IV_l. This detail is repeated in the next section where Grossmann & Lohse's theory is introduced.

3.3.6 Grossmann & Lohse's unifying theory

Grossmann & Lohse (2000 & 2001) devised a theory that involves whether the boundary layer or the bulk flow contributes to the global kinetic (ϵ_u) and global thermal (ϵ_θ) dissipation rates, and whether the thermal or the kinetic boundary layer is the thicker. They were able to derive ten regimes with different scalings. Only the more important results are summarised here. Refer to the original papers for the description of the theory, the derivation of the scalings and coefficients, and delineation of the different regimes in the $Pr - Ra$ diagram. Their theory is the most complete to date, covering a large range of Rayleigh and Prandtl numbers.

Table 3.3 shows some of the significant regimes. The theory has an advantage in allowing the determination of the range of Prandtl and Rayleigh numbers in which a particular scaling applies, rather than just indicating either $Pr \gtrsim 1$ or $Pr \lesssim 1$ as was done in previous sections. Refer to Figure 3.5 for the regime diagram in the $Pr - Ra$ plane. Regimes II_l', IV_l' and IV_u', shown in Figure 3.5 but not depicted in table 3.3, occur at higher Rayleigh numbers (to the right of the dashed line) where the kinetic boundary layer becomes turbulent. Grossmann & Lohse argue that the kinetic and thermal dissipations are then bulk dominated and so the regimes

Regime	Dominance of ϵ_u, ϵ_θ by	BL(Pr)	Ra range	Nu
I_l	BL, BL	$\delta_u < \delta_\theta(\lesssim 1)$	$< 10^{12}$	$0.22Ra^{1/4}Pr^{1/8}$
I_u	BL, BL	$\delta_u > \delta_\theta(\gtrsim 1)$	$< 10^{12}$	$0.31Ra^{1/4}Pr^{-1/12}$
I_∞	BL, BL	$\delta_u > \delta_\theta(\gg 1)$	$< 10^{12}$	$0.35Ra^{1/4}$
II_l	bulk, BL	$\delta_u < \delta_\theta(\lesssim 1, \ll 1)$	$> 10^6$	$0.37Ra^{1/5}Pr^{1/5}$
III_u	BL, bulk	$\delta_u > \delta_\theta(\gtrsim 1, \gg 1)$	$> 10^{12}$	$0.018Ra^{3/7}Pr^{-1/7}$
III_∞	BL, bulk	$\delta_u > \delta_\theta(\gg 1)$	$> 10^{12}$	$0.027Ra^{1/3}$
IV_l	bulk, bulk	$\delta_u < \delta_\theta(\lesssim 1, \ll 1)$	$> 10^{12}$	$0.0012Ra^{1/2}Pr^{1/2}$
IV_u	bulk, bulk	$\delta_u > \delta_\theta(\lesssim 1, \gtrsim 1)$	$> 10^{12}$	$0.050Ra^{1/3}$

Table 3.3: Scalings from different regimes according to Grosmann & Lohse(2000 & 2001). ϵ_u and ϵ_θ denote global kinetic and thermal dissipative rate respectively; BL denotes boundary layer; and 'bulk' denotes bulk flow. The Prandtl and Rayleigh numbers range are not to be interpreted rigorously(cross-refer figure 3.5). The coefficients, obtained from experiments, are also not to be interpreted rigorously as they are aspect ratio dependent, and the methods used to caculate them can be somewhat arbitrary. Refer to Grossmann & Lohse(2000, 2001) for details.

should have the same scalings as in regime IV_l, where the global kinetic and thermal dissipations are dominated by the bulk flow.

Most flows measured in laboratory experiments are located in regime I. However, the scalings observed are always corrected by those from neighbouring regimes. In this case, regime I_u by regimes IV_u and III_u. Grossmann & Lohse (2000) suggested the following combination (I_u & IV_u) for $Pr = 1$:

$$Nu = 0.27Ra^{1/4} + 0.038Ra^{1/3}, \tag{3.34}$$

which resembles $Nu = 0.22Ra^{0.2875\pm0.0175}$. This range of exponent encompasses $\gamma \approx 2/7$ from various experiments, as well as $\gamma \approx 0.3$ by Glazier *et al.*(1999) and Niemela *et al.*(2000) (see Table 3.2). Grossmann & Lohse claim that investigators (e.g. Chavanne *et al.*, 1997) who observed the transition to the ultimate regime of 1/2-scaling had in fact measured a regime I_u which was corrupted by regime III_u. Regime III_u has a 3/7-scaling and is more distinguishable from regime IV_u as Equation (3.34) illustrates. These combinations are not arbitrary. On the $Pr - Ra$

diagram, regimes III_u and IV_u are adjacent and located to the right, at higher Rayleigh number, of regime I_u. A combination of regimes I_u and III_u produces a local slope $0.37 \leq \gamma \leq 0.41$ in the range $10^8 \leq Ra \leq 10^{12}$ that incorporates the exponent 7/18 derived in Equation (3.32).

It is also expected that the dominance of both the ϵ_u and ϵ_θ at the boundary layers (regimes I) will be influenced by their dominance in the bulk flow (regimes IV_l, IV_l', IV_u') at higher Rayleigh number where the turbulent mixing in the bulk flow is present. So a transition to 1/2-scaling, or the 1/2-scaling itself (Roche *et al.*, 2001), can be observed after all.

3.3.7 Scalings from sealed rotating annuli

Bohn *et al.*(1995) carried out experiments on free convective heat transfer in sealed rotating annuli with radial heat flux. The inner cylinder was cold, outer cylinder hot, and the two side discs were insulated. The axis of rotation passes through the common centre of the cylinders (see Section 2.2.1). Buoyancy is set up in the centrifugal field, and affected by the Coriolis force; gravity may be neglected due to the high rotational speeds. These cases are a main subject of this thesis and will be studied in detail in later chapters. The rotating annulus flow can approximate Rayleigh-Bénard convection (King & Wilson, 2002), especially when the radial gap is small, i.e. when the radius ratio is approximately equal to unity. In such cases, Coriolis forces may be neglected. Bohn *et al.*(1995) made the same comment.

An important question is how much is the heat transfer affected when rotational effects cannot be ignored. Bohn *et al.*(1995) found that the scaling $Nu \propto Ra_\phi^\gamma$ still holds (see Equation 3.6). They found γ values of 0.211, 0.213 and 0.228 for three different rotating annuli. A typical correlation is plotted in Figure 3.2. It is seen that the Nusselt number (a measure of heat transfer efficiency) is considerably

lower than in Rayleigh-Bénard convection. Moreover, we may infer that the rotational effects may have stabilised the flow so that it remains laminar even at high Rayleigh numbers (laminar Rayleigh-Bénard convection has $\gamma \approx 0.25$, Rohsenow *et al.*, 1998), see Owen & Wilson (2000). There is no direct evidence for laminar flow at high Rayleigh number, as no measurements or visualisations were made by Bohn *et al.*(1995) for the flow structures.

Assuming that free convective heat transfer in all types of sealed enclosure, with heat flux anti-parallel to the external force (either gravitational or centrifugal) that sets up the buoyancy, can only produce those pure scalings in Table 3.3 (or Figure 3.5) identified by Grossmann & Lohse, albeit with different delineations and transitions, we can suggest a possible explanation for the scalings observed by Bohn *et al.*(1995). This assumption implies that free convective flow in a rotating annulus is still governed by the dominance of either the boundary layers or the bulk flows on the global kinetic and global thermal dissipations, as in the theory of Grossman & Lohse. All possibilities of contribution to the dissipations have been considered in the theory; thus, it is plausible that all pure scalings have already been revealed.

Here, we suggest that Regime I_l, with moderately low Prandtl number and moderately high Rayleigh number is corrected by regime II_l (see Figure 3.5). Thus (with Pr approximated as 1),

$$Nu = 0.27 Ra_\phi^{1/4} + 0.97 Ra_\phi^{1/5}. \tag{3.35}$$

As discussed in Section 3.3.3, the coefficients are dependent on aspect ratios (Wu & Libchaber, 1992), therefore equation (3.35) cannot be compared directly with the experimental data of Bohn *et al.*(1995) because of the differences in geometries. More importantly, however, the exponents are not affected. Plotting Equation (3.35) on a log–log scale shows that the local gradient(γ value) varies between approximately

0.218 and 0.226 (Figure 3.6.a) in the range $10^6 \leq Ra_\phi \leq 10^{12}$, within which Bohn *et al.*'s experiments were carried out. Although the range of gradients does not enclose those scalings obtained by Bohn *et al.*, it is close to them and has a median of about 0.222. Figure 3.6.b shows Nu from Equation (3.35), normalised by Ra_ϕ^γ, with different values of γ. The minimum and maximum values of γ obtained by Bohn *et al.*(1995) are 0.211 and 0.228 respectively. Except for $\gamma = 0.2$, the other two lines are almost straight and horizontal, indicating the scaling exponent cannot be represented by a pure scaling $\gamma = 0.2$. It is believed that $\gamma = 1/4$ from regime I_l and $\gamma = 1/5$ from Regime II_l is a suitable combination. It can be argued that this combination is not arbitrary as Regime II_l is just below Regime I_l in the phase diagram (see Figure 3.5). Moreover, it can be explained by the influence from the dominance of ϵ_u from the bulk flow (see Table 3.3), as the viscous boundary layer is weakened by the rotational effects because velocity fluctuations in the radial direction are inhibited. The extent to which this is true remains to be tested by more accurate study of the structures of the boundary layers in the rotational system (beyond the scope of this thesis). To recapitulate, it is suggested that the scalings obtained by Bohn *et al.*(1995) can be explained by an often observed 1/4-scaling being corrupted by a neighbouring 1/5-regime. It is not necessary to resort to the suggestion that the flows remained laminar at high Rayleigh number, therefore allowing the possiblity that the bulk flow might after all be turbulent.

3.4 Concluding remarks

In this chapter, the dimensionless groups governing heat transfer in Rayleigh-Bénard convection are derived. It is explained that Nusselt number and Rayleigh number can be related in the so-called scaling law $Nu \sim Ra^\gamma$.

We described derivations of some well-known values for γ such as $\gamma = \frac{1}{2}$ and

$= \frac{1}{3}$. Simple derivations inspired by the phenomenological model of Castaing *et al.*(1989) obtain various other common scalings, such as $\gamma = \frac{2}{7}$, $\gamma = \frac{1}{4}$, and $\gamma = \frac{1}{5}$, which were measured previously in experiments or derived with more complicated theory. The 'unifying' theory of Grossmann & Lohse that derives comprehensively most (if not all) of the pure scaling laws are also summarised.

Finally, the results of Grossmann & Lohse are used to suggest an alternative explanation to the scaling laws of $\gamma \approx 0.21$ measured in rotating annulus experiments by Bohn *et al.* There has been suggestion that the flows remained laminar even at high Rayleigh number (laminar flow has $\gamma \approx 0.25$). Since no flow visualisation was conducted, the latter suggestion has not been confirmed. The theory of Grossmann & Lohse permits well-mixed turbulent bulk flow. As is reported later in the thesis, computations performed here were not able to reproduce the $\gamma \approx 0.21$ for free convection in rotating annuli.

Chapter 4

Two-dimensional (radial-tangential) computations

4.1 Introduction

Free convective heat transfer inside sealed, air-filled rotating annuli with an imposed radial thermal gradient is the main object of this study. We are interested in particular in the relationship between Nusselt number and Rayleigh number. Factors which influence the heat transfer are identified.

In this chapter, flows in the radial-tangential plane are investigated. The flow is assumed to be invariant in the axial direction. The governing equations are derived and the computational methods and procedures used to solve these equations are described.

Free convective heat transfer in flat horizontal layers with heating from below, the so-called Rayleigh-Bénard convection, has been extensively studied for decades (see Chapter 3; Koschmieder, 1993; Siggia, 1994; and Grossmann & Lohse, 2000 & 2001). This type of flow can be approximated by a rotating annulus with large value of the ratio $\frac{a+b}{2(b-a)}$ (see Figure 2.7), and a suitable angular velocity Ω such that the centrifugal acceleration $r\Omega^2$ replaces the gravitational acceleration. Under these conditions the Coriolis forces are negligible; they can also be removed by

eliminating artificially certain terms in the governing equations. Results obtained for Rayleigh-Bénard-type convection also may assist understanding of rotating annulus convection.

It is accepted widely that $Nu \propto Ra^{\gamma}$ holds for Rayleigh-Bénard convection. Most laboratory experiments and theoretical analyses (refer to Section 2.1.1 and Chapters 3 for more details), beginning with those of Heslot *et al.*(1987) and Castaing *et al.*(1989), seem to suggest $\gamma = 0.282 \pm 0.006 \approx \frac{2}{7}$ as the most robust exponent (Grossman & Lohse, 2000). Grossman & Lohse devised a theory that produced a relationship

$$Nu = 0.27Ra^{\frac{1}{4}} + 0.038Ra^{\frac{1}{3}},$$

which resembles a $Nu \propto Ra^{2/7}$ relationship (see section 3.3.6). The coefficients in the above equation were determined with experimental input. Correlations proposed by other investigators (for e.g. Niemela *et al.*(2000) and Hollands *et al.*(1975)) will also be used for the purpose of comparison.

Bohn *et al.*(1995) carried out experiments, for $10^7 \leq Ra_{\phi} \leq 10^{11}$, for free convective heat transfer in sealed air-filled rotating annuli. They also reported a $Nu \propto Ra_{\phi}^{\gamma}$ relationship, with γ values close to 0.2. The heat transfer for rotating annuli, in the experiments of Bohn *et al.* is much lower than that for Rayleigh-Bénard convection (Chapters 2 & 3).

It is fairly well-known that free convective heat transfer in sealed enclosures of different shapes, geometries and orientations are rather similar (see Section 2.1 for examples). The main factors which cause heat transfer in a rotating annulus to differ from that in Rayleigh-Bénard convection deserve investigation. Using the approximation described above, computations for a stationary annulus approximating Rayleigh-Bénard convection are performed, and the effect of changing the radius ratio $\frac{a}{b}$ is investigated. Rotating annulus flows are then computed. The results in-

dicate that the curvature of the radial gaps and Coriolis effects cannot explain the significant reduction in heat transfer, for the Bohn *et al.* experiments, compared to that in Rayleigh-Bénard convection. The more important factors may be the boundary conditions of the enclosure walls, effects of the side discs, and possibly the behaviour of the bulk flow and boundary layers (as discussed in section 3.3.7).

4.2 Governing equations

The fluid density is assumed to depend linearly on temperature, and is not a function of pressure. This is the Boussinesq approximation:

$$\rho = \rho_0[1 - \beta(T - T_c)], \tag{4.1}$$

where $\beta(T - T_c) \ll 1$. The approximation is applied to the centrifugal terms (which gives rise to buoyancy) and Coriolis terms only and the fluid is considered to be incompressible in other terms.

Thus the three-dimensional Navier-Stokes equations in cylindrical polar coordinates and rotating frame of reference with the Boussinesq approximation are

$$\partial_r u + \frac{u}{r} + \frac{1}{r}\partial_\theta v + \partial_z w = 0, \tag{4.2}$$

$$\partial_t u + (\underline{u}.\nabla)u - \frac{v^2}{r} - \frac{\rho}{\rho_0}(2\Omega v + \Omega^2 r) = -\frac{1}{\rho_0}\partial_r p + \nu(\nabla^2 u - \frac{2}{r^2}\partial_\theta v - \frac{u}{r^2}), \tag{4.3}$$

$$\partial_t v + (\underline{u}.\nabla)v + \frac{uv}{r} + \frac{\rho}{\rho_0}(2\Omega u) = -\frac{1}{\rho_0 r}\partial_\theta p + \nu(\nabla^2 v - \frac{2}{r^2}\partial_\theta u - \frac{v}{r^2}), \tag{4.4}$$

$$\partial_t w + (\underline{u}.\nabla)w = -\frac{1}{\rho_0}\partial_z p + \nu\nabla^2 w, \tag{4.5}$$

$$\partial_t T + (\underline{u}.\nabla)T = \kappa\nabla^2 T, \tag{4.6}$$

where the divergence and Laplace operators are respectively,

$$(\underline{u}.\nabla) \equiv u\partial_r + \frac{v}{r}\partial_\theta + w\partial_z, \qquad \nabla^2 \equiv \partial_{rr}^2 + \frac{1}{r}\partial_r + \frac{1}{r^2}\partial_{\theta\theta}^2 + \partial_{zz}^2.$$

The equations above were not computed directly in this work. Instead further equations are derived from them; they are included here for completeness and will be referred to occasionally.

In the rest of this section, dimensionless radial-tangential flow equations in streamfunction–vorticity formulation are derived. A streamfunction–vorticity formulation is used to eliminate the difficulties in determining the pressure boundary values associated with a primitive variable formulation. It is also used in preference to the vorticity–velocity formulation as the latter requires more operations due to an additional Poisson equation and a staggered grid that is necessary for divergence-free velocity and vorticity fields (Lewis, 1999).

When axial velocity and z derivatives are neglected from Equations (4.2) to (4.6), the following equations are obtained:

$$\partial_r u + \frac{u}{r} + \frac{1}{r}\partial_\theta v = 0, \tag{4.7}$$

$$\partial_t u + (\underline{u}.\nabla)u - \frac{v^2}{r} - \frac{\rho}{\rho_0}(2\Omega v + \Omega^2 r) = -\frac{1}{\rho_0}\partial_r p + \nu(\nabla^2 u - \frac{2}{r^2}\partial_\theta v - \frac{u}{r^2}), \tag{4.8}$$

$$\partial_t v + (\underline{u}.\nabla)v + \frac{uv}{r} + \frac{\rho}{\rho_0}(2\Omega u) = -\frac{1}{\rho_0 r}\partial_\theta p + \nu(\nabla^2 v - \frac{2}{r^2}\partial_\theta u - \frac{v}{r^2}), \tag{4.9}$$

$$\partial_t T + (\underline{u}.\nabla)T = \kappa\nabla^2 T, \tag{4.10}$$

where the divergence and Laplace operators are

$$(\underline{u}.\nabla) \equiv u\partial_r + \frac{v}{r}\partial_\theta, \qquad \nabla^2 \equiv \partial^2_{rr} + \frac{1}{r}\partial_r + \frac{1}{r^2}\partial^2_{\theta\theta}.$$

The streamfunction, ψ, and vorticity, $\underline{\omega}$, are defined as

$$u = \frac{1}{r}\partial_\theta \psi, \qquad v = -\partial_r \psi, \tag{4.11}$$

$$\underline{\omega} = \nabla \times \underline{u} = \frac{1}{r}\begin{vmatrix} \underline{i} & r\underline{j} & \underline{k} \\ \partial_r & \partial_\theta & \partial_z \\ u & rv & w \end{vmatrix} = \begin{pmatrix} \frac{1}{r}\partial_\theta w - \partial_z v \\ \partial_z u - \partial_r w \\ \partial_r v + \frac{v}{r} - \frac{1}{r}\partial_\theta u \end{pmatrix}. \tag{4.12}$$

But here, due to the two-dimensionality,

$$\underline{\omega} = \begin{pmatrix} 0 \\ 0 \\ \partial_r v + \frac{v}{r} - \frac{1}{r}\partial_\theta u \end{pmatrix}.$$

The following substitutions are used for the non-dimensionalisation:

$$r = b\bar{r}, \qquad t = \frac{b^2}{\kappa}\bar{t}, \qquad \omega = \frac{\kappa}{b^2}\bar{\omega}, \qquad \psi = \kappa\bar{\psi}, \qquad \bar{T} = \frac{T - T_c}{T_h - T_c},$$

where overbars denote dimensionless variables. To eliminate the pressure terms, cross-differentiation is used on Equations (4.8) and (4.9). The dimensionless equations in a rotating frame of reference for radial-tangential flow in streamfunction-vorticity form are:

$$\bar{\omega} = \nabla^2\bar{\psi}, \tag{4.13}$$

$$\frac{1}{Pr}[\partial_{\bar{t}}\bar{\omega} + \frac{1}{\bar{r}}J(\bar{\omega},\bar{\psi})] + \frac{2Ra_b}{\bar{r}Re_bPr}J(\bar{T},\bar{\psi}) + Ra_b\partial_\theta\bar{T} = \nabla^2\bar{\omega}, \tag{4.14}$$

$$\partial_{\bar{t}}\bar{T} + \frac{1}{\bar{r}}J(\bar{T},\bar{\psi}) = \nabla^2\bar{T}, \tag{4.15}$$

where the Jacobian operator is given by

$$J(A,B) = \partial_{\bar{r}}A\partial_\theta B - \partial_{\bar{r}}B\partial_\theta A.$$

It is noted that the usual Coriolis term is eliminated in the streamfunction–vorticity formulation. However, the flow is not independent of the Reynolds number since it appears explicitly in the buoyancy correction to the Coriolis term:

$$\frac{Ra_b}{Re_bPr} = \frac{Re_b^2Pr\beta\Delta T}{Re_bPr} = Re_b\beta\Delta T.$$

4.3 Boundary and initial conditions

The sealed annulus is formed by a heated outer cylinder and a cooled inner cylinder. The following boundary and initial conditions are prescribed:

At $\bar{r} = 1 = r_o$,

$$\bar{\psi} = 0, \qquad \partial_{\bar{r}}\bar{\psi} = 0, \qquad \bar{T} = 1.$$

At $\bar{r} = \frac{a}{b} = r_i$,

$$\bar{\psi} = 0, \qquad \partial_{\bar{r}}\bar{\psi} = 0, \qquad \bar{T} = 0.$$

At $\theta = 0$ and 2π, periodic boundary conditions are applied.

The initial conditions of the fluid correspond to a solid-body rotation with a conducting temperature field between cylinders,

$$\bar{\psi} = 0, \qquad \bar{\omega} = 0, \qquad \bar{T} = 1 - \frac{\ln \bar{r}}{\ln r_i}.$$

A point perturbation is necessary to initiate the flow in the numerical simulations. The temperature field is slightly modified at a point given by,

$$\bar{T}\left(\frac{1}{4}(1 - r_i), \pi\right) \rightarrow \bar{T}\left(\frac{1}{4}(1 - r_i), \pi\right) - 0.02.$$

4.4 Computational methods and procedures

For computations in the current chapter, no modification was performed on the code developed by Lewis (1999). Therefore, only the essence of the methods are repeated here, refer to Chapters 3 and 4 of Lewis (1999) for details.

4.4.1 Finite difference approximations

Equations (4.13)–(4.15) are solved on a collocated uniform curvilinear mesh. Finite differencing is used for second-order accurate discretisations in space. The first and

second derivative approximations for an arbitrary variable, ζ, are given by,

$$\partial_x \zeta \approx \frac{\zeta_{i+1} - \zeta_{i-1}}{2\Delta x}, \qquad \partial^2_{xx} \zeta \approx \frac{\zeta_{i+1} - 2\zeta_i + \zeta_{i-1}}{\Delta x^2},$$

where x is an independent variable. The grid is defined by $x_i = i\Delta x$, where $i \in \mathbf{Z}^+$, Δx is the constant step-length, and ζ_i is the approximation to $\zeta(x_i)$. Usually ζ is a function of time and spatial coordinates.

The advective non-linear terms in the equations, $J(A, B)$, are evaluated using the Arakawa formulation (Arakawa, 1966). It overcomes nonlinear instabilities associated with other central differencing, and is less numerically diffusive than upwinding schemes, whilst retaining second-order accuracy. It is applicable to uniform grids only in its present form. The Arakawa approximation to the Jacobian is given by,

$$\begin{aligned} J(A,B) = \partial_x A \partial_y B - \partial_x B \partial_y A = [\frac{1}{12\Delta x \Delta y}][&(A_{i+1,j} - A_{i-1,j})(B_{i,j+1} - B_{i,j-1}) \\ &-(A_{i,j+1} - A_{i,j-1})(B_{i+1,j} - B_{i-1,j}) \\ &+(A_{i+1,j})(B_{i+1,j+1} - B_{i+1,j-1}) - (A_{i-1,j})(B_{i-1,j+1} - B_{i-1,j-1}) \\ &-(A_{i,j+1})(B_{i+1,j+1} - B_{i-1,j+1}) + (A_{i,j-1})(B_{i+1,j-1} - B_{i-1,j-1}) \\ &+(B_{i,j+1})(A_{i+1,j+1} - A_{i-1,j+1}) - (B_{i,j-1})(A_{i+1,j-1} - A_{i-1,j-1}) \\ &-(B_{i+1,j})(A_{i+1,j+1} - A_{i+1,j-1}) + (B_{i-1,j})(A_{i-1,j+1} - A_{i-1,j-1})]. \end{aligned}$$

The grid is defined by $x_i = i\Delta x$ and $y_j = j\Delta y$.

The application of the periodic boundary condition is straightforward.

4.4.2 Transient method

The time-dependent vorticity and energy equations are advanced in time using the Du–Fort Frankel method, in which the values of dependent variable are substituted

by averages of previous and new time values. As an example, the 2D Fourier's equation in cartesian coordinates,

$$\partial_t \zeta = \partial^2_{xx}\zeta + \partial^2_{yy}\zeta, \tag{4.16}$$

is discretised in second-order central differencing and Du Fort–Frankel method as,

$$\zeta^{n+1}_{i,j}[\frac{1}{2\Delta t}+\frac{1}{\Delta x^2}+\frac{1}{\Delta y^2}] = \zeta^{n-1}_{i,j}[\frac{1}{2\Delta t}-\frac{1}{\Delta x^2}-\frac{1}{\Delta y^2}]+\frac{\zeta^n_{i+1,j}+\zeta^n_{i-1,j}}{\Delta x^2}+\frac{\zeta^n_{i,j+1}+\zeta^n_{i,j-1}}{\Delta y^2}. \tag{4.17}$$

The Du–Fort Frankel method is unconditionally stable for one–, two– and three–dimensional Fourier's equation. However, if nonlinear terms are included in the governing equations, such as in Section 4.2, this property of unconditionally stability is lost. Factors that affect the stability limit of the timestep include the magnitudes of the rotational Rayleigh and Reynolds numbers.

4.4.3 Solving the Poisson equation

The Poisson equation for the streamfunction (Equation (4.13)) is solved with a multigrid routine in order to accelerate iterative convergence. It incorporates a V-cycling and a line relaxation (with Gauss–Seidel) scheme. This is a basic multigrid method decribed in Briggs *et al.*(2000).

Relaxation has a so-called *smoothing property*, it is efficient in removing high–frequency (relative to grid spacing) components of the error. The idea of multigrid is that by using successively coarser grids, a range of frequencies of the error can be removed quickly, and thus leading to faster convergence. Actually, only the errors, which also satisfy the original linear equations are passed to the coarser grids.

A three-level multigrid is used here to illustrate the method. The fine grid is denoted Ω^h; the next coarser is denoted Ω^{2h}; and the coarsest grid is Ω^{4h}. A coarse grid has grid spacing twice of that in the previous finer grid. The system of linear

equations is in the form $Au = f$, where A is the finite difference operator matrix, u is the exact solution matrix, and f is the known–function matrix . A single V–cycle loosely follows this procedure:

1. Relax on $A^h u^h = f^h$ on Ω^h to give an approximation v^h.
2. Compute the residual $r^h = f^h - A^h v^h$.
3. Restrict $(\Omega^h \rightarrow \Omega^{2h})$, $r^h \rightarrow f^{2h}$.
4. Relax on $A^{2h} u^{2h} = f^{2h}$ on Ω^{2h} to give an approximation v^{2h}.
5. Compute the residual $r^{2h} = f^{2h} - A^{2h} v^{2h}$.
6. Restrict $(\Omega^{2h} \rightarrow \Omega^{4h})$, $r^{2h} \rightarrow f^{4h}$.
7. Relax on $A^{4h} u^{4h} = f^{4h}$ on Ω^{4h} to give an approximation v^{4h}.
8. Prolong $(\Omega^{4h} \rightarrow \Omega^{2h})$, $v^{4h} \rightarrow e^{2h}$.
9. Correct on Ω^{2h}, $v^{2h} = v^{2h} + e^{2h}$.
10. Relax on $A^{2h} v^{2h} = f^{2h}$ to give new approximation v^{2h}.
11. Prolong $(\Omega^{2h} \rightarrow \Omega^h)$, $v^{2h} \rightarrow e^h$
12. Correct on Ω^h, $v^h = v^h + e^h$.

This cycle is repeated until convergence is reached where the residual (calculated in step 2.) is less than a certain very small limit. For the simulations performed in this thesis, a value 10^{-6} was used.

The restriction operator has a full weighting routine defined by $I_h^{2h} V^h = V^{2h}$, where

$$v_{i,j}^{2h} = \frac{1}{16}[(v_{2i+1,2j+1}^h + v_{2i-1,2j-1}^h + v_{2i+1,2j-1}^h + v_{2i-1,2j+1}^h)$$

$$+2(v_{2i+1,2j}^h + v_{2i-1,2j}^h + v_{2i,2j+1}^h + v_{2i,2j-1}^h) + 4v_{2i,2j}^h]. \qquad (4.18)$$

The prolongation operator is a linear interpolation routine given by $I_{2h}^h V^{2h} = V^h$, where

$$v_{2i,2j}^h = v_{i,j}^{2h},$$

$$v^h_{2i+1,2j} = \frac{1}{2}(v^{2h}_{i,j} + v^{2h}_{i+1,j}),$$

$$v^h_{2i,2j+1} = \frac{1}{2}(v^{2h}_{i,j} + v^{2h}_{i,j+1}),$$

$$v^h_{2i,2j+1} = \frac{1}{4}(v^{2h}_{i,j} + v^{2h}_{i+1,j} + v^{2h}_{i,j+1} + v^{2h}_{i+1,j+1}). \tag{4.19}$$

The relaxation procedure uses line-relaxation with Gauss–Seidel method; sweeps are performed in both the radial and tangential directions per relaxation procedure. Two relaxation procedures are performed on each level. The finite-difference operator matrix A is in tri–diagonal form for relaxation in the r direction, which can be solved using the well–known Tri–diagonal Matrix Algorithm. While relaxation in the θ direction, requires tri–diagonal matrices that have two extra entries, one at top right and another at bottom left. These are solved using a periodic tri–diagonal matrix algorithm (see Chapter 4 of Lewis, 1999).

4.4.4 Nusselt number calculation

Heat transfer across the cylindrical surfaces into the fluid can be represented by the Nusselt number, defined as the ratio of the heat transfer rate due to convection and conduction to that due to conduction alone. Both a global (over the total cylindrical surface area) and a local Nusselt number can be defined.

$$Nu_{global} = Nu = \frac{\dot{Q}_{cond,conv}}{\dot{Q}_{cond}}, \qquad Nu_{local} = \frac{\dot{q}_{cond,conv}}{\dot{q}_{cond}},$$

where $\dot{Q}$ has a dimension of $\frac{ENERGY}{TIME}$ and $\dot{q}$ has a dimension of $\frac{ENERGY}{TIME.AREA}$. Because Nu_{global} is used frequently, it is denoted Nu for simplicity.

Since

$$\dot{q}_{cond,conv} = -\frac{k\Delta T}{b}\partial_{\bar{r}}\bar{T}, \qquad \dot{q}_{cond} = \frac{k\Delta T}{b\,\bar{r}\ln r_i},$$

the local Nusselt is therefore given by

$$Nu_{local} = -\bar{r}\ln(r_i)\partial_{\bar{r}}\bar{T}. \tag{4.20}$$

And since

$$\dot{Q}_{cond} = \frac{k\Delta T}{b\ln r_i}\int_0^{2\pi}\int_0^{\bar{z}_{max}}\frac{1}{\bar{r}}(b\,d\bar{z})(b\bar{r}d\theta) = \frac{k\Delta T 2\pi b\bar{z}_{max}}{\ln r_i},$$

$$\dot{Q}_{cond,conv} = -\frac{k\Delta T}{b}\int_0^{2\pi}\int_0^{\bar{z}_{max}}\partial_{\bar{r}}\bar{T}(b\,d\bar{z})(b\bar{r}d\theta),$$

the global Nusselt number is therefore given by,

$$Nu = -\frac{\bar{r}\ln r_i}{\bar{z}_{max}2\pi}\int_0^{2\pi}\int_0^{\bar{z}_{max}}\partial_{\bar{r}}\bar{T}d\bar{z}\,d\theta \tag{4.21}$$

at either $\bar{r} = r_i$ or $\bar{r} = 1$. However due to the two-dimensionality of the problem here,

$$Nu = -\frac{\bar{r}\ln r_i}{2\pi}\int_0^{2\pi}\partial_{\bar{r}}\bar{T}d\theta. \tag{4.22}$$

The local Nusselt number remains unchanged as in Equation (4.20). The average Nusselt number cannot be smaller than 1 as the total heat transfer from a surface must always be equal to or exceed the average heat transfer due to conduction alone. More effective convective heat transfer gives larger Nu.

The integral in Equation (4.22) is calculated using the trapezoidal rule; the differential (the integrand in this case) is approximated at the boundaries using a fourth-order accurate finite difference representation.

4.4.5 Code structure

A single timestep has the following numerical procedure:

- Initialise all variables at $\bar{t} = 0$ (c.f. Section 4.3).
- Solve for $\bar{\omega}^{n+1}, \bar{T}^{n+1}$ from solutions at t^n and t^{n-1} on all internal grid points;

the values of the variable at $\bar{t}^{-1}$ and $\bar{t}^{0}$ are indentical (c.f. Sections 4.4.1 and 4.4.2).

- Evaluate Nu using values of $\bar{T}^{n+1}$ (c.f. Section 4.4.4).
- In the Poisson equation, solve for $\bar{\psi}^{n+1}$ with values of $\bar{\omega}^{n+1}$ using the multigrid method (c.f. Section 4.4.3).
- update values of $\bar{\omega}^{n+1}$ on the boundaries using values of $\bar{\psi}^{n+1}$ and the Poisson equation.

4.5 Results and discussion

4.5.1 Rayleigh-Bénard convection approximation

In this section results from the computations of heat transfer in a non-rotating annulus that approximates Rayleigh-Bénard convection are presented. The approximation is made by first substituting the term $b\Omega^2$ (in $\frac{b\Omega^2\beta\Delta T b^3}{\nu\kappa} = Ra_b$) with g, the gravitational acceleration. Secondly, the buoyancy correction to Coriolis term from the governing Equation (4.14) is removed artificially. Thus, if the radial gap is small, the centrifugal force, $r\Omega^2$, across the gap can be regarded as a uniform "gravitational" force directed away from the centre of the annulus. Thus, it can be said that *either* this is a rotating annulus with a uniform centrifugal force and absence of Coriolis effects *or* it is a non-rotating annulus with gravitational force directed away from the centre of the annulus. The latter description is preferred and used throughout this thesis.

The boundary and initial conditions, and point pertubation described in Section 4.3 are used. If the Rayleigh number is above the critical value a convective flow will develop from the initial pure conduction solution. For Rayleigh-Bénard convection with extensive horizontal layers, this critical value is $Ra = 1708$ (Chapter 2).

It is noted here that because of the less conventional definition of the rotational

Rayleigh number in the governing equations, i.e. $Ra_b = \frac{b\Omega^2\beta\Delta T b^3}{\nu\kappa}$, due care has been taken when comparisons are made with results obtained by other investigators using different definitions. Here the substitution $Ra = \frac{b^3}{d^3}Ra_b$ has been made so that comparisons are carried out consistently using Ra.

Figures 4.1 to 4.4 show results for an annulus having $r_o - r_i = 0.3$ $(a/b = 0.7)$. The isotherms, streamlines and the development with time of global Nusselt number are shown on the first, second and third rows respectively. The isotherms and streamline contours are the results at the end of the simulations. The flow develops into the familiar counter-rotating convective roll pairs. The Nusselt numbers in Figures 4.2 and 4.3 show that the flow becomes time-dependent at a Rayleigh number between 10^6 and $10^{6.7}$. It is also at this transition to time-dependent flow that both the plumes and the fluid regions with high thermal gradients become unstable, and the regular thermal convective rolls start to break down, eventually giving rise to a well-mixed flow dominated by turbulence as the Rayleigh number is increased further (Figure 4.4.).

An important observation can be made from the streamlines: coherent large-scale roll structures exist even at high Rayleigh number, at which the temperature fluctuations are turbulent in the bulk region. This means that even when the fluid is fluctuating chaotically at a small spatial scale, on the larger spatial scale the flow behaves in a coherent manner. This large-scale circulation is often called 'wind of turbulence' and has been observed experimentally (see Chapter 3). The wind is responsible for maintaining a shear flow that builds up the boundary layers, and to stir the fluid in the bulk (Grossmann & Lohse, 2000). These two effects are essential components in the phenomenological models used to derive some of the scaling laws that agree with experimental measurements, as described in Chapter 3.

Table 4.1 gives the numerical values of $\lg(Ra)$ and the time-averaged Nu for

the $r_o - r_i = 0.3$ annulus. The Nusselt number is time-averaged over a duration after the Nusselt number is considered to be stationary, i.e. when there is no change in its trend.

lg(Ra)	3.5	4	5	6	6.7	7.43	8	9.43
Nu	1.5	2.5	4.75	8.3	11	17.5	31.5	101

Table 4.1: Values of lg(Ra) and Nu from computations of non-rotating annulus flow approximating Rayleigh-Bénard convection. $r_o - r_i = 0.3$.

Figures 4.5 to 4.8 show the corresponding results for an annulus with $r_o - r_i = 0.5$. The transition to time-dependent flow occurs at a lower Rayleigh number, probably very near $Ra = 10^5$. Table 4.2 shows the numerical values of Ra and Nu.

lg(Ra)	3.67	4.17	5.17	6.17	7.1	8.1	8.67	9.1
Nu	1.76	2.65	5.1	8.9	16	31	55	78

Table 4.2: Values of Nu vs. lg (Ra) from computations of non-rotating annulus flow approximating Rayleigh-Bénard convection. $r_o - r_i = 0.5$.

Data from the above tables are plotted in Figure 4.9. The correlation of Hollands *et al.*(1975) (see Section 3.3.2) shows a change of gradient at around $Ra = 10^6$. If only the points with $Ra \geq 10^6$ are considered, the following correlation is obtained from a least-squares straight line fit to the computed data:

$$Nu_t = 0.0809 Ra^{0.325}. \tag{4.23}$$

The subscript 't' indicates turbulent bulk flow. Niemela *et al.*(2000) obtained $Nu = 0.124 Ra^{0.309 \pm 0.0043}$ from their measurements. At high Rayleigh numbers, Equation (3.10) of Hollands *et al.*(1975) becomes $Nu = 0.0556 Ra^{1/3}$. Despite the differences in the exponents and coefficients, Equation (4.23) is in reasonable agreement with the two correlations quoted above because of the large order of magnitude for the Rayleigh and Nusselt numbers involved. This is illustrated by Figure 4.9.

If only the computed results between $Ra = 10^4$ and $Ra = 10^6$ (inclusive) are

considered, the following scaling-law is obtained from a least-squares straight line fit:

$$Nu_l = 0.226 Ra^{0.261}. \tag{4.24}$$

The subscript 'l' indicates laminar bulk flow. Results at Rayleigh number less than 10^4 are discarded for this analysis because the Nusselt number is still increasing steeply just after the onset of convection. The exponent $\gamma = 0.261$ is close to the well-known $\gamma = 1/4$ regime for laminar convection, see Table 3.3 and Figure 3.5 from Chapters 3. That the γ value in Equation (4.24) is slightly higher than 1/4 is most probably because some results after the beginning of the transition to turbulent flow have been included.

To obtain a single correlation from the laminar and turbulent Nusselt numbers, a blending technique suggested by Churchill & Usagi (1972) is used:

$$Nu = (Nu_l^m + Nu_t^m)^{1/m},$$

where $4 \leq m \leq 20$. The value $m = 20$ gives the best fit for the present data, giving:

$$Nu = (1.21 \times 10^{-13} Ra^{5.22} + 1.44 \times 10^{-22} Ra^{6.48})^{0.05}, \tag{4.25}$$

which is a smooth correlation for all Rayleigh numbers greater than 10^4. Figure 4.9 is repeated in Figure 4.10 but also showing the fit to the computed results given by equation (4.25). Extrapolating to high Rayleigh number shows that Equation (4.25) still agrees well with results from other investigations.

Computations at Rayleigh numbers higher than those presented here were not carried out because non-Boussinesq effects may become important; another factor is the inadequate resolution, using the computing resources available, in both the temporal and spatial scales for turbulence, and in spatial scales for the very thin boundary layers. Non-Boussinesq effects need to be avoided in the computations because

governing equations with this approximation are used. Also, they are undesirable in both experiments and computations because the Boussinesq approximation underlies the statement that dynamical similarity of free convective flows depends on the Grashof and Prandtl numbers (Tritton, 1988, p.188). In non-Boussinesq flow, other dimensionless parameters appear, rendering the correlations between Nusselt and Rayleigh numbers presented in this thesis (and in virtually all other investigations quoted) invalid.

Using the physical properties for air at $20°C$ and 1 bar, maximum value of $\beta\Delta T = 0.3$, and $d = 1$ metre, the value of Rayleigh number at which non-Boussinesq effects begin can be approximated as $Ra = \frac{g\beta\Delta T d^3}{\nu\kappa} = \frac{(9.8)(0.3)(1^3)}{(1.53\times10^{-5})(2.17\times10^{-5})} \approx 10^{10}$. To the knowledge of the author, most convective chambers used in previous experiments were shorter than about 0.5 m. Niemela *et al.*(2000) managed to reach $Ra = 10^{17}$ while avoiding non-Boussinesq effects by using cryogenic helium and an exceptionally tall (1 metre) enclosure. Wu & Libchaber (1991) investigated non-Boussinesq effects in free thermal convection.

Thermal boundary layer thickness

To obtain a correlation for the thermal boundary thickness with Rayleigh number, a well-tested equation is used, c.f. Equation (3.14):

$$Nu = \frac{d}{2\delta_\theta} \Rightarrow \bar{\delta}_\theta = \frac{\bar{d}}{2Nu}, \tag{4.26}$$

where overbars denote dimensionless quantities. Equation (4.26) is based on the evidence that, at high Rayleigh number, the bulk flow is well-mixed with almost uniform temperature, and the steep temperature gradients ($= \frac{\Delta T}{2\delta_\theta}$) are confined to the thermal boundary layers where there is no, or only very small, fluid motion. This phenomenon was used frequently in Chapter 3 to formulate models that produce

different scaling laws.

Clearly, the isotherms in Figures 4.1 to 4.8 suggest that the thermal boundary layers are not uniform along the solid walls. This point is supported by the measurements of Lui & Xia (1998). However, their results suggest that the thermal layer will eventually become uniform at very high Rayleigh number. For this reason, only computed results above $Ra = 10^6$ are used in the derivation of the correlation here.

Tables 4.3 and 4.4 show the values of $\bar{\delta}_\theta$ for the $r_o - r_i = 0.3$ ($a/b = 0.7$) and $= 0.5$ ($a/b = 0.5$) annuli calculated using Equation (4.26). These results are shown in Figure 4.11.

Least-squares fits of these data lead to the following two correlations:

$$\bar{\delta}_\theta = 1.92 Ra^{-0.3258}, \tag{4.27}$$

$$\bar{\delta}_\theta = 2.88 Ra^{-0.3215}, \tag{4.28}$$

for $r_o - r_i = 0.3$ and $= 0.5$ annuli respectively.

$\lg(Ra)$	6	6.7	7.43	8	9.43
$\bar{\delta}_\theta$	0.0181	0.0136	0.00857	0.00476	0.00149

Table 4.3: Values of $\lg(Ra)$ and $\bar{\delta}_\theta$ for computations of non-rotating annulus flow approximating Rayleigh-Bénard convection. $r_o - r_i = 0.3$.

$\lg(Ra)$	6.17	7.1	8.1	8.67	9.1
$\bar{\delta}_\theta$	0.0281	0.0156	0.00806	0.00455	0.00321

Table 4.4: Values of $\lg(Ra)$ and $\bar{\delta}_\theta$ for computations of non-rotating annulus flow approximating Rayleigh-Bénard convection. $r_o - r_i = 0.5$.

Because of the way δ_θ is calculated from Equation (4.26), the correlation is necessarily of the form $\delta_\theta \sim Ra^{-\gamma}$. Direct measurements (e.g. Belmonte *et al.*, 1993 and Lui & Xia, 1996) of the thermal boundary layer thickness have confirmed the validity of Equation (4.26).

4.5.2 Concluding remarks

The stationary annuli appear to approximate Rayleigh-Bénard convection very well, with the curvature and separation of the radial gap having very little effect on the heat transfer. A local fluid region behaves as if in a 'flat' environment and with the surrounding gravity vectors parallel to each other. This implies that this convection process happens over a small length-scale in terms of the spatial geometry. Barenblatt (1996; see also Section 3.2) showed that Rayleigh-Benard convection has a very large characteristic length in the vertical direction, so that in most laboratory or industrial convection layers, the layers can be considered thin and there is no effect of the layer thickness on heat transfer. This conclusion is consistent with the computed result $\gamma \approx 1/3$ (Equation (4.23) which implies that the vertical length of the enclosure is not relevant (c.f. section 3.3.2).

The coherent large-scale circulations are preserved at high Rayleigh number at which the local temperature fluctuations are chaotic.

4.5.3 Rotating annulus

In this section, results for a computation of a rotating annulus flow corresponding to cavity B of Bohn *et al.*(1995) are presented; see Table 4.5 for the dimensions of cavity B. These are again time-dependent 2-D (radial-tangential plane) computations; the side discs are not modelled. This approach is justified as the cavity aspect ratio is (just) greater than unity; also, the range of Rayleigh numbers considered is above 10^7. It was explained in Section 2.1 that if the aspect ratio (l/d) is greater than 0.5 (or $Ra > 10^7$), then the side-disc boundary conditions and their effects on Nusselt number can be neglected. Moreover, despite a reported heat loss, of 10% to 20% of the total heat input, through the side-discs in the experiments the resulting heat transfer agreed very closely with that obtained from a computation carried out for

cavity C with insulated side discs (Bohn *et al.*, 1995). This all suggests that the effects of the side-discs and their thermal boundary conditions are not significant for the cases considered here.

For consistency in comparison with other results the rotational Rayleigh number (Ra_ϕ) has been converted to Ra. In fact $Ra_\phi \equiv Ra$ because $r_m\Omega^2$ in Ra_ϕ is equivalent to g in Ra. However, it should be remembered that, in terms of the forces involved, there are two major differences between flow in a rotating annulus and Rayleigh-Bénard convection layer: (i) gravity is uniform across the depth of a stationary horizontal layer, whereas centrifugal force changes linearly in $r\Omega^2$ across the gap of a rotating annulus; (ii) Coriolis force exists in the rotating annulus in a rotating reference frame; the strength of the Coriolis force is related to rotational Reynolds number.

Figures 4.12 and 4.13 show the computed isotherms and streamlines respectively for $a/b = 0.5$ and $10^{3.5} \leq Ra \leq 10^9$. The regular thermal convective rolls start to break down near $Ra = 10^6$. However, as discussed in the previous section, the large-scale coherent circulations are preserved (Figure 4.13) even at higher Rayleigh number.

Maubert & Randriamampianina (2001) solved numerically for *vertical* a vertical air-filled rotating annulus flow using a highly accurate spectral method. They investigated flows in the (Ta^*, Θ) plane for $\Delta T = 5K$, where $Ta^* = 4\Omega^2(b-a)^5/\nu^2 s$ is the Taylor number and $\Theta = gs\beta\Delta T/\Omega^2(b-a)^2$ is the thermal Rossby number. It can be shown that $\Theta = \frac{4g(b-a)^3}{\nu^2}\beta\Delta T(Ta^*)^{-1}$. Since ΔT is fixed during the experiment, Θ is dependent on Ta^*, or vice versa. Therefore the investigation was performed only along a straight line on the (Ta^*, Θ) plane. It can also be shown that $Ra_\phi = Ta^* Pr \frac{sr_m\beta\Delta T}{4(b-a)^2}$ or $Ra_\phi \approx 0.053 Ta^*$ if typical values of the parameters from Cavity B are substituted. Maubert and Randriamampianina found that the

regular waves start to break down at $Ta^* = 3 \times 10^7 \approx 10^{7.5}$, which is equivalent to $Ra_\phi \approx 10^{6.2}$. This value of Ra_ϕ at the transition to turbulent well-mixed flow is similar to the result obtained in the current study (see previous paragraph). The evolution of the flow structure with increasing Ra_ϕ obtained here is very similar qualitatively to the solutions obtained by the numerically more accurate method of Maubert and Randriamampianina (2001); giving confidence in the present results. However Maubert and Randriamampianina also conducted a more detailed study of the flows with multiple solutions of different wave-numbers and also statistical analysis of the temperature; these types of analyses are not performed by the current author.

From the definitions, rotational Rayleigh number and rotational Reynolds number can be related in the following way:

$$Ra_\phi = \beta\Delta T \frac{d}{r_m} Pr Re_\phi^2$$

$$\Rightarrow Re_\phi = (r_m/d)^{1/2} Pr^{-1/2} (\beta\Delta T)^{-1/2} Ra_\phi^{1/2}. \tag{4.29}$$

Due to certain restrictions in the experimental setup of Bohn *et al.*, the range of $\beta\Delta T$ is small; moreover, as rotational Rayleigh number is increased the realisable value of $\beta\Delta T$ decreases continuously. The experiments were carried out in such a way that $\beta\Delta T = C Ra_\phi^{-K}$, where C and K are positive constants whose numerical values are fixed by the experiment. Therefore, equation (4.29) becomes

$$Re_\phi = (r_m/d)^{1/2} Pr^{-1/2} C^{-1/2} Ra_\phi^{\frac{1+K}{2}}. \tag{4.30}$$

For convenience, Table 2.2 from section 2.2 is repeated here as Table 4.5.

For each cavity, Rayleigh number is the only controllable parameter throughout the experiments of Bohn *et al.*(1995), and the relationships between rotational Reynolds and Rayleigh number shown in Table 4.5 are obtained using equation

	Cavity A	Cavity B	Cavity C
a, b, z[mm]	125, 355, 120	125, 240, 120	125, 240, 120
Correlations	$Nu = 0.246 Ra_\phi^{0.228}$ $Re_\phi = 0.733 Ra_\phi^{0.573}$	$Nu = 0.317 Ra_\phi^{0.211}$ $Re_\phi = 1.441 Ra_\phi^{0.557}$	$Nu = 0.365 Ra_\phi^{0.213}$ $Re_\phi = 1.615 Ra_\phi^{0.556}$

Table 4.5: Rotating cavities studied experimentally (Bohn *et al.*, 1995)

(4.30). Figure 4.14.a displays Re_ϕ vs. Ra for the three cavities on log-log axes, and Figure 4.14.b shows $\beta\Delta T$ vs. Ra on log-log axes.

The time-dependent global Nusselt number for each Rayleigh number case computed is shown in Figure 4.15. These suggest that the flow becomes unsteady at $Ra = 10^6$. Table 4.6 gives the numerical values of $\lg(Ra)$ and time-averaged Nu.

$\lg(Ra)$	3.5	3.92	4.5	4.92	5.5	5.92	6.5	6.92	7.62	7.92	8.5	8.92	9.5	9.92
Nu	1.76	2.5	3.65	4.8	6.67	7.65	10.0	13.5	22.5	32	58	75	100	105

Table 4.6: Numerical values of $\lg(Ra)$ and Nu from computations of rotating annulus flow corresponding to Cavity B of Bohn *et al.*(1995). $r_o - r_i = 0.5$, $a/b = 0.5$.

The computed results for Nu are shown in Figure 4.16. Using values in the range $6.92 \leq \lg(Ra) \leq 9.5$, the following straight line least-squares fit is obtained:

$$Nu = 0.049 Ra_\phi^{0.354}. \tag{4.31}$$

Both the experimental results by Bohn *et al.*(1995) and computations carried out here suggest that the global Nusselt number is strongly dependent only on Rayleigh number. This statement is supported by the following three points:

(i) For fixed r_m/d and s/d (i.e. for a particular cavity), Nusselt number is a function of both the Rayleigh and Reynolds numbers. However, even while the Reynolds number was not kept constant during experiments for different Rayleigh numbers for each cavity (Figure 4.14.a), the resulting Nusselt number was not af-

fected discernibly both in terms of either magnitude or gradient (Figure 4.16). In fact the Reynolds number changed through three orders of magnitude for each cavity as the Rayleigh number was increased in the experiments. Also note that Reynolds number for cavity B is almost double that for cavity A.

(ii) Nusselt number is only weakly dependent on r_m/d or s/d. Cavities A, B and C have different values of r_m/d and z/d, however the resulting Nusselt number vs. Rayleigh number relations are not very greatly different (see Table 4.5 and Figure 4.16). This is most probably because s/d is greater than 0.5 and the Rayleigh number involved is greater than 10^7. As described in Section 2.1, under these conditions the Nusselt number is mainly dependent on Rayleigh number (even the side-disc thermal boundary condition such as conductivity can be ignored). Results from the previous section also suggested that the curvature and separation of the radial gap has only a small effect on the heat transfer.

(iii) Coriolis force is closely related to Reynolds number. The radial component of the Coriolis force is believed to inhibit heat tranfer (see Bohn *et al.*, 1994 & 1995). It can be seen that because Reynolds number in cavity B is almost double that in cavity A, the Nusselt number for cavity A is higher than that in cavity B. In cavity C, which is identical to cavity B except for the eight insulating equi-spaced radial walls (that reduce the Coriolis force), the Nusselt number is the highest among the three cavities. However, the differences are small when compared to the differences between these cavities and the corresponding Rayleigh-Bénard convection (see Figure 14.16).

Because of restrictions in varying the $\beta\Delta T$ term due to the experimental setup (and in view of the Boussinesq approximation), it was not possible to keep Re_ϕ constant while varying Ra_ϕ through a large order of magnitude in the experiments (see Equation (4.29)). However, as described above, even though Re_ϕ could not

be held constant througout the experiments, it did not affect the Nu vs. Ra_ϕ correlations obtained (this is also true for the axial heat transfer case, Bohn *et al.*, 1996). This is because Ra_ϕ has a much stronger influence than Re_ϕ on Nu if both Ra_ϕ and Re_ϕ are varied over similar range of orders of magnitude (as explained in the last paragraph). This last statement should not give the impression that if Ra_ϕ can be held constant, varying Re_ϕ has no significant effect on Nu. If increasingly large Re_ϕ can be applied with a constant Ra_ϕ (which is only possible if $\beta\Delta T$ can vary over a large range) Nu will eventually start to decrease. In other words, there is only great influence of Re_ϕ on Nu if $\beta\Delta T$ varies over a large range. As this was not possible in both the experiments of Bohn *et al.*, and computations by the current author, again Nu depends strongly on Ra_ϕ only for these cases.

Results from the current computations do not agree with those from the experiments of Bohn *et al.*(1995), but agree well with the results expected for Rayleigh-Bénard convection. Therefore, the important factors that affect the differences between heat transfer in Rayleigh-Bénard convection and free convective heat transfer in a rotating annulus are still not resolved.

One suggestion (Owen & Wilson, 2000) is that the flows measured by Bohn *et al.*(1995) may have remained laminar even at these high Rayleigh numbers, since laminar free convection from a horizontal surface (Rohsenow *et al.*, 1998) and laminar Rayleigh-Bénard convection (Equation (4.24)) give $\gamma \approx 0.25$ which is fairly close to $\gamma \approx 0.2$ as obtained by Bohn *et al.*.

In Section 3.3.7, an alternative explanation was suggested using the theory of Grossmann & Lohse, giving values for γ between 0.218 and 0.226 which is close to $\gamma \approx 0.2$ from the measurements of Bohn *et al.*. This allows for the possibility that the flows in the work of Bohn *et al* were turbulent with a large-scale 'wind' (see Section 3.3.7).

4.5.4 Concluding remarks

Computations carried out by Bohn *et al.*(1995), Bohn & Gier (1998), and by the current author suggest that unsteadiness and turbulence are responsible for the higher Nusselt numbers obtained in computations (King & Wilson, 2002; see also Section 2.2.1).

However, it is not clear why the computations cannot reproduce the experimental result as far as heat transfer is concerned. Possible reasons are inadequacy of turbulent thermal convection simulation, inability of the code to simulate changes in the boundary layers that give rise to different scaling laws, and a more subtle problem analogous to the dispute in Rayleigh-Bénard convection between the $\gamma \approx 2/7$ results and $\gamma \approx 1/2$ results from apparently equivalent experimental setups.

Nusselt number is strongly dependent on Rayleigh number for free convective heat transfer in a sealed rotating annulus. Nusselt number depends only weakly on the annulus geometrical dimensions (r_m/d & s/d) and rotational Reynolds number for the range of conditions studied here.

Chapter 5

Two-dimensional (radial-axial) computations

5.1 Introduction

Unsteady, axisymmetric computations are performed in this chapter for systems similar to those considered in Chapter 4: (i) a stationary annulus that approximates Rayleigh-Bénard convection; (ii) free convection in a rotating annulus.

The computational code was validated successfully against the benchmark solution of de Vahl Davis (1983) by Lewis (1999). Therefore, although Lewis showed subsequently that axisymmetric flow is not the preferred mode for the rotating annulus flow, it is instructive to use the code to study the heat transfer aspect of the flow. Two-dimensional time-dependent simulation is much less computationally intensive compared to fully three-dimensional direct numerical simulation. The results obtained are compared with more reliable published results, and conclusions are guided by these comparisons.

Firstly, the effects of altering the axial gap (s/d) are examined in stationary annuli that approximate Rayleigh-Bénard convection. It was not possible to study these effects directly in Chapter 4 where a 2D radial-tangential code was used. It was assumed (with supporting evidence from other studies) that if $s/d > 0.5$ or

$Ra > 10^7$, the side-disc effects on heat transfer can be neglected.

Secondly, the effects of rotation on the heat transfer is again investigated. In particular, the influence of rotational Reynolds number, which was found to be weak compared to Rayleigh number in Chapter 4, is studied. It is noticed that the present computations are more sensitive (compared to the model used in Chapter 4) to Reynolds number changes, hence its effect over a smaller range of values can be studied.

5.2 Governing equations

The flow is assumed to be axisymmetric and therefore

$$\partial_\theta = 0. \tag{5.1}$$

Hence, Equations (4.2) to (4.6) become

$$\partial_r u + \frac{u}{r} + \partial_z w = 0, \tag{5.2}$$

$$\partial_t u + (\underline{u}.\nabla)u - \frac{v^2}{r} - \frac{\rho}{\rho_0}(2\Omega v + \Omega^2 r) = -\frac{1}{\rho_0}\partial_r p + \nu(\nabla^2 u - \frac{u}{r^2}), \tag{5.3}$$

$$\partial_t v + (\underline{u}.\nabla)v + \frac{uv}{r} + \frac{\rho}{\rho_0}(2\Omega u) = -\frac{1}{\rho_0 r}\partial_\theta p + \nu(\nabla^2 v - \frac{v}{r^2}), \tag{5.4}$$

$$\partial_t w + (\underline{u}.\nabla)w = -\frac{1}{\rho_0}\partial_z p + \nu\nabla^2 w, \tag{5.5}$$

$$\partial_t T + (\underline{u}.\nabla)T = \kappa\nabla^2 T, \tag{5.6}$$

where the 2D divergence and Laplace operators are respectively:

$$(\underline{u}.\nabla) \equiv u\partial_r + w\partial_z, \qquad \nabla^2 \equiv \partial^2_{rr} + \frac{1}{r}\partial_r + \partial^2_{zz}.$$

As in Chapter 4, the streamfunction–vorticity formulation is again used. The streamfunction, ψ, is defined in such a way that the continuity equation (5.2) is

satisfied exactly with

$$u = \frac{1}{r}\partial_z \psi, \qquad w = -\frac{1}{r}\partial_r \psi, \tag{5.7}$$

and it is rescaled using

$$\psi = r\phi.$$

Here the definition of vorticity (c.f. Equation (4.12)) becomes

$$\underline{\omega} = \partial_z u - \partial_r w, \tag{5.8}$$

where only the component that is independent of v is retained, the other two components of the vorticity not being necessary to solve the resulting governing equations. Similar substitutions to those in Chapter 4 are used for the non-dimensionalisation:

$$r = b\bar{r}, \qquad z = b\bar{z} \qquad t = \frac{b^2}{\kappa}\bar{t}, \qquad v = \frac{\kappa}{b}\bar{v},$$

$$\omega = \frac{\kappa}{b^2}\bar{\omega}, \qquad \phi = \kappa\bar{\phi}, \qquad \bar{T} = \frac{T - T_c}{T_h - T_c},$$

where overbars denote dimensionless variables. Using the definitions of ϕ and ω, the non-dimensionalisation substitutions, and cross-differentiation between Equations (5.3) and (5.5), the following dimensionless governing equations in streamfunction–vorticity formulation are obtained:

$$\bar{\omega} = \nabla^2\bar{\phi} - \frac{\bar{\phi}}{\bar{r}^2}, \tag{5.9}$$

$$\frac{1}{Pr}[\partial_{\bar{t}}\bar{\omega} + J(\bar{\omega},\bar{\phi}) - \frac{1}{\bar{r}}(\bar{\phi}\partial_{\bar{z}}\bar{\omega} + \bar{\omega}\partial_{\bar{z}}\bar{\phi}) - \frac{2\bar{v}}{\bar{r}}\partial_{\bar{z}}\bar{v}] - 2Re_b\partial_{\bar{z}}\bar{v} + \frac{2Ra_b}{Re_bPr}(\bar{T}\partial_{\bar{z}}\bar{v} + \bar{v}\partial_{\bar{z}}\bar{T})$$

$$+\bar{r}Ra\partial_{\bar{z}}\bar{T} = \nabla^2\bar{\omega} - \frac{\bar{\omega}}{\bar{r}^2}, \tag{5.10}$$

$$\frac{1}{Pr}[\partial_{\bar{t}}\bar{v} + J(\bar{v},\bar{\phi}) + \frac{1}{\bar{r}}(\bar{v}\partial_{\bar{z}}\bar{\phi} - \bar{\phi}\partial_{\bar{z}}\bar{v})] + 2Re_b\partial_{\bar{z}}\bar{\phi} - \frac{2Ra_b}{Re_bPr}\bar{T}\partial_{\bar{z}}\bar{\phi} = \nabla^2\bar{v} - \frac{\bar{v}}{\bar{r}^2}, \tag{5.11}$$

$$\partial_{\bar{t}}\bar{T} + J(\bar{T},\bar{\phi}) - \frac{\bar{\phi}}{\bar{r}}\partial_{\bar{z}}\bar{T} = \nabla^2\bar{T}, \tag{5.12}$$

where the Jacobian operator is given by,

$$J(A,B) = \partial_{\bar{r}} A \partial_{\bar{z}} B - \partial_{\bar{r}} B \partial_{\bar{z}} A.$$

The rotatonal Rayleigh number appears in the buoyancy terms and rotational Reynolds number in the Coriolis terms. The buoyancy correction to the Coriolis terms (Equations (5.10) & (5.11)) have a factor $\frac{2Ra_b}{Re_b Pr}$ $(= 2Re_b \beta \Delta T)$.

5.3 Boundary and initial conditions

The sealed annulus flow is simulated in the radial-axial plane with no-slip boundaries, adiabatic discs, heated outer cylinder and cooled inner cylinder. The following boundary conditions are prescribed:

At $\bar{r} = 1 = r_o$,

$$\bar{\phi} = 0, \qquad \partial_{\bar{r}} \bar{\phi} = 0, \qquad \bar{v} = 0, \qquad \bar{T} = 1.$$

At $\bar{r} = \frac{a}{b} = r_i$,

$$\bar{\phi} = 0, \qquad \partial_{\bar{r}} \bar{\phi} = 0, \qquad \bar{v} = 0, \qquad \bar{T} = 0.$$

At $\bar{z} = 0, = \bar{s}$,

$$\bar{\phi} = 0, \qquad \partial_{\bar{z}} \bar{\phi} = 0, \qquad \bar{v} = 0, \qquad \partial_{\bar{z}} \bar{T} = 0.$$

The initial conditions of the fluid correspond to solid-body rotation with a conducting temperature field between the cylinders,

$$\bar{\phi} = 0, \qquad \bar{\omega} = 0, \qquad \bar{v} = 0, \qquad \bar{T} = 1 - \frac{\ln \bar{r}}{\ln r_i}.$$

A point perturbation in the temperature field is introduced to speed up the initiation of flow in a numerical simulation. The temperature field is slightly modified at a

point as follows,

$$\bar{T}\left(\frac{1}{4}(1-r_i),\frac{1}{4}\bar{s}\right) \rightarrow \bar{T}\left(\frac{1}{4}(1-r_i),\frac{1}{4}\bar{s}\right) + 0.01.$$

If this were not done, perturbations would enter the system through amplification of round–off errors, which requires extra computing time.

5.4 Computational methods and procedures

As for the code used in Chapter 4, the computational code used in the current chapter was developed by Lewis (1999). The computational methods used here are very similar to those in Chapter 4, so only the essential features are described here. For details, references are made to the relevant sections in Chapter 4 (or refer to Lewis, 1999).

5.4.1 Finite difference approximations

The governing Equations (5.9)–(5.12) are discretised in space with second-order accurate central finite differencing on uniform mesh. The Jacobian operators, $J(A,B)$, are evaluated using the Arakawa formulation (c.f. Section 4.4.1).

5.4.2 Transient method

The time–dependent equations for vorticity, velocity, and temperature are advanced in time using Du–fort Frankel method, in which the values of the dependent variables at the current timestep are substituted by averages of previous and new time values (c.f. Section 4.4.2).

5.4.3 Solving the Poisson equation

The Poisson equation for streamfunction (Equation (5.9)) is solved using the basic multigrid method described in Section 4.4.3. However, since the periodic boundary

condition is not required here, the resulting finite differencing operator matrices in both the radial and axial directions can be solved using the Tri–diagonal Matrix Algorithm.

5.4.4 Nusselt number calculation

The global Nusselt number given by Equation (4.21) is repeated here,

$$Nu = -\frac{\bar{r}\ln r_i}{\bar{z}_{max}2\pi}\int_0^{2\pi}\int_0^{\bar{z}_{max}} \partial_{\bar{r}}\bar{T}d\bar{z}\,d\theta.$$

Due to the axisymmetry imposed in this chapter, it can be reduced to

$$Nu = -\frac{\bar{r}\ln r_i}{\bar{z}_{max}}\int_0^{\bar{z}_{max}} \partial_{\bar{r}}\bar{T}d\bar{z}. \tag{5.13}$$

As before, the integral is evaluated using the trapezoidal rule, and the integrand is approximated using a fourth-order accurate finite difference.

5.4.5 Code structure

A single timestep has the following numerical procedure:

- Initialise all variables at $\bar{t} = 0$ (c.f. Section 5.3).
- Solve for $\bar{\omega}^{n+1}, \bar{v}^{n+1}, \bar{T}^{n+1}$ from solutions at t^n and t^{n-1} on all internal grid points; the values of the variables at $\bar{t}^{-1}$ and $\bar{t}^0$ are indentical (c.f. Sections 5.4.1 and 5.4.2). Solve for $\bar{T}^{n+1}$ on adiabatic surfaces (side–discs).
- Evaluate Nu using values of $\bar{T}^{n+1}$. (c.f. Section 5.4.4).
- In the Poisson equation, solve for $\bar{\phi}^{n+1}$ with values of $\bar{\omega}^{n+1}$ using the multigrid method (c.f. Section 5.4.3).
- update values of $\bar{\omega}^{n+1}$ on the boundaries using values of $\bar{\phi}^{n+1}$ and the Poisson equation.

5.5 Results and discussion

5.5.1 Rayleigh–Bénard convection approximation

In order to use the code that is based on the governing equations (5.9)–(5.12) for the simulation of Rayleigh-Bénard convection, all the terms containing Re_b were removed, and the term $r_m\Omega^2$ in Ra_b was substituted with g the gravitational acceleration. The rationale behind this approximation is explained in Chapter 4, and is not repeated here. The simulations were performed with an 80×80 interval grid and dimensionless timesteps of $\Delta\bar{t} = 10^{-5}$ for the smallest Rayleigh number flow to $\Delta\bar{t} = 5 \times 10^{-8}$ for the largest Rayleigh number flow. These values were determined by trial and error or by experience to attain numerical stability.

Figures 5.1 to 5.5 display the computed results for flows at various Rayleigh numbers from subcritical to $Ra \approx 10^9$ in an aspect ratio $s/d = 1.0$ enclosure. A higher Rayleigh number case was not investigated because non-Boussinesq effects begin at $Ra \approx 10^{10}$ (see Section 4.5.1). The isotherms and streamlines are the results at the end of the simulations.

The flow becomes time-dependent probably at $Ra \approx 10^6$. Also, as in the 2D radial–tangential computations, the flow retains its coherent circulations, indicated by the streamlines, even at high Rayleigh number (Figures 5.4 & 5.5).

Figures 5.6 to 5.10 show the correponding result for an $s/d = 0.5$ enclosure. The flow becomes time-dependent between $Ra = 10^{5.65}$ and $Ra = 10^{7.5}$.

Time-averaged global Nusselt number variation against Rayleigh number for the two cases above are shown in Figure 5.11. The two sets of data are also tabulated below.

For comparison, semi-empirical correlations by Hollands *et al.* for horizontal enclosures of aspect ratios 1.0 and 0.5, and an extensive horizontal enclosure (Rayleigh–Bénard convection, very large aspect ratio) are also shown in Figure 5.11.

$\lg(Ra)$	3.5	4.17	5.17	6.17	6.5	7.09	7.5	8.1	8.5	9.09
Nu	1	2	3	4.75	6.75	10	15	30	45	75

Table 5.1: Values of $\lg(Ra)$ and Nu for computations of non-rotating annulus flow approximating Rayleigh-Bénard convection. $r_o - r_i = 0.5$, $a/b = 0.5$, $s/b = 0.5$, $s/d = 1.0$.

$\lg(Ra)$	4	4.5	5	5.65	6	7	7.5	8.1	8.5	9.09
Nu	1	1.7	2.2	2.9	4.5	9.5	13.5	23.5	40	74

Table 5.2: Values of $\lg(Ra)$ and Nu from computations of non-rotating annulus flow approximating Rayleigh-Bénard convection. $r_o - r_i = 0.5$, $a/b = 0.5$, $s/b = 0.25$, $s/d = 0.5$

Although the computed results do not match the correlations perfectly, considering the large range of Rayleigh number being simulated, the agreement is reasonable qualitatively.

At $Ra < 10^6$ ($< 10^7$ for the smooth correlations), enclosures with higher aspect ratios produce higher Nu. As explained in Section 2.1, the temperature and velocity fluctuations in a low-aspect-ratio enclosure are damped by the side-walls. These effects are weak for large-aspect-ratio enclosures or for flows with $Ra > 10^7$. Figure 5.11 shows that, within the smooth correlations or the scattered data respectively, the variations 'merge' at $Ra > 10^7$.

Because there is no discernible difference between the two sets of computed results for $Ra > 10^7$, both sets of data can be used to derive the following correlation using a least-squares method:

$$Nu = 0.0109 Ra^{0.42}. \tag{5.14}$$

The value of the exponent ($\gamma = 0.42$) is larger than the 1/4-scaling for laminar free convection, and the more commonly observed 2/7-scaling. Recall that the 1/4-scaling is from the pure regimes I, whereas the 2/7-scaling is a combination of regimes I and IV_u of Grossmann & Lohse (see Figure 3.5). The scaling obtained in

Equation (5.14) can be interpreted as a combination of regimes I_u and III_u which gives rise to $0.37 \leq \gamma \leq 0.41$ in the range $10^8 \leq Ra \leq 10^{12}$ (also see Section 3.3.6).

Four additional points for flows in an aspect ratio $s/d = 1$ annulus were computed and the heat transfer results are also shown in Figure 5.11. However, here the annulus has a larger dimensionless inner radius $r_o = a/b = 0.75$ and an axial gap $s/b = 0.25$. The number of grid intervals for the mesh used in these computations is 64×64.

These four results show better agreement with the Hollands *et al.* correlation for the unity aspect ratio compared to the $s/b = 0.5$ annulus. As described in Chapters 3 and 4, the Rayleigh-Bénard heat transfer should be independent of the separation between the hot and cold walls; Nusselt number is usually a function of Rayleigh number, Prandtl number and aspect ratio only (see Equation (3.3)). There is an exception only for very thick layers, which excludes most (if not all) laboratory rigs and industrial machines. Here, the slight increase in Nusselt number compared with an annular enclosure having the same aspect ratio but smaller inner radius may be due to the larger area on the inner cylinder for the $a/b = 0.75$ annulus. However, the differences are not highly significant. The two-dimensional radial-tangential code used in Chapter 4 was did not show these differences.

5.5.2 Concluding remarks

Heat transfer in non-rotating annuli that approximates Rayleigh-Bénard convection was simulated to investigate the effects of aspect ratio (the side-disc effects). The results confirm that the side-disc effects become negligible as the aspect ratio increases or the flow is in the regime $Ra > 10^7$. Although the computed data do not match exactly the more reliable correlations from the literature, the qualitative agreement is good and the quantitative comparison is reasonable considering the large range

of Rayleigh numbers investigated. Differences are likely to be due to the imposed axisymmetry of the simulations and another reason described below regarding the surface area of the inner cylinder.

A further computation was carried out for an annulus with one of the aspect ratios considered above but with larger inner radius. It was found that the Nusselt number was slightly higher. Relying on the strong evidence that the heat transfer is independent of the separation between the hot and cold surfaces, it is suggested this increase in heat transfer is due to the larger surface area on the inner cylinder available for heat transfer. Of course, this peculiarity does not apply to a horizontal layer where the surface area of either the top or bottom wall is not affected with a change in separation.

5.5.3 Rotating annulus

Further computations were performed for rotating annulus flows using the same 2D radial-axial code. The terms containing Re_b in the governing equations (5.9)–(5.12) are now retained. The dimensions of the annulus are: $r_o - r_i = 0.5$, $a/b = 0.5$, $s/b = 0.5$, and $s/d = 1.0$. This is identical to the $s/d = 1.0$ annulus used in the previous section for the non-rotating annulus study. The simulations were performed with mesh of 64×64 intervals and dimensionless timestep of $\Delta\bar{t} = 5 \times 10^{-5}$ at the smallest Rayleigh number case, and a 128×128 mesh and $\Delta\bar{t} = 10^{-7}$ for the larger Rayleigh number cases.

The results are summarised in Figures 5.12 and 5.13. For each Rayleigh number, flows with different values of $\beta\Delta T$ (or Re_ϕ) were computed. Rotational Rayleigh number and rotational Reynolds number are related by:

$$Ra = Re_\phi^2 Prd/r_m\beta\Delta T. \tag{5.15}$$

Because g in $Ra = \frac{g\beta\Delta T d^3}{\nu\kappa}$ and $r_m\Omega^2$ in $Ra_\phi = \frac{r_m\Omega^2\beta\Delta T d^3}{\nu\kappa}$ are equivalent quantities, $Ra \equiv Ra_\phi$. Usually in this thesis, all the different definitions of Rayleigh number are transformed to Ra for consistent comparisons to be made with results from other investigations using different definitions.

If the constraint $\beta\Delta T \ll 1$ (usually ≤ 0.3 is adequate) for the Boussinesq approximation is first ignored, it is seen that in all cases, the Nusselt number decreases as Reynolds number increases (Figure 5.12).

Figures 5.12.a and 5.12.b indicate that for flows obeying the Boussinesq approximation, convection begins at $Ra \approx 10^6$. Attention is drawn to the results $\beta\Delta T = 0.492$ and $\beta\Delta T = 0.3$ in Figures 5.12.a and 5.12.b respectively. Since the Nusselt number values are so close to unity, it is clear that a further decrease in $\beta\Delta T$ would stop the convection. Hence, for these computed flows the critical Rayleigh number for convection in a rotating annulus is near 10^6. Linear stability studies carried out by Lewis (1999, Chapter 3) for 2D radial-axial flows suggest that this is a reasonable value to expect, although he did not analyse the exact case studied here (most of his studies, unfortunately, fall outside the Boussinesq approximation). This value of critical Rayleigh number is about three order of magnitude larger than that for Rayleigh-Bénard convection (which is $\approx 2 \times 10^3$).

Also, from Figures 5.12.b, 5.12.c, and 5.12.d, it is noted that the onset of time-dependent flow has been delayed (compared to results from the last section for non-rotating free convection). From these observations, it is suggested that the rotation has weakened the heat transfer (Nu), and delayed the onsets of both convection and time-dependent flow.

However, since it is very likely that axisymmetric flow is not the preferred convection pattern, it is believed that the 2D radial-tangential flow results presented in Chapter 4 are more realistic. This means that the influence of Reynolds number

is probably not as significant as implied from results of the current section. The experimental results for the three rotating annuli by Bohn *et al.* can be used to support this statement. Throughout the experiments, the values of $\beta\Delta T$ were always less than about 0.2 (Figure 4.14.b), while as shown in Figure 5.13, the results of Bohn *et al.* are closer to the computed results for $\beta\Delta T = 0.8$ or $= 0.7$, which correspond to smaller rotational Reynolds numbers than those implemented in Bohn *et al.*'s experiments. Equation (5.15) can be used to calculate their relative size, but Figure 5.12.d shows that the value of Re_ϕ at $\beta\Delta T = 0.8$ is about half of that at $\beta\Delta T = 0.2$.

5.5.4 Concluding remarks

Two-dimensional radial-axial computational results for rotating annulus flow suggest that the imposed axisymmetry has stabilised the flow. Thus, the onset of both convection and time-dependent flow is delayed. The influence of rotational Reynolds number is also increased and Nusselt numbers are reduced. It is concluded that the axisymmetric formulation is unsuitable for simulating free convective flow in a rotating annulus.

Chapter 6

Three-dimensional computations

6.1 Introduction

In this chapter, results from unsteady three-dimensional computations are reported. The cases investigated are similar to those presented in Chapters 4 and 5.

The governing equations, boundary and initial conditions, and the computational methods are first described. The results of the simulations are then used to describe the flow structures and heat transfer for the 3D air-filled sealed rotating annulus. The effects of the rotation and dimensions of the annulus on the heat transfer (represented by Nu) are discussed.

In the last section, results from the simulation of flow in a rotating annulus with a single insulated radial barrier are reported. The effect of this barrier on the heat transfer is investigated.

6.2 Governing equations

The governing equations in vorticity-velocity formulation are derived using the Navier–Stokes equations (4.2)– (4.6). The vorticity vector, which was defined in

Equation (4.12) is repeated here:

$$\underline{\omega} = \nabla \times \underline{u} = \frac{1}{r}\begin{vmatrix} \underline{i} & r\underline{j} & \underline{k} \\ \partial_r & \partial_\theta & \partial_z \\ u & rv & w \end{vmatrix} = \begin{pmatrix} \frac{1}{r}\partial_\theta w - \partial_z v \\ \partial_z u - \partial_r w \\ \partial_r v + \frac{v}{r} - \frac{1}{r}\partial_\theta u \end{pmatrix} \equiv \begin{pmatrix} A \\ B \\ C \end{pmatrix}, \tag{6.1}$$

where A, B, C are the vorticity components in the r, θ, z directions respectively. The non-dimensionalisation is achieved using the following substitutions:

$$r = b\bar{r}, \qquad z = b\bar{z}, \qquad t = \frac{b^2}{\kappa}\bar{t}, \qquad (A, B, C)^T = \frac{\kappa}{b^2}(\bar{A}, \bar{B}, \bar{C})^T,$$

$$(u, v, w)^T = \frac{\kappa}{b}(\bar{u}, \bar{v}, \bar{w})^T, \qquad \bar{T} = \frac{T - T_c}{T_h - T_c},$$

where overbars denote non-dimensional variables. Cross-differentiations are used to eliminate the pressure terms; the operators used in each case are given just before each equation below. Substitutions using the continuity equation (4.2) are also used to eliminate certain terms. The resulting non-dimensional governing equations for the vorticity components are given by (overbars are dropped for clarity),

$\frac{1}{r}\partial_\theta(4.5) - \partial_z(4.4)$ gives:

$$\frac{1}{Pr}[\partial_t A + (\underline{u}.\nabla)A - A\partial_r u - \frac{B}{r}\partial_\theta u - C\partial_z u] - 2Re_b\partial_z u + \frac{2Ra_b}{Re_b Pr}(T\partial_z u + u\partial_z T)$$
$$= \nabla^2 A - \frac{2}{r^2}\partial_\theta B - \frac{A}{r^2}, \tag{6.2}$$

$\partial_z(4.3) - \partial_r(4.5)$ gives:

$$\frac{1}{Pr}[\partial_t B + (\underline{u}.\nabla)B - A(\partial_r v - \frac{v}{r}) - \frac{B}{r}(u + \partial_\theta v) - C\partial_z v] - 2Re_b\partial_z v + \frac{2Ra_b}{Re_b Pr}(T\partial_z v + v\partial_z T)$$
$$+ rRa_b\partial_z T = \nabla^2 B + \frac{2}{r^2}\partial_\theta A - \frac{B}{r^2}, \tag{6.3}$$

$\frac{-1}{r}\partial_\theta(4.3) + \partial_r(4.4) + \frac{(4.4)}{r}$ gives:

$$\frac{1}{Pr}[\partial_t C + (\underline{u}.\nabla)C - A\partial_r w - \frac{B}{r}\partial_\theta w - C\partial_z w] - 2Re_i\partial_z w + \frac{2Ra_b}{Re_b Pr}(T\partial_z w - u\partial_r T - \frac{v}{r}\partial_\theta T)$$
$$-Ra_b\partial_\theta T = \nabla^2 C. \tag{6.4}$$

The Poisson equations for velocity are derived using the curl of the vorticity and the continuity equations. The velocity expressed in terms of vorticity are given by,

$$\nabla^2 w = \frac{1}{r}\partial_\theta A - \partial_r B - \frac{B}{r}, \tag{6.5}$$

$$\nabla^2 v + \frac{2}{r}\partial_r v + \frac{v}{r^2} = \partial_r C + \frac{2C}{r} - \partial_z A, \tag{6.6}$$

$$\nabla^2 u + \frac{2}{r}\partial_r u + \frac{u}{r^2} = \partial_z B - \frac{1}{r}\partial_\theta C - \frac{2}{r}\partial_z w. \tag{6.7}$$

It is noted that the equation for the velocity component u involves the axial velocity w and so may not be solved before w.

The energy equation is,

$$\partial_t T + (\underline{u}.\nabla)T = \nabla^2 T. \tag{6.8}$$

6.3 Boundary and initial conditions

As in the previous two chapters, the sealed annulus is simulated with no-slip boundaries, adiabatic discs, heated outer cylinder and cooled inner cylinder. The boundary conditions according to the vorticity-velocity formulation presented in the previous section are:

At the outer cylinder $\bar{r} = 1 = r_o$,

$$u = v = w = 0, \qquad A = 0, \qquad B = -\partial_r w, \qquad C = \partial_r v, \qquad T = 1.$$

At the inner cylinder $\bar{r} = a/b = r_i$,

$$u = v = w = 0, \qquad A = 0, \qquad B = -\partial_r w, \qquad C = \partial_r v, \qquad T = 0.$$

At the discs $\bar{z} = 0, \bar{s}$,

$$u = v = w = 0, \qquad A = -\partial_z v, \qquad B = \partial_z u, \qquad C = 0, \qquad \partial_z T = 0.$$

Periodic boundary conditions are applied at $\theta = 0, 2\pi$.

As in the two chapters previously, the initial conditions of the fluid correspond to solid-body rotation with a conducting temperature field between the cylinders,

$$A = B = C = 0, \qquad u = v = w = 0, \qquad T = 1 - \frac{\ln r}{\ln r_o}$$

Again, to perturb this initial solution, a point perturbation is introduced in the temperature field as follows:

$$T\left(\frac{1}{4}(1 - r_i), \pi, \frac{1}{4}s\right) \rightarrow T\left(\frac{1}{4}(1 - r_i), \pi, \frac{1}{4}s\right) - 0.02.$$

6.4 Computational methods and procedures

This code was developed originally by Lewis (1999). In the current study, an improvement to the convergence of the multigrid scheme was achieved by using a combination of V-cycling and Successive Over-Relaxation (SOR). Some minor modifications were also made. The description of the methods in this section is intended to be self-contained, however, additional information can be found in Chapter 5 of Lewis (1999).

The computations described here were carried out on single R10,000 processor of a 20–node Silicon Graphics Origin 2000 machine with shared memory. Each

computation required about 50MB memory or less.

6.4.1 Staggered grid

Computations are carried out on a uniform three-dimensional cylindrical polar mesh in which the velocity and vorticity vectors are staggered. The staggered grid implementation is used to satisfy the divergence-free constraint for velocity and vorticity. Figure 6.1 shows the locations of the velocity and vorticity vectors, and the temperature (a scalar), on an internal computational cell and a cell at the corner formed by the boundaries of a disc and the inner cylinder.

6.4.2 Finite-difference approximations

In this section, the interpolations and second-order accurate finite difference approximations used are presented. Terms requiring straightforward treatments are not described, and similar strategies are not repeated for every occurance. The physical location $(r_i + i\Delta r, j\Delta z, k\Delta\theta)$ is denoted by (i, j, k).

Equation (6.2) for vorticity $A_{(i+\frac{1}{2},j,k)}$ is used to illustrate the interpolations and finite differencing on an *internal* cell (Figure 6.1.b):

$$u_{(i+\frac{1}{2},j,k)} \approx \frac{1}{8}[u_{(i+1,j+\frac{1}{2},k+\frac{1}{2})} + u_{(i+1,j-\frac{1}{2},k+\frac{1}{2})} + u_{(i+1,j-\frac{1}{2},k-\frac{1}{2})} + u_{(i+1,j+\frac{1}{2},k-\frac{1}{2})} +$$

$$u_{(i,j+\frac{1}{2},k+\frac{1}{2})} + u_{(i,j-\frac{1}{2},k+\frac{1}{2})} + u_{(i,j-\frac{1}{2},k-\frac{1}{2})} + u_{(i,j+\frac{1}{2},k-\frac{1}{2})}],$$

$$\partial_r A_{(i+\frac{1}{2},j,k)} \approx \frac{A_{(i+\frac{3}{2},j,k)} - A_{(i-\frac{1}{2},j,k)}}{2\Delta r},$$

$$\partial_r u_{(i+\frac{1}{2},j,k)} \approx \frac{u_{(i+1,j,k)} - u_{(i,j,k)}}{\Delta r},$$

$$u_{(i+\frac{1}{2},j,k+\frac{1}{2})} \approx \frac{1}{4}[u_{(i+1,j+\frac{1}{2},k+\frac{1}{2})} + u_{(i+1,j-\frac{1}{2},k+\frac{1}{2})} + u_{(i,j-\frac{1}{2},k+\frac{1}{2})} + u_{(i,j+\frac{1}{2},k+\frac{1}{2})}],$$

$$\partial_\theta u_{(i+\frac{1}{2},j,k)} \approx \frac{u_{(i+\frac{1}{2},j,k+\frac{1}{2})} - u_{(i+\frac{1}{2},j,k-\frac{1}{2})}}{\Delta\theta},$$

$$\partial_z T_{(i+\frac{1}{2},j,k)} \approx \frac{T_{(i+\frac{1}{2},j+\frac{1}{2},k)} - T_{(i+\frac{1}{2},j-\frac{1}{2},k)}}{\Delta z},$$

$$\partial^2_{rr} A_{(i+\frac{1}{2},j,k)} \approx \frac{A_{(i+\frac{3}{2},j,k)} - 2A_{(i+\frac{1}{2},j,k)} + A_{(i-\frac{1}{2},j,k)}}{\Delta r^2}.$$

Due to the locations of A on the inner cylindrical surface some of the corresponding approximations on a boundary cell are slightly more complicated. A 'corner' boundary cell $(0,0,k)$ (see Figure 6.1.d) is considered for the discretisations in the computation of vorticity $A_{(\frac{1}{2},1,k)}$; discretisations which are similar to those above are not repeated,

$$\partial_r A_{(\frac{1}{2},1,k)} \approx \frac{-\frac{4}{3}A_{(0,1,k)} + A_{(\frac{1}{2},1,k)} + \frac{1}{3}A_{(\frac{3}{2},1,k)}}{\Delta r},$$

$$\partial^2_{rr} A_{(\frac{1}{2},1,k)} \approx \frac{3.2A_{(0,1,k)} - 5A_{(\frac{1}{2},1,k)} + 2A_{(\frac{3}{2},1,k)} - 0.2A_{(\frac{5}{2},j,k)}}{\Delta r^2}.$$

6.4.3 Application of boundary conditions to the Poisson Equations

The Poisson Equation (6.5) for velocity component w is used to demonstrate the strategy employed to resolve the difficulty in applying the boundary conditions for vorticity and velocity, which must be solved simultaneously at the same time level. To solve, for example, $w_{(\frac{1}{2},1,k+\frac{1}{2})}$ (see Figure 6.1.c), Equation (6.5) in second-order accurate finite difference form is:

$$\frac{-5w_{(\frac{1}{2},1,k+\frac{1}{2})} + 2w_{(\frac{3}{2},1,k+\frac{1}{2})} - 0.2w_{(\frac{5}{2},1,k+\frac{1}{2})}}{\Delta r^2} + \frac{1}{r}\frac{w_{(\frac{1}{2},1,k+\frac{1}{2})} + \frac{1}{3}w_{(\frac{3}{2},1,k+\frac{1}{2})}}{\Delta r}$$

$$+\frac{w_{(\frac{1}{2},1,k+\frac{3}{2})} - 2w_{(\frac{1}{2},1,k+\frac{1}{2})} + w_{(\frac{1}{2},1,k-\frac{1}{2})}}{r^2\Delta\theta^2} + \frac{-2w_{(\frac{1}{2},1,k+\frac{1}{2})} + w_{(\frac{1}{2},2,k+\frac{1}{2})}}{\Delta z^2}$$

$$\approx \frac{A_{(\frac{1}{2},1,k+1)} - A_{(\frac{1}{2},1,k)}}{r\Delta\theta} - \frac{B_{(1,1,k+\frac{1}{2})} - B_{(0,1,k+\frac{1}{2})}}{\Delta r} - \frac{B_{(1,1,k+\frac{1}{2})} + B_{(0,1,k+\frac{1}{2})}}{2r}. \quad (6.9)$$

The value of $B_{(0,1,k+\frac{1}{2})}$ is yet to be computed. The boundary condition from Section 6.3, $B = -\partial_r w$, is required. In second-order accurate form, it is expressed as

$$B_{(0,1,k+\frac{1}{2})} \approx -\frac{3w_{(\frac{1}{2},1,k+\frac{1}{2})} - \frac{1}{3}w_{(\frac{3}{2},1,1+\frac{1}{2})}}{\Delta r}. \tag{6.10}$$

This equation is substituted in Equation (6.9), then rearranged so that the unknown w's appear in the L.H.S., the R.H.S. then consists of known internal A and B values:

$$\left(\frac{-2}{\Delta r^2} - \frac{1}{2r\Delta r} - \frac{2}{r^2\Delta\theta^2}\right) w_{(\frac{1}{2},1,k+\frac{1}{2})} + \left(\frac{5}{3\Delta r^2} + \frac{1}{2r\Delta r}\right) w_{(\frac{3}{2},1,k+\frac{1}{2})} + \left(\frac{-0.2}{\Delta r^2}\right) w_{(\frac{5}{2},1,k+\frac{1}{2})} +$$

$$\frac{w_{(\frac{1}{2},1,k-\frac{1}{2})} + w_{(\frac{1}{2},1,k+\frac{3}{2})}}{r^2\Delta\theta^2} \approx \frac{A_{(\frac{1}{2},1,k+1)} - A_{(\frac{1}{2},1,k)}}{r\Delta\theta} - \left(\frac{1}{\Delta r} + \frac{1}{2r}\right) B_{(1,1,k+\frac{1}{2})}. \tag{6.11}$$

Similar expressions are obtained for the Poisson equations for v and u based on the staggered grid of Figure 6.1. This set of linear equations are then solved using the multigrid method described below.

N.B. Lewis (1999) reported that the second-order accurate differencing of vorticity boundary conditions involving the tangential velocity v produced unsatisfactory results when compared to results from computations using the radial-tangential and radial-axial codes described in Chapters 4 and 5 of the current thesis. Therefore, Lewis resorted to using first-order accurate differencing for the tangential velocity derivatives at the boundaries. The current author modified the code to use second-order accurate differencing for velocity v every where in the computational domain. Some trial results showed that this had insignificant effect when compared to the results obtained by the original code of Lewis. It is possible that the second-order conditions were not applied correctly in his code, this is one of the three possible reasons suggested by him (see Section 5.4.3 of Lewis, 1999). The modified code was used for all of the work described here.

6.4.4 Transient method

The time-dependent equations for vorticities and temperature are solved using Du-Fort Frankel method. To illustrate the method, two-dimensional Fourier's equation,

$$\partial_t \zeta = \partial^2_{xx}\zeta + \partial^2_{yy}\zeta,$$

is discretised as

$$\zeta^{n+1}_{i,j}[\frac{1}{\Delta t} + \frac{1}{\Delta x^2} + \frac{1}{\Delta y^2}] = \zeta^{n-1}_{i,j}[-\frac{1}{\Delta x^2} - \frac{1}{\Delta y^2}] + \frac{\zeta^n_{i,j}}{\Delta t} + \frac{\zeta^n_{i+1,j} + \zeta^n_{i-1,j}}{\Delta x^2} + \frac{\zeta^n_{i,j+1} + \zeta^n_{i,j-1}}{\Delta y^2}. \tag{6.12}$$

Comparing this with Equation (4.17) shows that here the time-derivative is discretised using an explicit method (also called forward Euler). Lewis (1999) found that in computing the current governing equations the second-order central differencing for the time-derivative produced numerically unstable solutions.

6.4.5 Multigrid method for the Poisson equations

For convergence efficiency a multigrid method is used to solve Equations (6.5)-(6.7). The idea of the method is described in Chapter 4. Here the solution strategy remains similar.

The solution of the Poisson equations is the most computationally intensive part of the code. As there are three such equations, instead of one in a two-dimensional problem, computing time is considerably affected. Various attempts to improve the convergence, including for example W-cycling, were tested. It was found that two modifications to the original scheme could be used to reduce the computing time by almost 50%.

The first modification is to use an extrapolation to obtain a better initial guess at the start of the iteration (Rees, 2000). The system of linear equations is in the

form $Au = f$, where A is the finite difference operator, u the matrix of unknowns to be calculated, and f a known-function matrix. A good initial guess will reduce the iterations required for convergence. The linear extrapolation to improve the initial guess is,

$$v^h_{new} = 2u^h_{now} - u^h_{old}, \tag{6.13}$$

where u^h_{now} and u^h_{old} are the converged solutions from previous timesteps, v^h_{new} is an initial guess or approximation for u^h_{new} which is to be iterated, and 'h' denotes the finest grid. Previously, the initial guess was set as,

$$v^h_{new} = u^h_{now}.$$

The second improvement is a simplified version of the so-called iterant recombination method (Trottenberg *et al.*, 2001). The approximate solution after m V-cylce sweeps is denoted by v^h_m and the number of linear combination pairs is denoted by $\tilde{m}$ (where $\tilde{m} < m$). The recombinant, between sweep m and sweep $m+1$, can then be represented by

$$v^h_m \rightarrow v^h_m + \sum_{i=1}^{\tilde{m}} \alpha_i (v^h_m - v^h_{m-i}), \tag{6.14}$$

where α_i are weights that can be calculated in a certain error minimisation method which is not discussed here. It can be seen that if $\tilde{m} = 1$, the equation above becomes

$$v^h_m \rightarrow v^h_m + \alpha_1 (v^h_m - v^h_{m-1}). \tag{6.15}$$

Note that if $\alpha_1 = 1$, an extrapolation similar to Equation (6.14) is obtained. In practice, this extrapolation between the V-cycles delayed convergence, and was modified instead to an SOR method:

$$v^h_m \rightarrow v^h_{m-1} + \alpha_1 (v^h_m - v^h_{m-1}). \tag{6.16}$$

Figure 6.2 is a schematic representation of the iteration process with a combination of multigrid V-cycles and SOR between the V-cycles. To minimise the number of V-cycle sweeps the value of α_1 was found by trial and error to be around 1.1 or 1.2. Ideally, α_1 should be a variable whose values are determined by an error minimisation calculation between sweeps, and it can even be variable between points or lines of points in the relaxation. However, considering that without a variable α_1 the computing time was already reduced by about half, implementing a variable α_1 calculation may be more costly than the above improvement in terms of both implementation and the resulting omputating times.

Within the V-cycles, the multigrid grid method remains the same as that described in Section (4.4.3), except that the Gauss-Seidel line-relaxations are performed for three directions, instead of two previously. Also, the restriction and prolongation are different because of the three spatial dimensions. The method is exactly as described in Lewis (1999). It is repeated here for completeness.

For restriction $I_h^{2h}V^h = V^{2h}$ takes the form of a full weighting operator:

$$\begin{aligned}
v^{2h}_{i,j,k} = \frac{1}{64}[&(v^h_{2i+1,2j+1,2k+1} + v^h_{2i+1,2j+1,2k-1} + v^h_{2i+1,2j-1,2k+1} + v^h_{2i+1,2j-1,2k-1} \\
&+v^h_{2i-1,2j-1,2k+1} + v^h_{2i-1,2j-1,2k-1} + v^h_{2i-1,2j+1,2k+1} + v^h_{2i-1,2j+1,2k-1}) \\
&+2(v^h_{2i+1,2j+1,2k} + v^h_{2i+1,2j-1,2k} + v^h_{2i-1,2j+1,2k+1} + v^h_{2i-1,2j-1,2k} \\
&+v^h_{2i+1,2j,2k+1} + v^h_{2i+1,2j,2k-1} + v^h_{2i-1,2j,2k+1} + v^h_{2i-1,2j,2k-1} \\
&+v^h_{2i,2j+1,2k+1} + v^h_{2i,2j+1,2k-1} + v^h_{2i,2j-1,2k+1} + v^h_{2i,2j-1,2k-1}) \\
&+4(v^h_{2i+1,2j,2k} + v^h_{2i-1,2j,2k} + v^h_{2i,2j+1,2k} + v^h_{2i,2j-1,2k} \\
&+v^h_{2i,2j,2k+1} + v^h_{2i,2j,2k-1}) + 8v^h_{2i,2j,2k}].
\end{aligned}$$

The prolongation operator is represented by $I_{2h}^h V^{2h} = V^h$, and the components

of V^h are given by

$$v^h_{2i,2j,2k} = v^{2h}_{2i,2j,2k}$$

$$v^h_{2i+1,2j,2k} = \frac{1}{2}(v^{2h}_{2i,2j,2k} + v^{2h}_{2i+1,2j,2k})$$

$$v^h_{2i,2j+1,2k} = \frac{1}{2}(v^{2h}_{2i,2j,2k} + v^{2h}_{2i,2j+1,2k})$$

$$v^h_{2i,2j,2k+1} = \frac{1}{2}(v^{2h}_{2i,2j,2k} + v^{2h}_{2i,2j,2k+1})$$

$$v^h_{2i,2j+1,2k+1} = \frac{1}{4}(v^{2h}_{2i,2j,2k} + v^{2h}_{2i,2j+1,2k} + v^{2h}_{2i,2j,2k+1} + v^{2h}_{i,j+1,k+1})$$

$$v^h_{2i+1,2j,2k+1} = \frac{1}{4}(v^{2h}_{2i,2j,2k} + v^{2h}_{2i+1,2j,2k} + v^{2h}_{2i,2j,2k+1} + v^{2h}_{i+1,j,k+1})$$

$$v^h_{2i+1,2j+1,2k} = \frac{1}{4}(v^{2h}_{2i,2j,2k} + v^{2h}_{2i+1,2j,2k} + v^{2h}_{2i,2j+1,2k} + v^{2h}_{i+1,j+1,k})$$

$$v^h_{2i+1,2j+1,2k+1} = \frac{1}{8}(v^{2h}_{2i,2j,2k} + v^{2h}_{2i+1,2j,2k} + v^{2h}_{2i,2j+1,2k} + v^{2h}_{i+1,j+1,k}$$

$$+v^{2h}_{2i,2j,2k+1} + v^{2h}_{i+1,j,k+1} + v^{2h}_{i,j+1,k+1} + v^{2h}_{i+1,j+1,k+1}).$$

6.4.6 Nusselt number calculation

Equation (4.21) is used for calculation global Nusselt number. It is repeated here:

$$Nu = -\frac{\bar{r}\ln r_i}{\bar{z}_{max} 2\pi}\int_0^{2\pi}\int_0^{\bar{z}_{max}} \partial_{\bar{r}}\bar{T}\, d\bar{z}\, d\theta, \tag{6.17}$$

where $\bar{r} = r_i$ (for inner cylinder) or $\bar{r} = 1$ (outer cylinder). As before the integral is calculated using trapezoidal rule and the derivative (the integrand) is approximated with a fourth-order accurate finite differencing.

6.4.7 Code structure

A single time-step has the following numerical procedure:

- Initialise all variables at $\bar{t} = 0$ (Section 6.3).
- Solve for A^{n+1}, B^{n+1}, C^{n+1}, T^{n+1} on all internal grid points (including the adiabatic surfaces for T^{n+1}) from solutions at t^n and t^{n-1} (Sections 6.4.2 and 6.4.4).

• Solve the Poisson velocity equations using the multigrid method (Section 6.4.5) using vorticities at t^{n+1} and subject to the vorticity boundary conditions (Section 6.4.3).

• Update A^{n+1}, B^{n+1} and C^{n+1} on all boundaries using the boundary conditions (Section 6.3).

6.5 Results

6.5.1 Approximating horizontal layers

As in the previous two chapters, the code was modified to compute free convective heat tranfer in a non-rotating annulus with gravity directed away from the annulus centre. This type of flow has been shown in previous chapters to be able to approximate Rayleigh-Bénard convection very well. Lewis (1999) validated the 3D code by comparison with the two-dimensional radial-tangential and radial-axial computational results. Here, the performance of the 3D code was investigated using published results for Rayleigh-Bénard convection. In order to do this, terms containing Re_b in Equations (6.2)-(6.3) are removed (refer to Chapters 4 and 5 for more explanation of this approximation).

The computations were performed on a $16 \times 16 \times 128(r - z - \theta)$ interval grid and a non-dimensional timestep $\Delta\bar{t} = 0.001$ for lower Rayleigh number cases, and a $32 \times 32 \times 128$ interval grid and $\Delta\bar{t} = 5 \times 10^{-8}$ for the higher Rayleigh number cases. The annulus has dimensions of $r_i = 0.7, r_o = 1.0, s/b = 0.5$.

The heat transfer results are presented in Figure 6.3. The computed results agree well with the semi-empirical correlation by Hollands *et al.*(1975). The highest Rayleigh number that can be computed is limited by the spatial and temporal resolutions (i.e. grid intervals and timestep), and also the computing time required. For example, the flow at $Ra = 10^{5.69}$ required 4 weeks of computing time; it was

decided not to compute further cases with higher Rayleigh numbers because of time constraint in the current study.

The average (global) Nusselt number on both the inner and outer cylindrical surfaces are presented in Figure 6.3. There is no systematic difference between the two. This is an expected result as the time-averaged values are calculated after the flow has become fully-developed (no change in the trend of Nusselt number time series) and so heat transfer into the fluid from the outer (hot) cylinder must be equal to heat transfer out of the fluid from the inner (cold) cylinder. The slight differences in a few cases may be due to the inaccuracies from the finite difference approximation used in calculating the temperature gradients near the surfaces. Another reason may be that Nu was not time-averaged over long enough period. It is also noted in Figure 6.3 that the computation was able to predict the onset of convection near the theoretical critical Rayleigh number of 1708 ($\approx 10^{3.23}$).

The correlation of Hollands *et al.*(1975) (Equation (3.10)) is repeated here,

$$Nu_{(Pr\approx 0.7)} = 1 + 1.44 max\left\{\left(1 - \frac{1708}{Ra}\right), 0\right\} + max\left\{\left(\frac{Ra}{5830}\right)^{1/3} - 1, 0\right\}. \quad (6.18)$$

It is clear that this equation has three components on the R.H.S. The first term represents heat transfer by conduction alone ($Nu = 1$), the second term represents steady convection, and the third unsteady convection. The contributions of these three components to Nu are shown separately in Figure 6.3 as the dashed lines. It is seen that the critical Rayleigh number is 1708 and the third term contribution (unsteadiness) begins at $Ra = 5830 \approx 10^{3.77}$. From here there is separation of at least three decades before the unsteadiness finally dominates. It is near this stage ($Ra = 10^7$) where the so-called hard-turbulence sets in, the bulk-flow becomes well-mixed, and so the 1/3-scaling prevails (see also Sections 2.1, 3.3.1 and 3.3.2). Recall from Section 2.1 that fully developed convective turbulence and aperiodic convec-

tion are not the same. For example in the experiment by Castaing *et al.*(1989) hard turbulence began at 4×10^7 which is three decades higher than the value of Ra at the onset of chaotic flow measured by Krishnamurti (1970b) (although she called this chaotic flow turbulence, the true convective turbulence which is characterised by a certain exponential distribution in the probability density function of the temperature fluctuation was later observed by Castaing *et al.* and Helslot *et al.* in the late 1980's). Also, this hard turbulence occurs before the boundary layers become turbulent that may give rise to the so-called ultimate regime with a 1/2-scaling. So far, there is only one definitive observation of this 1/2-scaling which was triggered by rough surfaces and began at $Ra = 10^{12}$ (Roche *et al.*, 2001).

Figures 6.4 and 6.5 show the velocity vectors and the isotherms on the mid-axial plane ($z/b = 0.25$) for different Rayleigh number cases. These are instantaneous solutions at the end of the simulations (as opposed to time-averaged plots). The convecitve rolls with their distinctive plumes, and the concentrated isotherms at the boundaries for the higher Rayleigh number cases are observed.

6.5.2 Rotating annuli with radial heat flux

The computed 3D solutions for sealed rotating annuli with imposed radial thermal gradient are presented in the subsections below. The behaviours of the flow and heat transfer according to changes in the dimensionless parameters Ra_ϕ and Re_ϕ, and the geometrical dimensions of the annuli are discussed.

Solutions for $\beta\Delta T \approx 0.3$, $r_i = 0.5$, $r_o = 1.0$, $z_{max} = 0.5$

This subsection presents results for $\beta\Delta T \approx 0.3$ with increasing Ra_ϕ. Recall that $Ra_\phi = Re_\phi \frac{d}{r_m} \beta\Delta T Pr$. Thus, an increase in Ra_ϕ with $\beta\Delta T \approx 0.3$ requires a corresponding increase in Re_ϕ. The computational mesh has intervals of $16 \times 16 \times 128$ (in $r - z - \theta$) and non-dimensional timestep $\Delta\bar{t} = 0.0002$ for low Rayleigh number,

and $32 \times 32 \times 144$, $\Delta\bar{t} = 5 \times 10^{-8}$ at the higher Rayleigh number simulations.

Figures 6.6 to 6.8 show velocity vectors, axial velocity isolines, and isotherms contours in selected radial-tangential planes. The flow at $Ra_\phi = 10^{3.9}$ is shown at three equi-spaced axial positions in Figure 6.6. The annulus rotates anticlockwise. There are four cyclonic-anticyclonic pairs (also called rolls hereafter). The cyclones circulates in the same sense as the annulus, the anticyclones in the opposite sense. Lewis (1999) ascribed the larger size of the cyclones to strengthening by the relative angular motion between the annulus and the rolls. The rolls are actually precessing clockwise (Lewis, 1999). So, relative to the rolls, the cylinder rotates anticlockwise, thus enhancing the cyclones near the outer cylinder. The effect is relatively small at the inner cylinder because the radius is smaller. Similarly, the precession of the rolls has a weakening effect to the anticyclones and hence their smaller size.

The appearance of the rolls can be explained by assuming a geostrophic condition in which the dominant terms in the governing equation are the Coriolis force and the pressure gradients. Equation (4.4) is then simplified to

$$\rho(2\Omega u) = -\frac{1}{r}\partial_\theta p. \tag{6.19}$$

From the equation above, it is seen that a positive u (radial outflow) requires a negative pressure gradient in the positive tangential direction. A negative u (radial inflow) requires a positive pressure gradient in the positive tangential direction. This implies that the cyclonic regions are at lower pressure relative to that in the anticyclonic regions. Because of this, the flow is away from the discs at the cyclones and toward the discs at the anticyclones. Figure 6.6.b shows this phenomenon clearly. The discs are located at $z/b = 0$ and $z/b = 0.5$, therefore, the directions of the axial velocity reverse across the mid-axial plane. In fact, the flow is symmetrical about the mid-axial plane, hence, the zero axial velocity at mid-axis.

Results for four further cases are shown in Figures 6.7 and 6.8. The flows are always symmetrical about the mid-axial plane, so only the contours at $z/b = 0.125$ are displayed. Although, in general, the number of roll pairs increases with increasing Ra_ϕ, it is difficult to make any conclusion about the exact number of roll pairs associated with a certain Ra_ϕ. More detailed analyses in this respect by, for example, Lewis (1999) and Maubert & Randriamampianina (2000) have found that, depending on the initial perturbations, solutions with different numbers of roll pairs can be obtained. Some solutions may be more dominant than the others, but there are also cases where two or more solutions can coexist.

Figure 6.8.c shows that for $Ra_\phi = 10^{5.49}$, the bulk-flow becomes almost isothermal and the temperature gradients are confined to thin boundary layers near the inner and outer cylinders. The cyclonic-anticyclonic pairs are either absent or cannot be indentified clearly.

The Nusselt numbers obtained are given in Table 6.1, and are also shown in Figure 6.11. It is clear that at this 'low' Rayleigh number case, Nu increases with Ra_ϕ in agreement with the correlation for Rayleigh-Bénard convection by Hollands *et al.*(1975). Computations, at a higher Rayleigh numbers were not performed because of long computing times (more than one month!) required.

$\lg(Ra_\phi)$	3.9	4.22*	4.5	4.62	4.9	5.49
Nu	2.14	2.6*	2.92	3.1	4	7.5

Table 6.1: Values of $\lg(Ra_\phi)$ and Nu from computations of 3D rotating annulus flow $\beta\Delta T \approx 0.3$. $r_o = 1.0$, $r_i = 0.5$, $z_{max} = 0.5$. **data from Lewis (1999).*

Solutions for $Ra_\phi = 1 \times 10^{3.9}$, $r_i = 0.5$, $r_o = 1.0$, $z_{max} = 0.5$

Here, results at $Ra_\phi = 1 \times 10^{3.9}$ for increasing Re_ϕ are presented. The value of $\beta\Delta T$ is decreased according to $Ra_\phi = Re_\phi \frac{d}{r_m} \beta\Delta T Pr$. Figures 6.9 and 6.10 show the velocity vectors, axial velocity isolines and isotherms on the radial-tangential

plane at $z/b = 0.125$. The corresponding results for heat transfer are given in Table 6.2.

Re_ϕ	219	291	546	1821	3643
$\beta\Delta T$	0.39	0.22	0.062	0.0056	0.0014
Nu	2.14	2.0	1.547	1.12	1.0

Table 6.2: Values of Re_ϕ (and the corresponding values of $\beta\Delta T$) and Nu from computations of 3D rotating annulus flow at $Ra_\phi = 10^{3.9}$. $r_o = 1.0$, $r_i = 0.5$, $z_{max} = 0.5$.

These heat transfer results are also plotted in Figure 6.11. It is clear that the value of Nu decreases with increasing Re_ϕ. At high rotational Reynolds numbers the rolls break down due to the large Coriolis force present; as a result, the radial temperature gradients are greatly reduced. Previous results (see Sections 2.2.1 and 4.5.3) suggest that the effect of Reynolds number at high Rayleigh number is not significant.

An additional result obtained was $(4.62, 3.2)$ for $Re_\phi = 728$ ($\beta\Delta T \approx 0.17$). Two cases computed by Lewis (1999) were also used to obtain the points $(4.9, 3.5)$ for $Re_\phi = 1822$ ($\beta\Delta T \approx 0.056$), and $(4.9, 3.5)$ for $Re_\phi = 3644$ ($\beta\Delta T \approx 0.014$). The data are shown in Figure 6.11. These last two points are further indications that the influence of Reynolds number at higher Rayleigh is weakened considerably. As discussed in Chapter 4, Ra_ϕ and $\beta\Delta T$ are the dominant influences on Nu. Comparing the values of $\beta\Delta T$ in Figure 4.14.b with those in Table 6.2 suggests again that when $\beta\Delta T$ cannot be altered over a large range (usually the constraint in experiments and real engines), only Ra_ϕ has a significant effect on the heat transfer efficiency as quantified by Nu. Note that the smallest $\beta\Delta T$ in Table 6.2 is about 30 times smaller than the smallest in the experiments of Bohn *et al.*(1995). Therefore, the decrease in Nu observed here cannot normally happen in a system where $\beta\Delta T$ is variable over a small range.

Solutions for $\beta\Delta T \approx 0.3$, $r_i = 0.5$, $r_o = 1.0$, $z_{max} = 0.25$

Computations similar to those described above for $z_{max} = 0.5$ were performed for an annulus with a smaller axial gap, $z_{max} = 0.25$. The flow structures are shown in Figure 6.12 and 6.13. There is no significant difference in the basic qualitative flow structures from those for the $z_{max} = 0.5$ annulus.

The heat transfer result is also essentially indistinguishable from those for the $z_{max} = 0.5$ annulus. This is not surprising because the aspect ratios for these two annuli are $z_{max}/d = 1.0$ and $z_{max}/d = 0.5$. Results from previous chapters and other publications suggest that these values of aspect ratio are not small enough for the heat transfer to be significantly reduced. The weak dependence of the heat transfer to the aspect ratio in the flows computed here is also in agreement with Bohn & Gier (1998), who reported that three-dimensionality in their computations had only a small impact on the global heat transfer even though the local flow structures might be different. The weak effect of the three-dimensionality to heat transfer is also discussed in details in Chapter 4 and King & Wilson (2002). No computations for smaller values of z_{max}/d have been carried out in the present work.

Since the reduced axial separation is $z_{max} = 0.25$, fewer grid intervals in the axial direction were required than for the $z_{max} = 0.5$ cases. So, an additional computation was possible for $Ra_\phi = 10^6$, which is slightly higher than the highest achievable for the $z_{max} = 0.5$ annulus. This additional result, $(6, 7.5)$, is shown in Figure 6.11, and is in agreement with the trends of other computations and the correlation for Rayleigh-Bénard convection.

Solutions for $Ra_\phi = 1 \times 10^{5.35}$, $r_i = 0.3$, $r_o = 1.0$, $z_{max} = 0.5$

Results from a simulation for an annulus with a smaller inner radius of $r_i = 0.3$ is discussed here. The computational mesh used had intervals of $32 \times 24 \times 128$ and

the non-dimensional timestep was $\Delta\bar{t} = 1 \times 10^{-5}$. Only a single simulation for the flow at $Ra_\phi = 10^{5.35}$, $\beta\Delta T = 0.056$ ($Re_\phi = 2273$) was performed.

The computed flow structures are presented in Figure 6.14. It is noted that the flow is also symmetrical about the mid-axial plane. The cyclonic-anticyclonic pairs are not distinct and not organised around the annular space in a regular manner. Four cold 'jets' moving radially outward can be seen clearly, while the bulk of the fluid has fairly uniform temperature. Note the steep temperature gradient near the inner cylinder. The heat transfer result is $(5.35, 3.8)$. A further data point of $(5.35, 5)$ is obtained from Lewis (1999) for the flow at $Ra_\phi = 10^{5.35}$, $\beta\Delta T = 0.35$ and $Re_\phi = 729$. These two points are shown in Figure 6.11. In agreement with the conclusions in Chapters 4 and 5, it is again argued that the radial separation of the cylindrical walls has only a very small effect on the heat transfer. Note that the value of $\beta\Delta T$ was decreased from 0.35 to 0.056 for Nu to drop from 5 to 3.8.

6.5.3 Concluding remarks

Unsteady three-dimensional computations were conducted to investigate both the general flow structure and heat transfer for air-filled sealed rotating annuli. It was found that the dimensions of the annuli have only small effects on the heat transfer. Also, if the value $\beta\Delta T$ is not varied through a large range, Nu is only strongly dependent on Ra_ϕ. These results are in agreement with the conclusions from previous chapters for simplified two-dimensional radial-tangential or axisymmetric models. For the flows at $\beta\Delta T \approx 0.3$ and increasing Ra_ϕ, the computed results for Nu agree with the Rayleigh-Bénard convection correlation. For flows at $Ra_\phi = 10^{3.9}$ and increasing Re_ϕ, it was found that the value of Nu decreases with increasing Re_ϕ until no convective flow occurs (i.e. $Nu = 1.0$).

The computational methods used in the current work to solve the governing

equations are very likely to be inadequate for the simulation of the turbulent flow at higher Rayleigh numbers. It was also not possible to produce solutions in tolerable computing times. Thus simulations for flow at Rayleigh numbers investigated experimentally by Bohn *et al.* could not be conducted here. The flow physics involves very thin boundary layers, and sufficiently high resolution is also needed to capture the behaviour of convective and rotating turbulence. These problems are the subjects of many other advanced investigations.

Because of limitations in computing resources and time, some conclusions reached in this chapter are somewhat tentative. However, results from previous chapters and publications are used cautiously to guide interpretations of the data obtained in the current chapter. More systematic investigation by unsteady three-dimensional computation using the current or other more elaborate computer codes is recommended.

6.5.4 Rotating annuli with a single radial barrier

In this section, computed results for flows in a rotating annulus with a fully blocking radial barrier are presented. This type of flow has been studied extensively by the geophysical fluid dynamics community (e.g., see Rayer *et al.*, 1998). In an unobstructed annulus, such as that investigated in the previous section, rotation can significantly reduce heat convection at the relatively low Rayleigh number cases investigated by the geophysicists. This is because the radial flows (responsible for heat transfer) are sustained by circumferential pressure gradients which in turn are supplied by cyclonic-anticyclonic rolls. At high rotational Reynolds numbers these rolls break down due to the large Coriolis force present, so that the radial temperature gradients are greatly reduced (see Figure 6.10).

It was suggested (Hide, 1968) that a radial barrier can provide the circum-

ferential thermal and pressure gradients required by the radial flows, so that heat transfer would be unaffected by rotation. Previous laboratory investigations had confirmed this statement (Rayer *et al.*, 1998 and references therein). In this section, results from computer simulations are discussed.

In addition to the boundary conditions reported in Section 6.3, the following boundary conditions are also applied to either side of the insulating radial barrier located at $\theta = 0$, $\theta = 2\pi$,

$$u = v = w = 0, \qquad A = \frac{1}{r}\partial_\theta w, \qquad B = 0, \qquad C = \frac{-1}{r}\partial_\theta u, \qquad \partial_\theta T = 0.$$

The periodic boundary condition is no longer valid.

The flow structures for three selected cases are shown in Figures 6.15 and 6.16. Except for the regions near the radial barrier, there is no apparent difference in the qualitative flow structures from those in the unobstructed annulus. Comparing Figure 6.15 with Figures 6.7 and 6.12 indicate that distinct hot and cold plumes are still present in the blocked annulus even at relatively higher Rayleigh number.

Heat transfer results for $\beta\Delta T \approx 0.3$ are given in Table 6.3; the data is also shown in Figure 6.16. The results again agree very well with the Rayleigh-Bénard convection correlation.

$lg(Ra_\phi)$	2.9	3.9	4.6	4.9	5.5	5.9
Nu	1.0	2.04	2.74	3.58	5.6	6.8

Table 6.3: Values of $\lg(Ra_\phi)$ and Nu from computations of 3D flow in a rotating annulus with an insulating radial barrier $\beta\Delta T \approx 0.3$. $r_o = 1.0$, $r_i = 0.5$, $z_{max} = 0.5$.

Four further cases for the flow in the same radially blocked annulus at $Ra_\phi = 10^{3.9}$ with increasing Re_ϕ were computed. The computed flow structures are displayed in Figures 6.18 to 6.21.

Figures 6.21 and 6.10 show a clear difference due to the presence of the barrier.

In Figure 6.20, the rolls and the cold and hot plumes are still present at this relatively high Rayleigh number flow. The time-dependent variation of Nusselt number for each of the four cases are shown in Figure 6.22. The results are in contrast to those obtained for an unblocked rotating annulus (see Figure 6.10). It is noted that at $Re_\phi = 10^{3.9}$ ($\beta\Delta T \approx 0.3$), flows in both the unblocked and blocked annulus produce similar Nu values (see Tables 6.3 and 6.1). The values of $\beta\Delta T$ in the blocked annulus flow simulation varies in similar range to those in the unblocked annulus flows computed in the last section.

These results show very clearly that the radial barrier can support the circumferential pressure and temperature gradients required to maintain Nu at increasing Re_ϕ. It seems that the 'support' provided by the barrier is transmitted throughout the annular cavity. The cyclonic-anticyclonic rolls are sustained and giving rise to radial inflows and outflows which are able to transport heat effectively even at higher Re_ϕ.

It should be commented here that the flow structures obtained here are different from those observed by Rayer *et al.*(1998). For their blocked annulus, gravity (characterised by a thermal Rossby number $\Theta = \frac{g\beta\Delta Ts}{\Omega^2(b-a)^2}$) along the rotational axis is significant. On the radial-tangential plane, they observed a single large circulation around the whole of the annular cavity.

6.5.5 Concluding remarks

Flow and heat transfer in a rotating annulus with a single insulating radial barrier have been simulated. The results show that for flow at $\beta\Delta T \approx 0.3$ and increasing Ra_ϕ, the values of Nu obtained agree with the correlation for Rayleigh-Bénard convection. For flows at $Ra_\phi = 10^{3.9}$ with increasing Re_ϕ, it was found that the resulting Nu were maintained at around 2, in contrast to results obtained for an

unblocked annulus.

It is concluded that the radial barrier can provide the pressure gradients required to support the covective radial flows. The barrier provides support that is transmitted throughout the annular cavity, thus sustaining the crucial convective rolls at high Re_ϕ.

Chapter 7

Heat transfer in cavities with axial throughflow

7.1 Introduction

This chapter presents correlations of dimensionless parameters for flow in rotating and stationary cavities with throughflow. Similar rotating cavities can be found in gas-turbine high-pressure compressors with cooling air which passes through the axial bores of compressor discs; the cavities are formed between adjacent discs. Figure 7.1 shows schematic representation of two configurations. There are a number of possible heating situations: discs and/or shroud (outer cylinder) heated, air and walls (discs and shroud) isothermal (no heating), etc.

The present discussion is restricted to the 'heated shroud' case, which has stationary counterparts in horizontal flat plate and Rayleigh-Bénard convection. These two latter cases have the benefit of the methods and the phenomenological models which were applied satisfactorily in Chapter 3.

Farthing *et al.*(1992a & 1992b) conducted experiments for the heated discs case; Long (1994) and Long & Tucker (1994) made measurements for a rotating cavity with a circular inlet (Figure 7.1.a) for the cases where the discs and/or shroud were heated. Long *et al.*(1997) conducted measurements and computations for two

cases: (i) a 'simple' cavity with circular inlet (Figure 7.1.a) in which the shroud and discs were heated independently; (ii) a compressor cavity with annular inlet (Figure 7.1.b) in which the shroud was heated and heat was conducted to the discs. Owen & Rogers (1995), Owen (1999) and Owen & Wilson (2000) reviewed some previous investigations.

Owen (1999) describes buoyancy-induced flow as the most intractable of all rotating-disc flows. Most cases of industrial interest are usually three-dimensional and unsteady; it is unclear if the flows are laminar or turbulent, periodic or aperiodic. This poses difficulties for both experiments and computations.

Using techniques of dimensional and scaling analyses similar to those described in Chapter 3, correlations that quantify the global heat transfer are derived. Since the governing and boundary-layer equations, which are relatively complicated, are not used here, the exact quantitative and qualitative descriptions and local behaviour of the flow cannot be known from the analyses. The *ad hoc* method ('*ad hoc*' because certain parameters are specially selected to give promising scalings) can be arbitrary, and so validation with other suitable results is needed. It will be indicated clearly where validation is not possible because of lack of data. It is suggested that an unvalidated scaling-law is not necessarily incorrect, it may lie in a regime in which no experiment has yet been conducted.

It can be shown that $Nu_z = f(Re_z, Ra_z, Re_b, Pr)$ for a rotating cavity with axial throughflow. Definitions of the dimensionless parameters are given in the nomenclature but are repeated here for convenience: $Nu_z = \frac{\dot{q}s}{2k\Delta T}$, $Ra_z = \frac{b\Omega^2\beta\Delta T s^3}{8\nu\kappa}$ (or $= \frac{g\beta\Delta T s^3}{8\nu\kappa}$ for stationary cavities), $Re_z = \frac{W2\Delta d}{\nu}$ (or $= \frac{W2a}{\nu}$), $Re_b = \frac{\Omega b^2}{\nu}$ and $Pr = \nu/\kappa$. Note that following the conventional usage in the literature the characteristic length in Nu_z and Ra_z is $s/2$.

7.2 Axial throughflow and heated shroud

As in the studies of free convection in a sealed rotating annulus, the problem is simplified to a stationary cavity with heating from below, but now with the additional inlet and outlet, near the top wall, with inlet fluid velocity W and inlet temperature T_i (Figure 7.2).

The fluid velocity (u_c) in the cavity is driven by the throughflow (with velocity W) and can be scaled as

$$u_c \sim \frac{W2\Delta d}{s}. \tag{7.1}$$

Therefore,

$$(Re = \frac{u_c s}{\nu}) \sim (\frac{W2\Delta d\, s}{s\nu} = Re_z), \tag{7.2}$$

which establishes that Re and Re_z can be used interchangeably. Note that Re is defined using the characteristic length s instead of d ($d = b-a$). The phenomenological model of Castaing *et al.*(1989) (see Section 3.3.3) is modified for forced convection here. Equations (3.11), (3.12), (3.14) and (3.15) are repeated:

$$u_c \sim (\beta g \Delta T_{fluc} s)^{1/2}, \tag{7.3}$$

$$\dot{q} \sim c_p \rho_0 u_c \Delta T_{fluc}, \tag{7.4}$$

$$Nu_z \sim \frac{s}{\delta_\theta}, \tag{7.5}$$

$$\delta_u \sim \frac{s}{Re_z^{1/2}}. \tag{7.6}$$

These equations are still applicable because a large scale wind u_c, which is now forced by W, still drives the convection that gives rise to temperature fluctuations ΔT_{fluc} which enables the heat flux $\dot{q}$ in the well-mixed bulk region. Equation (7.5) originates from both the definition and the assumption that the well-mixed bulk flow pushes a steep temperature gradient to the thermal boundary layer. Equation

(7.6) applies to laminar boundary layer flow over a flat plate.

Studies of convective heat transfer show that the flow is in the forced convection regime if $Ra_z/Re_z^2 \ll 1$ and is in the free convection regime if $Ra_z/Re_z^2 \gg 1$. For $Ra_z/Re_z^2 \sim 1$ the flow is in the mixed convection regime. A similar parameter called the buoyancy number ($Bo = Gr_z/Re_z^2$) is defined in Owen (1999), Bo is a measure of the relative strength of centrifugal buoyancy to axial inertia.

7.2.1 Forced convection and turbulent boundary layer

The equivalent of Equation (3.16) is now formulated. For forced convection a balance of inertial force and viscous force is required instead of the balance of buoyancy and viscous forces as in free convection:

$$\rho_0 \delta_\theta \frac{1}{\delta_\theta}(\frac{\delta_\theta}{\delta_u} u_c)^2 \sim \mu \frac{u_c}{\delta_u}. \tag{7.7}$$

The term $\frac{\delta_\theta}{\delta_u} u_c$ is an estimate of the velocity inside the viscous boundary layer but just outside thermal boundary layer (Figure 7.3). Combining Equations (7.7), (7.5) and (7.6) gives

$$Nu_z \sim Re_z^{3/4}. \tag{7.8}$$

This value of the exponent is close to that for a forced convective turbulent boundary layer across a flat plate ($Nu_z \sim Re_z^{0.8}$) calculated by analytical methods (see Chapter 4 in Kreith & Bohn, 1986). Strictly speaking $Nu_z \sim Re_s^{0.8}$ (where $Re_s = Ws/\nu$) for flow over a flat plate, but it can be argued that $2\Delta d \sim s$ (i.e. they have similar order of magnitude) and so $Re_s \sim Re_z$.

Note that although Equation (7.6) is derived from laminar boundary layer flow, it is still valid as an estimate of viscous sub-layer thickness inside a tubulent boundary layer. Outside this viscous sub-layer, the fluid velocity increases quickly to the freestream velocity u_c, therefore δ_u can be regarded as the viscous sub-layer

thickness, instead of the total thickness of the turbulent boundary layer. This viscous sub-layer is in essence equivalent to a laminar boundary layer having the character of the phenomenological picture of Figure 7.3. Equations (7.3), (7.4) and the definition of Nu_z are used to form

$$Re_z \sim Nu_z^{1/3} Ra_z^{1/3} Pr^{-2/3}. \tag{7.9}$$

Equations (7.8) and (7.9) are then used to obtain

$$Nu_z \sim Ra_z^{1/3} Pr^{-2/3}. \tag{7.10}$$

This agrees exactly with the scaling for forced turbulent boundary layer flow over a flat plate (Chapter 4 of Rohsenow *et al.*, 1998).

7.2.2 Forced convection and laminar boundary layer

Simply using Equations (7.5) and (7.6) gives the following relationship,

$$Nu_z \sim Re_z^{1/2}. \tag{7.11}$$

The ratio δ_u/δ_θ can be scaled with Pr^n, where n is a real number; since n cannot be known without further analysis of the boundary-layer equations (see Equation (3.17)), the effect of Pr is not considered here. Equations (7.9) and (7.11) are used to obtain

$$Nu_z \sim Ra_z^{1/5}. \tag{7.12}$$

Equation (7.11) agrees exactly with the analytical result for forced laminar flow over a flat plate (Kreith & Bohn, 1986, Chapter 4), while the value of the exponent in Equation (7.12) differs slightly with the ubiquitous scaling for convective flow (which is 1/4; see Chapter 4 of Rohsenow *et al.*, 1998).

7.2.3 Free convection and turbulent boundary layer

If the flow is dominated by free convection and boundary layer turbulence, the scalings from regime IV_l of Grossmann & Lohse could be used (see Table 3.3 and Figure 3.5):

$$Nu_z \sim Pr^{1/2} Ra_z^{1/2}. \tag{7.13}$$

The equation above is again obtained using Equation (3.17), which is repeated here:

$$Nu_z \sim Re_z^{1/2} Pr^{1/3}. \tag{7.14}$$

It is discussed in Chapter 3 that flow satisfying this regime is 'rare'. Experiments designed to observe it have met with many difficulties, the main reasons probably being that this regime exists at very high Rayleigh number for low Prandtl number fluids. Therefore in the current context of convection with throughflow, this problem has reduced to the pure free convective flow case.

7.2.4 Free convection and laminar boundary layer

If the flow is dominated by free convection and laminar boundary layer, Equation (3.27) from Chapter 3 can be used directly,

$$Nu_{z(Pr \gtrsim 1)} \sim Pr^{-1/12} Ra_z^{1/4}. \tag{7.15}$$

The above equation is again obtained using Equation (3.17), which is repeated here:

$$Nu_z \sim Re_z^{1/2} Pr^{1/3}. \tag{7.16}$$

These scalings are similar to those in the 'forced convection and laminar boundary layer' flow (Section 7.2.2). The 1/4-scaling from Equation (7.15) is observed in many types of laminar boundary layer convection, including that for free convection from

a horizontal flat plate.

Figure 3.5, which summarises the results by Grossmann & Lohse (see also Section 3.3.6), indicates that each of the three regimes I has a 1/4–scaling. However, the other regimes surrounding regimes I have different γ values of $\frac{1}{5}$, $\frac{1}{3}$, $\frac{3}{7}$ and $\frac{1}{2}$. As discussed previously, in a real flow a pure scaling may be corrected by scalings from neighbouring regimes. This suggests that the derivation of Equation (7.15) may be simplistic, and γ values obtained from measurements for this regime are likely to be different.

7.2.5 Mixed convection

The mixed convection regime occurs in the transition between free and forced convections where both of these convections are significant. Here correlations between Rayleigh and Reynolds number are derived to estimate the delineations among the free, mixed, and forced convection regimes.

At the transition from free to forced convection in laminar boundary layer flow, i.e. moving from low to high Reynolds number at some low or moderate Rayleigh number, equating Equations (7.15) and (7.11), gives

$$\frac{Ra_z}{Re_z^2} \sim Pr^{1/3}. \tag{7.17}$$

The fraction on the left-hand-side is equivalent to the 'Buoyancy parameter', $Bo = Gr/Re^2$, suggested by Owen (1999). If this fraction is larger than order 1, free convection occurs; if it is order 1, mixed convection occurs, if it is much less than order 1, forced convection dominates.

Equation (7.17) can be rewritten in the following form:

$$Re_z^2 = C Ra_z Pr^{-1/3} \Rightarrow \log Re_z = \frac{1}{2}\log Ra_z - \frac{1}{6}\log Pr + \frac{1}{2}\log C, \tag{7.18}$$

where C is a constant of proportionality which can usually be determined only by laboratory experiments (see Chapter 3). The region near this logarithmic variation of Re_z with Ra_z is the mixed convective regime. Above this line, forced convection dominates, and below, free convection prevails (see Figure 7.4).

It can be suggested from Equation (7.18) that, by increasing the Reynolds number, the flow at low or moderate Rayleigh number (laminar free convection) first reaches the mixed convective regime and then the laminar forced convective regime (since $Re_z \sim Ra_z^{1/2}$ at mixed convection, Re_z just at the onset of forced convection is still small because of the low to moderate Rayleigh numbers), and eventually to turbulent forced convection ($Re_z \gg Ra_z^{1/2}$). At high Rayleigh number (turbulent free convection), increasing the Reynolds number moves the flow to mixed convection then straight to turbulent forced convection (since $Re_z \sim Ra_z^{1/2}$ at mixed convection, Re_z after mixed convection is now beyond the transition to turbulent flow because the Rayleigh number is high). Therefore, laminar free convective flow will cross the mixed convection regime *not* to become turbulent forced convection immediately (but reaching laminar forced convection first), and a turbulent free convective flow *cannot* become laminar by increasing its Reynolds number (later, this statement will be slightly modified).

Next we consider the transition from turbulent free convection to turbulent forced convection by equating Equations (7.8) and (7.13),

$$\frac{Ra_z}{Re_z^{3/2}} \sim Pr^{-1} \Rightarrow \log Re_z = \frac{2}{3}(\log Ra_z + \log Pr + \log C). \tag{7.19}$$

This implies that the gradient of the 'mixed convective' line becomes steeper at very high Rayleigh number range. In other words, a proportionally much higher Reynolds number is required to move a turbulent free convective flow to the turbulent forced convective regime.

Despite the statement made above, it is necessary to consider the transition between laminar free convective flow and turbulent forced convective flow. This is due to the evidence that the scaling in Equation (7.13) is seldom observed even at very high Rayleigh number. Therefore, equating Equations (7.8) and (7.15), gives

$$\frac{Ra_z}{Re_z^3} \sim Pr^{1/3} \Rightarrow \log Re_z = \frac{1}{3}\log Ra_z - \frac{1}{9}\log Pr + \frac{1}{3}\log C, \tag{7.20}$$

which contradicts the conclusion drawn from Equation (7.19) in the previous paragraph. In fact, since the 1/4-scaling from Equation (7.15) is much more common, most measurements agree qualitatively with Equation (7.20) (i.e. the 'mixed convective' line becomes less steep at high Rayleigh number).

Figure 7.4 shows schematic delineations of the different convective regimes. These delineations are indicated by the analyses performed in Section 7.2. From Figure 3.5, the Ra_z value at the transition from laminar free convection to turbulent free convection is estimated at $Ra_z > 10^{16}$ for $Pr \gtrsim 1$ (non-liquid-metal fluids such as air, helium and water). A shear Reynolds number is defined as

$$Re_{shear} = u_c \delta_u / \nu.$$

Since $\delta_u \sim \frac{d}{Re^{1/2}}$ and $Re = u_c d/\nu$, this gives

$$Re_{shear} \sim Re^{1/2}.$$

At the onset of turbulence $Re_{shear} = 420$ typically (Grossmann & Lohse, 2000), therefore at the transition from forced convection with laminar boundary layer to forced convection with a turbulent boundary layer,

$$Re \sim (420^2 \approx 2 \times 10^5). \tag{7.21}$$

At the beginning of Section 7.2 it was shown that $Re \sim Re_z$. The exact values of

the transitions are unknown without further studies.

Analysis using Bo alone is inadequate as it can only indicate if the flow is free, or mixed, or forced convection dominated. However, it has been shown here that the laminar and turbulent regimes also give different scaling–laws. Therefore, Figure 7.4 presents a broader picture of the flow regimes by retaining the values of Ra_z and Re_z; if required, the value of $Bo = Ra_z/Re_z^2$ can always be calculated.

7.3 Concluding remarks

Correlations of dimensionless parameters for free, mixed and forced convection in cavities with throughflow have been derived in this chapter using scaling analysis. The correlations compare well with those obtained by other methods for flows over a flat plate. A regime diagram delineating the different types of convection is also obtained from the same correlations and equations. The analysis is carried out without reference to the boundary layer equations, and it is remarkable what the relatively simple technique used here can yield.

Unfortunately, the correlations cannot be compared rigorously with published results for rotating cavities with throughflow because the data on global heat transfer are too sparse to form a correlation with a precise gradient (γ value). However, other authors also compared their rotating cavity heat transfer results with those from horizontal surfaces, and commented on their similarity. For example Long & Tucker (1994) concluded that '... an established correlation for free convection from horizontal surfaces can be used to predict the shroud heat transfer in a rotating cavity with an axial throughflow of cooling air.'

Typical values of Ra_z and Re_z from some previous investigations (e.g. Long & Tucker, 1994 and Long *et al.*, 1997) indicated that the laboratory and computational experiments were usually conducted in the laminar free convection and laminar

forced convection regimes. So, the correlations thus obtained are combinations of $Nu_z \sim Ra_z^{1/4}$ and $Nu_z \sim Ra_z^{1/5}$.

It is noticed that throughout this thesis, especially from Chapters 1, 3, and the current chapter, how similar the values of exponents in the correlations can be for convection heat transfer of apparently very different conditions. The simple dimensional and scaling analyses employed give us a more unified understanding of the processes involved in giving rise to these correlations.

Chapter 8

Conclusions and recommendations for future work

8.1 Conclusions

In this research, free convective heat transfer in a sealed rotating annulus has been investigated. The annulus is assumed to have a hot outer cylinder, a cold inner cylinder, and two insulated discs. Some cases investigated are relevant to the flow between compressor discs or turbine discs of gas-turbine engines. Of particular interest is the heat transfer efficiency characterised by Nu vs. Ra correlations or the $Nu \sim Ra^{\gamma}$ scaling laws. The factors that influence these correlations are identified. The main methodology is computer simulation with unsteady two-dimensional and three-dimensional formulations. Dimensional analyses and simple phenomenological models are also used to derive some scaling laws for Rayleigh-Bénard convection and cavities with axial throughflow.

Here, the main conclusions from Chapters 3 to 7 are summarised. More details can be found in the 'Concluding remarks' sections in the respective chapters.

Chapter 3 Dimensional and scaling analyses of Rayleigh-Bénard convection: The dimensionless groups governing heat transfer in Rayleigh-Bénard convection in particular and any free convection in general are derived. It is shown that

Nusselt number and Rayleigh number can be related as $Nu \sim Ra^{\gamma}$. Simple derivations inspired by the phenomenological model of Castaing *et al.*(1989) give some scaling laws found commonly in measurements including $\gamma = \frac{2}{7}, \frac{1}{4}$, and $\frac{1}{5}$. Finally, the unifying theory for scaling laws of Grossmann & Lohse (2000 & 2001) is used to suggest an alternative explanation for the $\gamma \approx 0.21$ scaling laws measured by Bohn *et al.*(1995) in rotating annulus experiments. The validity of this explanation in terms of the boundary layer behaviour remains to be tested.

Chapter 4 Two-dimensional (radial-tangential) computations: Unsteady 2D computations are performed with a streamfunction–vorticity formulation. A non-rotating annulus with gravity directed radially outward is able to approximate flow and heat transfer in Rayleigh-Bénard convection very well. The computed result $\gamma \approx 1/3$ is consistent with the observation that Nu is not affected by the radial separation between the inner and outer cylinders. A rotating annulus computation produced no significant difference in Nu to that of a corresponding non-rotating annulus. Although the Coriolis force term has been scaled out in the derivation of the governing equations, the formulation is not independent of rotational Reynolds number Re_{ϕ}. However, the computed results show that the effect of the terms containing Re_{ϕ} is insignificant. Hence, the heat transfer in a rotating annulus is essentially the same as that in a non-rotating annulus which approximates Rayleigh-Bénard convection. The computed flows have regular counter-rotating convective rolls aligned around the annular space at low Rayleigh number. At higher Rayleigh number, these rolls break down, the bulk-flow becomes well-mixed with almost uniform temperature, and the thermal and kinetic boundary layers on the cylindrical surfaces also become very thin.

Chapter 5 Two-dimensional (radial-axial) computations: Unsteady radial-axial computations are performed using a streamfunction–vorticity formula-

tion. Investigations similar to those in Chapter 4 are performed. The aspect ratio (z/d) effect on the heat transfer is investigated. In non-rotating annuli, it is found that the value of Nu approaches that of Rayleigh-Bénard convection with increasing aspect ratio or for $Ra > 10^7$. This is in agreement with other published results. It is found that the axisymmetry imposed on the rotating annulus flow delays the onset of both convection and time-dependent flow. The influence of Reynolds number in reducing heat transfer is also stronger in the axisymmetric model. It is concluded that the axisymmetric formulation is not suitable to simulate the free convective flow in a rotating annulus.

Chapter 6 Three-dimensional computations: Unsteady three-dimensional computation in vorticity–velocity formulation is conducted. Heat transfer results for simulation of flow in a non-rotating annulus agree very well with Rayleigh-Bénard convection. In a rotating annulus, for flows at $\beta\Delta T \approx 0.3$ with increasing rotational Rayleigh number Ra_ϕ, the computed values of Nu agree with Rayleigh-Bénard convection correlations. For flows at $Ra_\phi = 10^{3.9}$ and increasing Re_ϕ, it was found that the values of Nu decrease with increasing Re_ϕ until no convective flow occurs. The radial separation between the cylinders and aspect ratio are also found to have minimal effect on the global heat transfer. Finally, flow in a rotating annulus with a single insulating radial barrier is simulated. For flows at $Ra_\phi = 10^{3.9}$, it was found that the resulting Nu are maintained at round 2 with increasing Re_ϕ. This suggests that the barrier is able to provide the pressure gradient needed by the cyclonic-anticyclonic convective rolls. The highest Rayleigh number computed is 10^6, which is much lower than the range investigated experimentally by Bohn *et al.* relevant to gas-turbines. Limitations in the computational methods and computing resources are the main difficulties, due to the very thin boundary layers that occur at these conditions, and the convective and rotating turbulence.

Chapter 7 Heat transfer in cavities with axial throughflow: Using dimensional considerations and a modified phenomenological model similar to that used in Chapter 3, heat transfer scaling laws for a cavity with axial throughflow are derived. Depending on the comparative strengths of axial Rayleigh number and axial Reynolds number, free, mixed, or forced convection can occur. A regime diagram delineating different types of convection with their respective scaling laws is obtained. It is suggested that the buoyancy parameter $Bo = Ra_z/Re_z^2$ (which indicates whether the flow is free, or mixed, or forced convective) alone is not sufficient in identifying suitable regime. The values of both Ra_z and Re_z are needed because, depending on their values, the flow can be either laminar or turbulent. The correlations derived here agree well with those for flat plates. Other investigators of rotating cavities with axial throughflow have previously remarked on the similarity between their results from laboratory experiments and those for flat plate.

8.2 Recommendations for future work

Three main ideas for future work are suggested here.

1. The main unresolved problem is computational work which reproduces the measured global heat transfer correlations of Bohn *et al.*(1995). There appears to be a lack of computational studies of the global heat transfer and boundary layer structures. More accurate and efficient computer codes are required for this application. A pseudospectral Direct Numerical Simulation code used by Randriamampianina*et al.* (see, for example, Randriamampianina *et al.*(1998) and Maubert & Randriamampianina (2001)) for simulations of rotating flows has been successful in the simulations of many rotating flow cases. In light of the 'new' explanation suggested in Section 3.3.7, the simulated behaviours of the boundary layers can be used to test if the corresponding heat transfer scaling laws are as expected. Of course, the simu-

lation can also be used to verify the theoretical suggestion mentioned above. Other promising methods are being developed by Smirnov (2002). Various turbulence models have been used for simulations of rotating Rayleigh-Bénard convection, low Prandtl number thermal convection, and rotating cavities with axial throughflow (Smirnov *et al.*, 2002). These methods will be able to provide solutions relatively more than direct simulation. Since Bohn *et al.* did not measure the velocity structures nor make any flow visualisations, the computations will be able to provide information in these regards.

2. Experimental investigation of the spatial structures of the thermal and viscous boundary layers for both rotating Rayleigh-Bénard convection and free convection in a rotating annulus should also include measurement of global (and local) heat transfer. Similar investigations have been carried out for stationary Rayleigh-Bénard convection (see Lui & Xia, 1998 and Qiu & Xia, 1998). The investigations suggested should identify the change in the behaviour of boundary layers which give rise to corresponding changes in the heat transfer scaling laws. The results obtained can be compared to the unifying theory of Grossmann & Lohse for stationary Rayleigh-Bénard convection. Robust instrumentation and/or non-intrusive optical methods will be required for the rotating application, posing a challenge for current and emerging experimental techniques.

3. The axial throughflow correlations derived in Chapter 7 should be tested against flow and heat transfer data from both experiments and computations. Some experimental data has already been taken but not published (Owen, 2001 & 2002). The codes mentioned in **1.** above can also be used to produce computational results. There have been a number of previous studies for rotating cavities with axial throughflow, however, because of the difficulties in rotating buoyancy-affected flows, few rigorous studies of the flow regimes and heat transfer correlations have so far

been conducted.

References

Arakawa, A., 1966, Computational design for long–term numerical integration of the equations of fluid motion: two-dimensional incompressible flow. Part 1, *J. Comp. Phys.*, **1**, pp.119–143.

Arnold, J.N., Edwards, D.K. & Catton, I., 1977, Effect of tilt and horizontal aspect ratio on natural convection in rectangular honeycombs, *J. Heat Transfer*, **99**, pp.120–122.

Ashkenazi, S. & Steinberg, V., 1999, High Rayleigh number turbulent convection in a gas near the gas-liquid critical point, *Phys. Rev. Lett.*, **83(18)**, pp.3641–3644.

Barenblatt, G.I., 1996, *Scaling, self-similarity, and intermediate asymptotics*, Cambridge University Press.

Belmonte, A., Tilgner, A. & Libchaber, A, 1993, Boundary layer length scales in thermal turbulence, *Phys. Rev. Lett.*, **70(26)**, pp.4067–4070.

Bohn, D., Dibelius, G.H., Deuker, E. & Emunds, R., 1994, Flow pattern and heat transfer transfer in a closed rotating annulus, *ASME Journal of Turbomachinery*, **116**, pp.542–547.

Bohn, D., Deuker, E., Emunds, R. & Gorzelitz, V., 1995, Experimental and theoretical investigations of heat transfer in close gas-filled rotating annuli, *ASME Journal of Turbomachinery*, **117**, pp.175–183.

Bohn, D., Emunds R., Gorzelitz, V. & Krüger, U., 1996, Experimental and theoretical investigations of heat transfer in close gas-filled rotating annuli II, *ASME Journal of Turbomachinery*, **118**, pp.11–19.

Bohn, D. & Gier, J., 1998, The effect of turbulence on the heat transfer in closed gas-filled rotating annuli, *ASME Journal of Turbomachinery*, **120**, pp.825–830.

Briggs, W.L., Hensen, V.E. & McCormick, S.F. , 2000, *A multigrid tutorial, 2nd Ed.*, SIAM.

Castaing, B., Gunaratne, G., Heslot, F., Kadanoff, L., Libchaber, A., Thomae, S., Wu, X–Z., Zaleski, S. & Zanetti, G., 1989, Scaling of hard thermal turbulence in Rayleigh–Bénard convection, *J. Fluid Mech.*, **204**, pp.1–30.

Chandrasekhar, S., 1961, *Hydrodynamic and hydromagnetic stability*, Clarendon Press.

Chavanne, F.H., Chilla, F., Castaing, B., Hebral, B., Chabaud, B. & Chaussy, J., 1997, Observation of the ultimate regime in Rayleigh-Bénard convection, *Phys. Rev. Lett.*, **79**, pp.3648–3651.

Churchill, S.W. & Usagi, R., 1972, A general expression for the correlation of the rates of transfer and other phenomena, *AIChEJ.*, **18**, pp.1121–1128.

Cioni, S., Ciliberto, S. & Sommeria, J., 1997, Strongly turbulent Rayleigh-Bénard convection in mercury: comparison with results at moderate Prandtl number, *J. Fluid Mech.*, **335**, pp.111–140.

Du, Y.–B.& Tong, P., 2000, Turbulent thermal convection in a cell with ordered

rough boundaries, *J. Fluid Mech.*, **407**, pp.57–84.

ElSherbiny, S.M., Raithby, G.D. & Hollands, K.G.T., 1982, Heat transfer by natural convection across vertical and inclined air layers, *J. Heat Transfer*, **104**, pp.96–102.

Farthing, P.R., Long C.A., Owen, J.M. & Pincombe, J.R., 1992a, Rotating cavity with axial through flow of cooling air: flow structure, *J. Turbomachinery*, **114**, pp.237–246.

Farthing, P.R., Long C.A., Owen, J.M. & Pincombe, J.R., 1992b, Rotating cavity with axial through flow of cooling air: heat transfer, *J. Turbomachinery*, **114**, pp.229–236.

Glazier, J.A., Segawa, T., Naert, A. & Sano, M., 1999, Evidence against 'ultrahard' thermal turbulence at very high Rayleigh numbers, *Nature*, **398**, pp.307–310.

Gill, A.E., 1966, The boundary layer regime for free convection in a rectangular cavity, *J. Fluid Mech.*, **26(3)**, pp.515–536.

Gille, J., 1967, Interferometric measurement of temperature gradient reversal in a layer of convecting air, *J. Fluid Mech.*, **30**, pp.371–384.

Goldstein, R.J., Chiang, H.D. & See, D.L., 1990, High-Rayleigh-number convection in a horizontal enclosure, *J. Fluid Mech.*, **213**, pp.111–126.

Grossmann, S., & Lohse, D., 2000, Scaling in thermal convection: a unifying theory, *J. Fluid Mech.*, **407**, pp.27–56.

Grossmann, S., & Lohse, D., 2001, Thermal convection for large Prandtl numbers, *Phys. Rev. Lett.*, **86(15)**, pp.3316–3319.

Heslot, F., Castaing, B. & Libchaber, A., 1987, Transition to turbulence in helium gas, *Phys. Rev. A*, **36**, pp.5870–5873.

Hollands, K.G.T., Raithby, G.D. & Konicek, L., 1975, Corrrelation equations for free convection heat transfer in horizontal layers of air and water, *Int. J. Heat Mass Transfer*, **18**, pp.879–884.

Hollands, K.G.T., 1984, Multi-Prandtl number correlation eqution for natural covection in layers and enclosures, *Int. J. Heat Mass Transfer*, **27(3)**, pp.466–468.

Howard, L.N., 1966, Convection at high Rayleigh number, *Applied Mechanics, Proc. of the 11th Congr. of Appl. Mech. Munich(Germany)(ed. H. Görtler)* pp. 1109–1115, Springer

Kadanoff, L.P., 2001, Turbulent heat flow: structures and scaling, *Physics Today*, **August**, pp.34–39.

King, M.P. & Wilson, M., 2002, Free convective heat transfer within rotating annuli, *Proceedings of the 12th International Heat Transfer Conference, pp. 465-470* Éditions scientifiques et médicales Elsevier SAS.

Koschmieder, E.L., 1993, *Bénard cells and Taylor vortices*, Cambridge University Press.

Kraichnan, R.H., 1962, Turbulent thermal convection at artbitrary Prandtl number, *Phys. Fluids*, **5**, pp.1374–1389.

Kreith, F. & Bohn, M.S., 1986, *Principles of heat transfer, 4th Ed.*, Harper & Row.

Krishnamurti, R., 1970a, On the transition to turbulent convection. Part 1. The transition from two- to three-dimensional flow, *J. Fluid Mech.*, **42**, pp.295–

307.

Krishnamurti, R., 1970b, On the transition to turbulent convection. Part 2. The transition to time-dependent flow, *J. Fluid Mech.*, **42**, pp.309–320.

Krishnamurti, R., 1973, Some further studies on the transition to turbulent convection, *J. Fluid Mech.*, **60**, pp.285–303.

Kutateladze, S.S., Ivakin, V.P., Kirdyashkin, A.G. & Kekalov, A.N., 1978, Thermal free convection in a liquid in a vertical slot under turbulent flow conditions, *Heat Transfer Sov. Res.*, **10/5**, pp.118–125.

Kuyper et al, 1993, Numerical study of laminar and turbulent natural convection in an inclined square cavity, *Int J. Heat Mass Transfer*, **36/11**, pp.2899–2911.

Lewis, T.W., 1999, *Numerical simulation of buoyancy-induced flow in a sealed rotating cavity*, PhD thesis, University of Bath, U.K.

Lui, S.L. & Xia, K.Q., 1998, Spatial structure of the thermal boundary layer in turbulent convection, *Phys. Rev. E*, **57**, pp.5494–5503.

Long, C.A., 1994, Disk heat transfer in a rotating cavity with an axial throughflow of cooling air, *Int. J. Heat Fluid Flow*, **15**, pp.307–316.

Long, C.A. & Tucker, P.G., 1994, Shroud heat transfer measurements from a rotating cavity with an axial throughflow of air, *J. Turbomachinery*, **116**, pp.525–534.

Long, C.A., Morse, A.P. & Tucker, P.G., 1997, Measurement and computation of heat transfer in high pressure compressor drum geometries with axial throughflow, *J. Turbomachinery*, **119**, pp.51–60.

Malkus, M.V.R., 1954, The heat transport and spectrum of thermal turbulence, *Proc. R. Soc. Lond. A*, **225**, pp.196–212.

Maubert, P. & Randriamampianina, A., 2001, Transition vers la turbulence géostrophique pour un écoulement d'air en cavité tournante différentiellement chauffée, *Mécanique des Fluides, C.R. Acad. Sci. Paris*, **t. 329, série II b**, pp.1–?.

Niemela, J.J., Skrbek, L., Sreenivasan, K.R. & Donnelly, R.J., 2000, Turbulent convection at very high Rayleigh numbers, *Nature*, **404**, pp.837–840.

Niemela, J.J., Skrbek, L., Sreenivasan, K.R. & Donnelly, R.J., 2001, The wind in confined thermal convection, *J. Fluid Mech.*, **449**, pp.169–178.

Owen, J.M. & Rogers, R.H., 1995, *Flow and heat transfer in rotating-disc systems. Volume 2: Rotating cavities*, Research Studies Press Ltd., Taunton, England.

Owen, J.M., 1999, *Buoyancy-induced flow in rotating cavities*, Internal Report No. 01/99, Department of Mechanical Engineering, University of Bath, U.K.

Owen, J.M., 2001, *Flow and heat transfer in a single-cavity rotating-disc rig (Final report for ICAS-GT Sub-task 2.1*, Internal Report No. 04/01, Department of Mechanical Engineering, University of Bath, U.K.

Owen, J.M., 2002, Private communication

Owen, J.M. & Wilson, M., 2000, Some current research in rotating-disc systems, *Turbine 2000 Int. Symp. on heat transfer in gas turbine systems, Turkey, Aug 13-18 in Heat tranfer in gas turbine systems, Annals of the New York Academy of Sciences*, **934**, pp.206–221, ISBN 1-57331-329-7.

Priestley, C.H.B., 1954, Convection from a large horizontal surface, *Austral. J. Phys.*, **7**, pp.176-201.

Qiu, X.–L., Yao, S.H. & Tong, P., 2000, Large-scale coherent rotation and oscillation in turbulent thermal convection, *Phys. Rev. E*, **61(6)**, pp.6075–6078.

Qiu, X.–L. & Tong, P., 2001, Large-scale velocity structures in turbulent thermal convection, *Phys. Rev. E*, **64(3)**, pp.36304–1–36304–13.

Raithby, G.D. & Hollands, K.G.T., 1975, A general method of obtaining approximate solutions to laminar and turbulent free convection problems, *Adv. Heat Trans.*, **11**, pp.265–315.

Randriamampianina, A., Leonardi, E. & Bontoux, P., 1998, A numerical study of the effects of Coriolis and centrifugal forces on buoyancy driven flows in a vertical rotating annulus, *Adv. Comp. Heat Trans. Eds. de Vahl Davis, G. & Leonardi, E.*, pp. 322–329.

Rayer, Q.G., Johnson, D.W. & Hide, R., 1998, Thermal convection in a rotating fluid annulus blocked by a radial barrier, *Geophys. Astrophys. Fluid Dynamics*, **87**, pp.215–252.

Read, P.L., 1992, Chapter IV.3 Rotating annulus flows and baroclinic waves, *Rotating fluids in geophysical and industrial applications (Ed. Hopfinger, E.J.), International Centre for Mechanical Sciences*, Courses and Lectures No. 329, pp. 185–213, Springer–Verlag.

Rees, D.A.S., 2000, *Private communication.*

Roche, P.–E., Castaing, B., Chabaud, B. & Hébral, B., 2001, Observation of the 1/2 power law in Rayleigh- Bénard convection, *Phys. Rev. E*, **63**, pp.045303–1–045303–4.

Rohsenow, W.M., Hartnett, J.P. & Cho, Y.I.(Eds), 1998, *Handbook of heat transfer*, McGraw–Hill.

Shewen, E., Hollands, K.G.T. & Raithby, G.D., 1996, Heat transfer by natural convection across a vertical air cavity of large aspect ratio, *J. Heat Transfer*, **118**, pp.993–995.

Shen, Y.T., Tong, P. & Xia, K.Q., 1996, Turbulent convection over rough surfaces, *Phys. Rev. Lett.*, **76**, pp.908–911.

Siggia, E.D., 1994, High Rayleigh number convection, *Ann. Rev. Fluid Mech.*, **26**, pp.137–168.

Smirnov, E.M., 2002, Recent advances in numerical simulation of 3D unsteady convection controlled by buoyancy and rotation–Keynote Lecture, *Proceedings of the 12th International Heat Transfer Conference*, Éditions scientifiques et médicales Elsevier SAS.

Sommeria, J., 1999, The elusive 'ultimate state' of thermal convection, *Nature*, **398**, pp.294–295.

Tritton, D.J., 1988, *Physical fluid dynamics*, Oxford University Press.

Trottenberg, U., Oosterlee, C. & Schüller, A., 2001, *Multigrid*, Academic Press.

de Vahl Davis, G., 1983, Natural convection of air in a square cavity: A benchmark numerical solution, *Int. J. Num. Meths. Fluids.*, **3**, pp.249–264.

Wu, X.Z. & Libchaber, A., 1992, Scaling relations in thermal turbulence: The aspect ratio dependence, *Phys. Rev. A*, **45**, pp.842–845.

Wu, X.Z. & Libchaber, A., 1991, Non-Boussinesq effects in free thermal convection, *Phys. Rev. A.*, **43**, pp.2833–2839.

Xin, Y.–B., Xia, K.–Q., & Tong, P., 1996, Measured velocity boundary layers in

turbulent convection, *Phys. Rev. Lett.*, **77(7)**, pp.1266–1269.

Appendix

Unsteady flow in a rotating cavity with a stationary casing

A.1 Abstract

Isothermal flow within an annular space formed by corotating discs, inner cylinder (also called the hub), and a stationary outer cylinder (or casing) is investigated. The time-dependent, axisymmetric governing equations are solved in the streamfunction-vorticity formulation. We devise a consistency check based on the moment balance to verify the solutions. It is found that a previously computed result, despite good apparent agreement with measured velocity data, does not achieve a satisfactory moment balance. While a new solution computed with a finer computational mesh is found to have a better balance. This new solution compares less well with measured velocity data but is closer to results obtained by another investigator using a high accuracy method.

A.2 Introduction

This study concerns isothermal fluid flow inside a rotating annular cavity with a stationary outer cylinder, see Figure A.1.a. Similar flows can be found in some cooling systems in gas-turbine engines and in the rotating disc-stacks of computer hard-drives; these configurations also involves heat transfer (where one or more surfaces are heated) and peripheral flow (where there are inlets and outlets of air, Figure A.1.b). Even when there is no peripheral flow, the shear at the casing causes counter-rotating secondary recirculations (see Figure A.1.a), and different

flow regions identified by Schuler *et al.*, 1990.

Previously, Gan *et al.*(1996) conducted Laser-Doppler Anemometry measurements for u (radial velocity) and v (tangential velocity) for flows in a rotating cavity with a stationary casing and a peripheral inlet and outlet of air. Heat transfer data was measured subsequently by Mirzaee *et al.*(1998). It was found that the radial distribution of tangential velocity, v, away from the disc boundary layers followed a Rankine vortex relationship:

$$\frac{v}{\Omega r} = Ax^{-2} + B, \tag{A.1}$$

where Ω is the angular velocity of the cavity, r the radial coordinate, and $x = r/b$ the radial coordinate non-dimensionalised with outer radius b, and A and B are constants. The first term on the R.H.S represents the free (irrotational) vortex and the second term the forced (rotational) vortex.

Wilson *et al.*(1997), Lewis *et al.*(1998) and Lewis (1999) studied the unsteady fluid and heat flows in a sealed rotating cavity with a stationary casing. These time-dependent axisymmetric computations were motivated by the inability of the previous axisymmetric steady computations (Mirzaee *et al.*, 1998) to capture the measured behaviour (see Figure A.2). The flow obtained by Wilson *et al.*(1997) at a rotational Reynolds number $Re_b = \Omega^2 b/\nu = 10^4$ was periodic and that at $Re_b = 1.46 \times 10^5$ was aperiodic. In the latter case, the number, locations and strengths of the secondary flow recirculations changed with time. Time-averaging of the results gave a Rankine vortex relationship that agreed very well with the measured data. The solution was obtained using a non-uniform 128×96 $(r \times z)$ mesh.

Randriamampianina *et al.*(2001) carried out high resolution spectral, axisymmetric and three-dimensional time-dependent numerical investigations for the rotating cavity with stationary casing flow. They studied the spatial and temporal

behaviour of the different flow regimes. Their 3D result shows that the flow start to become unsteady and three-dimensional at $Re_b \approx 3350$.

The current time-dependent, axisymmetric computation is performed for flows in a cavity having the geometry $a/b = 0.5$, $G \equiv s/b = 0.3$. In Section A.3, moment coefficient C_m is defined, and the condition for its balance is shown. This moment balance is used to verify the numerical solutions obtained subsequently. Section A.4 presents the governing equations and the numerical methods employed. Results and discussions are reported in Section A.5.

A.3 Calculation of moment coefficient and its balance

The moment coefficient is a normalised value of the torque (moment) exerted by a solid surface, rotating or stationary, on the fluid. The term *disc moment coefficient* refers to the equal and opposite normalised torque experienced by a disc surface. Referring to Figure A.1.a, the moment coefficient $C_{m,w}$ is defined as

$$C_{m,w} = -\int_0^{2\pi}\int_{x_1}^{x_2} r^2 \tau_{\theta,w} dx \; d\theta / \frac{1}{2}\rho_0 \Omega^2 b^5, \tag{A.2}$$

where,

$$\begin{cases} dx = dr, x_1 = a, x_2 = b \text{ and } w = 0 \text{ or } s & \text{for disc surfaces} \\ dx = dz, x_1 = 0, x_2 = s \text{ and } w = s \text{ or } b & \text{for hub and casing} \end{cases}$$

The tangential shear force on a surface w is denoted by $\tau_{\theta,w}$.

A moment balance is arrived at by integration, over the entire volume, of the angular momentum equation (Owen, 1999). From Owen and Rogers (1995), the angular momentum equation in cylindrical polar coordinates and a stationary frame of reference is

$$\partial_t(\rho v) + \frac{1}{r^2}\partial_r(\rho r^2 uv) + \frac{1}{r}\partial_\theta(\rho v^2) + \partial_z(\rho uw)$$

$$= \frac{-1}{r}\partial_\theta p + \frac{1}{r^2}\partial_r(r^2\sigma_{\theta r}) + \frac{1}{r}\partial_\theta\sigma_{\theta\theta} + \partial_z\sigma_{\theta z}, \tag{A.3}$$

where σ is the stress tensor and there are no body forces.

Applying an operator $I[u] = \int_0^{2\pi}\int_0^s\int_a^b ur^2 dr\ dz\ d\theta$ to Equation (A.3), it follows that since $u = 0$ at $r = a$, $r = b$ and $w = 0$ at $z = 0$, and $= s$,

$$I\left[\frac{1}{r^2}\partial_r(\rho r^2 uv)\right] = 0, \qquad I\left[\frac{1}{r}\partial_\theta(\rho v^2)\right] = 0 \qquad I\left[\partial_z(\rho uw)\right] = 0,$$

$$I\left[\frac{1}{r}\partial_\theta p\right] = 0, \qquad I\left[\frac{1}{r}\partial_\theta\sigma_{\theta\theta}\right] = 0, \qquad I[\partial_t(\rho v)] = \frac{d}{dt}I[\rho v],$$

$$I\left[\frac{1}{r^2}\partial_r(r^2\sigma_{\theta r})\right] = \int_0^{2\pi}\int_0^s [r^2\sigma_{\theta r}]_a^b dz\ d\theta, \quad I[\partial_z\sigma_{\theta z}] = \int_0^{2\pi}\int_a^b [r^2\sigma_{\theta z}]_0^s dr\ d\theta. \tag{A.4}$$

For laminar flow:

$$\sigma_{\theta r} = \mu(\frac{1}{r}\partial_\theta u + \partial_r v - \frac{v}{r}), \quad \sigma_{\theta z} = \mu(\partial_z v + \frac{1}{r}\partial_\theta w). \tag{A.5}$$

From the last three expressions in Equations (A.4), the momentum integral form of the angular momentum equation is

$$\int_0^{2\pi}\int_0^s [r^2\sigma_{\theta r}]_{r=b} dz\ d\theta - \int_0^{2\pi}\int_0^s [r^2\sigma_{\theta r}]_{r=a} dz\ d\theta + \int_0^{2\pi}\int_a^b [r^2\sigma_{\theta z}]_{z=s} dr\ d\theta$$

$$- \int_0^{2\pi}\int_a^b [r^2\sigma_{\theta z}]_{z=0} dr\ d\theta = \frac{d}{dt}I[\rho v]. \tag{A.6}$$

Dividing both sides of Equation (A.6) by $\frac{1}{2}\rho_0\Omega^2 b^5$, gives,

$$C_{m,b} + C_{m,a} + C_{m,s} + C_{m,0} = \frac{2}{\rho\Omega^2 b^5}\frac{d}{dt}I[\rho_0 v] \equiv I_m. \tag{A.7}$$

The four terms on the L.H.S denote the moment coefficients at the casing, hub, and two disc surfaces respectively. The term on the R.H.S. is the normalised time rate of change of angular momentum of the fluid, denoted by I_m. For a steady state problem, I_m is zero and thus the sum of all moment coefficients must also be zero. A balance of moment coefficients and I_m should occur for an unsteady flow. This

requirement may be applied as a measure of the validity of the numerical solutions to the governing equations.

Rewriting Equations (A.7) for an axisymmetric incompressible flow and expanding using Equations (A.5) and (A.6) gives

$$\frac{2}{\rho_0\Omega^2 b^5}[2\pi\mu(b^3\int_0^s[\partial_r(v/r)]_{r=b}dz - a^3\int_0^s[\partial_r(v/r)]_{r=a}dz + \int_a^b[r^2\partial_z v]_{r=s}dr$$

$$-\int_a^b[r^2\partial_z v]_{r=0}dr)] = \frac{4\pi}{\Omega^2 b^5}\frac{d}{dt}\int_0^s\int_a^b vr^2 dr\ dz. \tag{A.8}$$

For computations, integrands on the L.H.S. are approximated with a three-point second-order finite differencing at boundaries (with non-uniform grid spacing). Trapezoidal summation is used to compute integrals on the L.H.S., while that of the R.H.S. is approximated by summation over all of the grid cells in the $r-z$ plane.

Since the computation is time-dependent, a time-averaged form of Equation (A.7) is required,

$$\bar{C}_{m,b} + \bar{C}_{m,a} + \bar{C}_{m,s} + \bar{C}_{m,0} = \frac{2}{\rho_0\Omega^2 b^5} I[\rho v]_t^{t+\Delta t}, \tag{A.9}$$

where all the terms are time-averaged values over a period Δt.

A.4 Governing equations and numerical methods

In order to remove the difficulty of determining the boundary pressure values arising from a primitive variable formulation, a vorticity-streamfunction formulation is chosen. Vorticity, ω is given by,

$$\omega = \partial_z u - \partial_r w. \tag{A.10}$$

Streamfunction, ψ, is defined in the following relationships which satisfy the continuity equation exactly,

$$u = \frac{1}{r}\partial_z \psi, \qquad w = \frac{-1}{r}\partial_r \psi, \tag{A.11}$$

and re-scaled, for convenience for the later derivation of the governing equations, using $\psi = r\phi$,

$$u = \frac{1}{r}\partial_z \phi, \qquad w = -\partial_r \phi - \phi/r. \tag{A.12}$$

The following scalings are used in the non-dimensionalisation,

$$r = b\bar{r}, \qquad z = b\bar{z}, \qquad v = \frac{\kappa}{b}\bar{v}, \qquad t = \frac{b^2}{\kappa}\bar{t},$$

$$\omega = \frac{\kappa}{b^2}\bar{\omega}, \qquad \phi = \kappa\bar{\phi}, \qquad \bar{T} = \frac{T - T_c}{T_h - T_c},$$

where over-bars denote dimensionless variables. The rotational Rayleigh number, rotational Reynolds number, and Prandtl number are given by,

$$Ra_b = \frac{\Omega^2 b^4 \beta (T_h - T_c)}{\nu\kappa}, \qquad Re_b = \frac{\Omega b^2}{\nu}, \qquad Pr = \nu/\kappa. \tag{A.13}$$

The non-dimensional governing equations in a rotating frame of reference and cylindrical polar coordinates and with Boussinesq approximation then become (with over-bars omitted for clarity),

$$\omega = \nabla^2 \phi - \frac{1}{r}\phi, \tag{A.14}$$

$$\frac{1}{Pr}\left[\partial_t \omega + J(\omega, \phi) - \frac{1}{r}(\phi\partial_z\omega + \omega\partial_z\phi) - \frac{2v}{r}\partial_z v\right] - 2Re_b\partial_z v + \frac{2Ra_b}{Re_b Pr}(T\partial_z v + v\partial_z T)$$

$$+ rRa_b\partial_z T = \nabla^2\omega - \frac{\omega}{r^2}, \tag{A.15}$$

$$\frac{1}{Pr}\left[\partial_t v + J(v, \phi) + \frac{1}{r}(v\partial_z\phi + \phi\partial_z v)\right] + 2Re_b\partial_z\phi - \frac{2Ra_b}{Re_\phi Pr}T\partial_z\phi = \nabla^2 v - \frac{v}{r^2}, \tag{A.16}$$

$$\partial_t T + J(T, \phi) - \frac{\phi}{r}\partial_z T = \nabla^2 T, \tag{A.17}$$

where the Jacobian operator is,

$$J(A,B) = \partial_r A \partial_z B - \partial_r B \partial_z A.$$

The boundary conditions are,

at the shroud, $x = 1$

$$\phi = 0, \quad \omega = \partial^2_{rr}\phi, \quad \partial_z\phi = 0, \quad v = -Re_b \times Pr, \quad \partial_r\phi = 0,$$

at the hub, $x = a/b$,

$$\phi = 0, \quad \omega = \partial^2_{rr}\phi, \quad \partial_z\phi = 0, \quad v = 0, \quad \partial_r\phi = 0,$$

at the discs, $z = 0, = s/b$,

$$\phi = 0, \quad \omega = \partial^2_{zz}\phi, \quad \partial_z\phi = 0, \quad v = 0, \quad \partial_r\phi = 0,$$

All the simulations were started impulsively, i.e. at the initial time the discs and hub take up the required angular speed immediately, with the fluid stationary. Details of the numerical method used in the solutions of the governing equations given above appear in Chapters 3 and 6 of Lewis (1999). A non-uniform mesh and second-order finite-difference approximations with coefficients weighted by neigbouring grid sizes are used. Figure A.3 shows the 128×96 $(x - z)$ used by Lewis (1999) in the $Re_b = 1.46 \times 10^5$ case. The fine grids near the boundaries are expanded geometrically over a given distance, with equal spacings (separately in each direction) over the remainder of the computational domain.

The convective terms are treated using a hybrid-differencing scheme, where first-order upwinding is used for grid Reynolds numbers $(= v\Delta x/\nu)$ greater than two; otherwise second-order central differencing is used.

A Du-Fort Frankel method is employed for the time derivative and all other

terms. Values of the dependent variable at the current time-step are substituted with the average of the new (still to be computed) and old (previous timestep) values. The vorticity and the velocity for a timestep are solved before the streamfunction is computed from the Poisson type equation A.14. A multigrid method with V-cycling and line-relaxation is implemented to accelerate the iterative convergence. See Chapter 5 of this thesis for more details.

A.5 Results and discussion

Coding of the moment balance calculation was tested with a solid-body rotating flow and one case of steady rotor-stator flow (one disc rotating and all other surfaces stationary). It was found that the flows reached a satisfactory balance of moment coefficients and very low I_m in the steady state. A rotating cavity with stationary casing flow at $Re_b = 2000$ was also computed. The flow reached steady state with a stable inward shear flow. A satisfactory moment balance was also achieved.

At higher Reynolds number, the unstable inward shear flow at the mid-plane and powerful shear flow between the casing and the discs poses difficulties for computations. Two cases are considered in details here. Firstly, $Re_b = 10^4$, which is just after the onset of unsteadiness and, secondly, the aperiodic flow at $Re_b = 1.46 \times 10^5$, which is the lowest Reynolds number case measured by Gan *et al.*(1996).

As the flows are unsteady, the piecewise time-averaged transient behaviour of moment coefficients ($C_{m,i}$), their sum ($\sum C_{m,i}$), and I_m values are plotted in Figures A.4 and A.5. Non-dimensional timesteps of 2×10^{-6} and 2×10^{-8} respectively were used for the $Re_b = 10^4$ (using a non-uniform 96×80 mesh) and $Re_b = 1.46 \times 10^5$ (using a non-uniform 128×96 mesh) computations. These two computations repeat those of Lewis (1999) to check the results against the additional moment balance condition.

Figures A.4 and A.5 both show that the moment coefficient sum ($\sum C_{m,i}$) for the surfaces does not have a net value of zero over time. The imbalance for $Re_b = 1.46\times10^5$ is around 1.5×10^{-3} over time, with a peak error $e = (\sum C_{m,i} - I_m)/\sum |C_{m,i}|$ of 20%. The major contribution to the error is from the non-zero $\sum C_{m,i}$. The I_m value is always close to zero and oscillates about the abscissa.

Figures A.2 and A.6 show the time-averaged tangential velocity distributions for $Re_b = 1.46 \times 10^5$ and $= 10^4$ respectively. For $Re_\phi = 1.46 \times 10^5$, there is good agreement with measured data, although the moment balance as described above is unsatisfactory.

In both this work and that of Wilson *et al.*(1997), obtaining grid independence was found to be difficult, and this suggested that a more suitable mesh might give a solution with better balance of moments. After numerous tests, an improved solution was obtained with the non-uniform 192 × 128 mesh shown in Figure A.7. Note that the width of the fine grid regions close to the discs are smaller than that at the casing.

The moment balance result obtained using this mesh is shown in Figure A.8. The transient behaviour of $\sum C_{m,i}$ is improved. The corresponding time-averaged tangential velocity distribution, shown in Figure A.9, does not agree well with the measured data but compares satisfactorily with a result by Randriamampianina (1999) who used a highly accurate numerical method. Shown in Figure A.10 are the time-averaged axial distributions of radial velocity at $x = 0.75$ and $= 0.85$. These radial velocity profiles are almost identical to those obtained by Lewis (1999) with the 128 × 96 mesh, except that the standard deviations are smaller for the new results.

Table A.1 below shows the C_m values computed for the discs in the current work, in an axisymmetric steady computation using an in-house code BURF (Bath

Univeristy Rotating Flows) as used by Gan *et al.*(1996), and by Randriamampianina (1999). These are the average values from results for $C_{m,0}$ and $C_{m,s}$, themselves time-averaged for unsteady flows.

	average C_m at discs		
Re_b	current study	BURF	Randriamampianina (1999)
2000	3.186×10^{-2}	2.905×10^{-2}	2.730×10^{-2}
10^4	1.093×10^{-2}	-	0.948×10^{-2}
1.46×10^5	2.258×10^{-3}	1.982×10^{-3}	2.282×10^{-3}

Table A.1: Average disc moment coefficients computed by three studies. BURF is a steady axisymmetric computation.

The computation performed by Lewis (1999), at $Re_b = 1.46 \times 10^5$ using the 128×96 mesh, repeated in the current study gave a time-averaged value for C_m of 3.016×10^{-3}. This higher value is consistent with the lower normalised tangential velocity of the fluid, as shown in Figure A.2.

The highly unsteady and possibly three-dimensional nature of the inward shear flow requires suitable computational methods. The 'discontinuity' in the boundary conditions between the rotating discs and the stationary casing also requires suitable treatment. It is very likely that this 'discontinuity' causes the grid independence difficulties of the solutions.

A.6 Conclusions

Calculation of the moment balance has been carried out to provide a measure of the validity of numerical solutions for time-dependent, axisymmetric flow in a rotating cavity with a stationary casing. Earlier computations by Lewis (1999) were repeated with the additional moment balance calculation. It was found that the flow achieved satisfactory moment balance at the lower Reynolds number cases ($Re_b = 2000$ and $= 10^4$) computed.

A computation at $Re_b = 1.46 \times 10^5$ using a 128×96 mesh did not reach a

satisfactory moment balance. However, the computed radial distribution of tangential velocity agreed well with measured data. In the current study, a finer mesh (192×128) was used to obtain a different solution with an improved balance of moments. This solution gives a tangential velocity profile which mainly overpredicts the measured data, but agrees reasonably well with that obtained in the high-accuracy computation of Randriamampianina (1999).

References

Gan, X., Mirzaee, I., Owen, J.M., Rees, D.A.S. & Wilson, M., 1996, Flow in a rotating cavity with a peripheral inlet and outlet of cooling air, *ASME Int. Gas Turbines and Aeroengines Cong. Birmingham*, paper 96-GT-309.

Lewis, T.W., Rees, D.A.S. & Wilson, M., 1998, Unsteady axisymmetric flow in a rotating cavity with a stationary outer surface, *Proceedings of Mini-Workshop on Applied Mathematics, Shahjalal University of Science and Technology, Sylhet, Bangladesh*, pp. 23–30.

Lewis, T.W., 1999, *Numerical simulation of buoyancy-induced flow in a sealed rotating cavity*, Ph.D. Thesis, University of Bath, U.K.

Mirzaee, I., Gan, X., Wilson, M. & Owen, J.M., 1998, Heat transfer in a rotating cavity with a peripheral inflow and outflow of cooling air, *ASME J. Turbomachinery*, **120**, pp. 818–823.

Owen, J.M. & Rogers, R.H., 1995, *Flow and heat transfer in rotating-disc systems, Vol.2: Rotating cavities*, Research Studies Press Ltd., Taunton, England.

Owen, J.M.,1999, Private communication.

Randriamampianina, A., 1999, Private communication.

Randriamampianina, A., Schiestel, R. & Wilson, M., 2001, Spatio-temporal behaviour in an enclosed corotating disk pair, *J. Fluid Mech.*, **434**, pp. 39–64.

Schuler, C.A., Usry, W., Weber, B., Humphrey, J.A.C. & Greif, R., 1990, On the flow in the unobstructed space between shrouded corotating disks, *Phys. Fluids A*, **2(10)**, pp. 1760–1770.

Wilson, M., Arnold, P.D., Lewis, T.W., Mirzaee, I., Rees, D.A.S. & Owen, J.M., 1997, Stability of flow and heat transfer in a rotating cavity with a stationary outer casing, *Eurotherm 55–Heat transfer in Single Phase Flows 5, Santorini, Greece.*

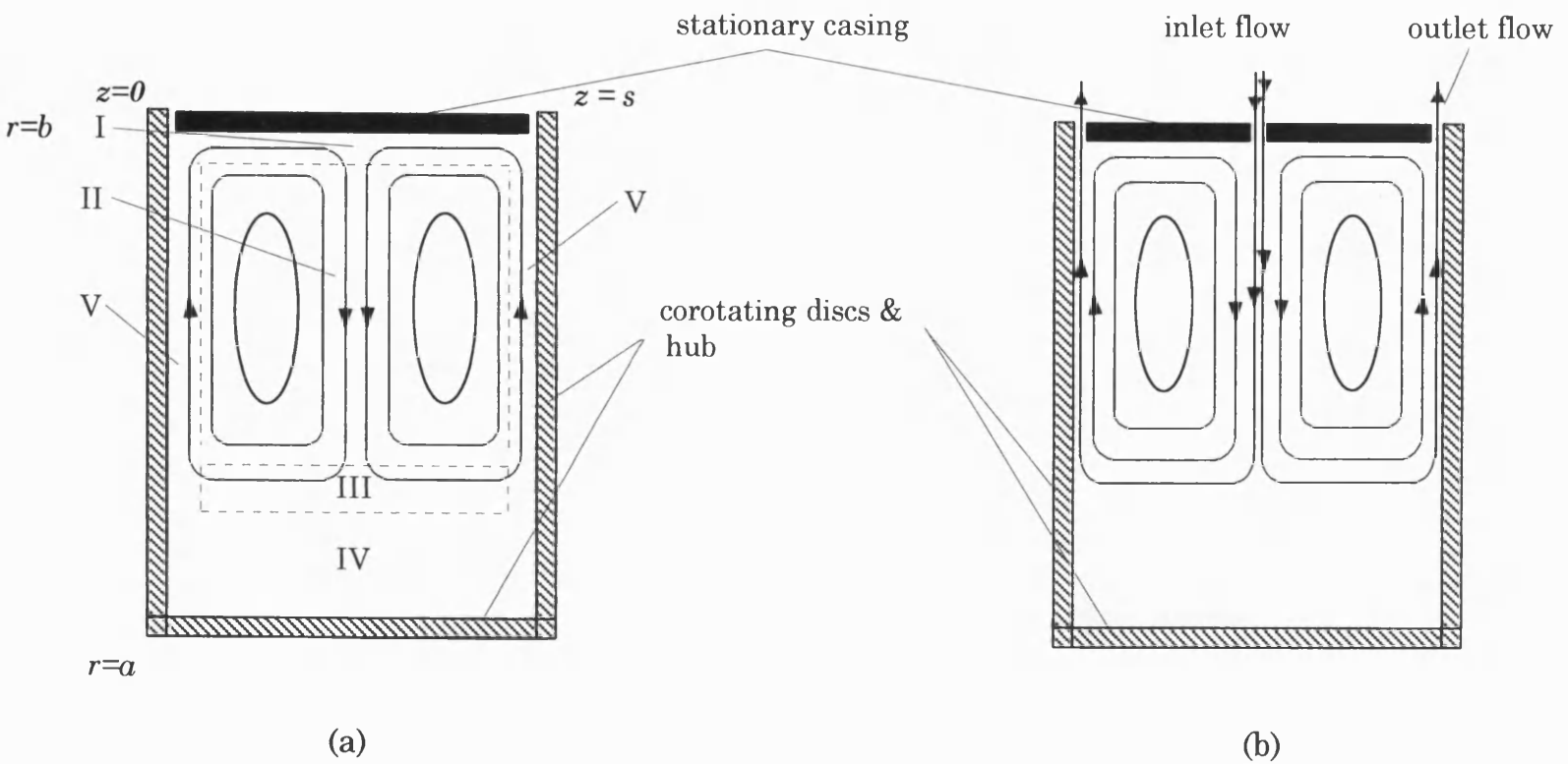

Figure A.1 Schematic diagram of rotating cavities with stationary casing.

(a) sealed rotating cavity with flow regions identified by Schuler *et al* (1990)

(b) peripheral flow

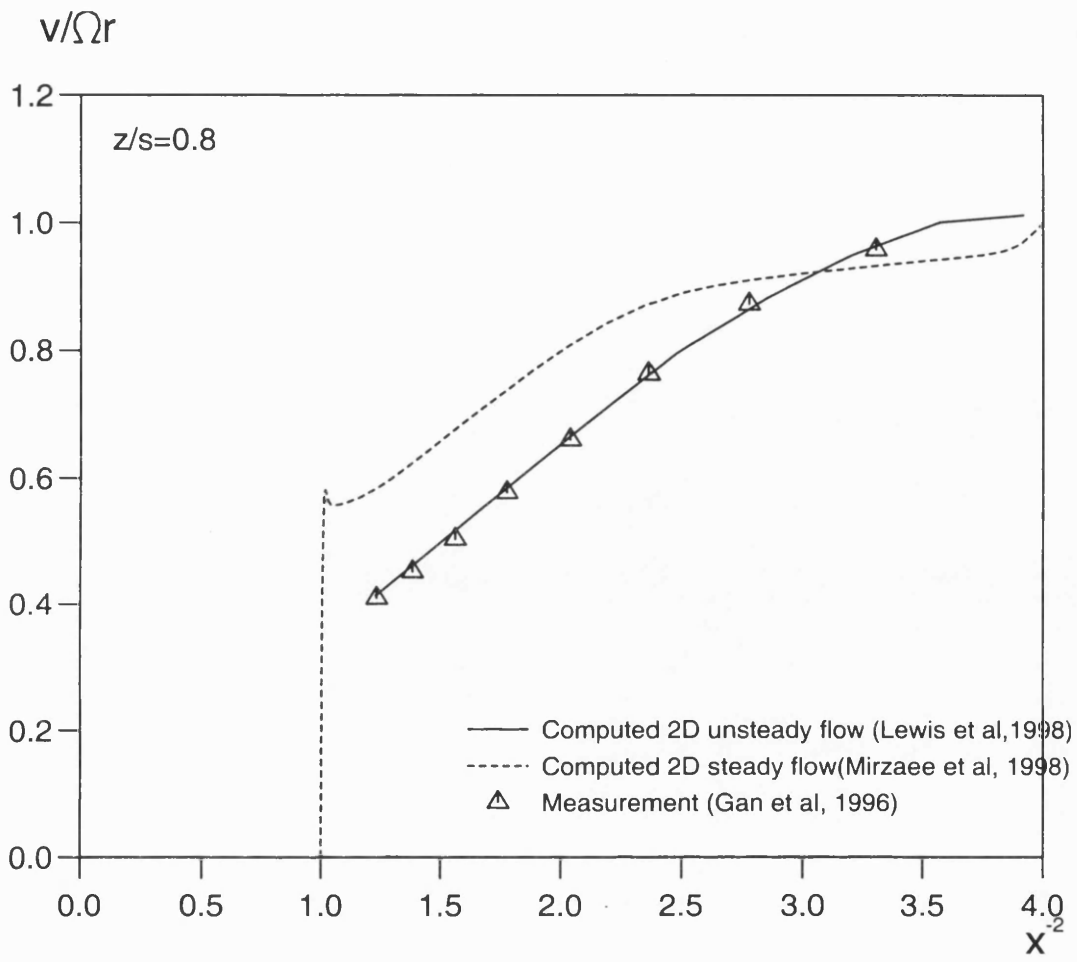

Figure A.2 Computed and measured Rankine vortex profiles for Re_b=*1.46x105*, *G=0.3*, and *a/b=0.5*. Comparisons among computed time-averaged (for unsteady computation), steady flow, and measured tangential velocity distributions.

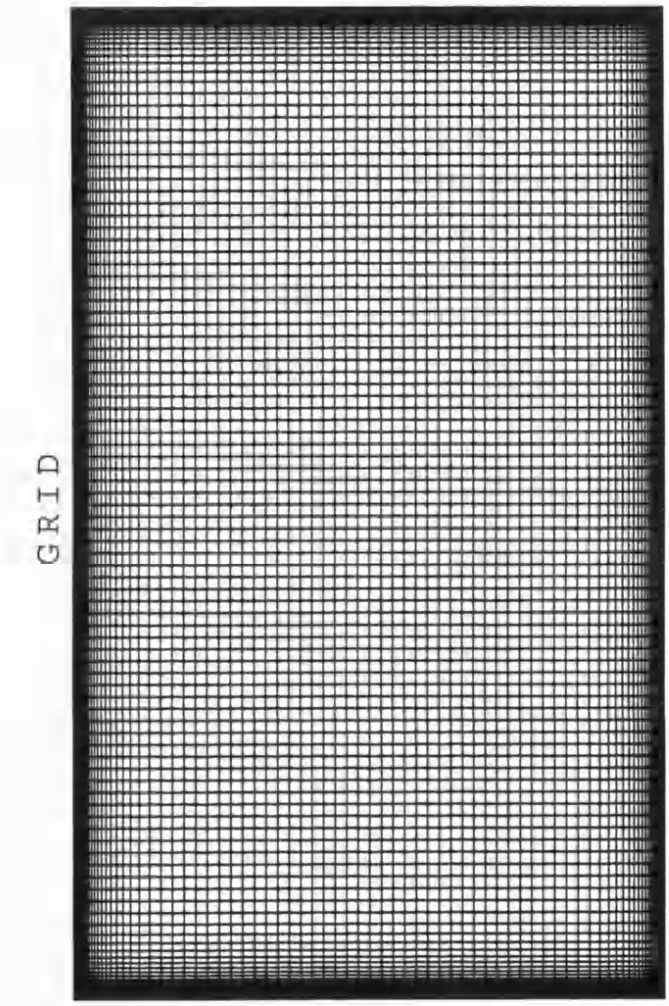

Figure A.3 The *128x96* non–uniform mesh used in the computation of a rotating cavity with a stationary casing for $Re_b=1.46x10^5$ by Lewis (1999).

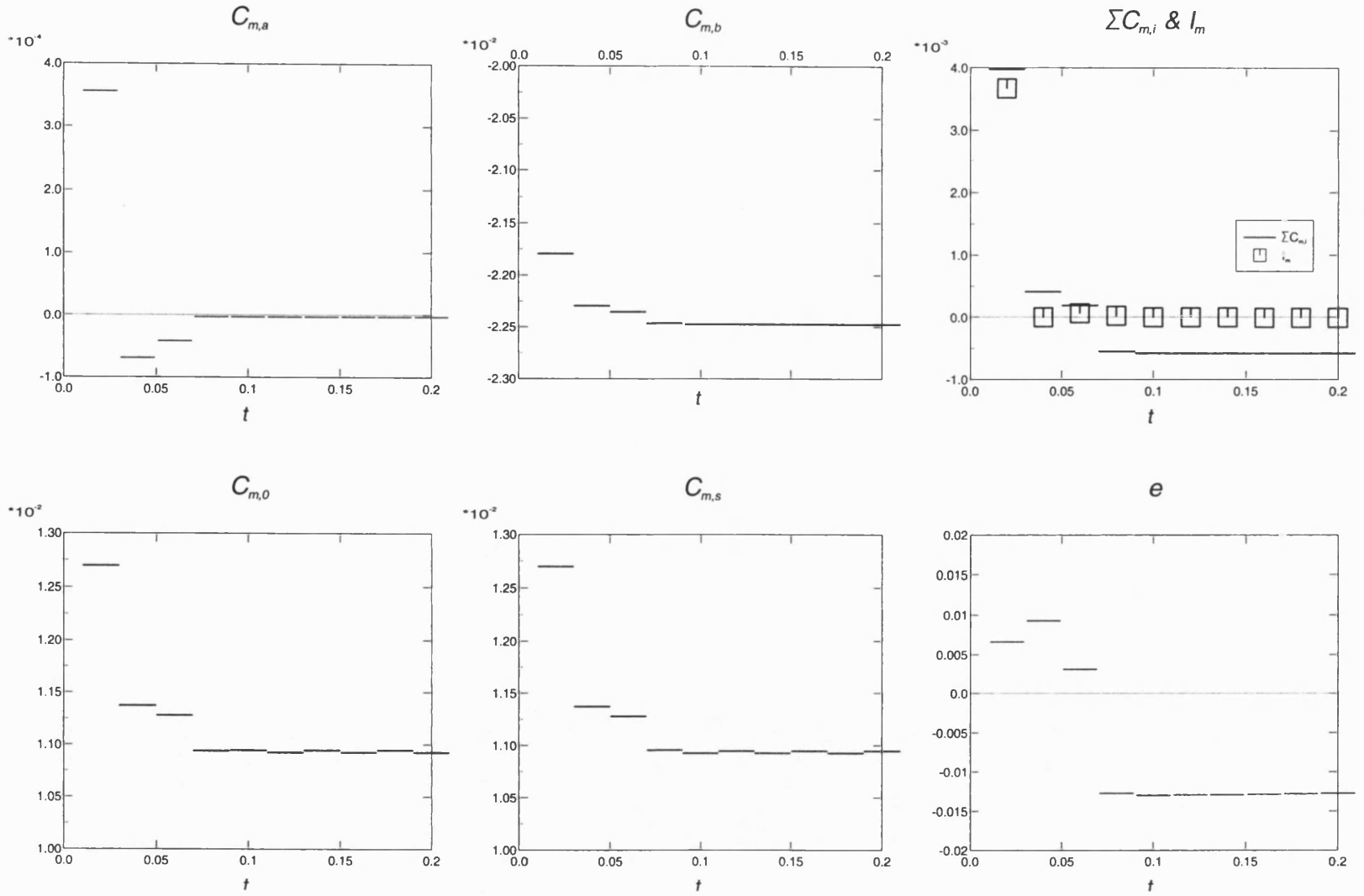

Figure A.4 Computed moment coefficients for a rotating cavity with a stationary casing at $Re_b=10^4$, $G=0.3$, $a/b=0.5$. Non–uniform mesh 96x80. $t=0.2$ corresponds to disc revolutions. Time averaged over \Delta t=0.02.

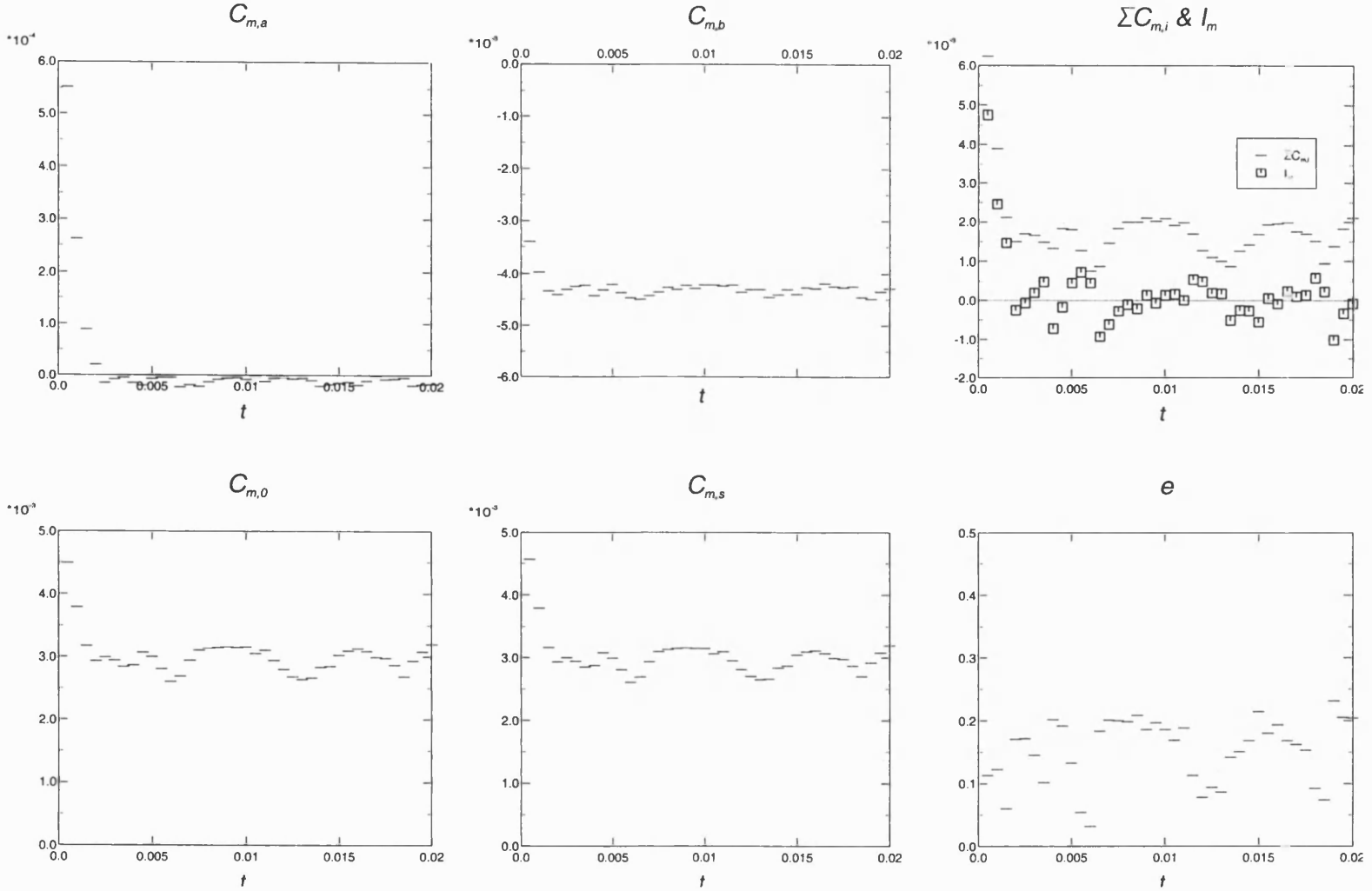

Figure A.5 Computed moment coefficients for a rotating cavity with stationary casing at $Re_b=1.46x10^5$, $G=0.3$, $a/b=0.5$. Non uniform mesh *128x96*. $t=0.02$ corresponds to *329* disc revolutions. Time averaged over $\Delta t = 5x10^{-4}$.

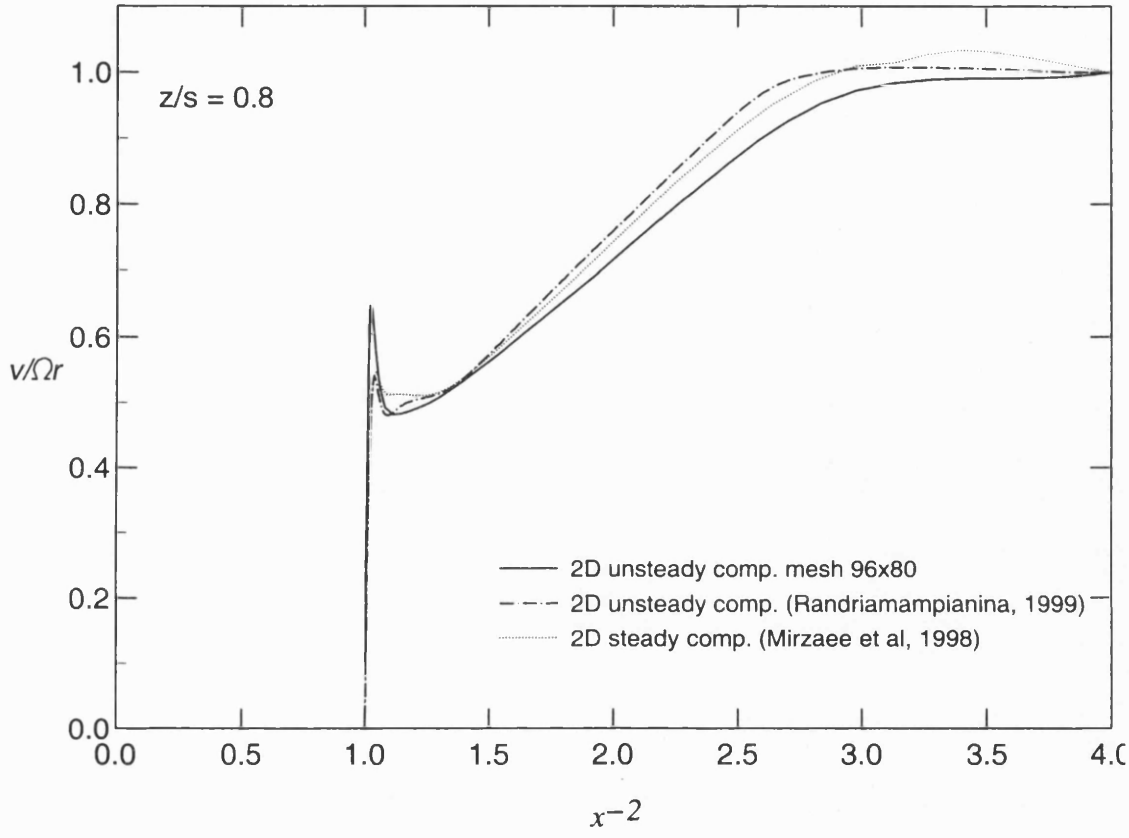

Figure A.6 Time–averaged Rankine vortex profiles for $Re_b=10^4$, $G=0.3$, and $a/b=0.5$.

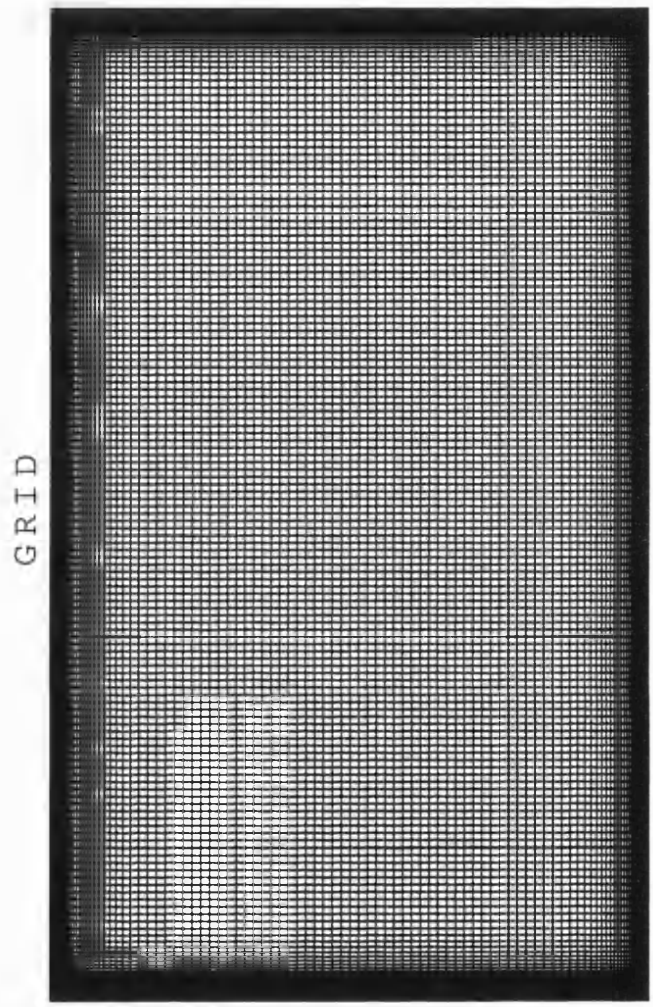

Figure A.7 The *192x128* ($r-z$) non–uniform mesh used in the computation of a rotating cavity with a stationary casing flow for $Re_b=1.46x10^5$ in the current work.

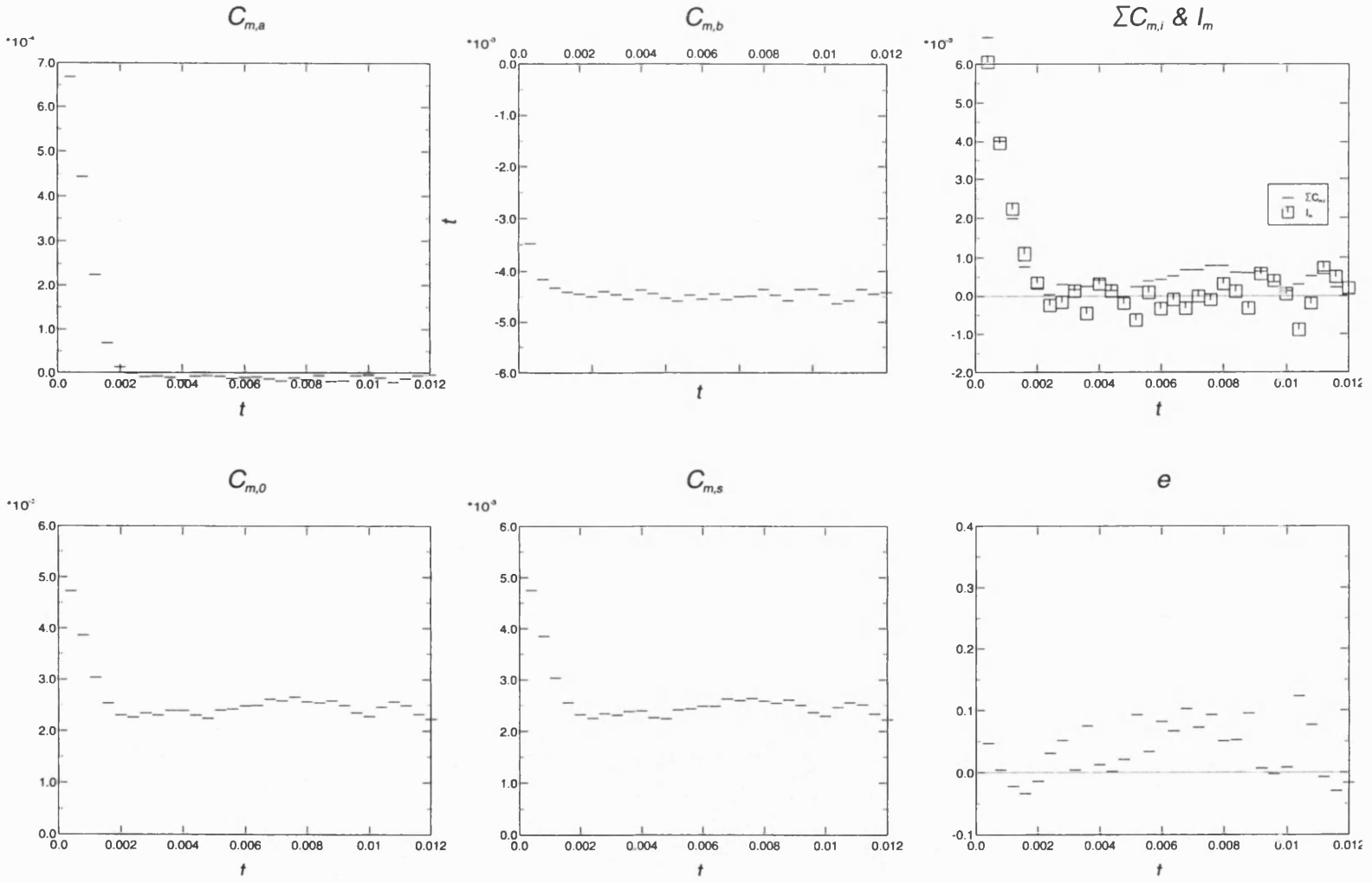

Figure A.8 Computed moment coefficients for a rotating cavity with stationary casing at $Re_b=1.46x10^5$, $G=0.3$, $a/b=0.5$. Non–uniform *192x128* mesh. $t=0.012$ corresponds to *197* disc revolutions. Time–averaged over \Delta t = $4x10^{-5}$.

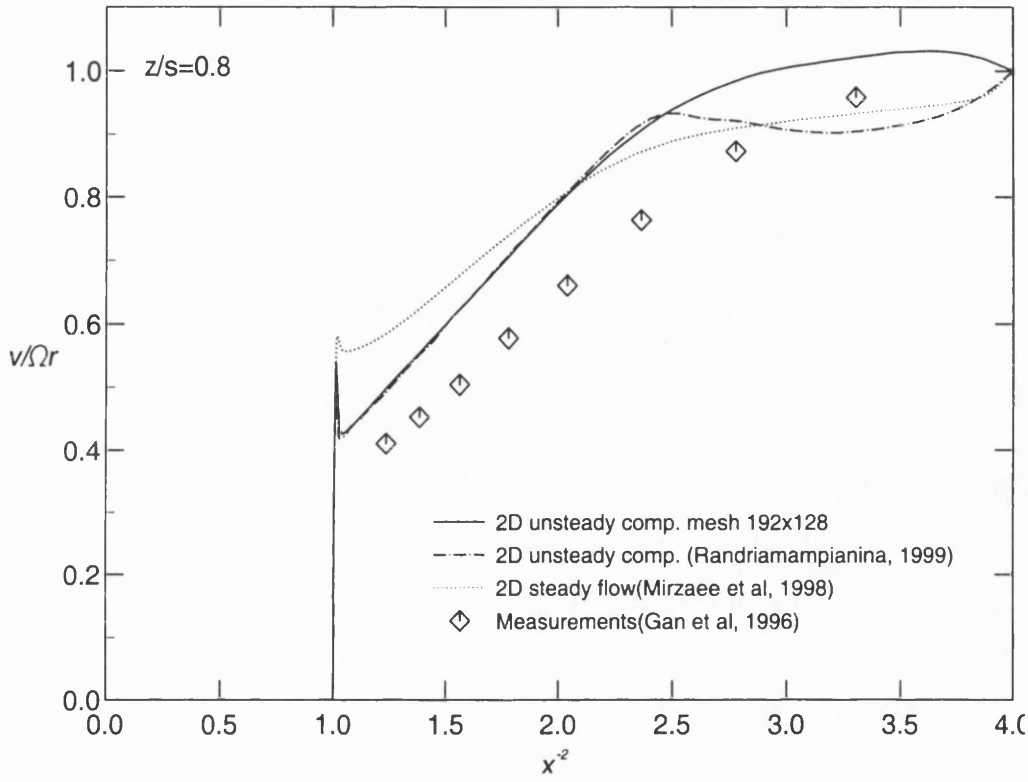

Figure A.9 Rankine vortex profiles for $Re_b=1.46x10^5$, $G=0.3$, $a/b=0.5$. The unsteady result is a new solution obtained with a *192x128* (in $r-z$) mesh.

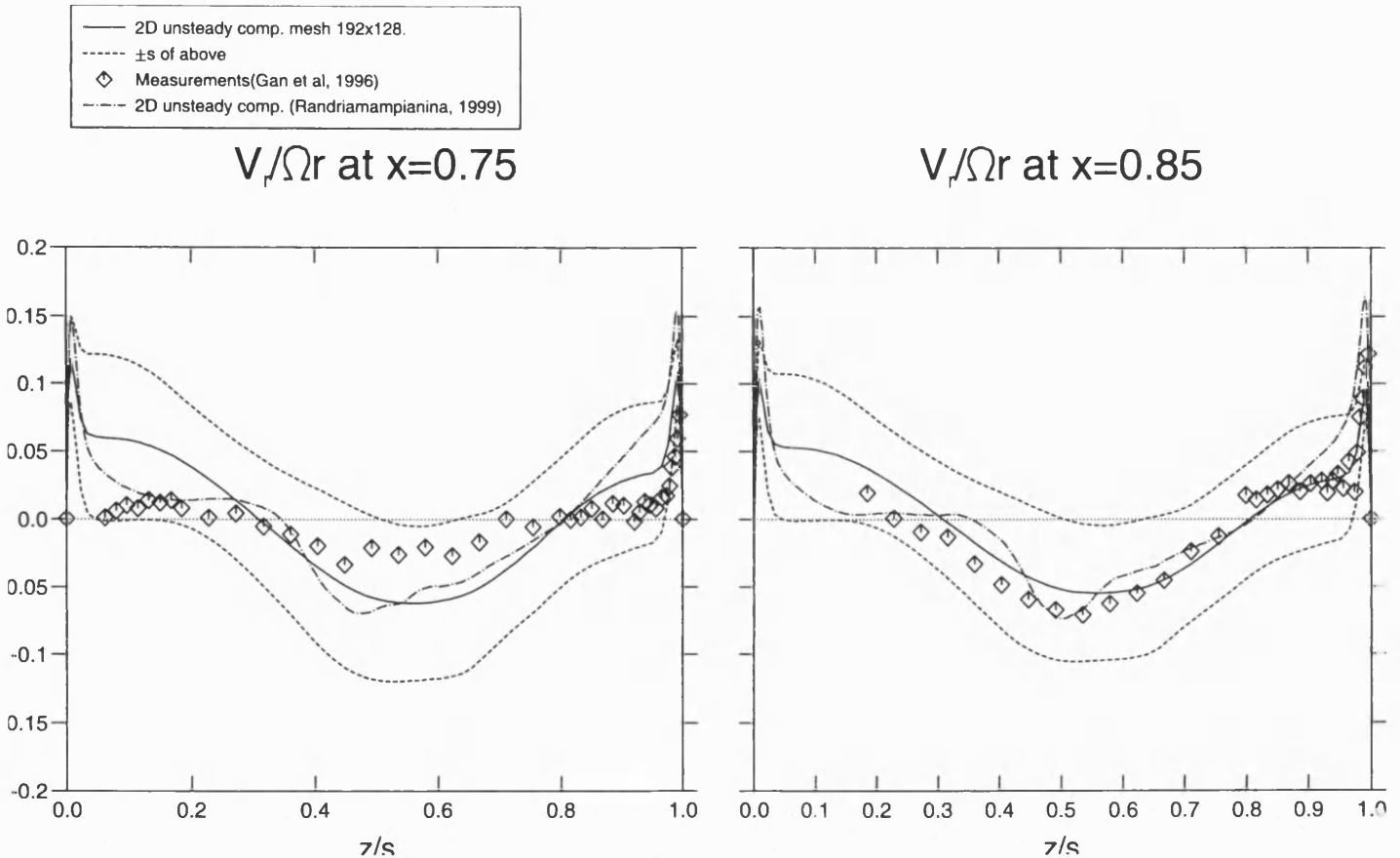

Figure A.10 Computed axial distributions radial velocity at $x=0.75$ and $=0.85$, for $Re_b=1.46x10^5$, $G=0.3$ and $a/b=0.5$.

FIGURES

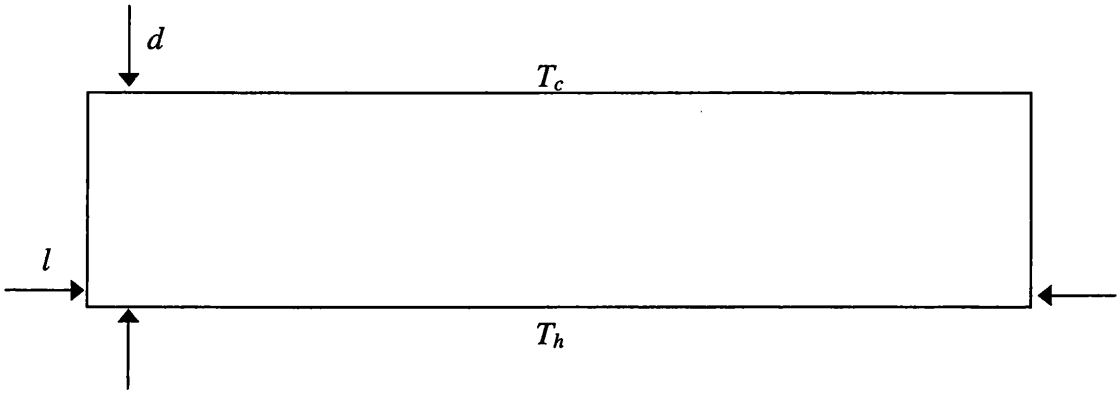

Figure 2.1 Horizontal enclosure with uniform heating from below.

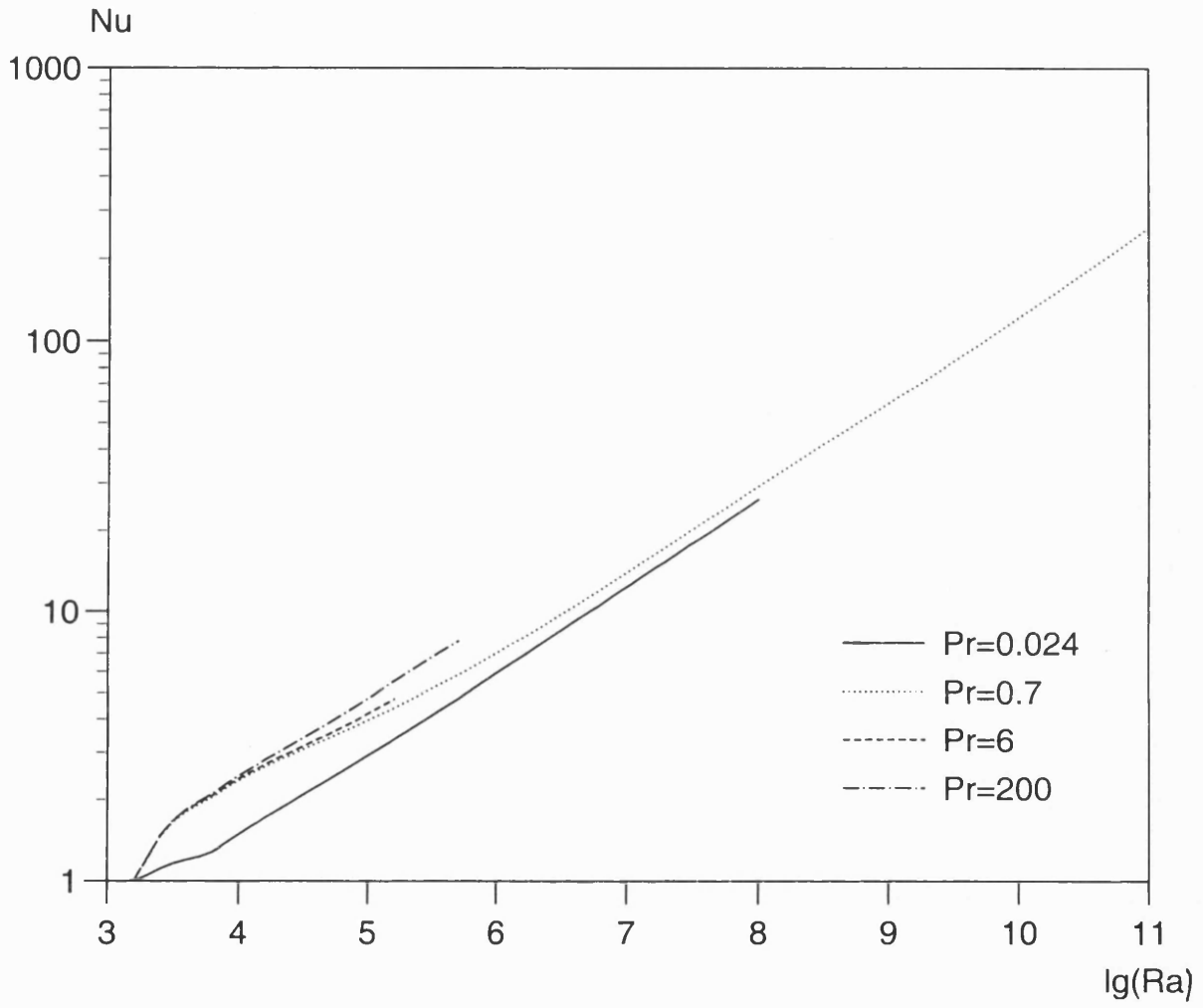

Figure 2.2 *Nu vs. Ra* for various Prandtl numbers on a log–log plot.
Rayleigh–Benard convection. Correletion by Hollands *et al*(1984).

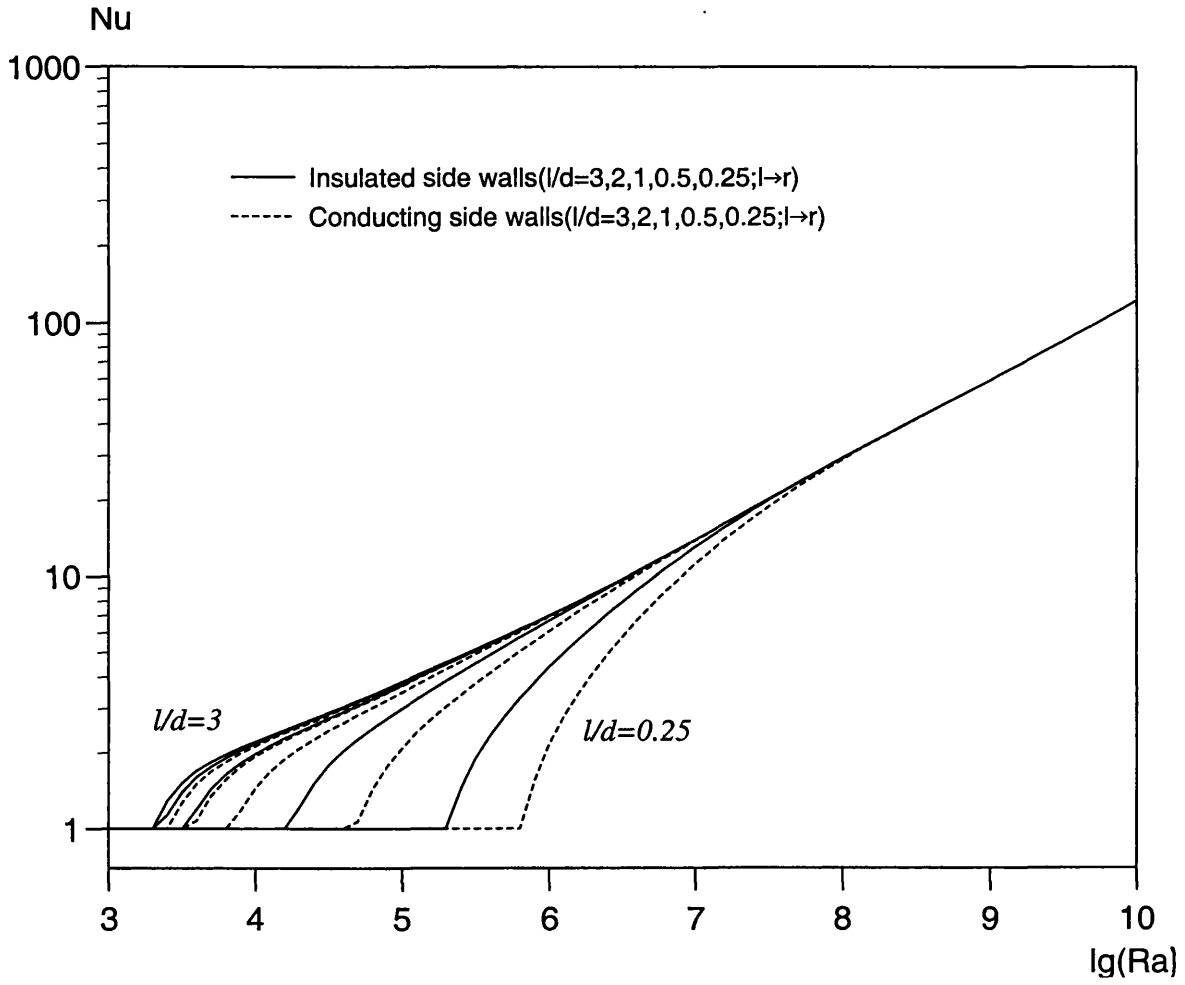

Figure 2.3 *Nu vs. Ra* for various aspect ratios on a log–log plot. *Pr=0.7*. From correlation for horizontal enclosure by Hollands *et al* (1984).

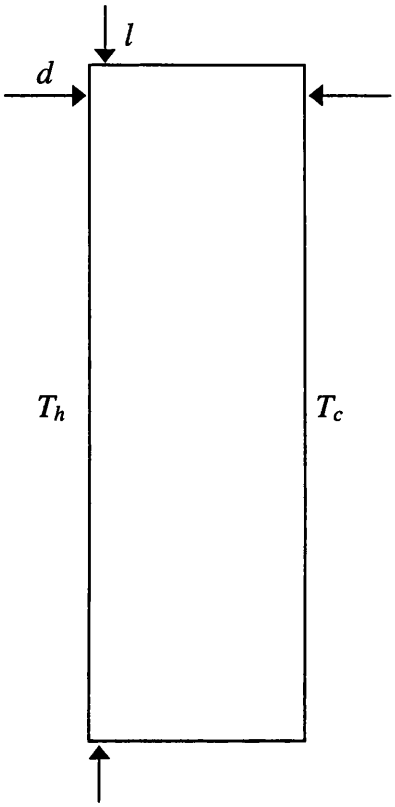

Figure 2.4 Vertical enclosure with a heated side-wall

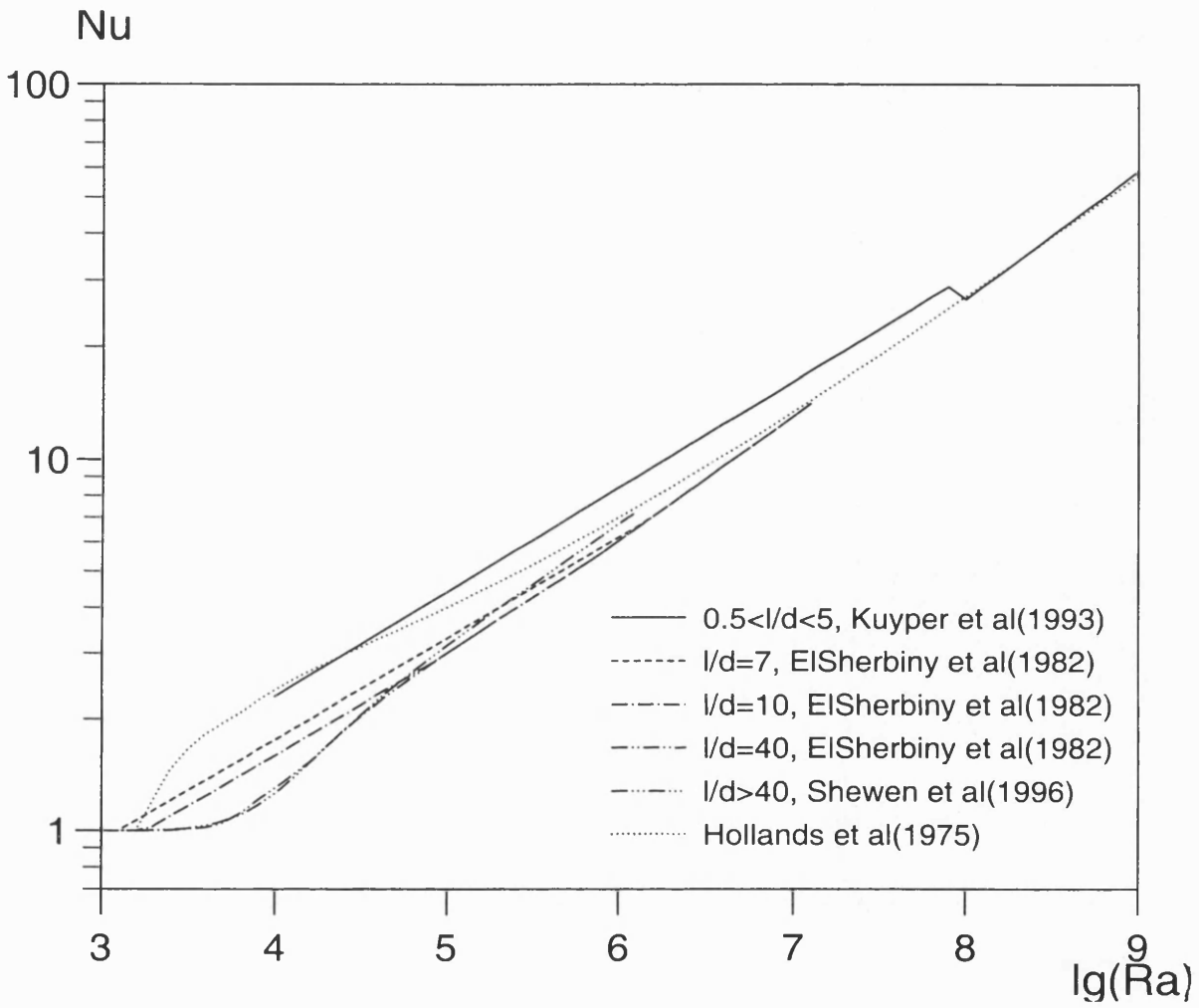

Figure 2.5 *Nu vs. Ra* for vertical enclosures of various aspect ratios. *Pr=0.7.*

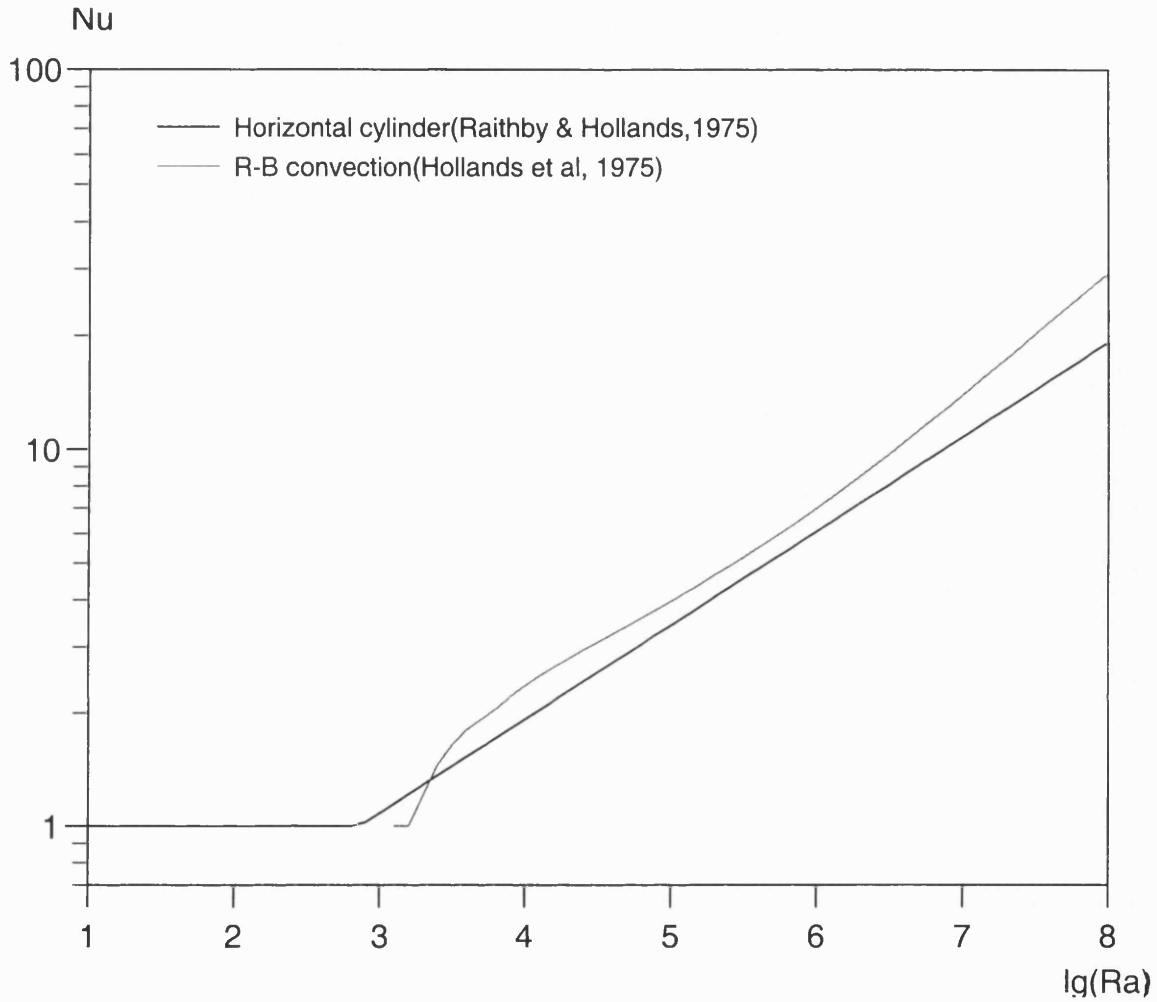

Figure 2.6 *Nu vs. Ra* for horizontal concentric cylinders. *b−a=0.5*; *a/b=0.5*.

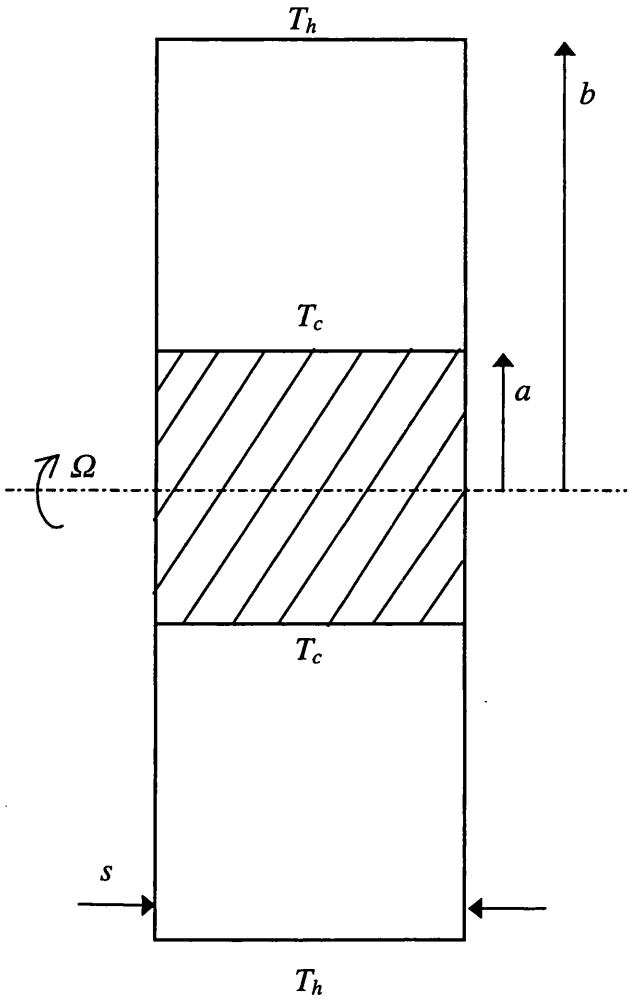

Figure 2.7 Longitudinal cross-section of a cylindrical annulus. The inner cylinder is uniformly cooled and the outer cylinder is uniformly heated. The side-discs are usually insulated but can also be partially conducting.

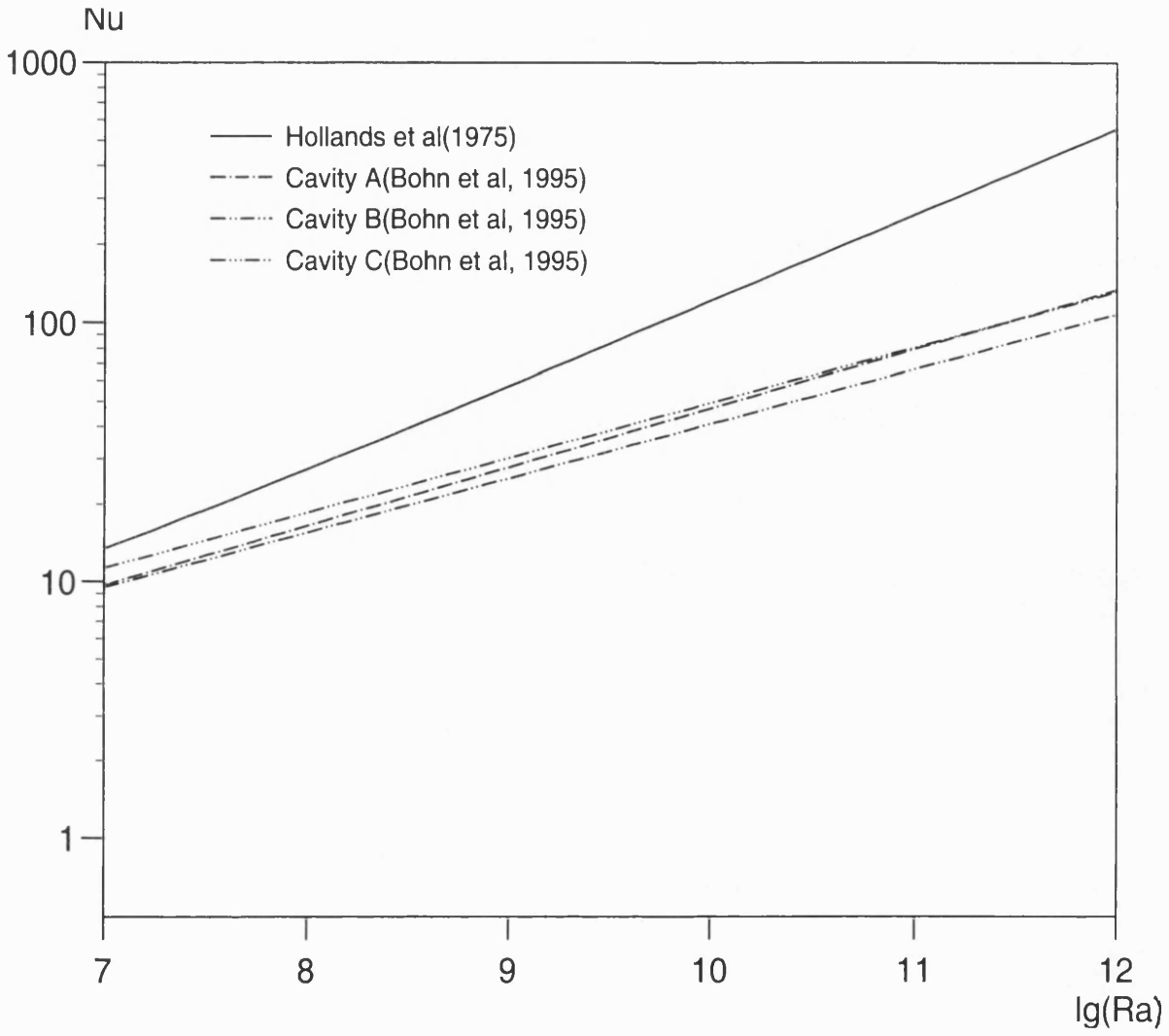

Figure 2.8 *Nu vs. Ra* for rotating annuli with radial heat flux, comparison with Rayleigh–Benard convection.

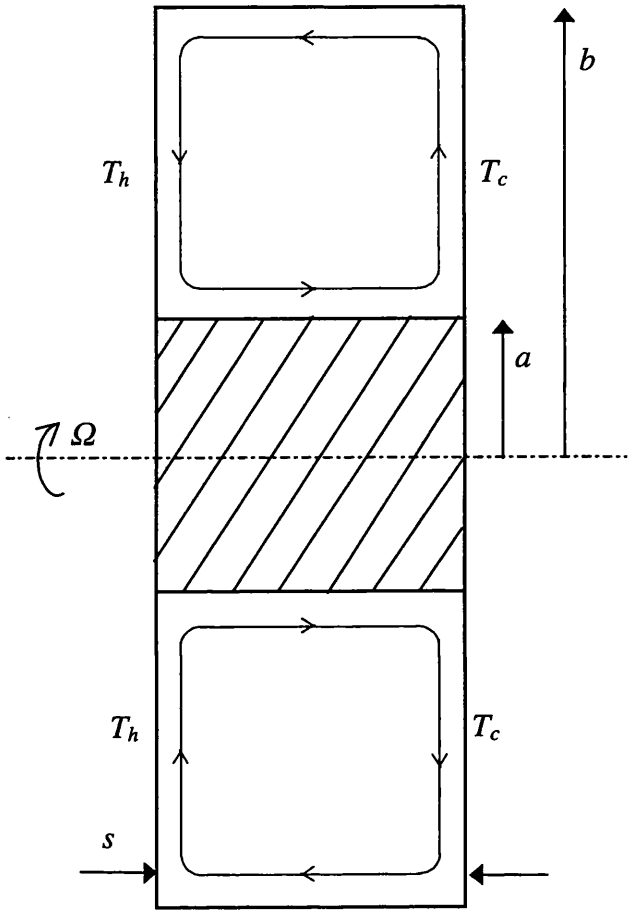

Figure 2.9 Longitudinal cross-section of a cylindrical annulus with a heated side-disc. The cylindrical surfaces can be insulated *or* conducting partially.

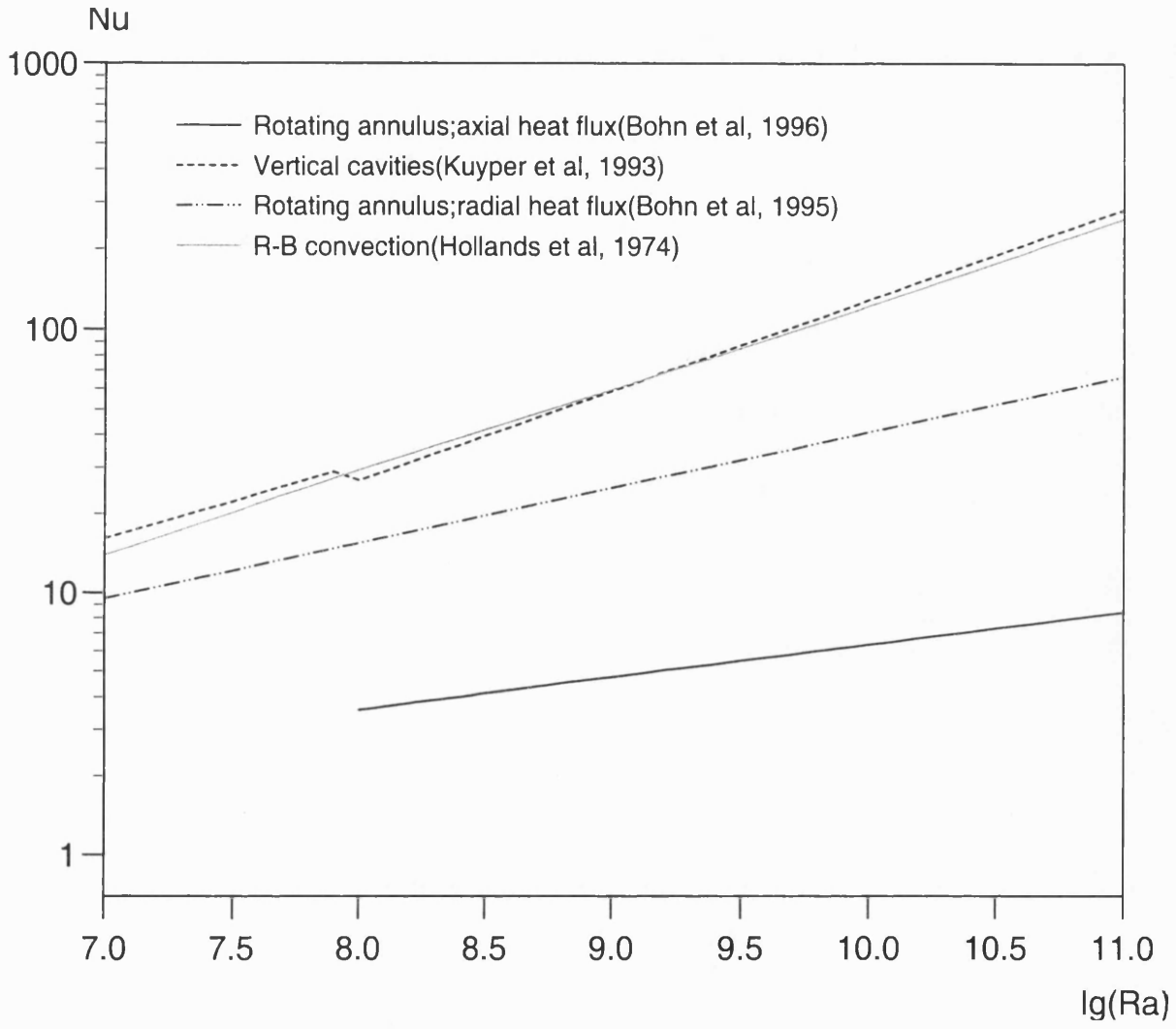

Figure 2.10 *Nu vs. Ra* rotating annulus with axial heat flux, comparison with other correlations.

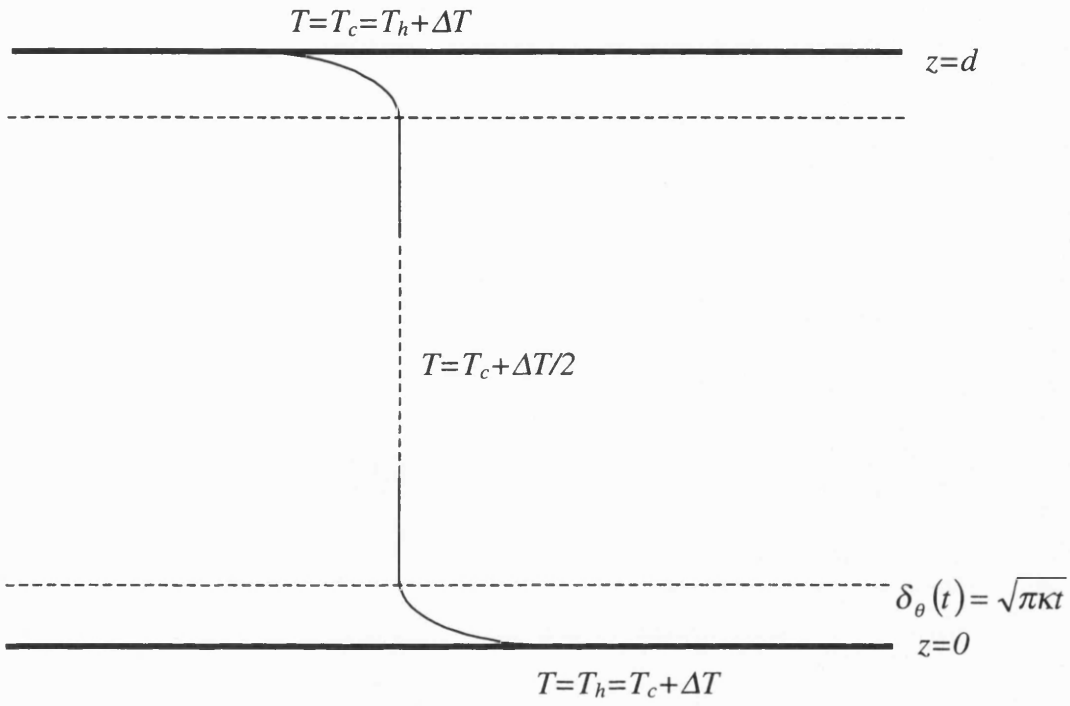

Figure 3.1 Vertical temperature profile. The thickness of the marginally stable thermal conductive layer is growing at $\delta_\theta(t)=\sqrt{\pi\kappa t}$. Temperature gradients are confined to the boundary layers at the bottom and top plates.

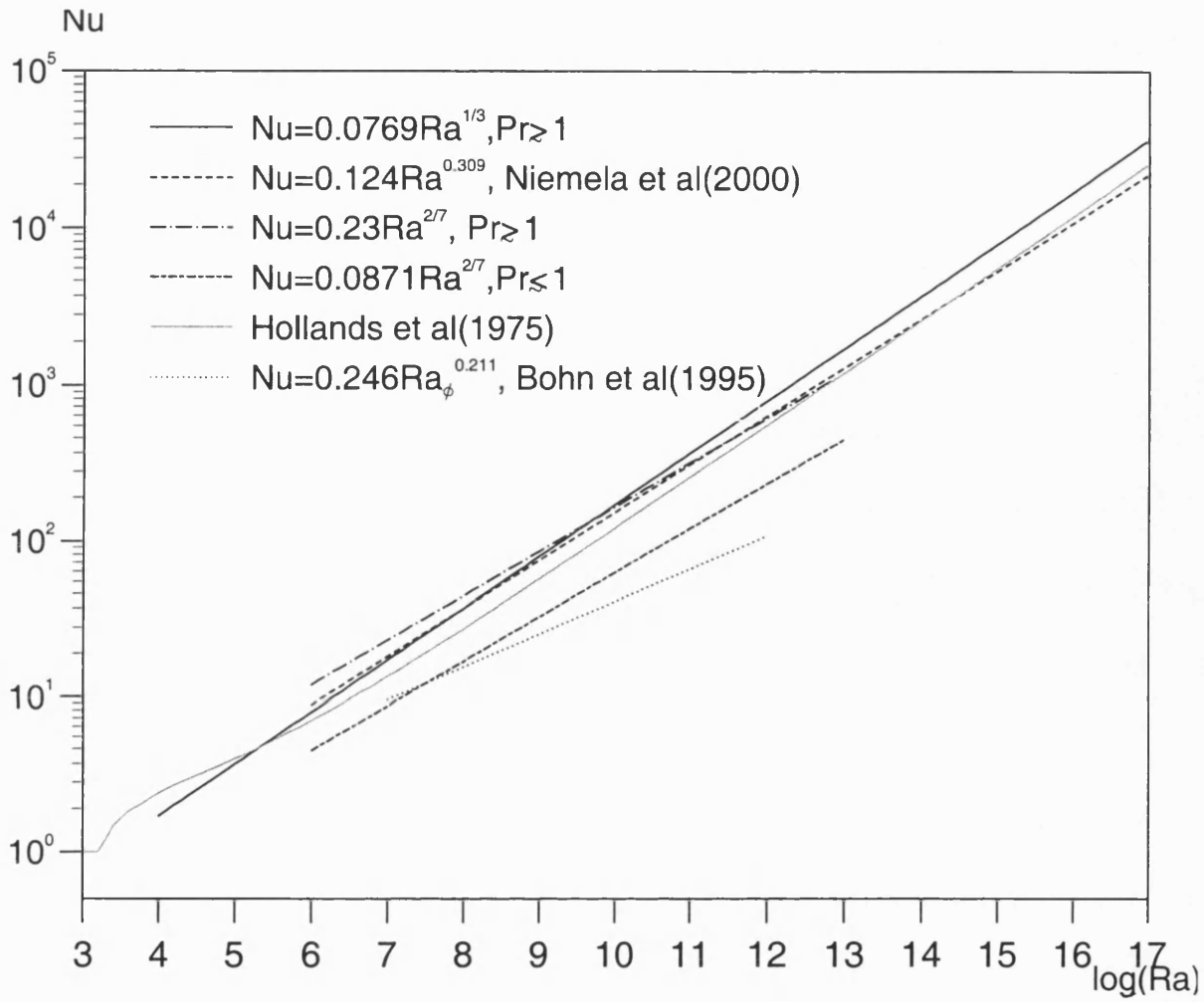

Figure 3.2 Power–law correlations from various derivations on a log–log plot.

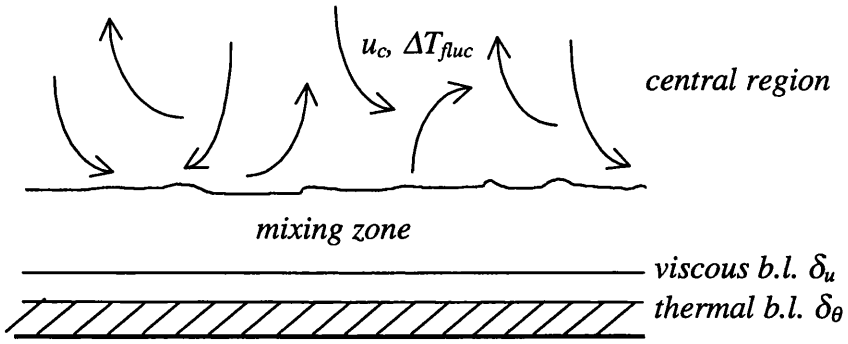

Figure 3.3.a $Pr \gtrsim 1$. The thermal boundary layer is nested within the viscous boundary layer. Temperature change across the thermal boundary layer is $\Delta T/2$. Only the bottom plate is shown.

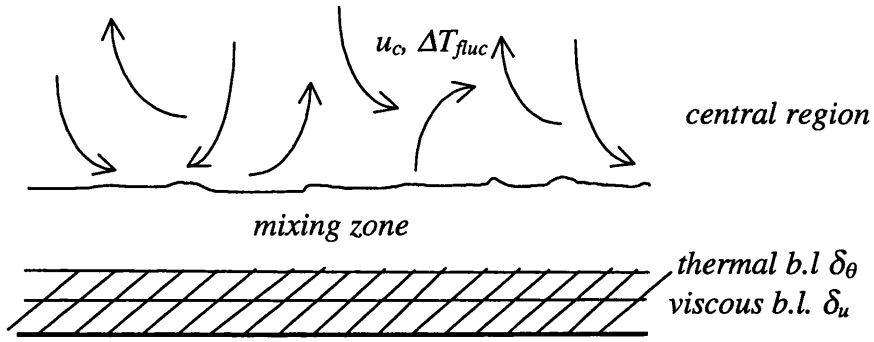

Figure 3.3.b $Pr \lesssim 1$. The viscous boundary layer is nested within the thermal boundary layer. Temperature change across the thermal boundary layer is $\Delta T/2$. Only the bottom plate is shown.

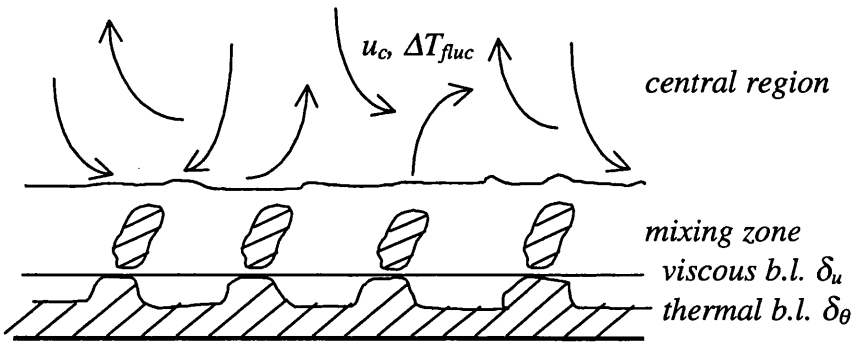

Figure 3.4.a $Pr \gtrsim 1$. Cross-refer to figure 3.3.a. The detaching thermal filaments have a length-scale of δ_θ.

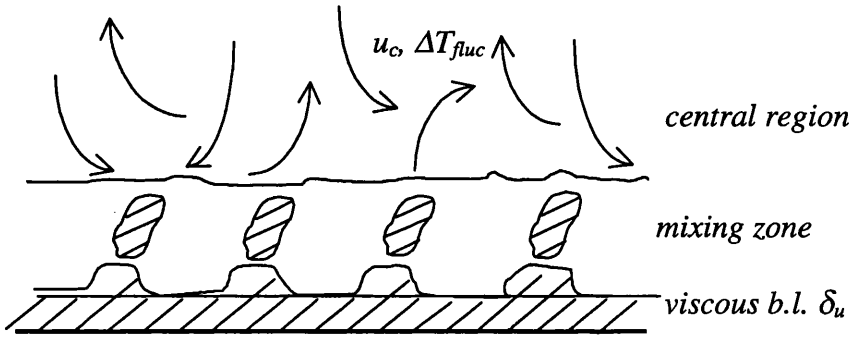

Figure 3.4.b $Pr \lesssim 1$. Cross-refer to figure 3.3.b. Thermal boundary layer outside the viscous boundary layer cannot exist stably due to strong turbulence wind. Detaching thermal filaments have length-scale of δ_u.

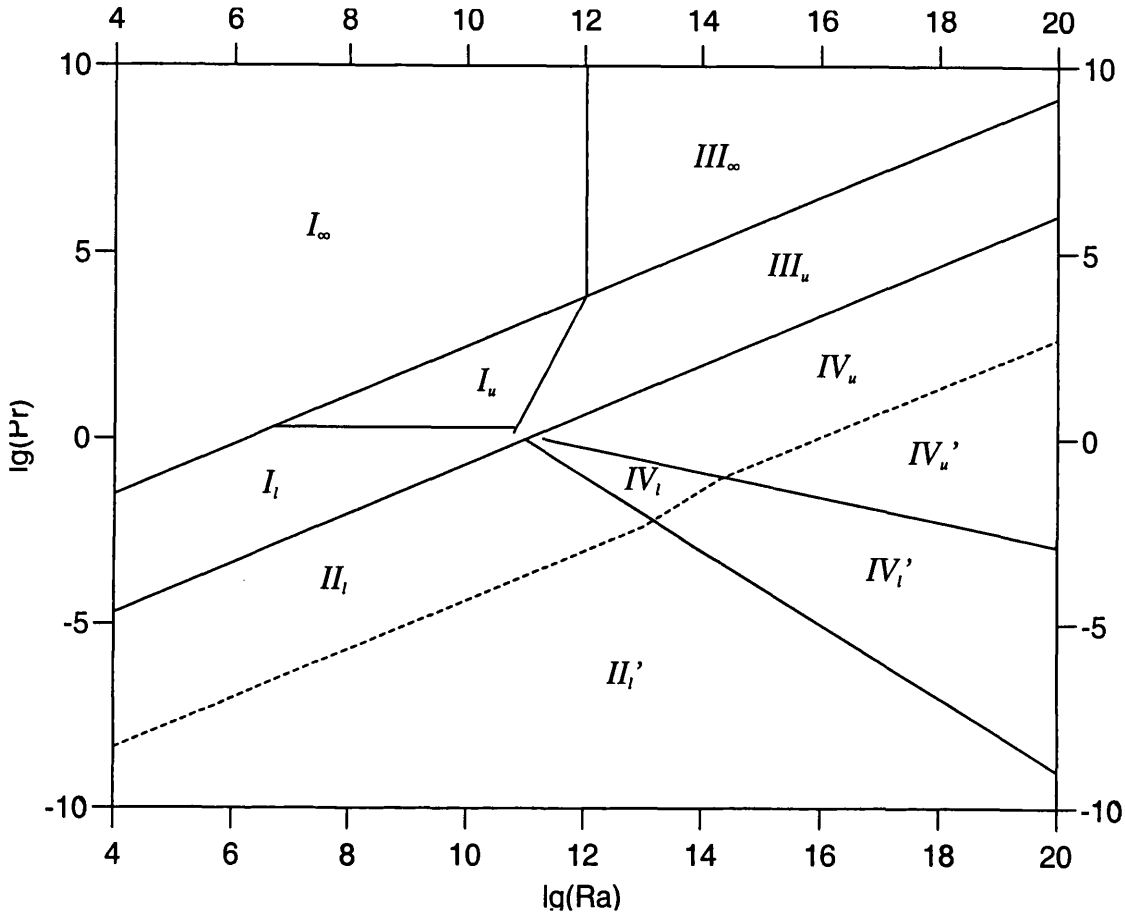

Figure 3.5 Pr–Ra phase diagram(Grossmann & Lohse, 2000 & 2001). Refer to table 3.3 for the scaling relation of each regime.

I_l : $Nu=0.22Ra^{1/4}Pr^{1/8}$
I_u : $Nu=0.31Ra^{1/4}Pr^{-1/12}$
I_∞: $Nu=0.35Ra^{1/4}$
II_l : $Nu=0.37Ra^{1/5}Pr^{1/5}$
III_u : $Nu=0.018Ra^{3/7}Pr^{-1/7}$
III_∞: $Nu=0.027Ra^{1/3}$
IV_l : $Nu=0.0012Ra^{1/2}Pr^{1/2}$
IV_u : $Nu=0.050Ra^{1/3}$

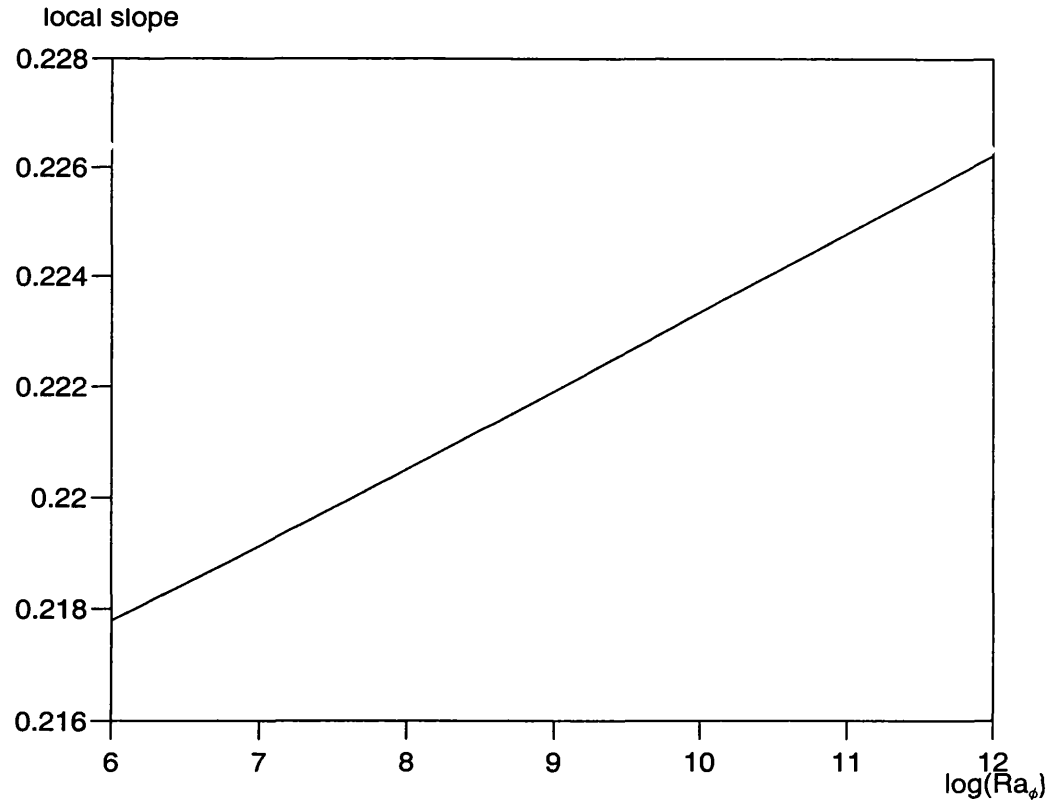

Figure 3.6.a Local slope of Equation (3.35)

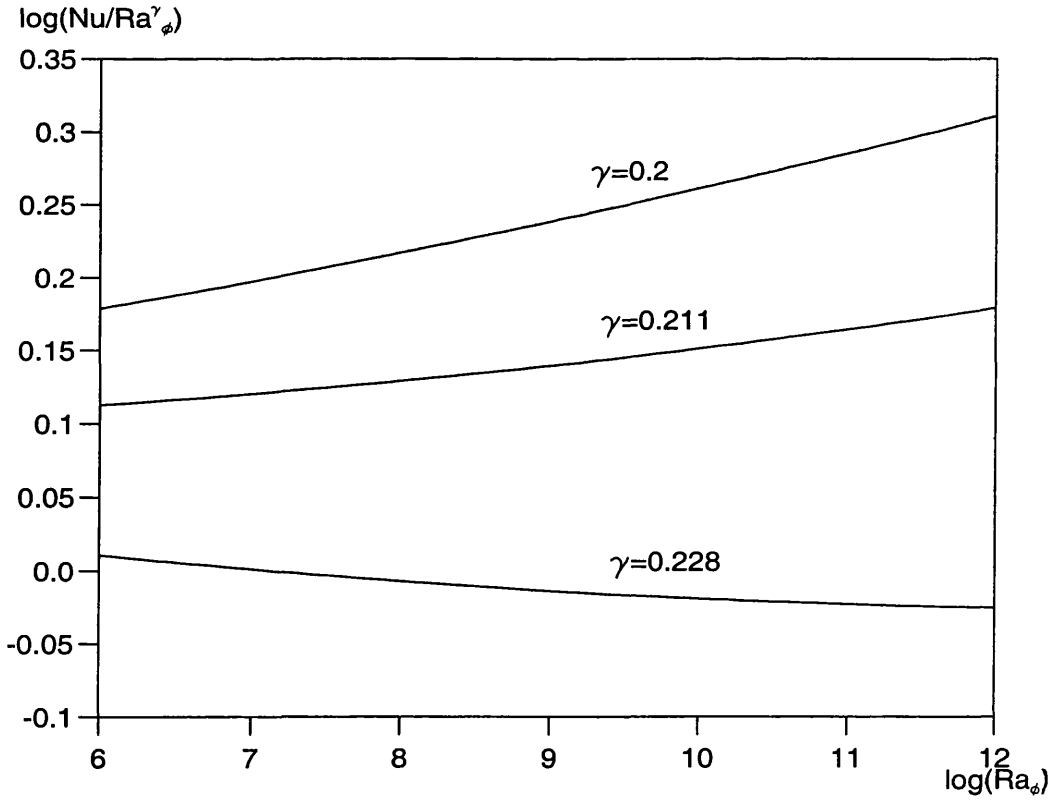

Figure 3.6.b Normalised *Nu* from Equation (3.35)

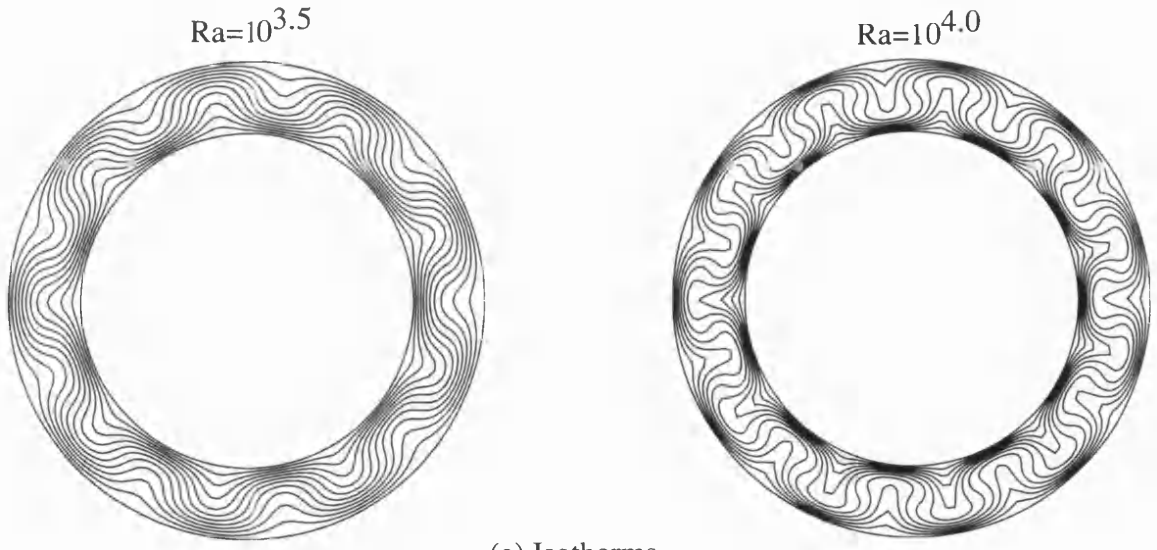

(a) Isotherms

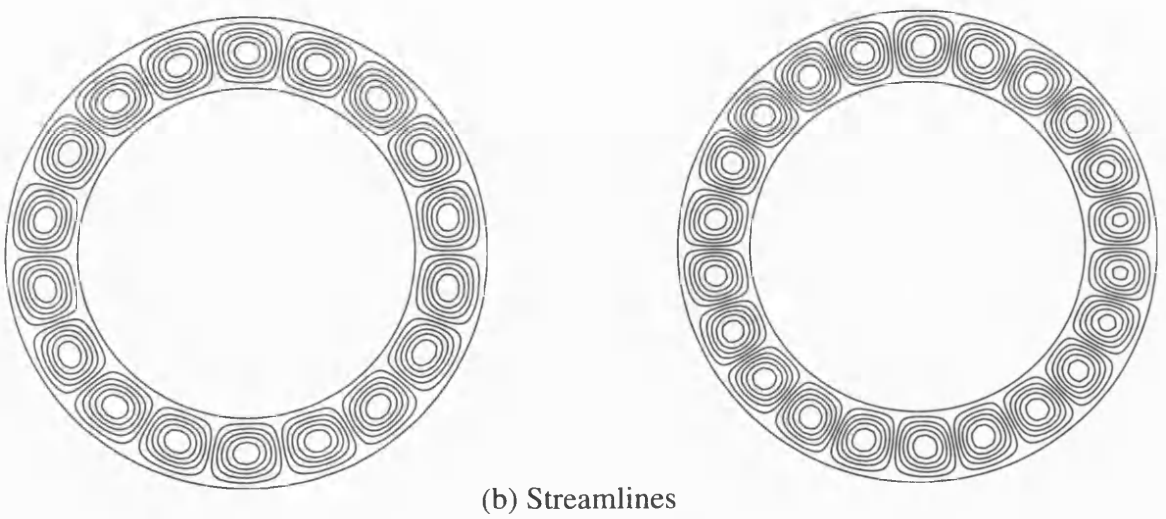

(b) Streamlines

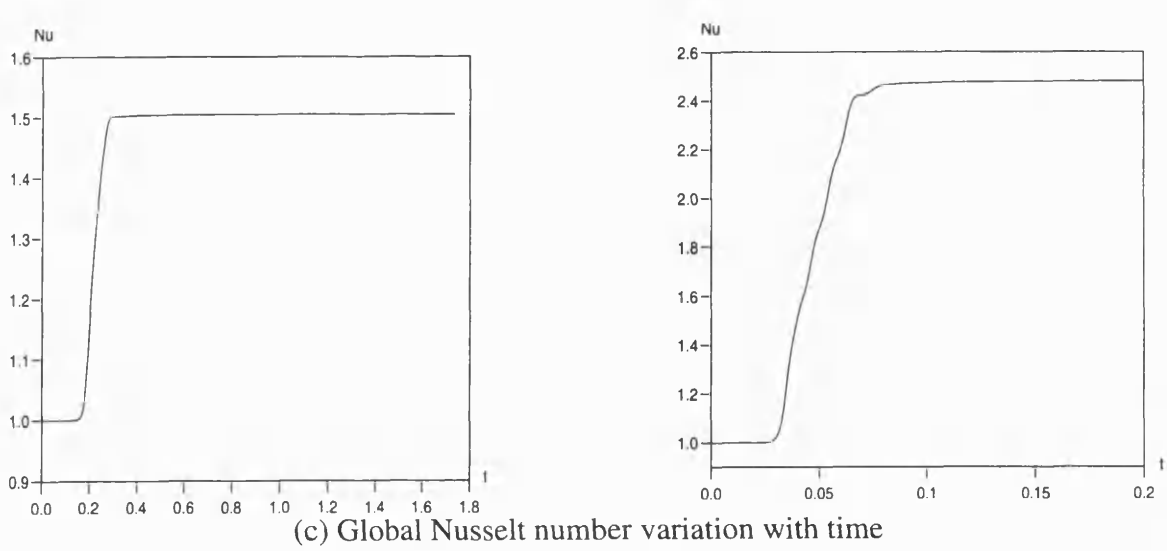

(c) Global Nusselt number variation with time

Figure 4.1 Solutions for non–rotating 2D radial–tangential flow (approx. R–B conv.) for Ra=$10^{3.5}$ and Ra=$10^{4.0}$. $r_o - r_i = 0.3$.

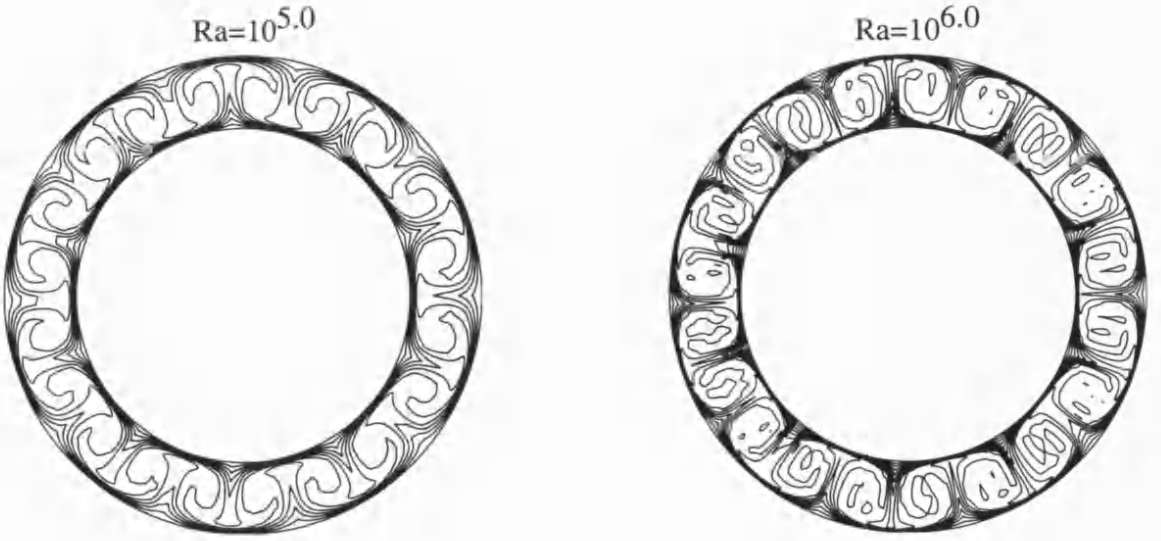

(a) Isotherms

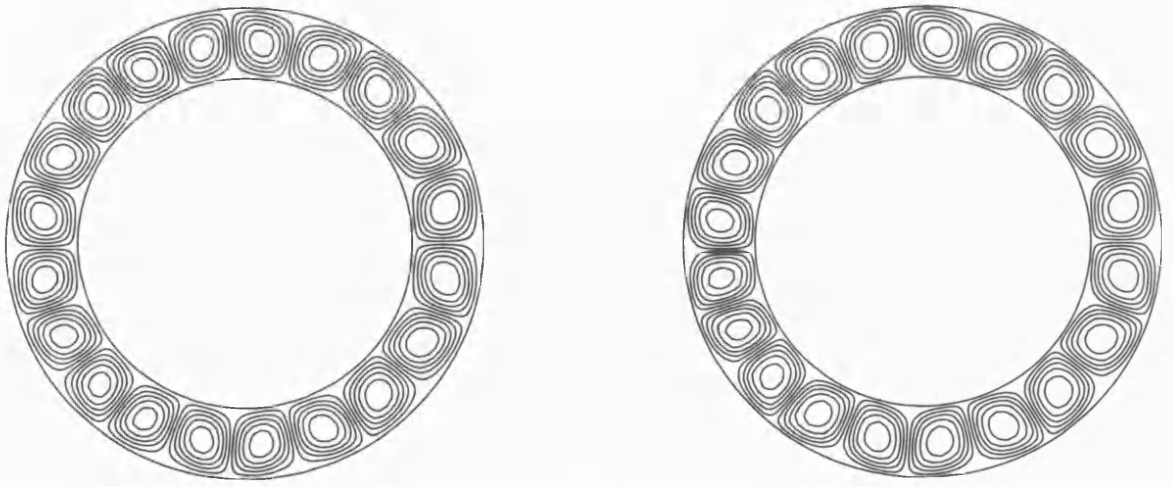

(b) Streamlines

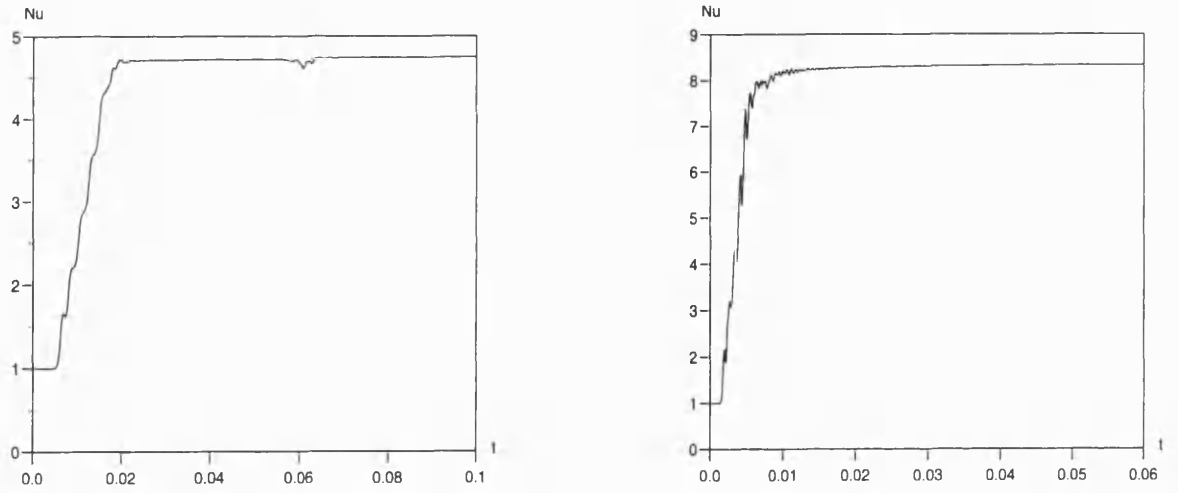

(c) Global Nusselt number variation with time

Figure 4.2 Solutions for non–rotating 2D radial–tangential flow (approx. R–B conv.) for $Ra=10^{5.0}$ and $Ra=10^{6.0}$. $r_o - r_i = 0.3$.

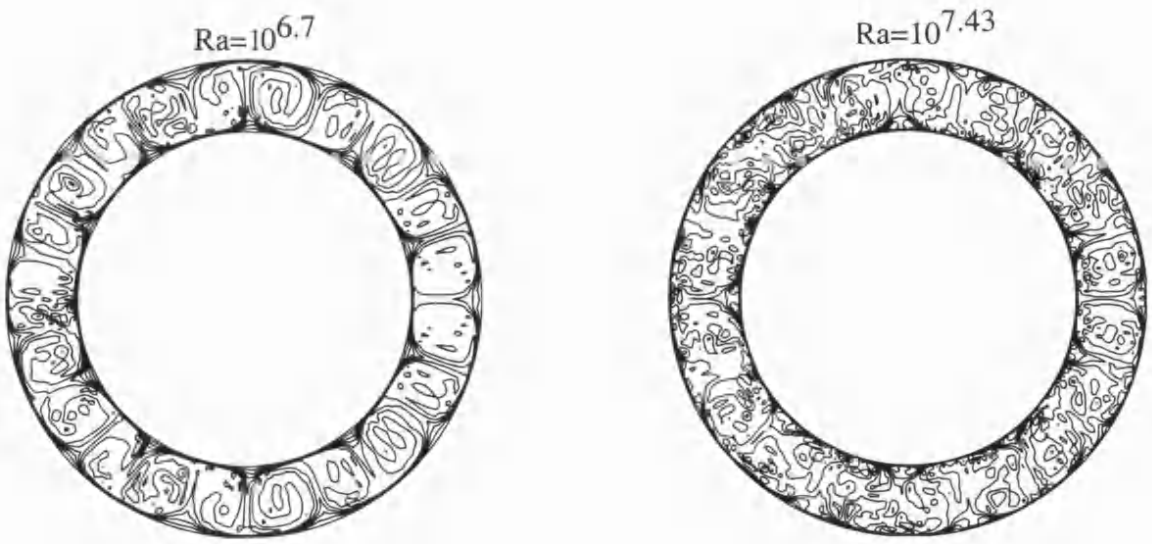

(a) Isotherms

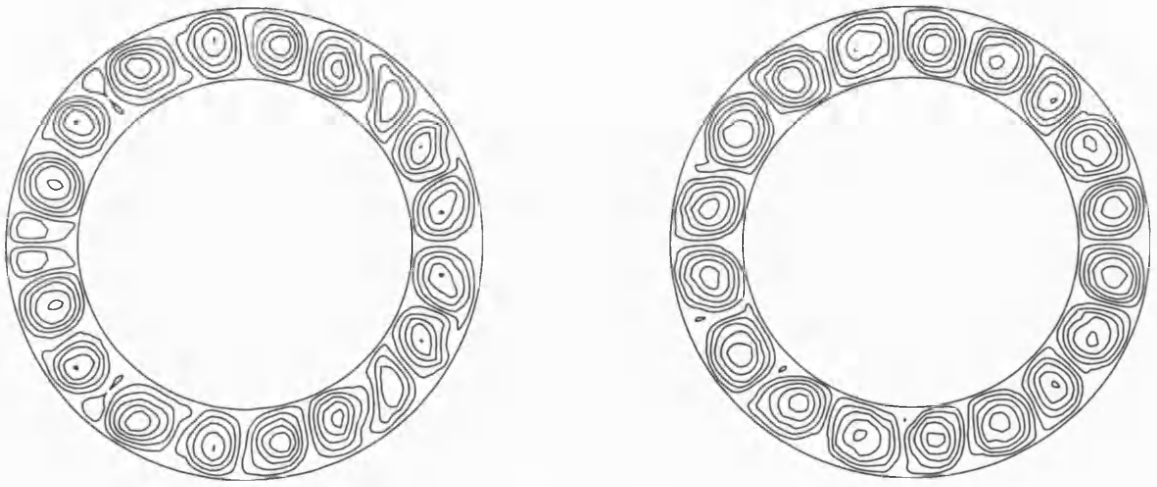

(b) Streamlines

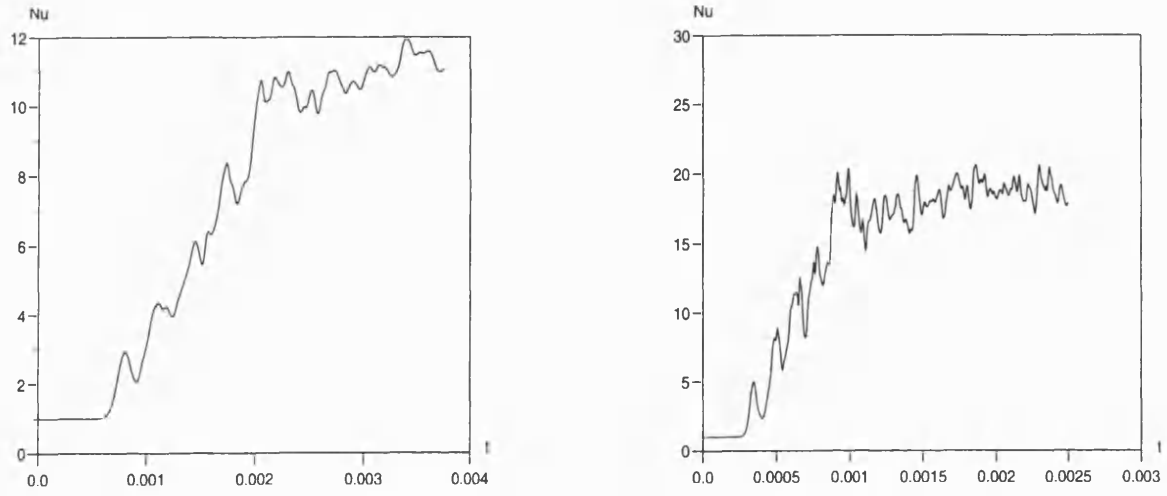

(c) Global Nusselt number variation with time

Figure 4.3 Solutions for non–rotating 2D radial–tangential flow (approx .R–B conv.) for Ra=$10^{6.7}$ and Ra=$10^{7.43}$. $r_o - r_i = 0.3$.

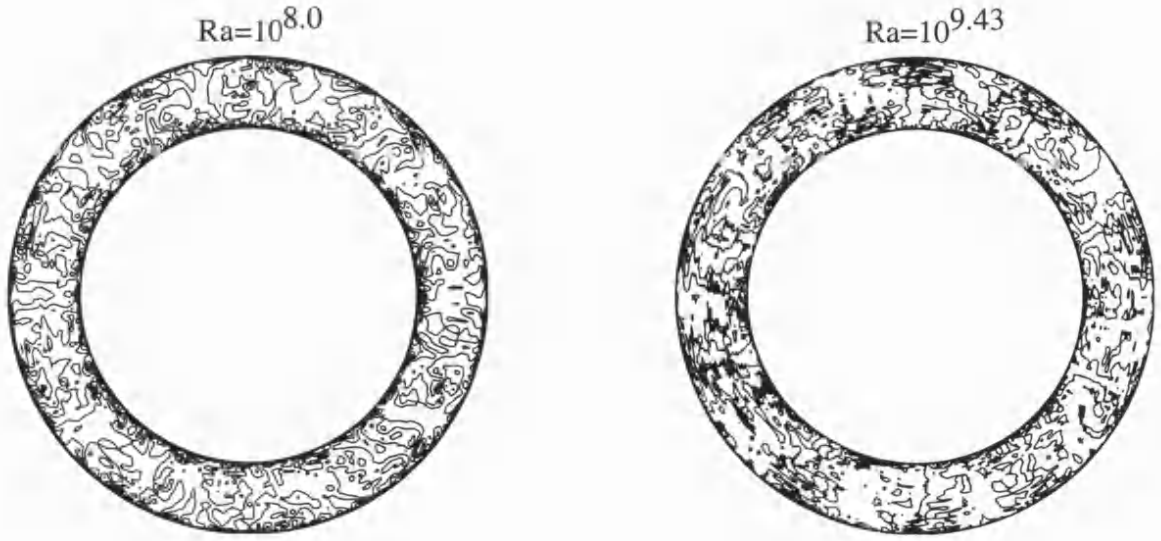

(a) Isotherms

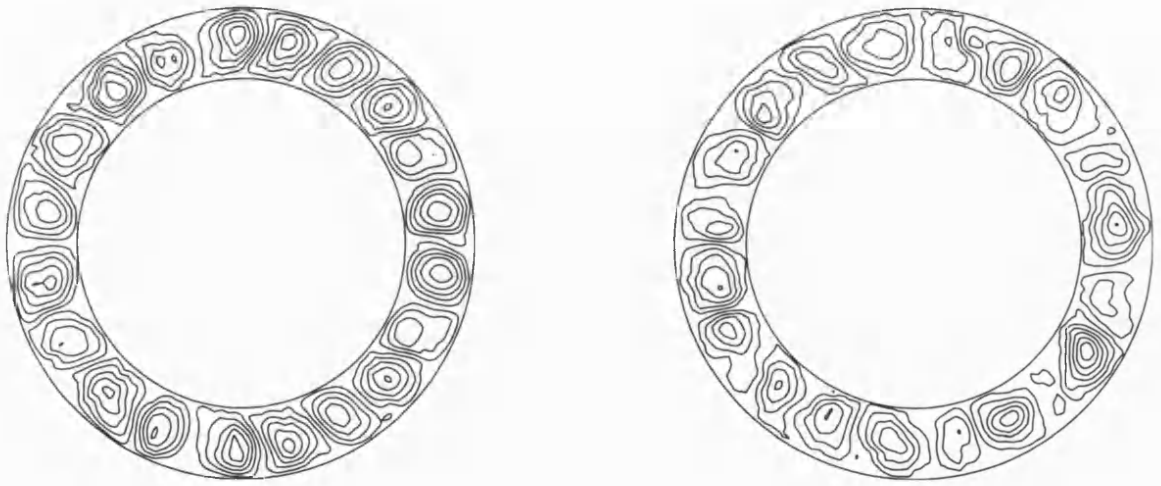

(b) Streamlines

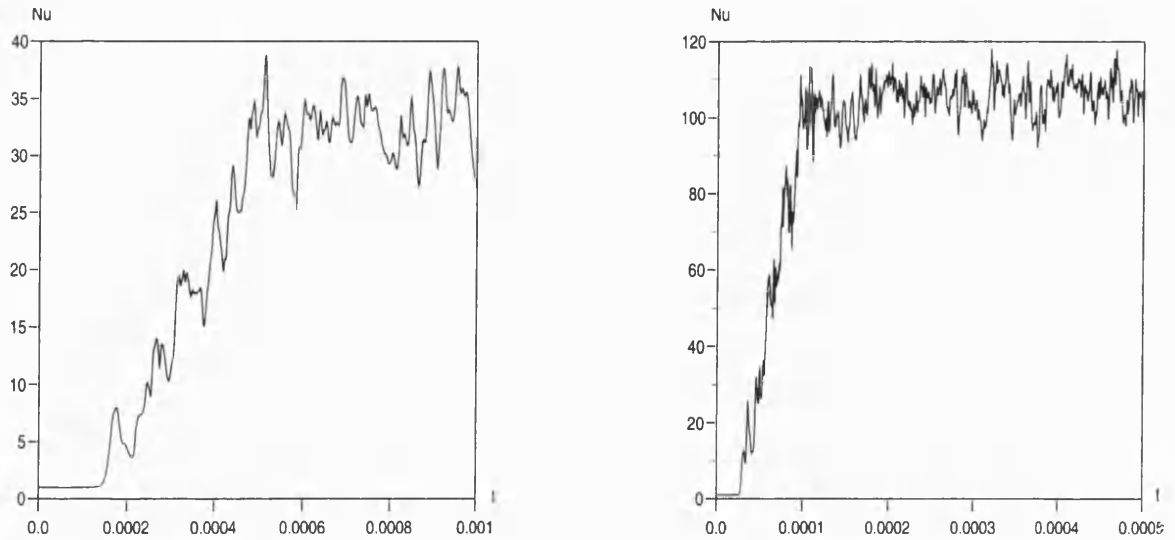

(c) Global Nusselt number variation with time

Figure 4.4 Solutions for non–rotating 2D radial–tangential flow (approx. R–B conv.) for Ra=$10^{8.0}$ and Ra=$10^{9.43}$. $r_o - r_i = 0.3$.

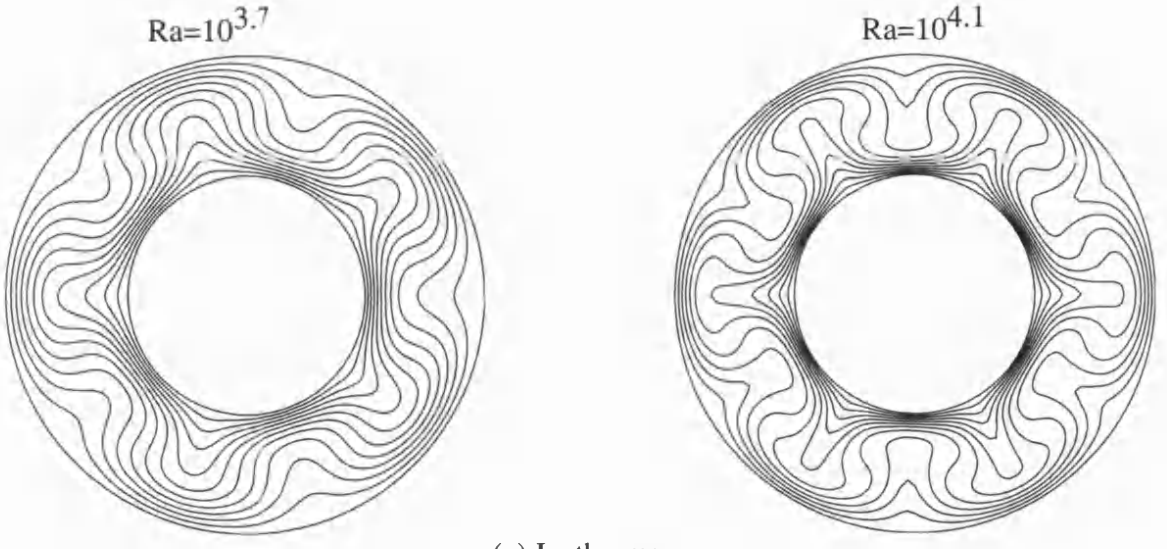

(a) Isotherms

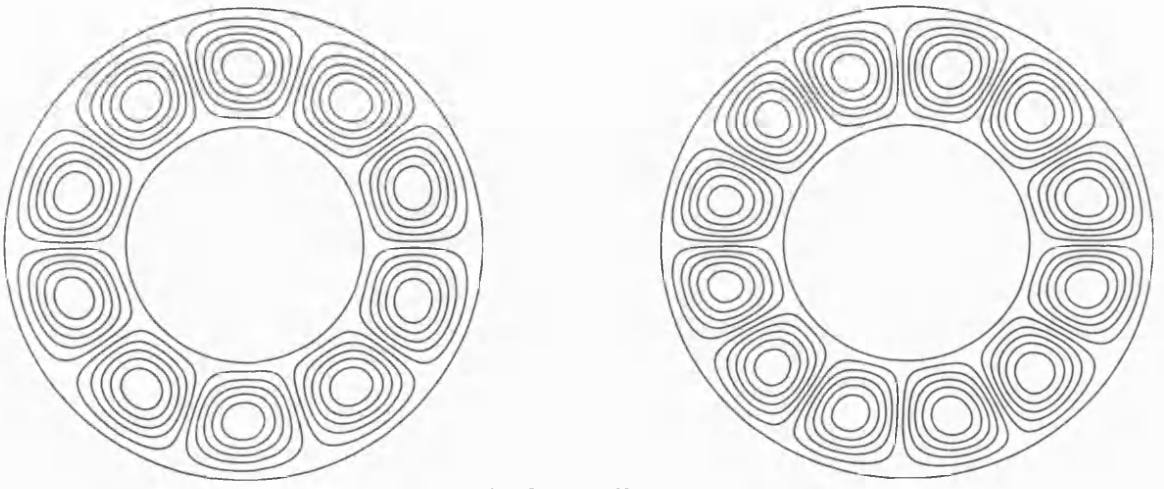

(b) Streamlines

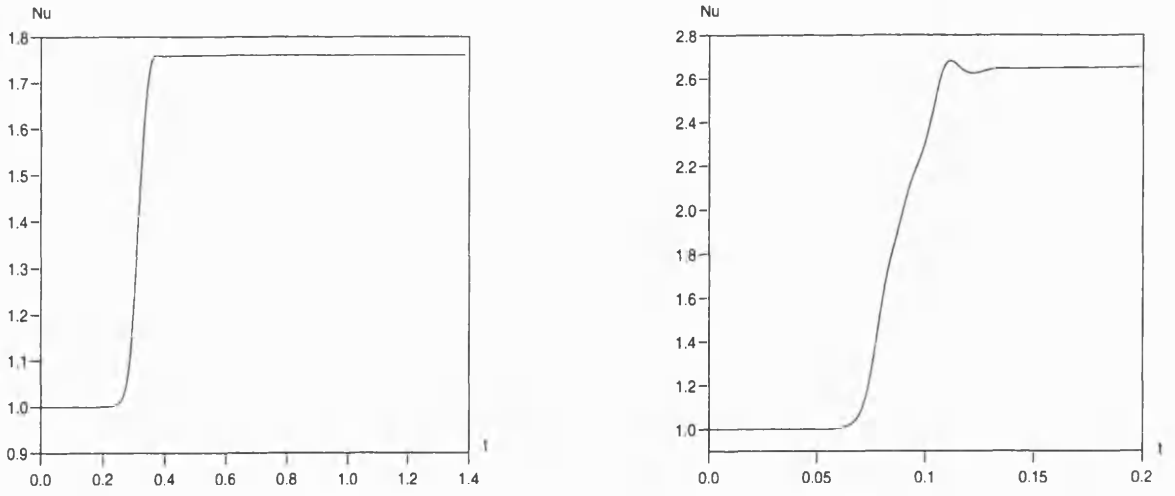

(c) Global Nusselt number variation with time

Figure 4.5 Solutions for non–rotating 2D radial–tangential flow (approx. R–B conv.) for Ra=$10^{3.7}$ and Ra=$10^{4.1}$. $r_o - r_i = 0.5$.

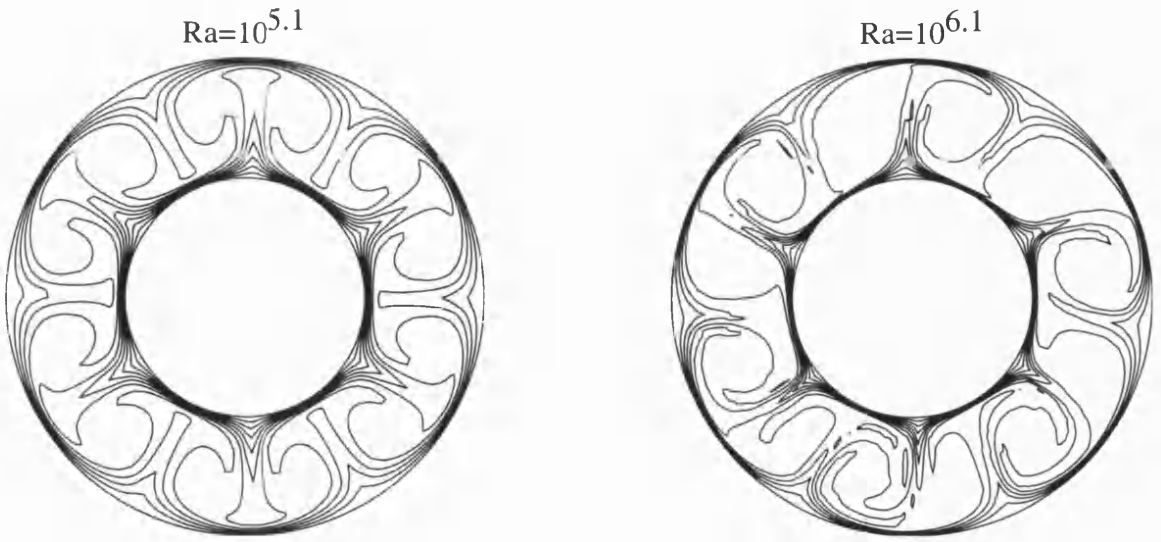

(a) Isotherms

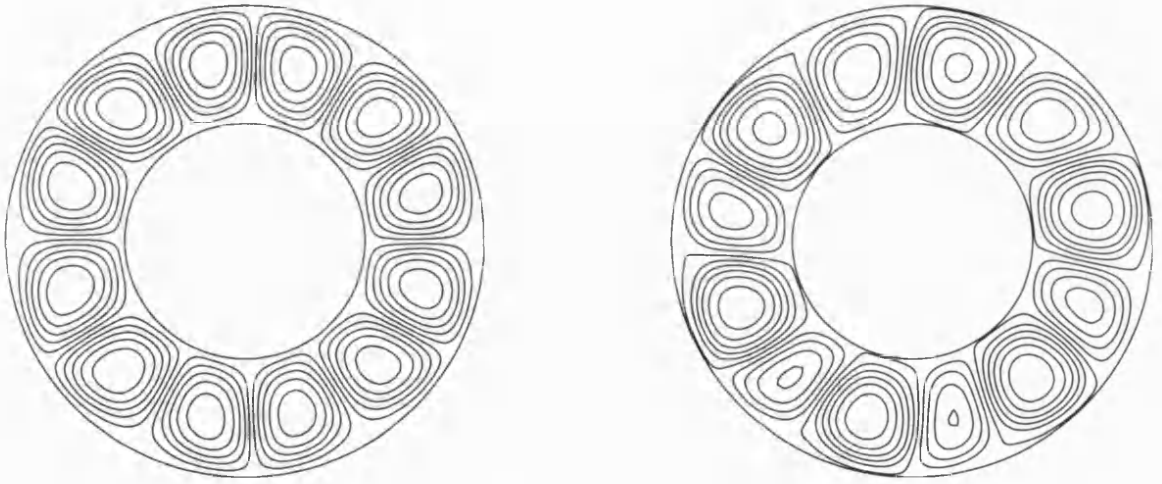

(b) Streamlines

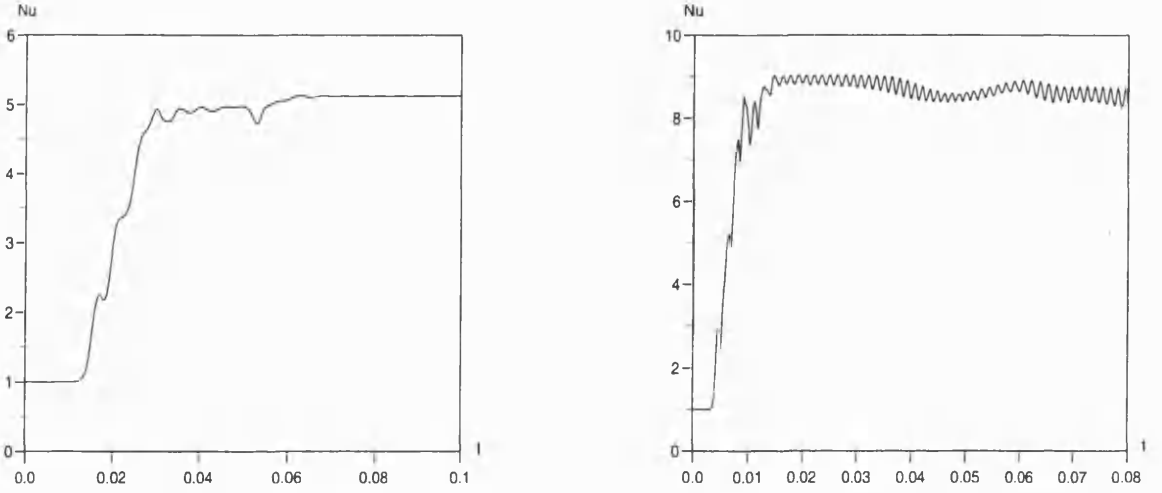

(c) Global Nusselt number variation with time

Figure 4.6 Solutions for non–rotating 2D radial–tangential flow (approx. R–B conv.) for Ra=$10^{3.5}$ and Ra=$10^{4.0}$. $r_o - r_i = 0.5$.

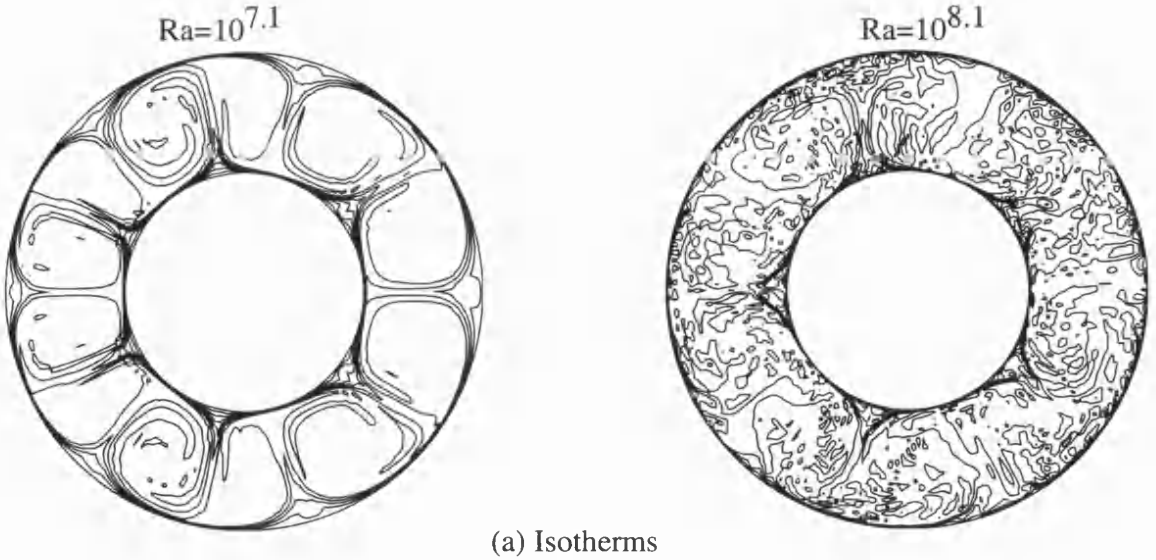

(a) Isotherms

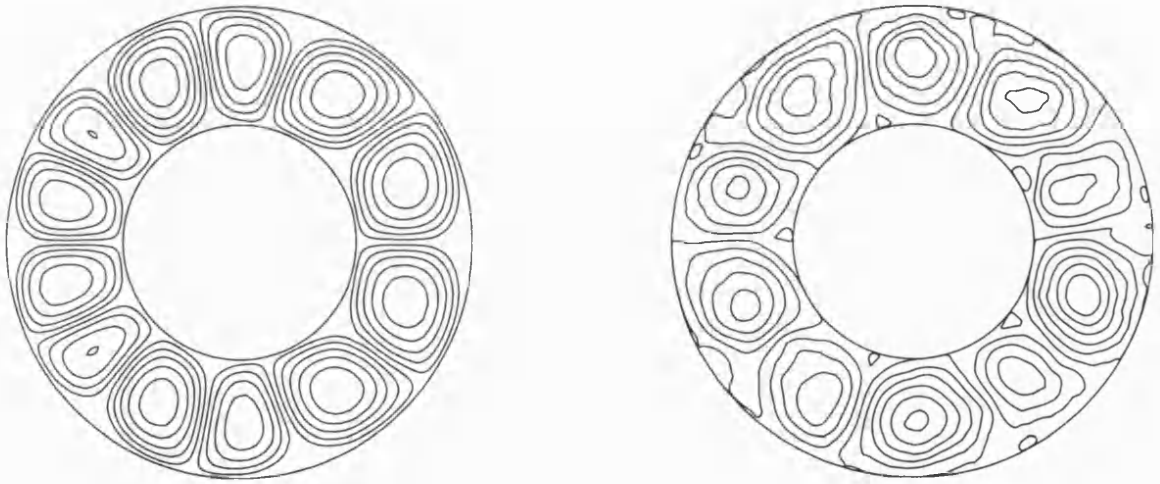

(b) Streamlines

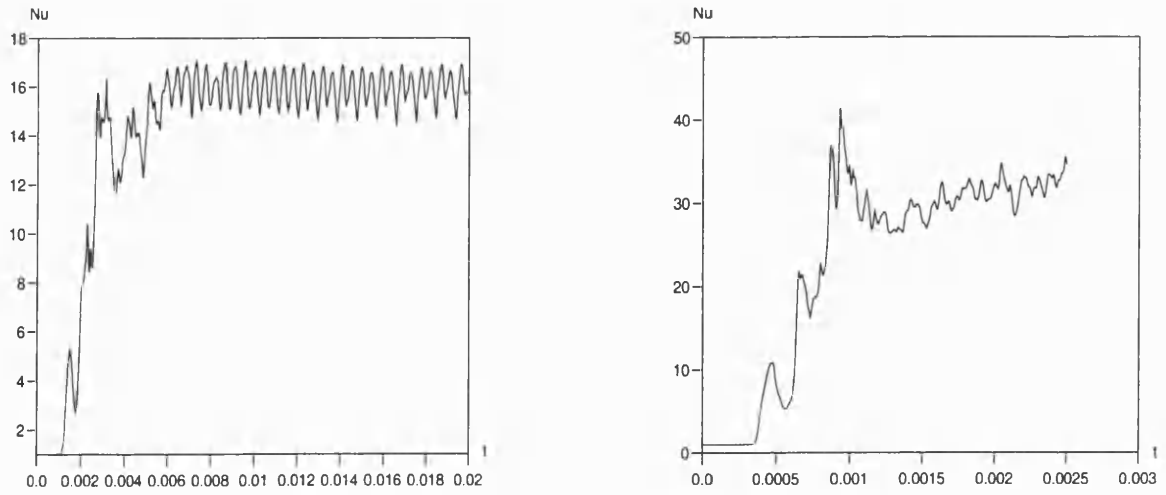

(c) Global Nusselt number variation with time

Figure 4.7 Solutions for non–rotating 2D radial–tangential flow (approx. R–B conv.) for Ra=$10^{7.1}$ and Ra=$10^{8.1}$. $r_o - r_i = 0.5$.

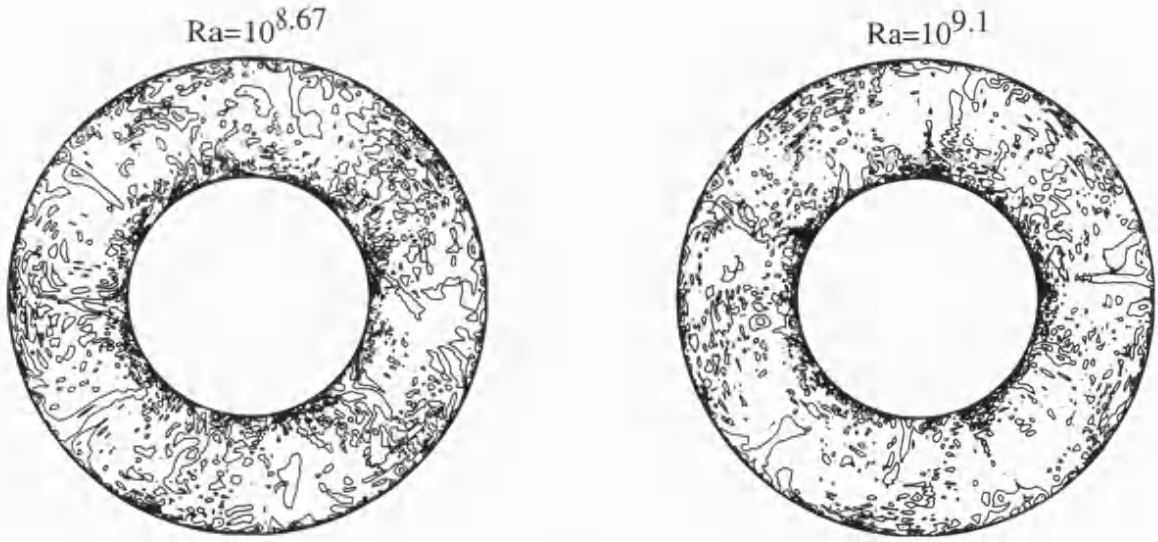

(a) Isotherms

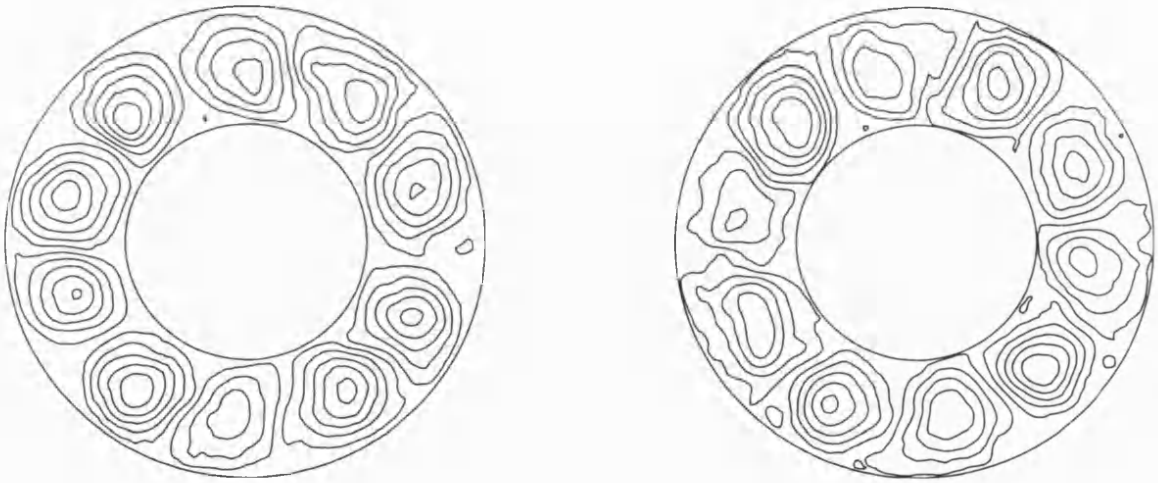

(b) Streamlines

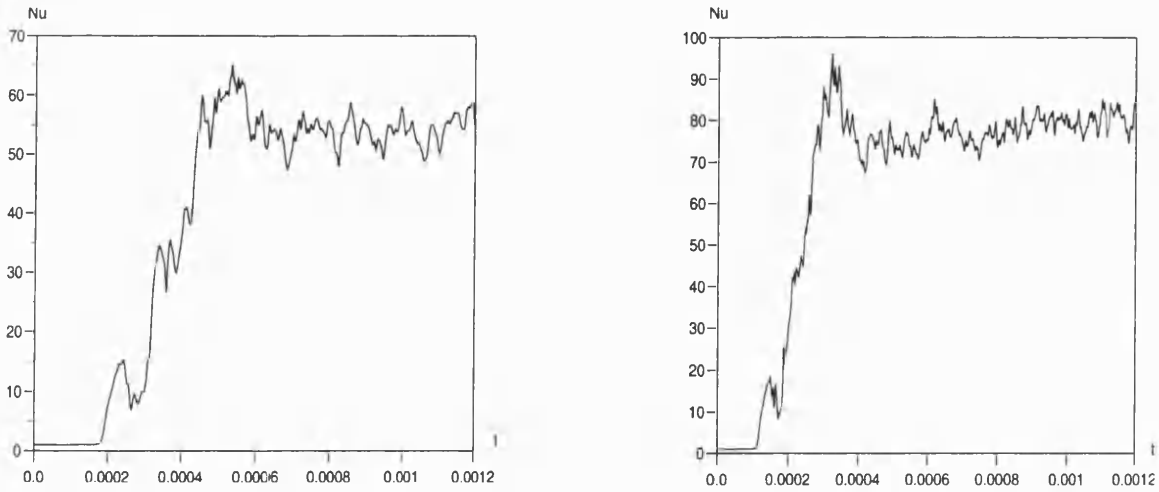

(c) Global Nusselt number variation with time

Figure 4.8 Solutions for non–rotating 2D radial–tangential flow (approx. R–B conv.) for Ra=$10^{8.67}$ and Ra=$10^{9.1}$. $r_o - r_i = 0.5$.

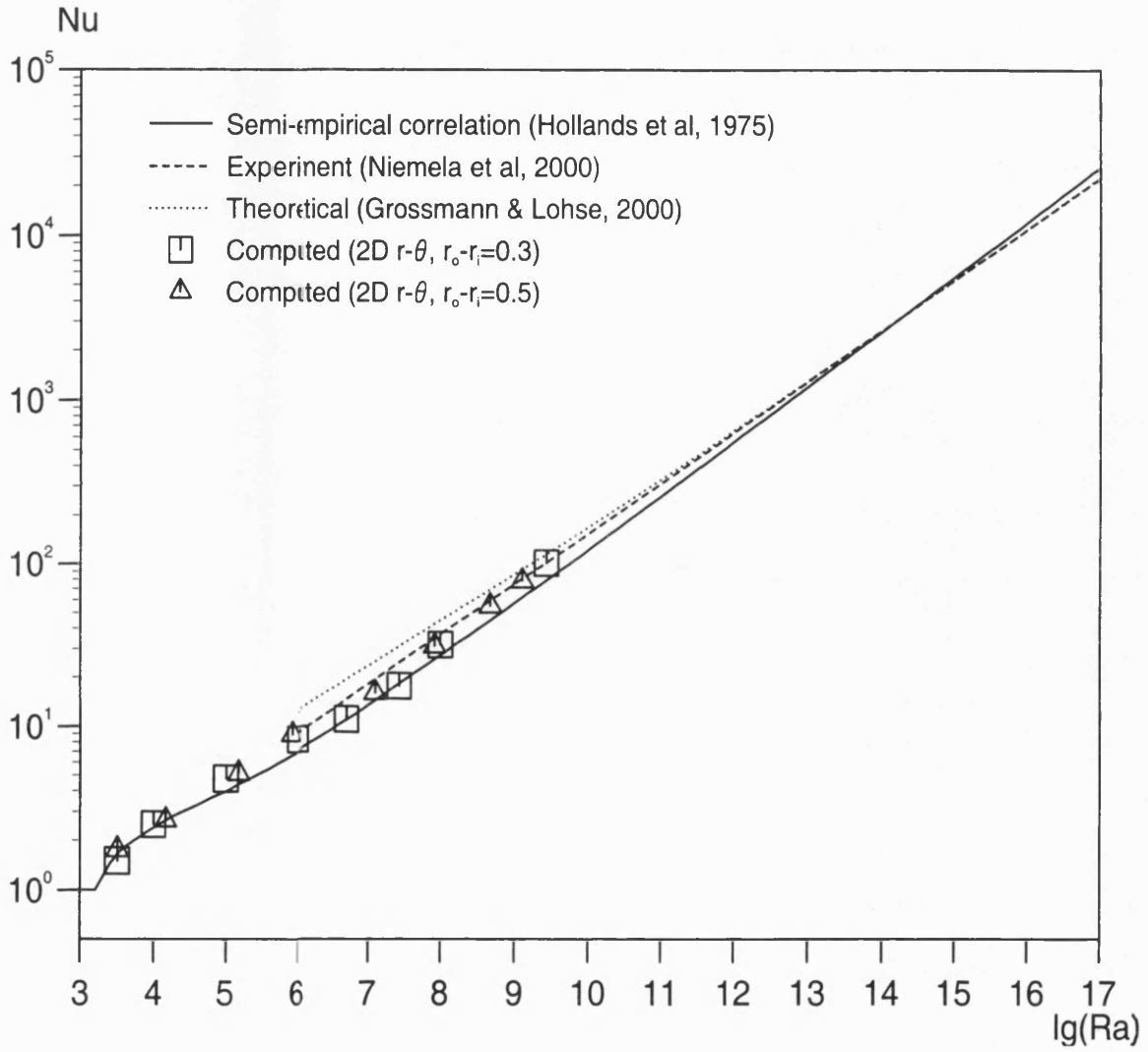

Figure 4.9 Comparison between computed *Nu* for 2D non−rotating annulus and published correlations for Rayleigh−Benard convection, *Pr=0.7*.

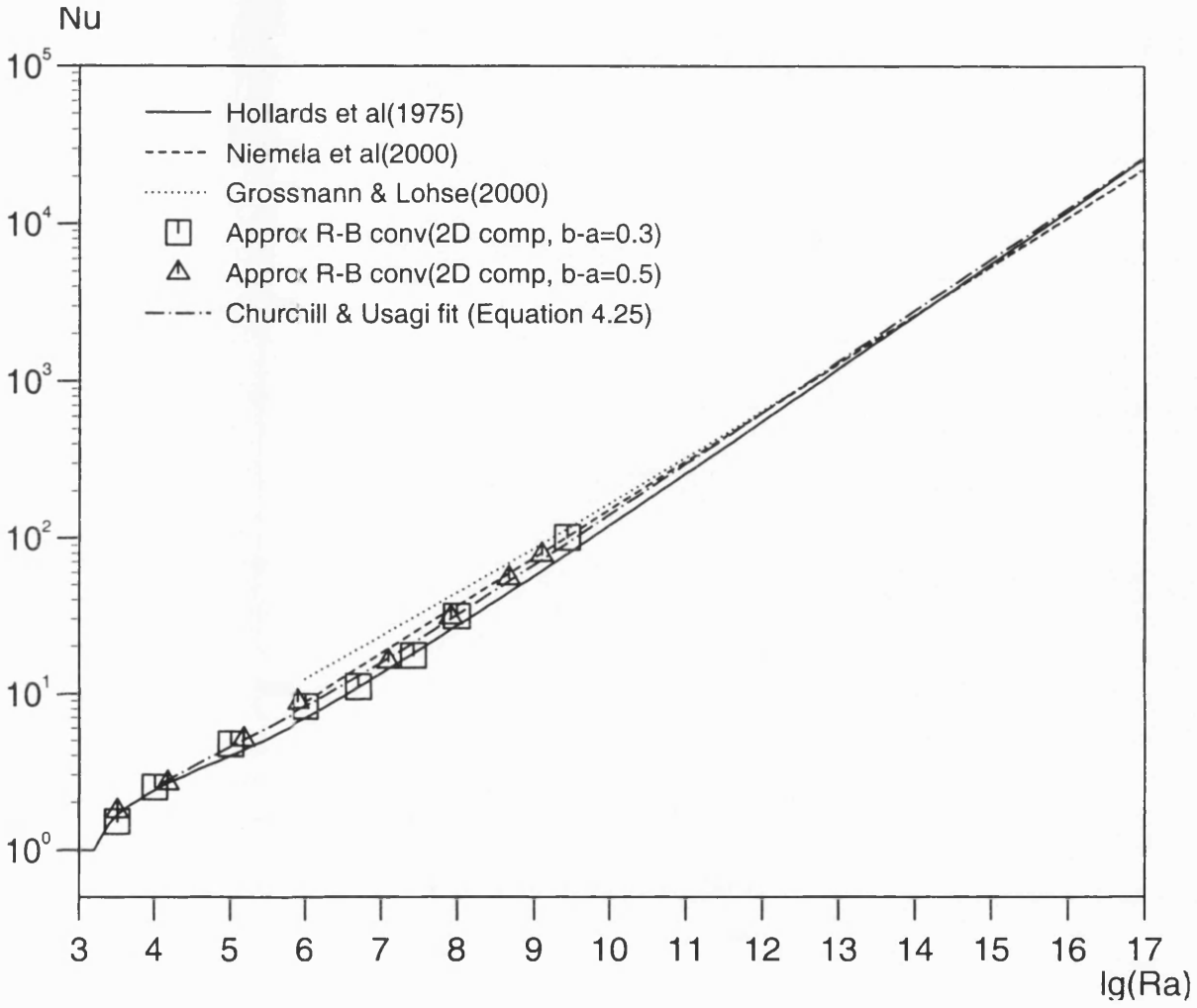

Figure 4.10 Correlation of computed results for a 2D non−rotating annulus using the blending method of Churchill & Usagi (1972), *Pr=0.7*.

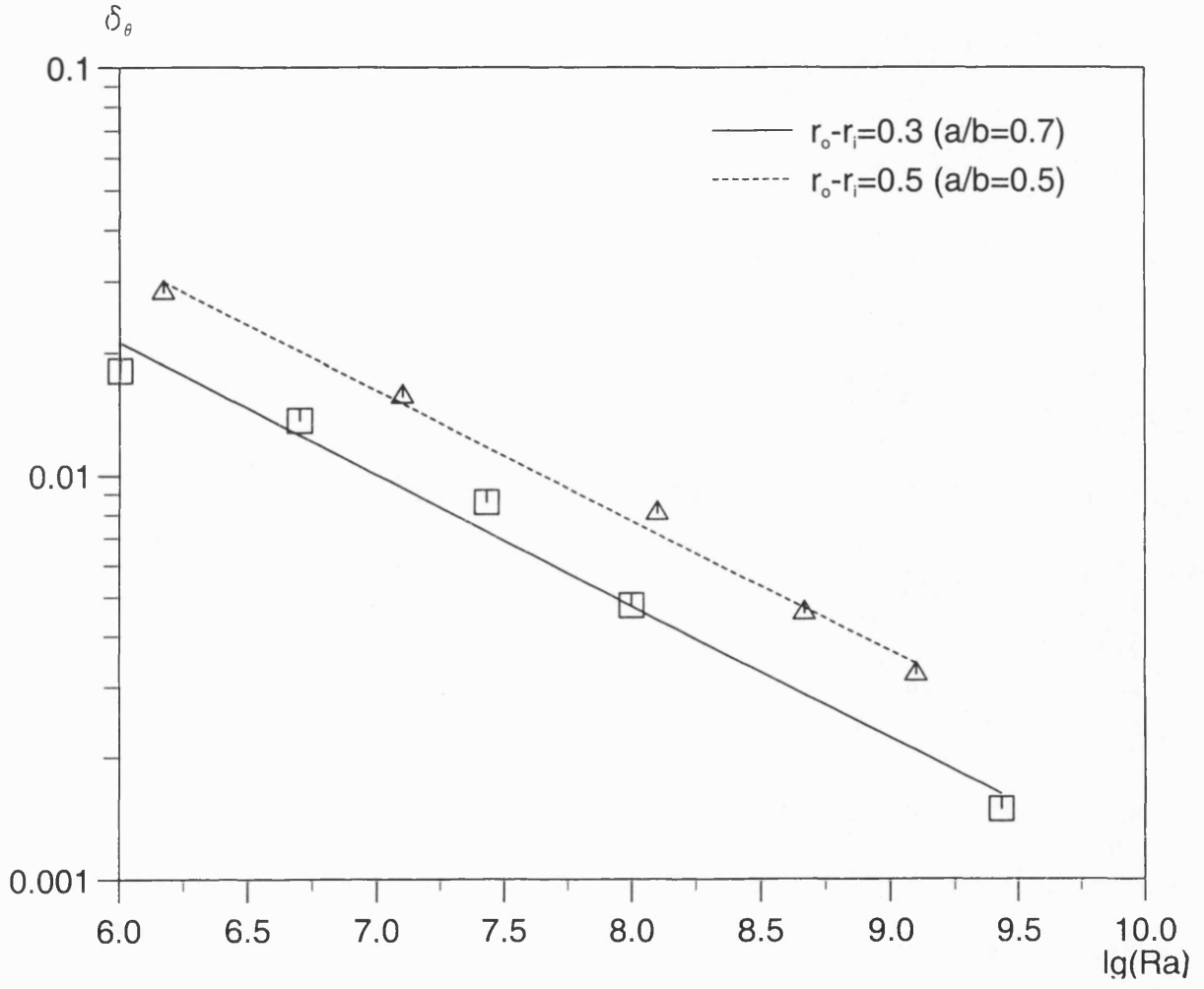

Figure 4.11 Variation of non–dimensional thermal boundary layer thickness with Rayleigh number *Pr=0.7*. See Equations 2.27 and 2.28.

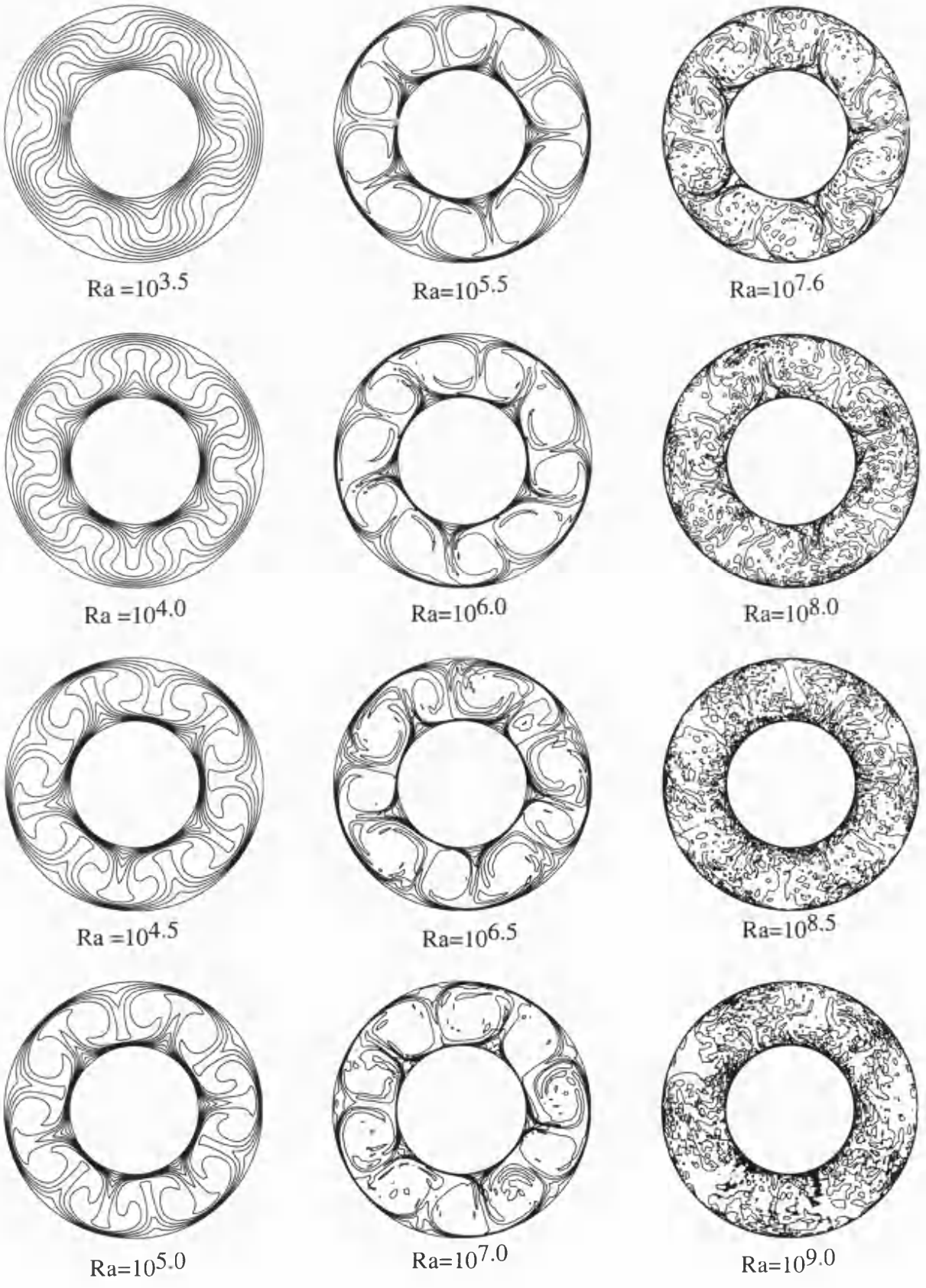

Figure 4.12 Computed isotherms for a 2D (radial–tangential) rotating annulus. $r_o - r_i = 0.5$.

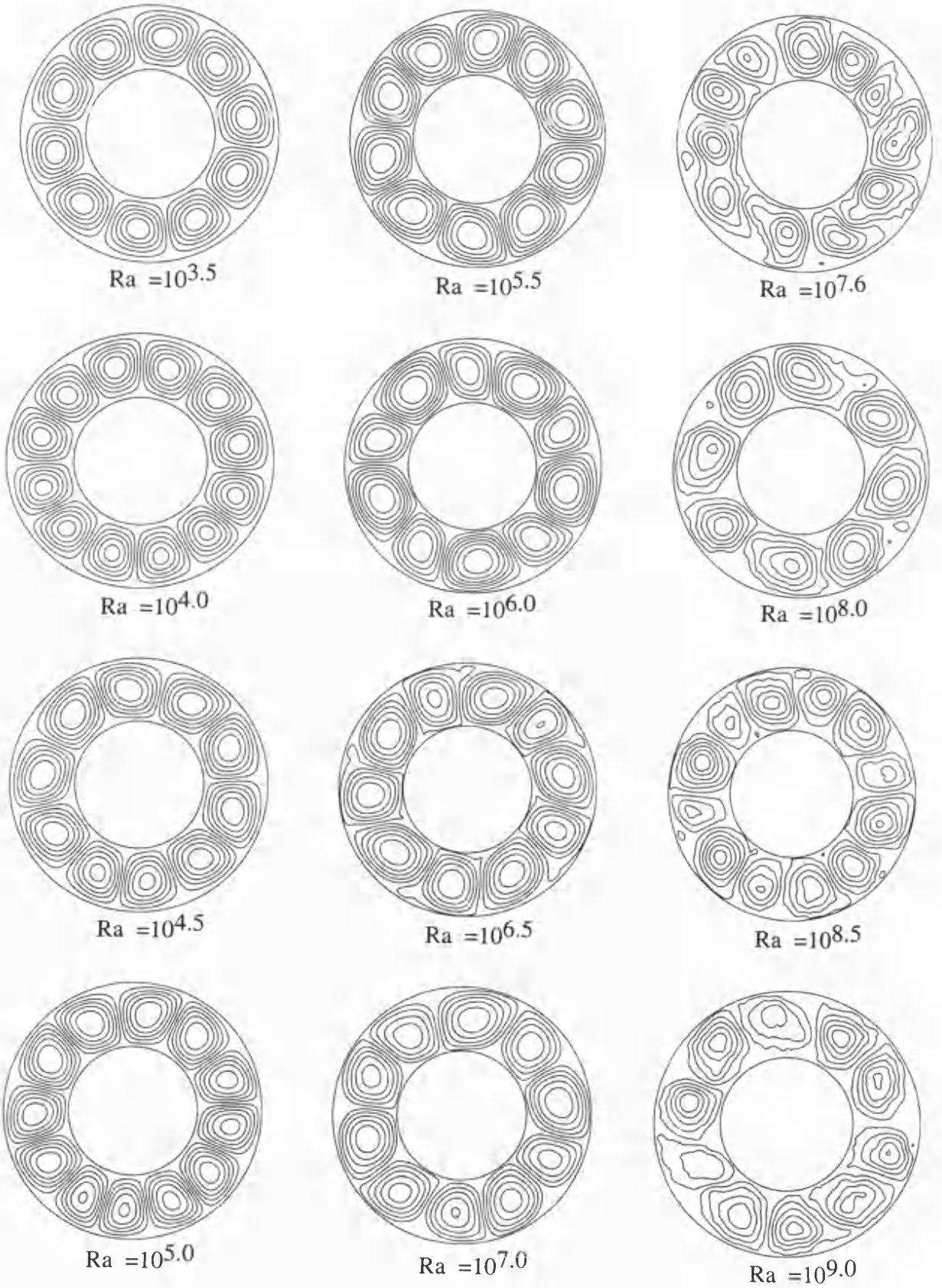

Figure 4.13 Computed streamlines for a 2D (radial–tangential) rotating annulus. $r_o - r_i = 0.5$.

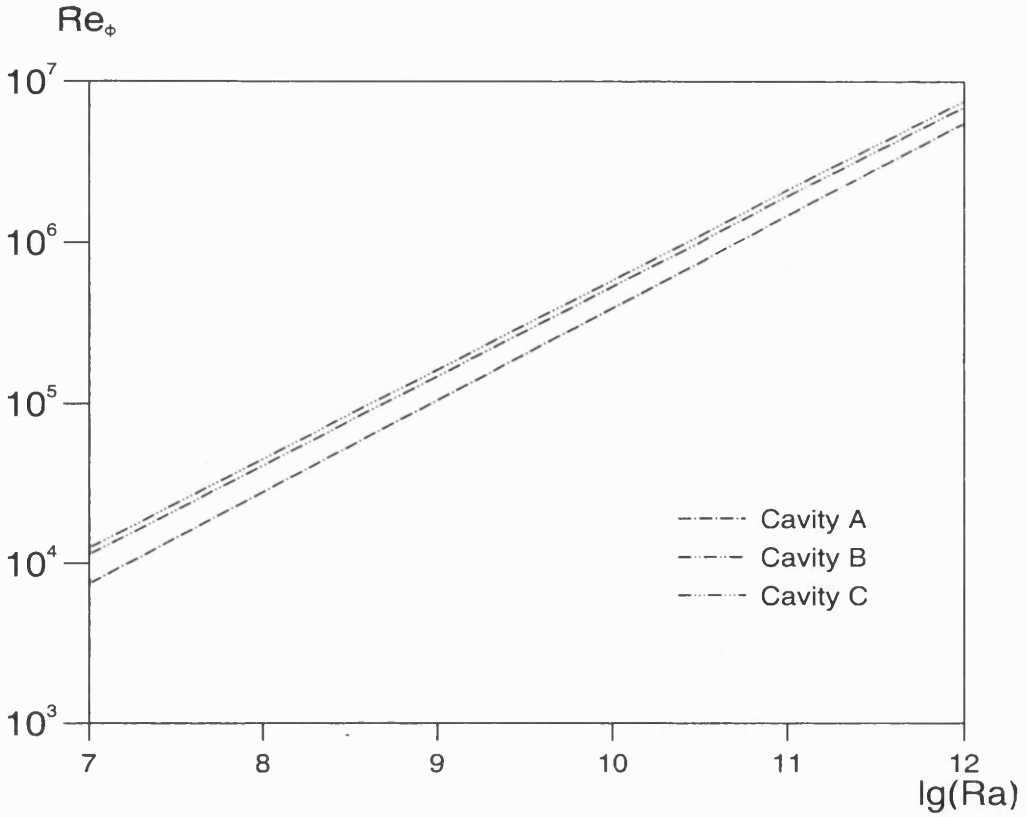

Figure 4.14.a Reynolds number against Rayleigh number on log–log axes.
For three different cavities in the experiments of Bohn *et al*(1995).
The lines are obtained using relationships given in this reference.

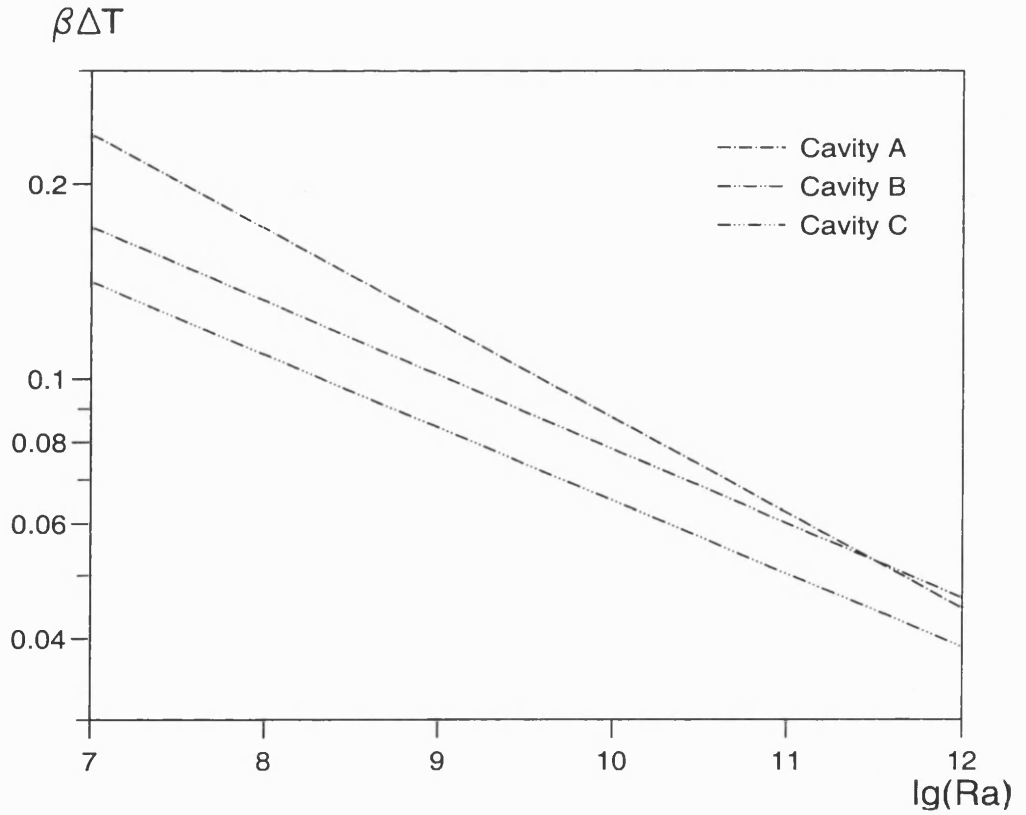

Figure 4.14.b (\beta \Delta T) against Rayleigh number on log–log axes.
For three different cavities in the experiments of Bohn *et al*(1995).
The lines are obtained using relationships given this reference.

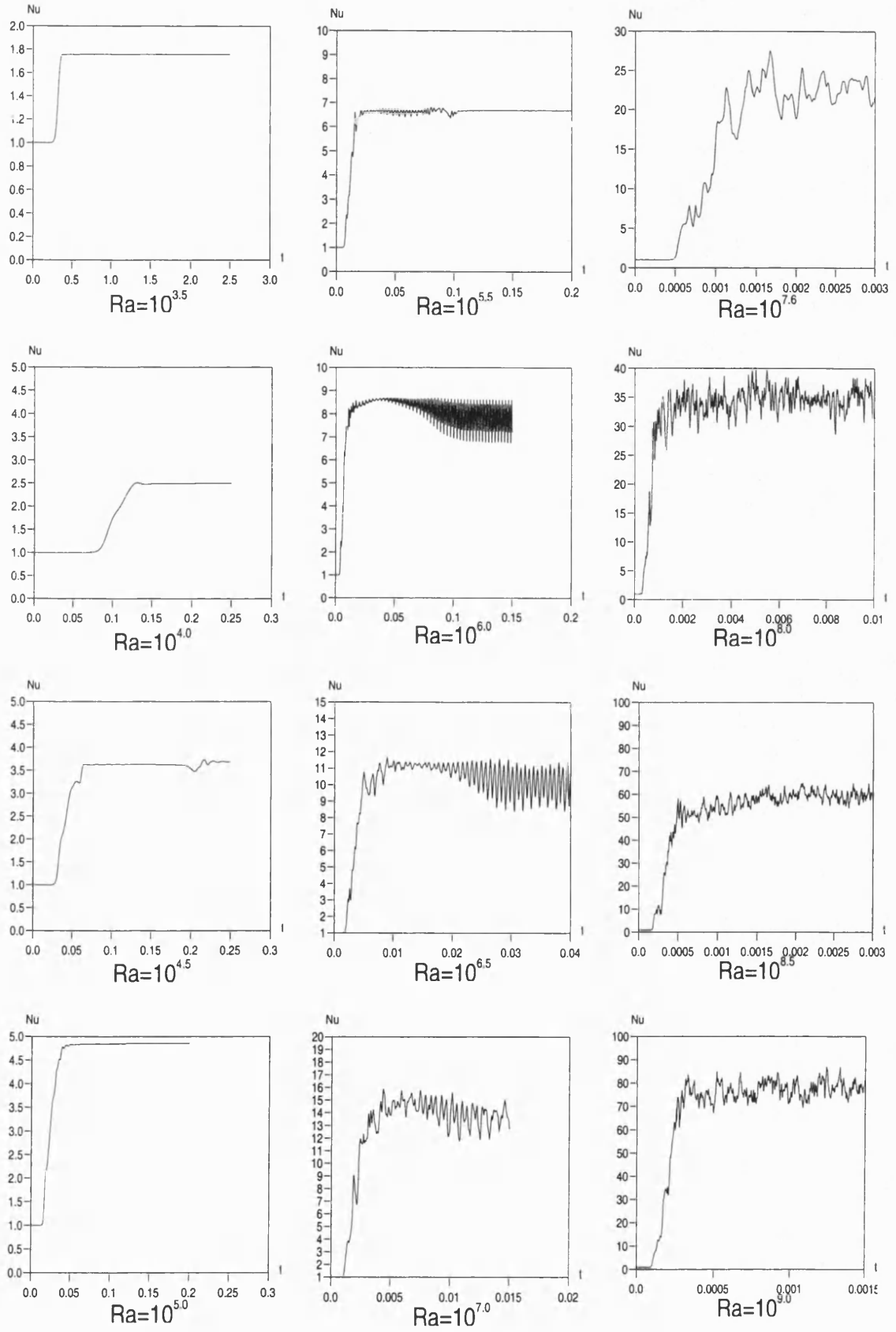

Figure 4.15 Time–developing global Nusselt number for 2D radial–tangential rotating annulus flow.

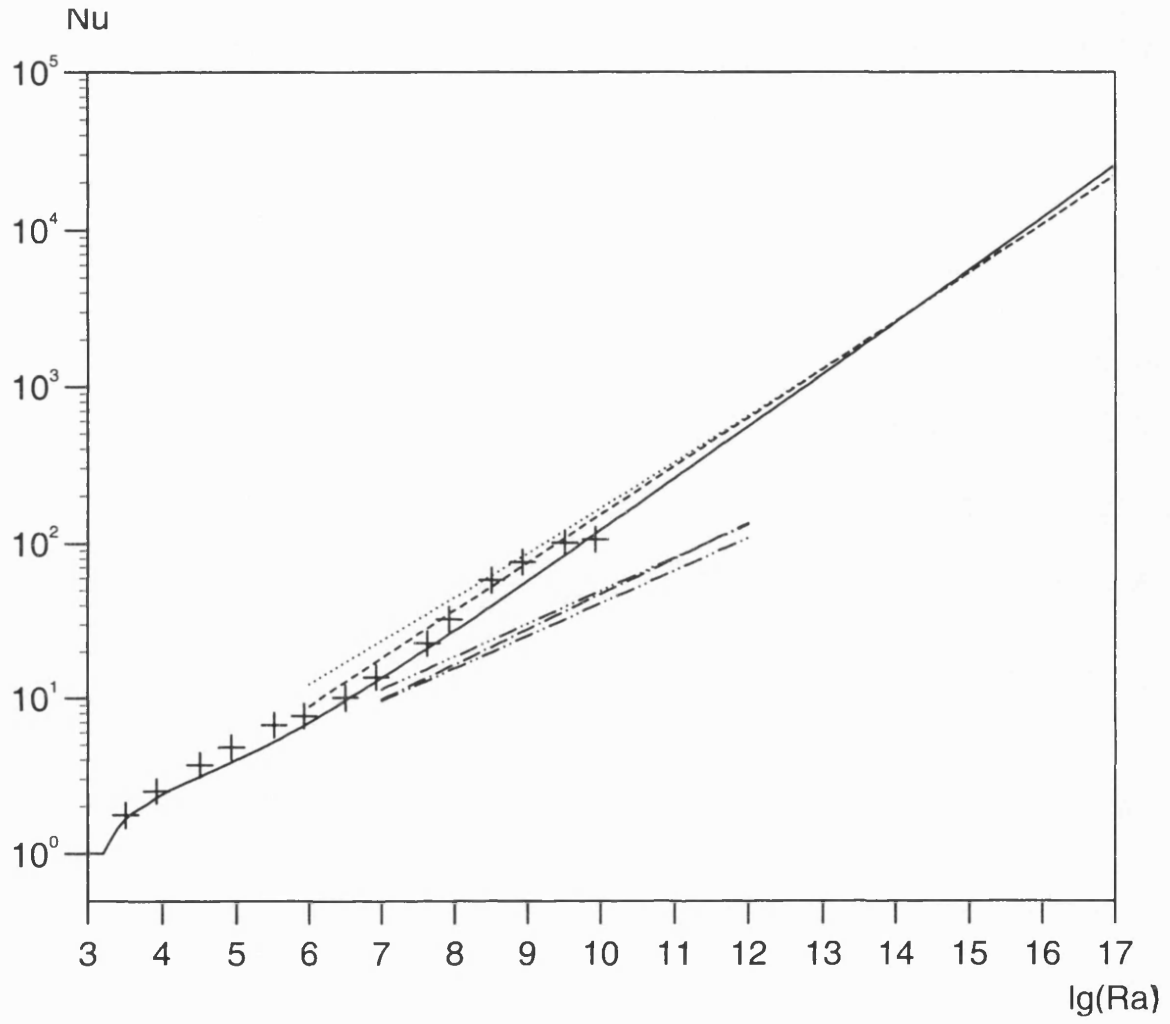

Figure 4.16 Variation of *Nu* with *Ra* for rotating annulus flow, *Pr=0.7.*

Rayleigh–Benard convection:
- ——— Semi–empirical (Hollands *et al,* 1975)
- - - - - - Experiment (Niemela *et al*, 2000)
- ---------- Theory (Grossmann & Lohse, 2000)

Rotating annulus:
- ·—·—·— Cavity A (Bohn *et al,* 1995*)*
- — ··— Cavity B (")
- — ···—Cavity C (")
- \+ Computed (2D, $r_o - r_i = 0.5$)

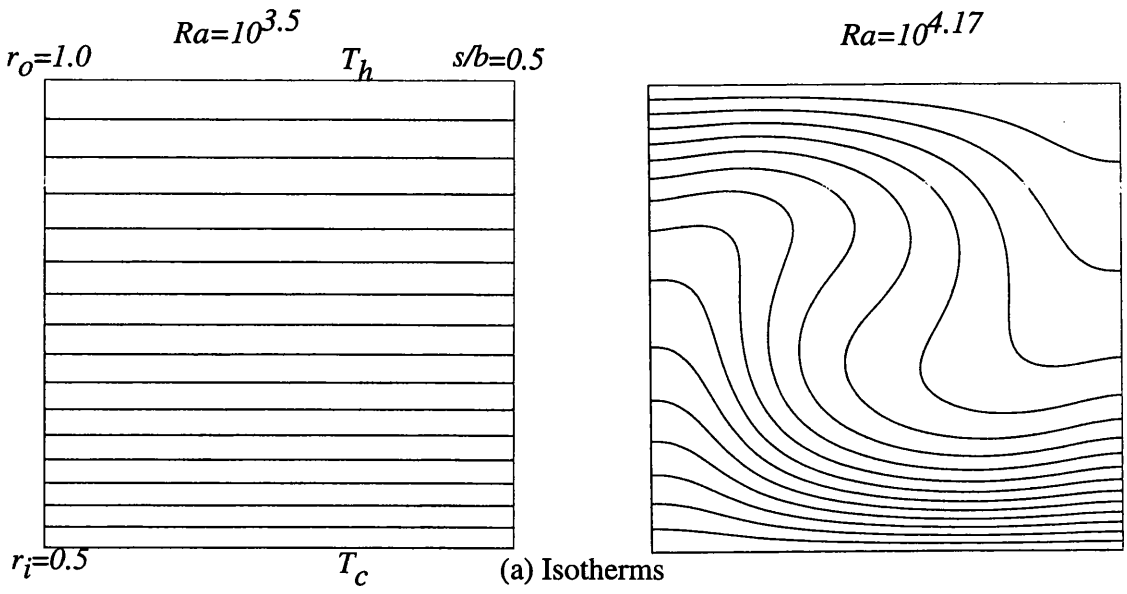

(a) Isotherms

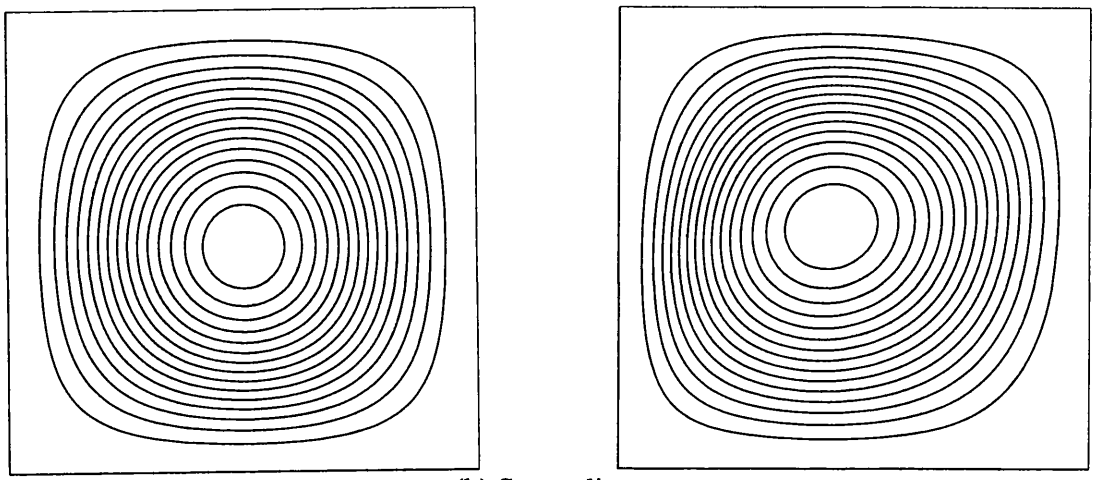

(b) Streamlines

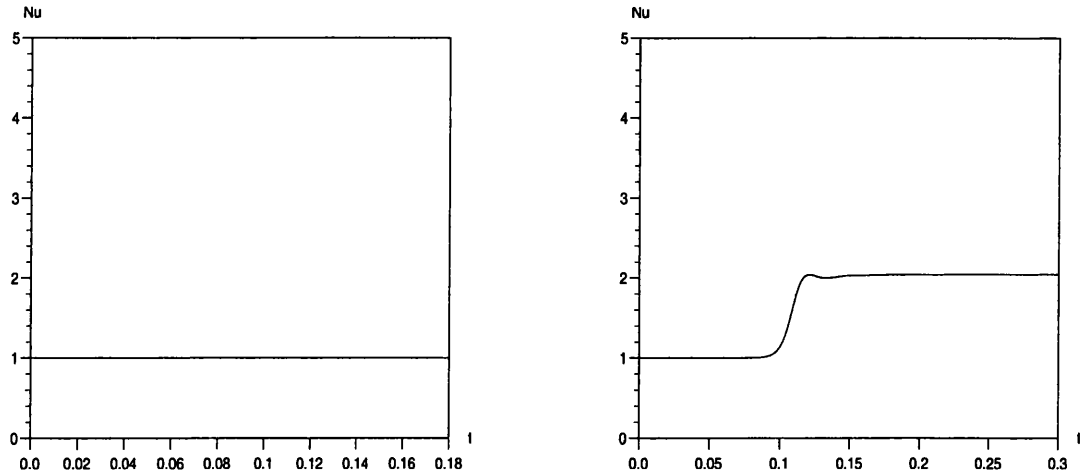

(c) Global Nusselt number variation with time

Figure 5.1 Computed solutions for non–rotating 2D radial–axial flow (approximate R–B convection) for $Ra=10^{3.5}$ and $Ra=10^{4.17}$; r_o= 1.0, r_i = 0.5, s/d=1.0.

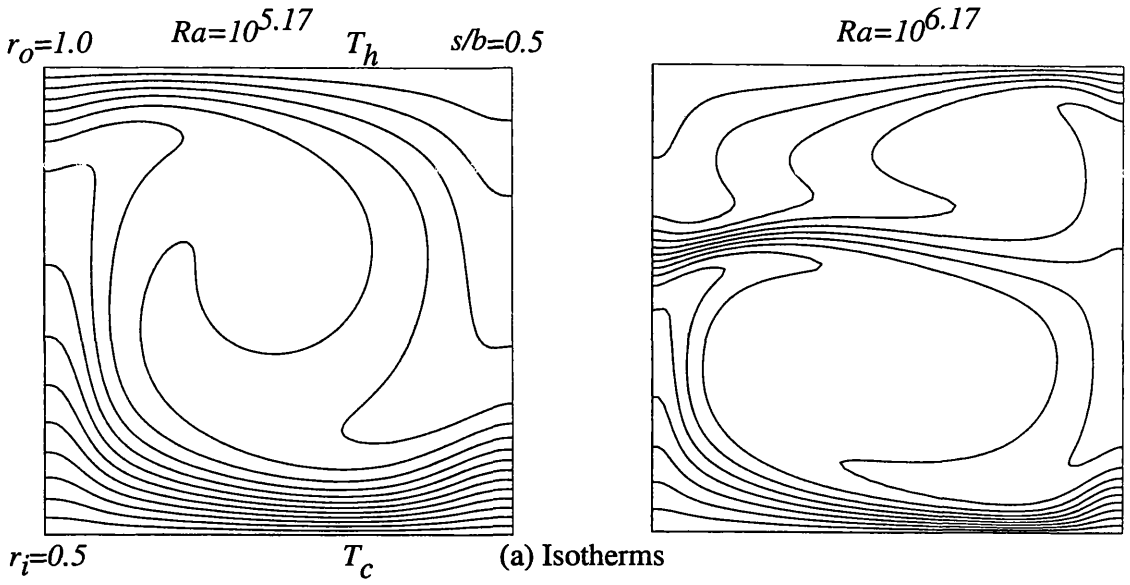

(a) Isotherms

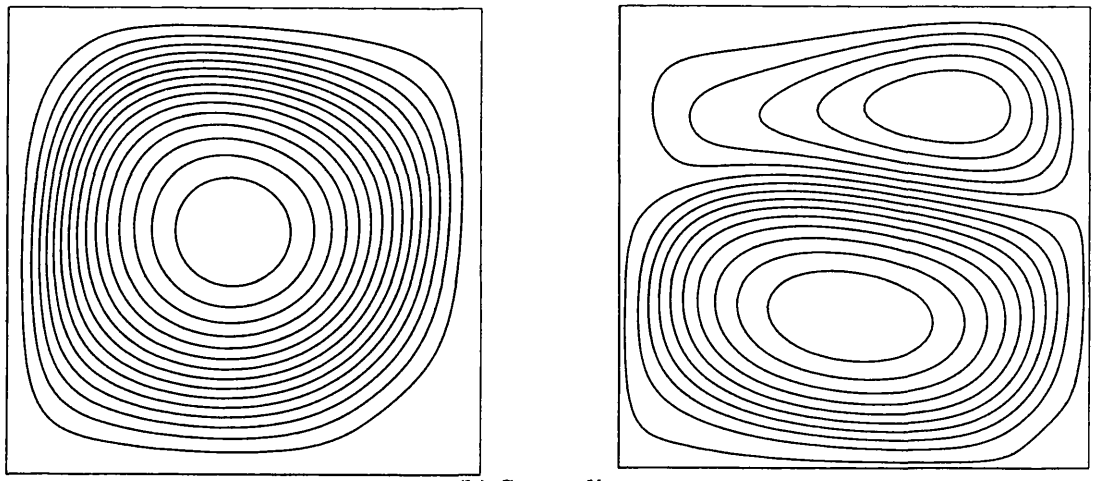

(b) Streamlines

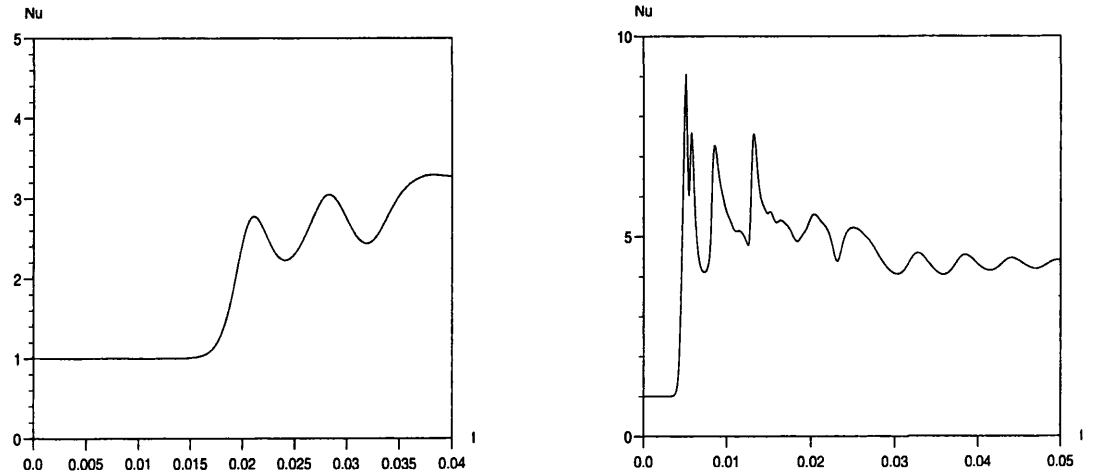

(c) Global Nusselt number variation with time

Figure 5.2 Computed Solutions for non–rotating 2D radial–axial flow (approximate R–B convection) for $Ra=10^{5.17}$ and $Ra=10^{6.17}$; r_o= 1.0, r_i = 0.5, s/d=1.0.

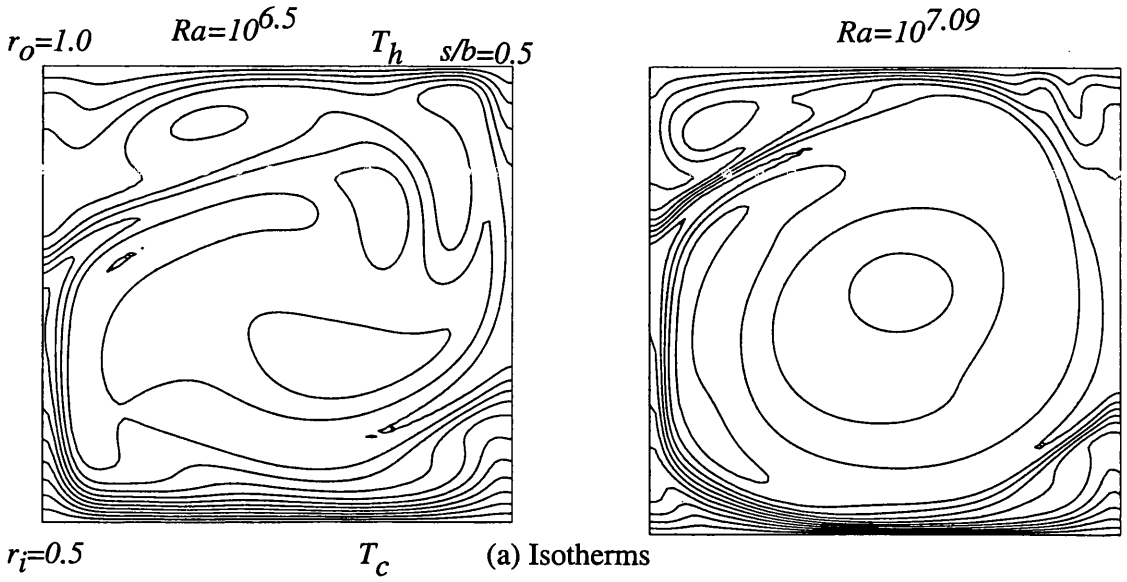

(a) Isotherms

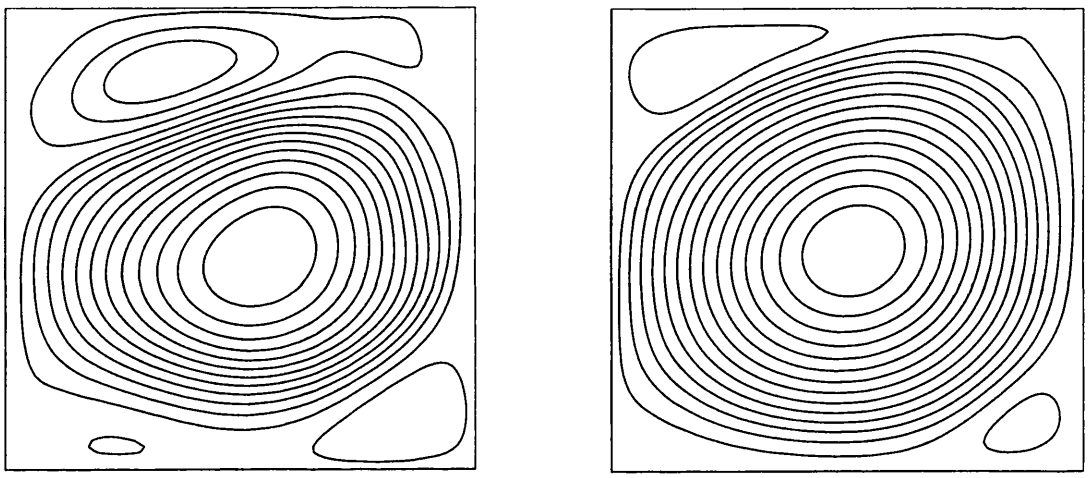

(b) Streamlines

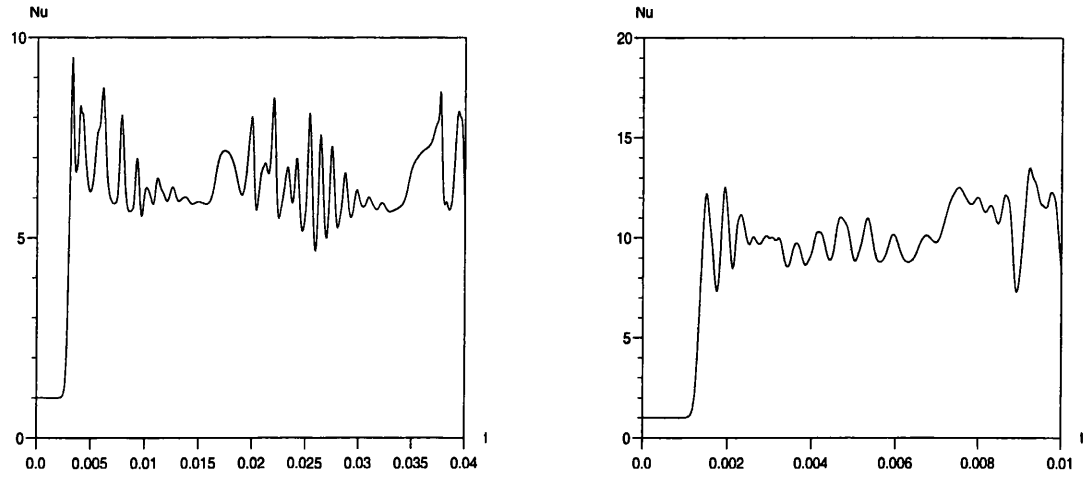

(c) Global Nusselt number variation with time

Figure 5.3 Computed solutions for non–rotating 2D radial–axial flow (approximate R–B convection) for $Ra=10^{6.5}$ and $Ra=10^{7.09}$; r_o= 1.0, r_i = 0.5, s/d=1.0.

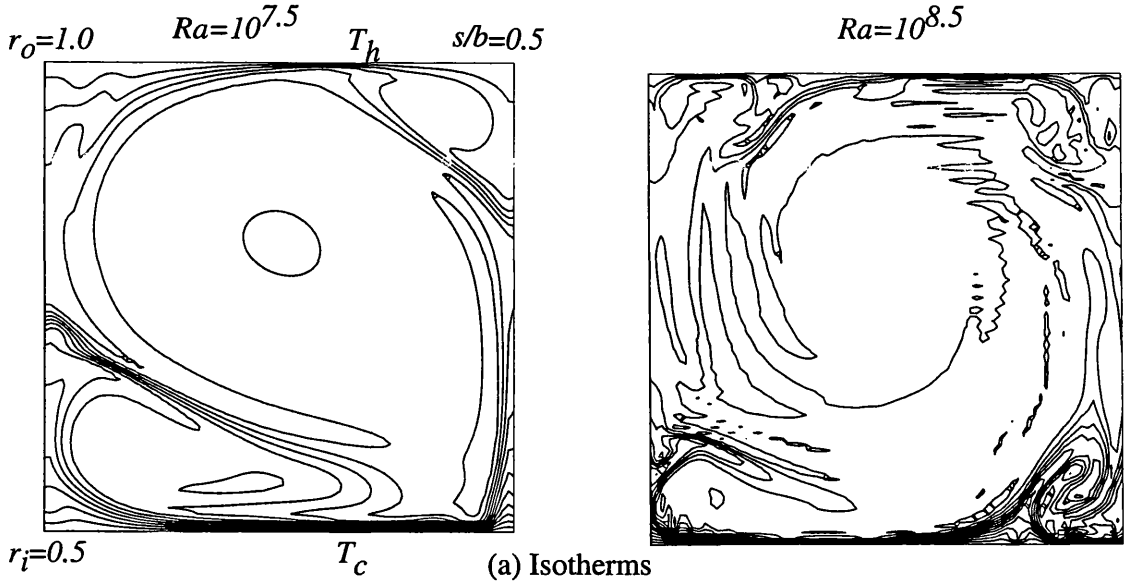

(a) Isotherms

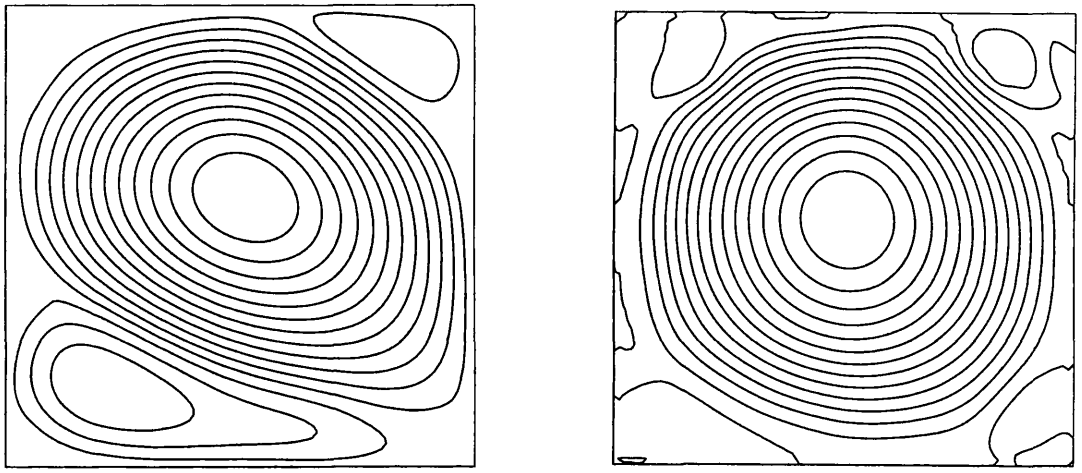

(b) Streamlines

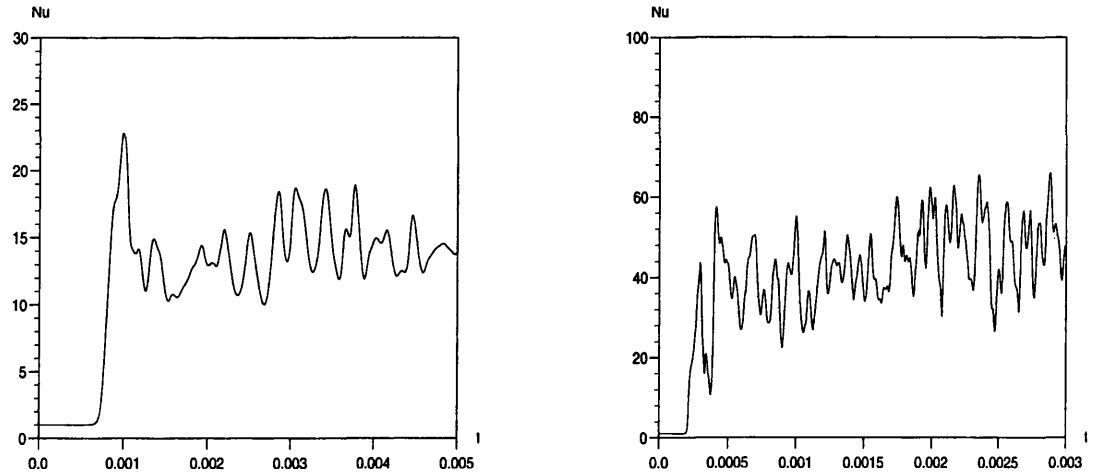

(c) Global Nusselt number variation with time

Figure 5.4 Computed solutions for non–rotating 2D radial–axial flow (approximate R–B convection) for $Ra=10^{7.5}$ and $Ra=10^{8.5}$; r_o= 1.0, r_i = 0.5, s/d=1.0.

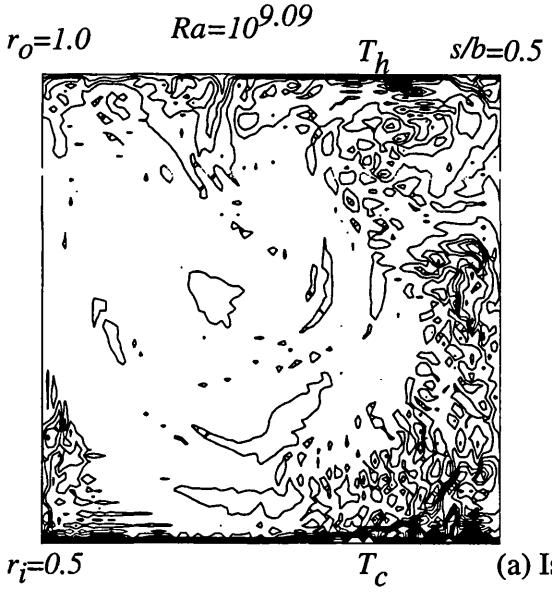

(a) Isotherms

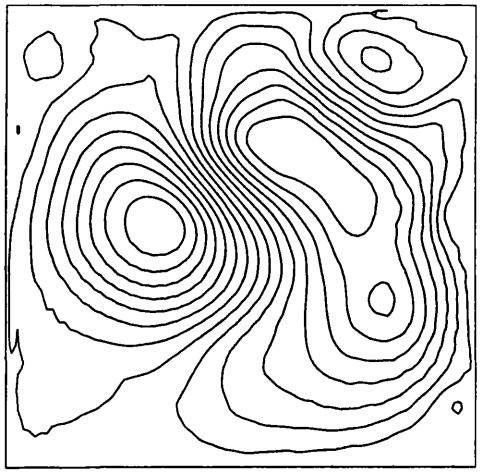

(b) Streamlines

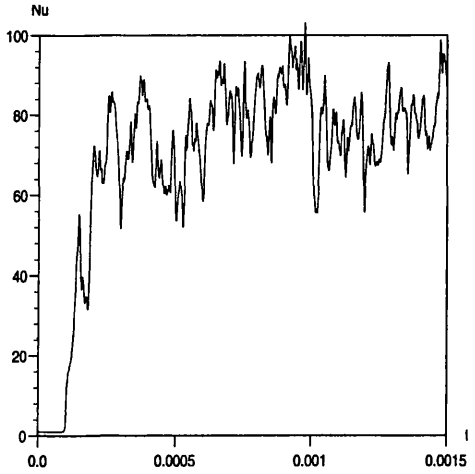

(c) Global Nusselt number variation with time

Figure 5.5 Computed solutions for non–rotating 2D radial–axial flow (approximate R–B convection) for $Ra=10^{9.09}$; r_o= 1.0, r_i = 0.5, s/d=1.0.

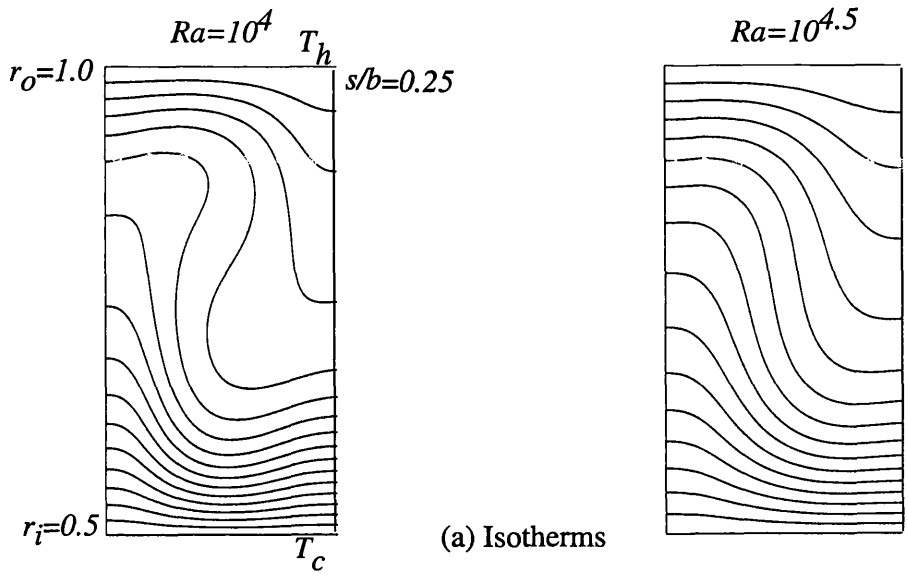

(a) Isotherms

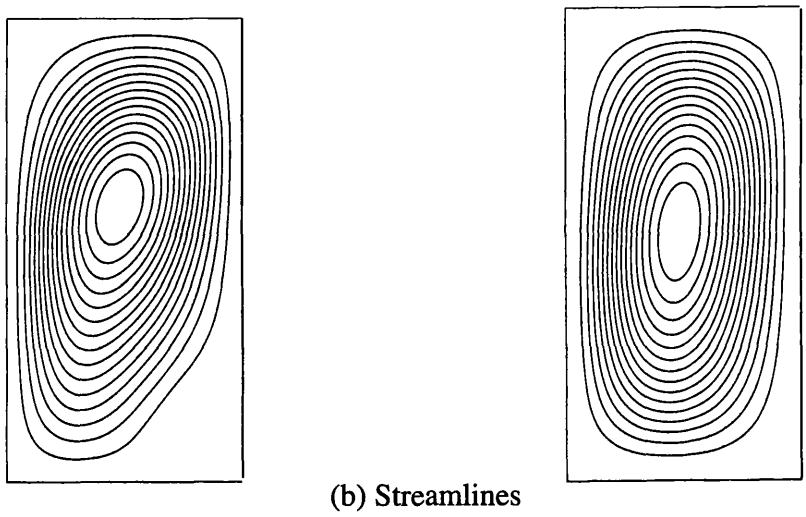

(b) Streamlines

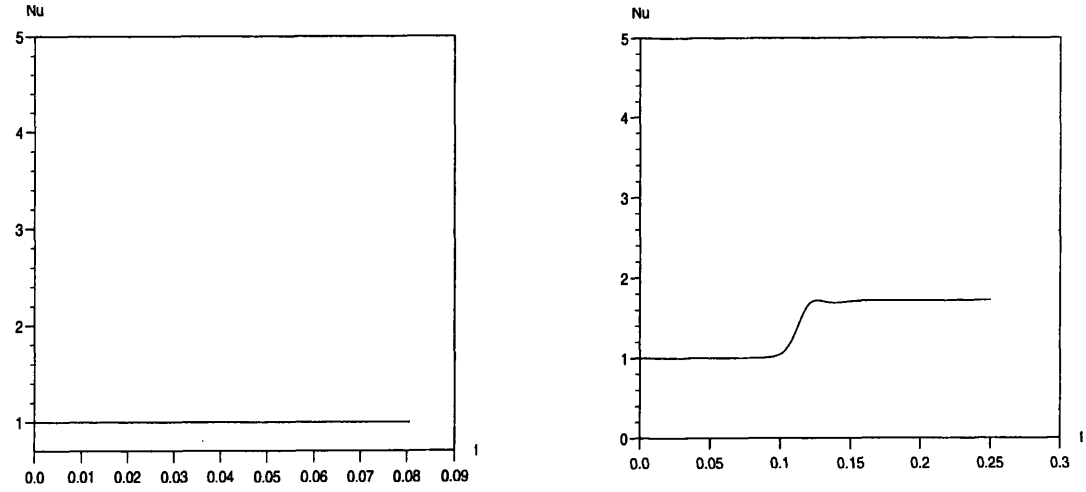

(c) Global Nusselt number variation with time

Figure 5.6 Computed solutions for non–rotating 2D radial–axial flow (approximate R–B convection) for $Ra=10^4$ and $Ra=10^{4.5}$; $r_o = 1.0$, $r_i = 0.5$, $s/d=0.5$.

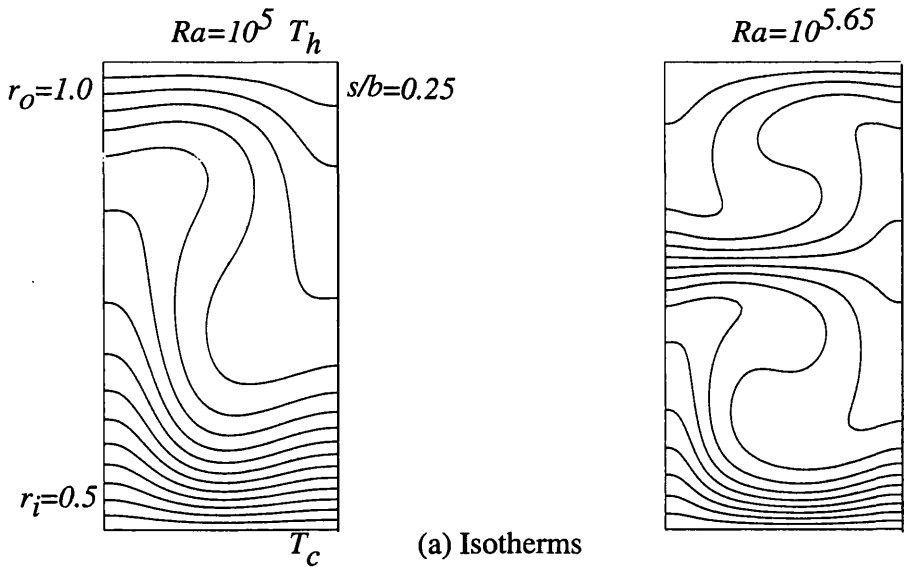

(a) Isotherms

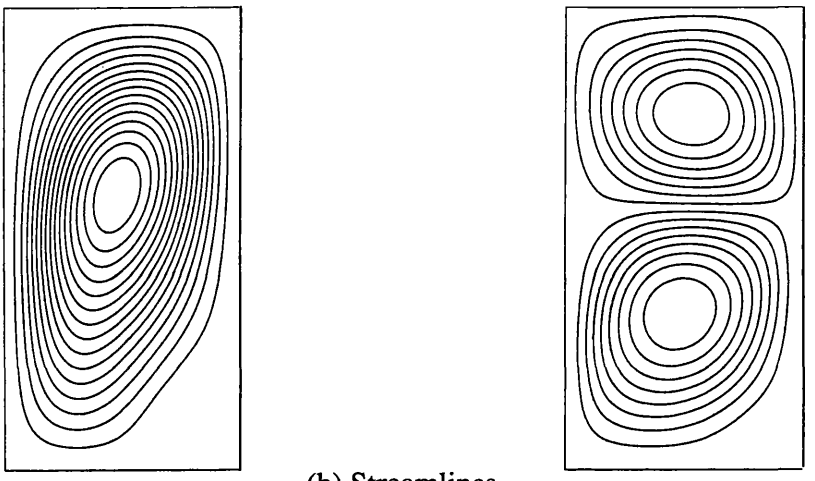

(b) Streamlines

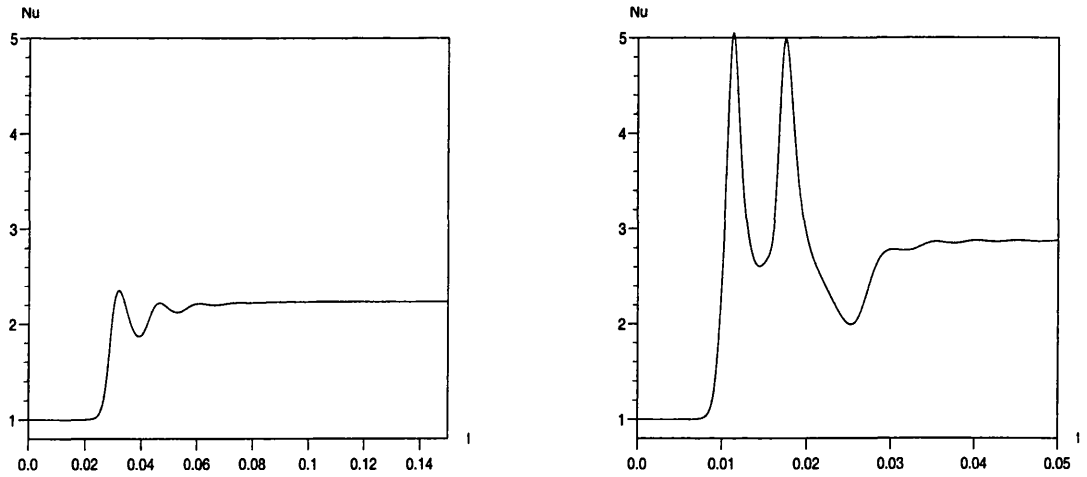

(c) Global Nusselt number variation with time

Figure 5.7 Computed solutions for non–rotating 2D radial–axial flow (approximate R–B convection) for $Ra=10^5$ and $Ra=10^{5.65}$; $r_o = 1.0$, $r_i = 0.5$, $s/d=0.5$.

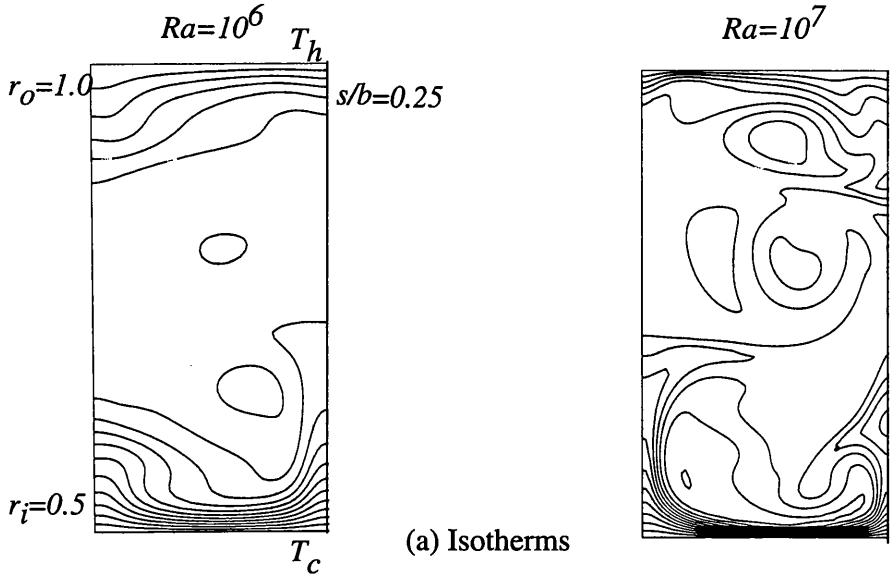

(a) Isotherms

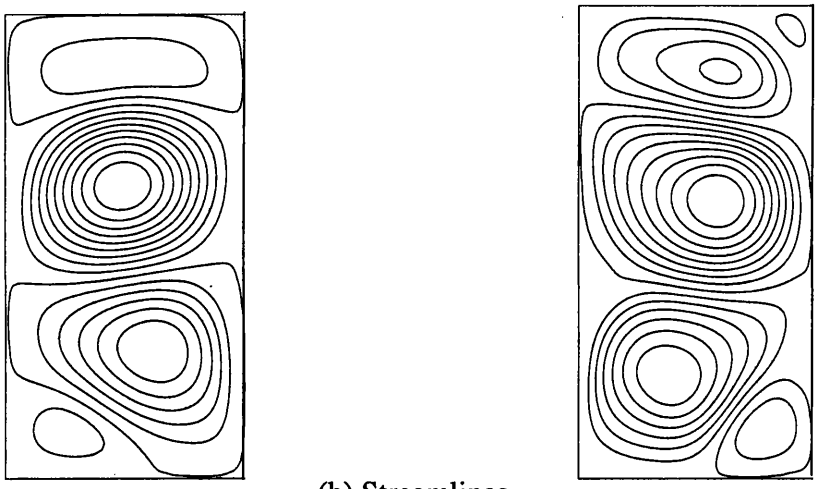

(b) Streamlines

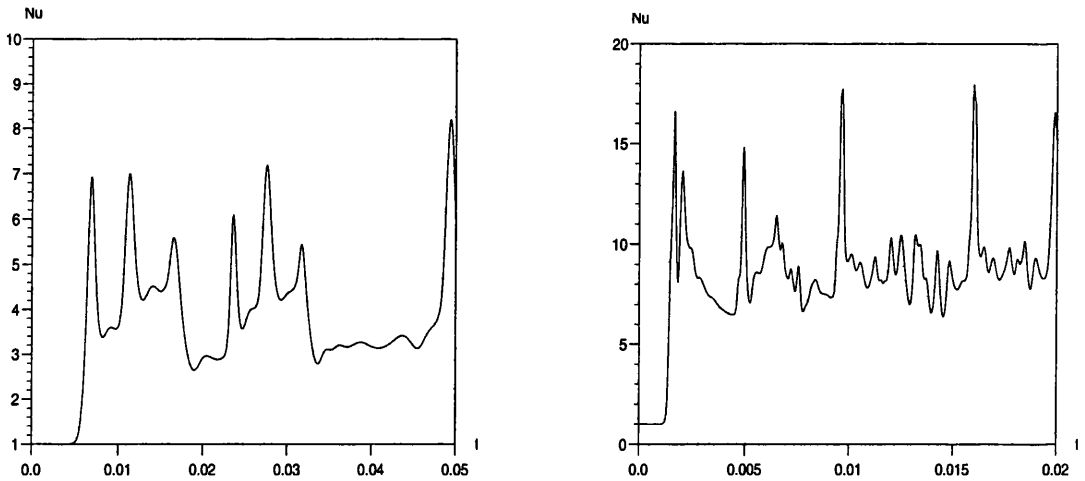

(c) Global Nusselt number variation with time

Figure 5.8 Computed solutions for non–rotating 2D radial–axial flow (approximate R–B convection) for $Ra=10^6$ and $Ra=10^7$; $r_o= 1.0$, $r_i = 0.5$, $s/d=0.5$.

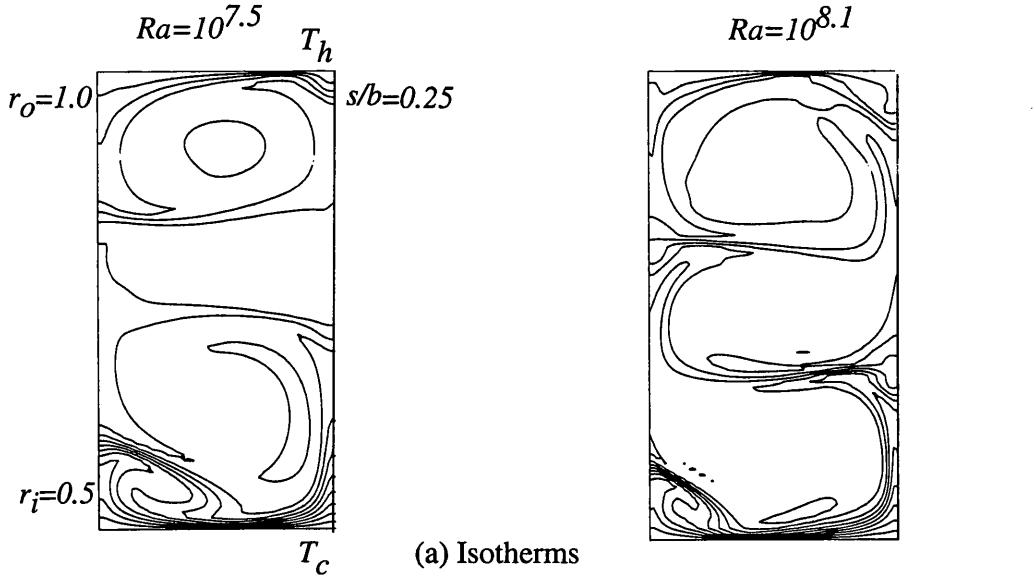

(a) Isotherms

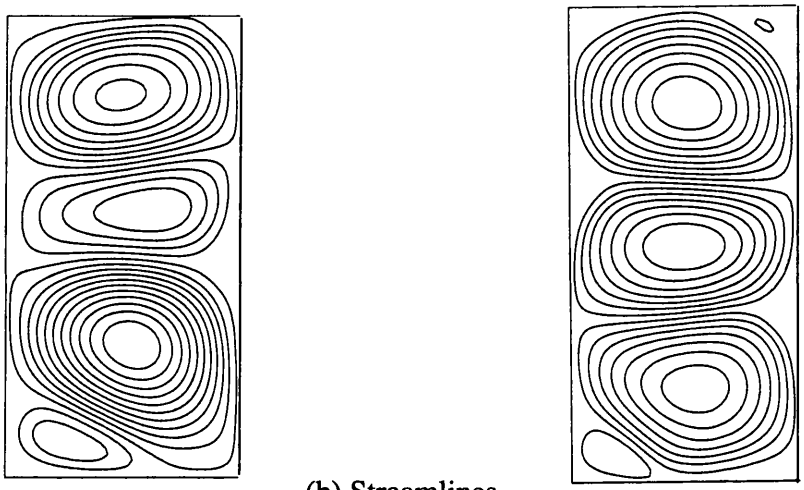

(b) Streamlines

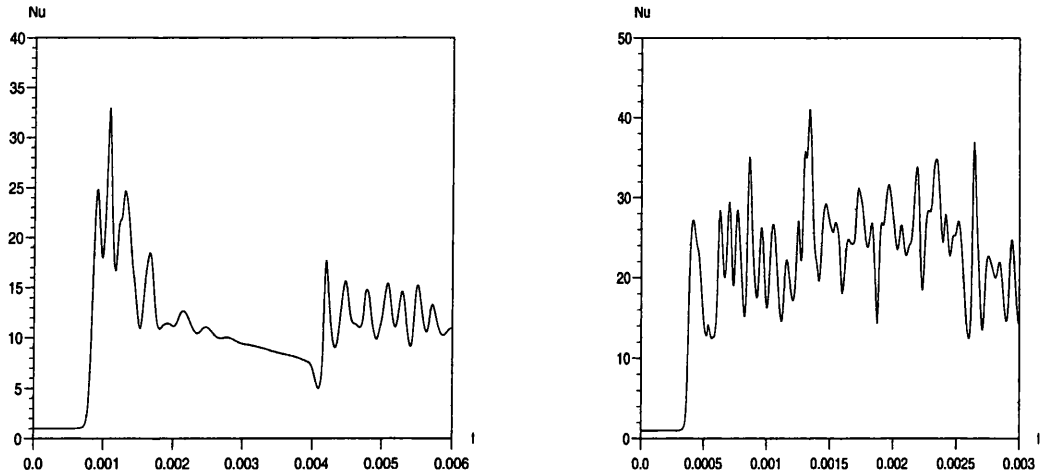

(c) Global Nusselt number variation with time

Figure 5.9 Computed solutions for non–rotating 2D radial–axial flow (approximate R–B convection) for $Ra=10^{7.5}$ and $Ra=10^{8.1}$; $r_o= 1.0$, $r_i = 0.5$, $s/d=0.5$.

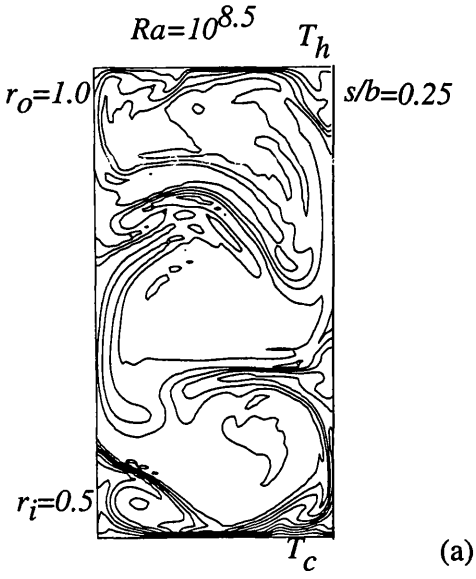

(a) Isotherms

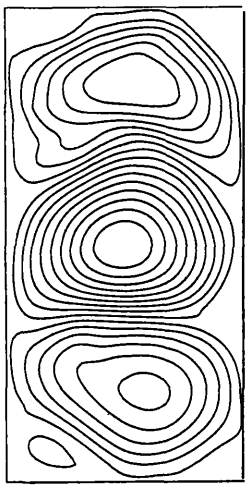

(b) Streamlines

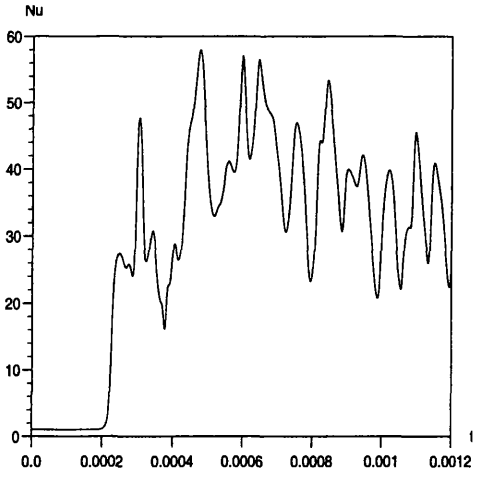

(c) Global Nusselt number variation with time

Figure 5.10 Computed solutions for non–rotating 2D radial–axial flow (approximate R–B convection) for $Ra=10^{8.5}$; $r_o= 1.0$, $r_i = 0.5$, $s/d=0.5$.

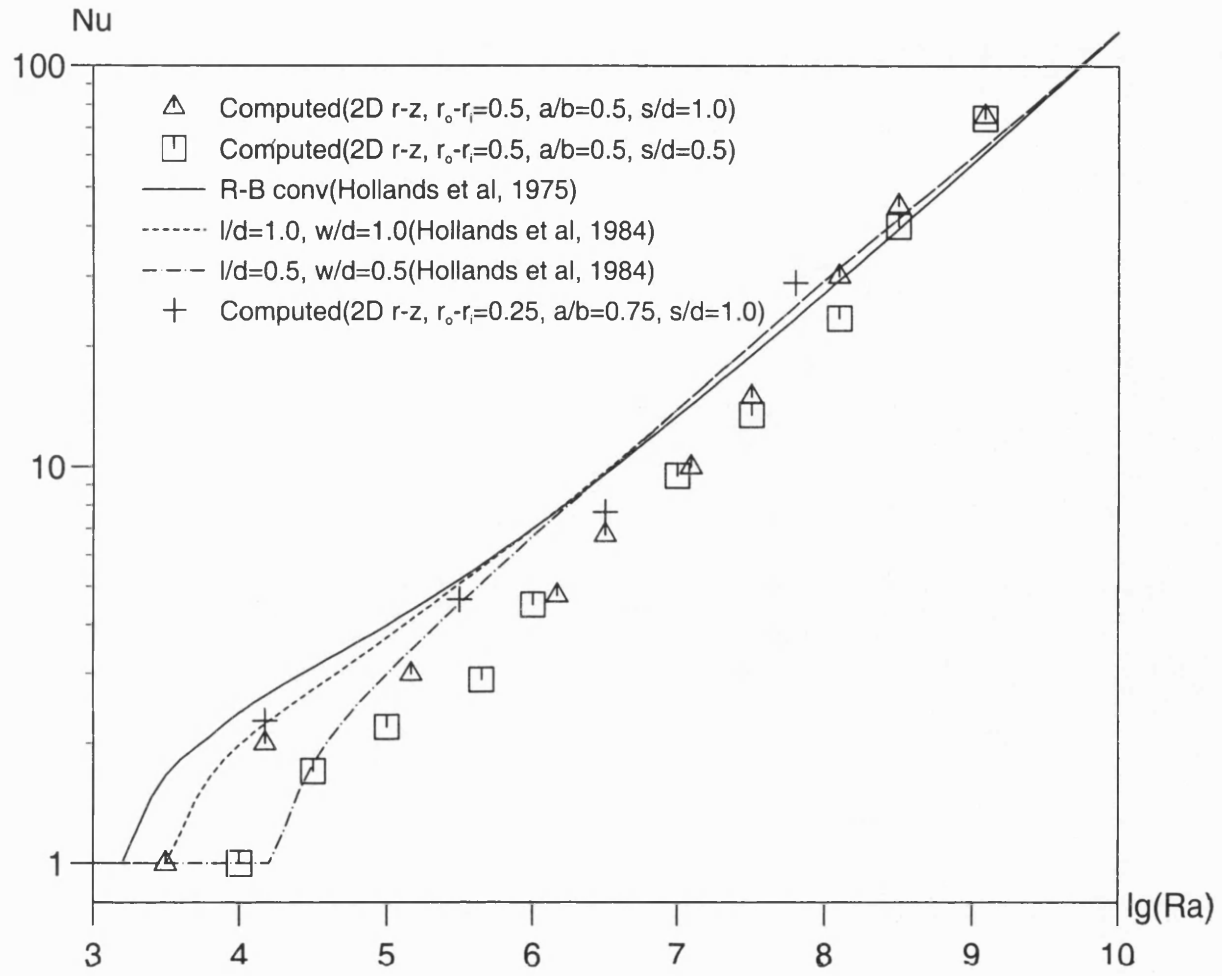

Figure 5.11 Variation of *Nu* with *Ra*. 2D (radial–axial) computed results for two aspect ratios. Comparisons with correlations for an extensive cavity, and two non–extensive cavities whose aspect ratios correspond to the computed cavities.

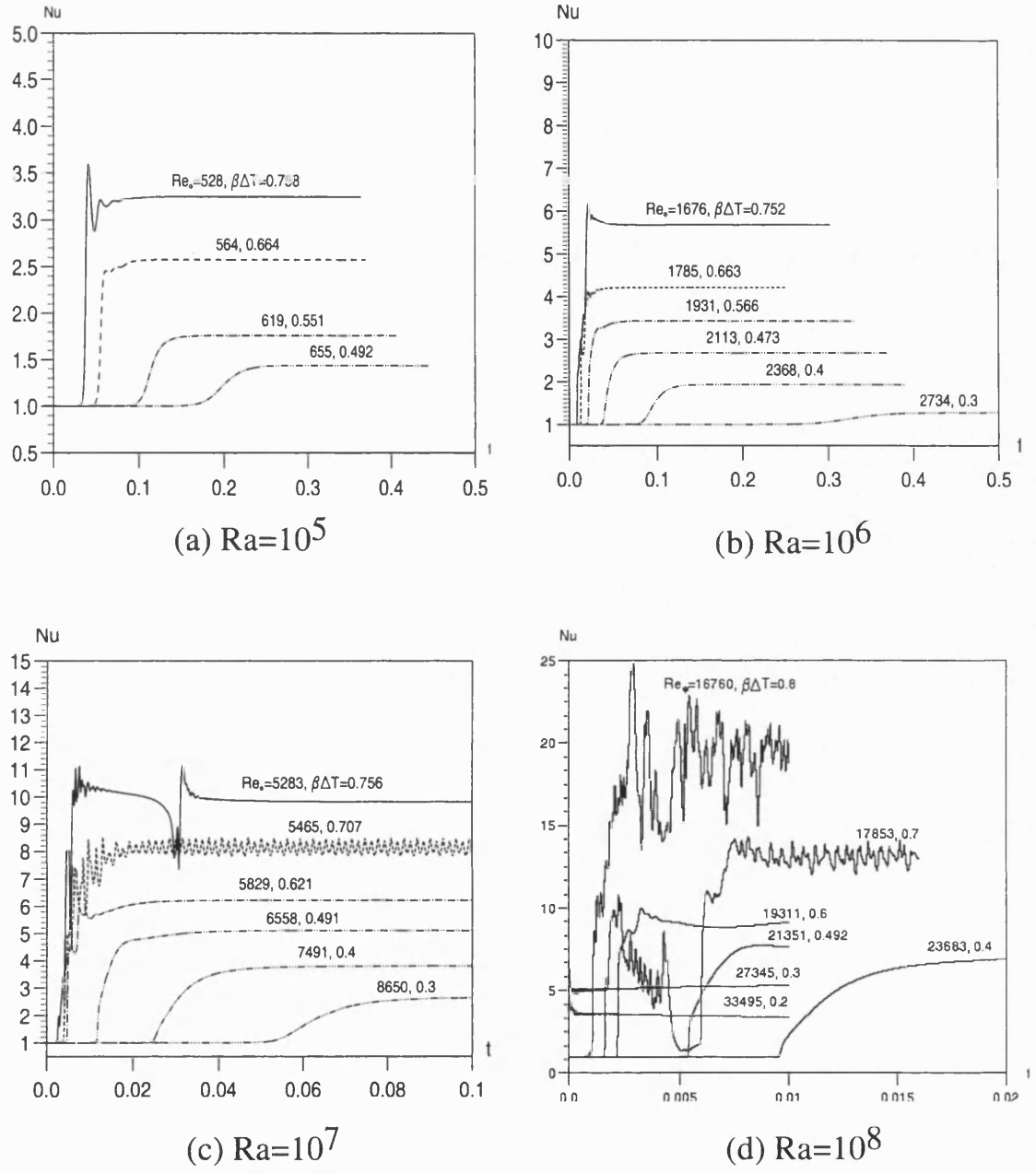

Figure 5.12 Global Nusselt number variations with time for four different Rayleigh numbers. 2D radial–axial computations for rotating annulus of $r_O=1$; $r_i=0.5$; $s/b=0.5$; $s/d=1.0$. Rotational Rayleigh number and Reynolds number are related in: $Ra_\phi = Re_\phi^2 Pr\, d/r_m \beta \Delta T$.

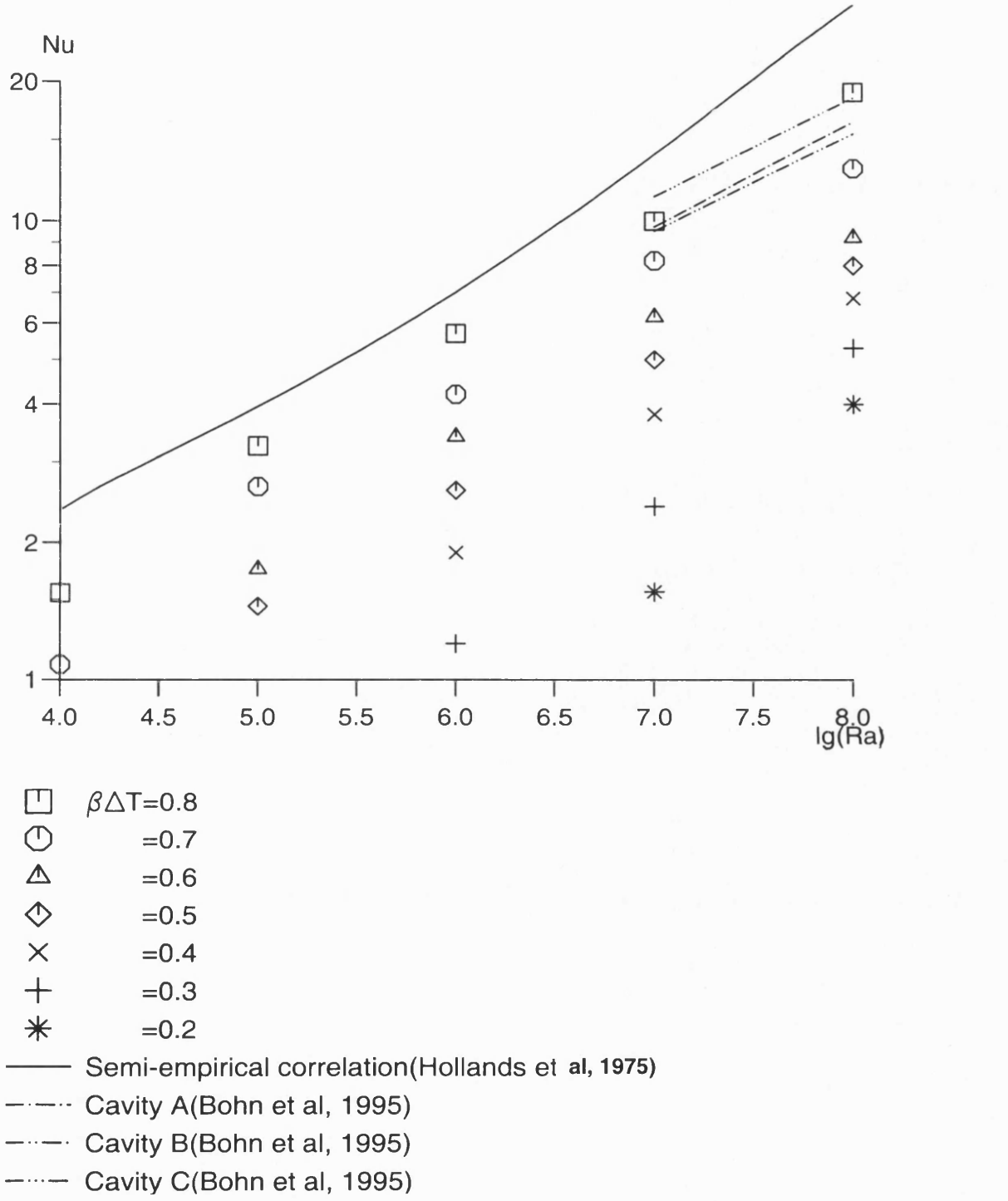

Figure 5.13 Variations of *Nu* with *Ra* for rotating annulus flows. Time–averaged values of global Nusselt numbers on *lg*(*Nu*) vs. *lg*(*Ra*) plane. C.f. Figure 5.12.

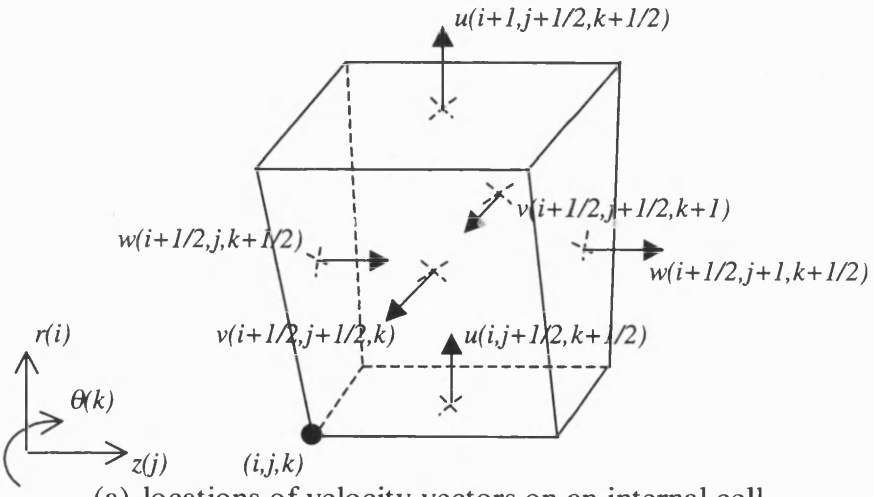

(a) locations of velocity vectors on an internal cell

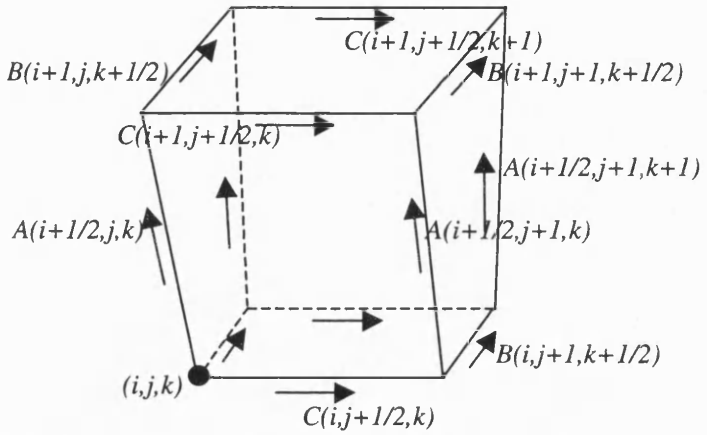

(b) locations of vorticity vectors on an internal cell

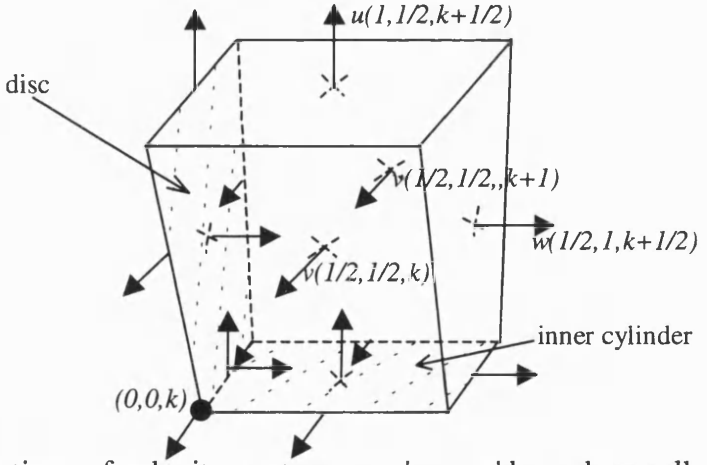

(c) locations of velocity vectors on a 'corner' boundary cell

Figure 6.1 Three dimensional staggered grid. In the figures, the velocity and vorticity vectors and temperature on the same computational cell are displayed separately. Also displayed are locations of the vectors and temperature on a boundary cell. Some vectors are not labelled due to lack of space. (*Cont'd.*)

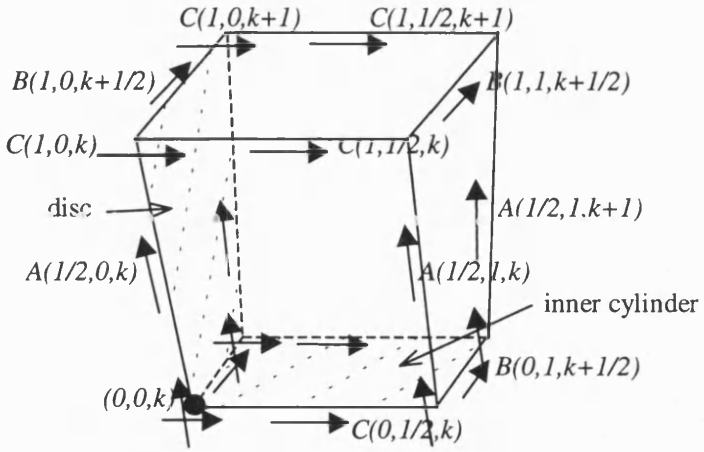

(d) locations of vorticity vectors on a 'corner' boundary cell

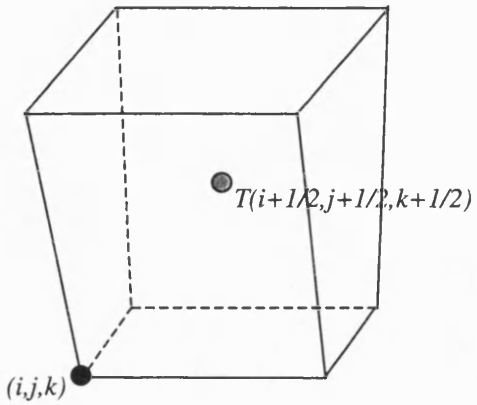

(e) location of temperature at the centre of an internal cell

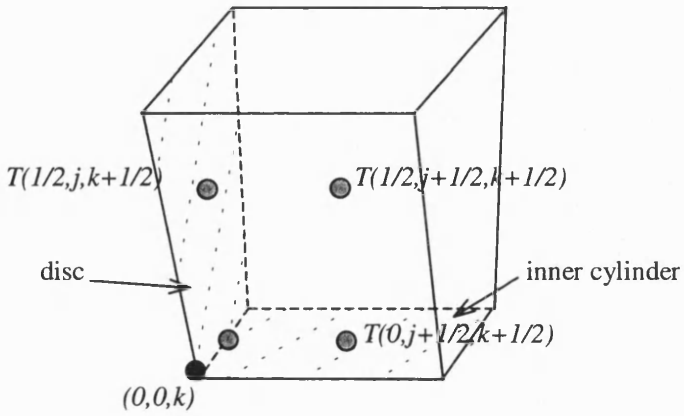

(f) locations of temperature on a 'corner' boundary cell

Figure 6.1 (continued from previous page)

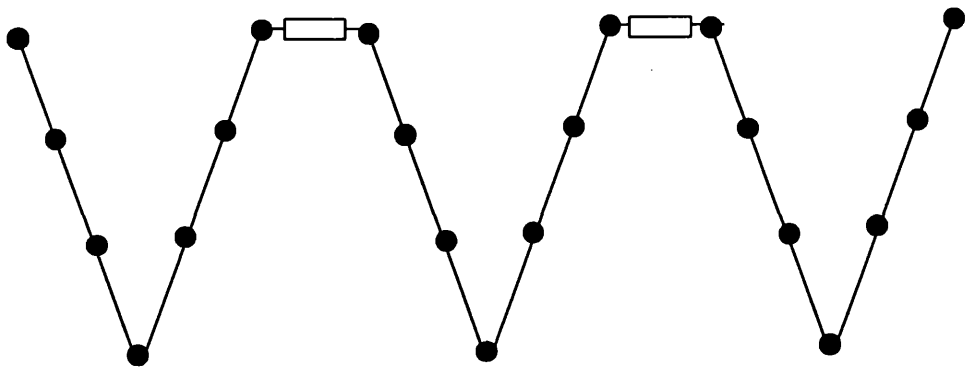

Figure 6.2 Recombination of V-cycle multigrid iterants

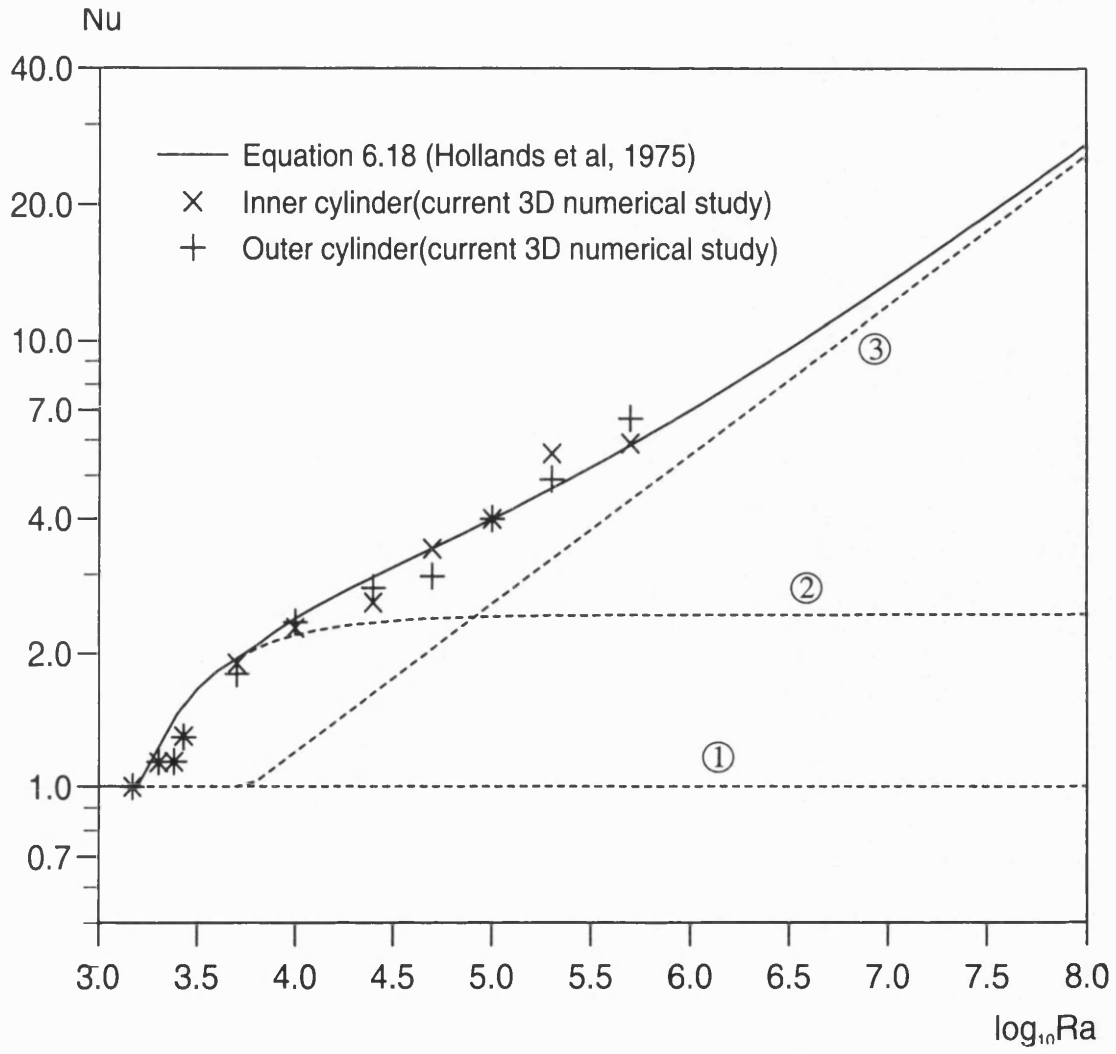

Figure 6.3 Comparison between computed *Nu* for 3D non–rotating annulus and published correlations for Rayleigh–Benard convection, *Pr=0.7*.

- - - - Individual terms in Equation 6.18
① conduction
② (steady convection) +1
③ (unsteady convection) + 1

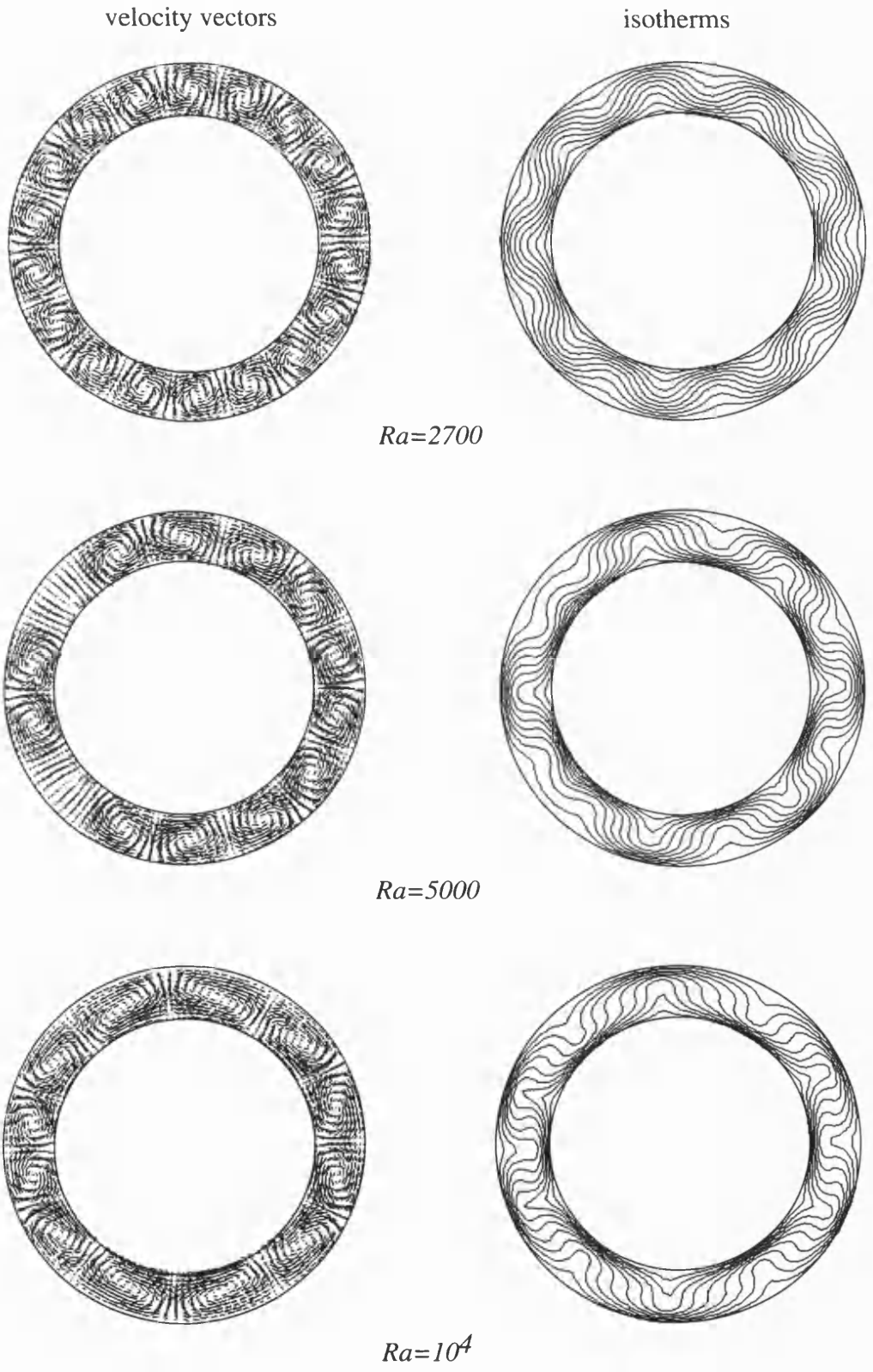

Figure 6.4 Solutions for 3D non–rotating annulus flow (approx. R–B conv) at the mid–axial plane ($s/b=0.25$). The annulus has dimensions of $r_o=1.0$, $r_i=0.7$, and $z_{max}=0.5$.

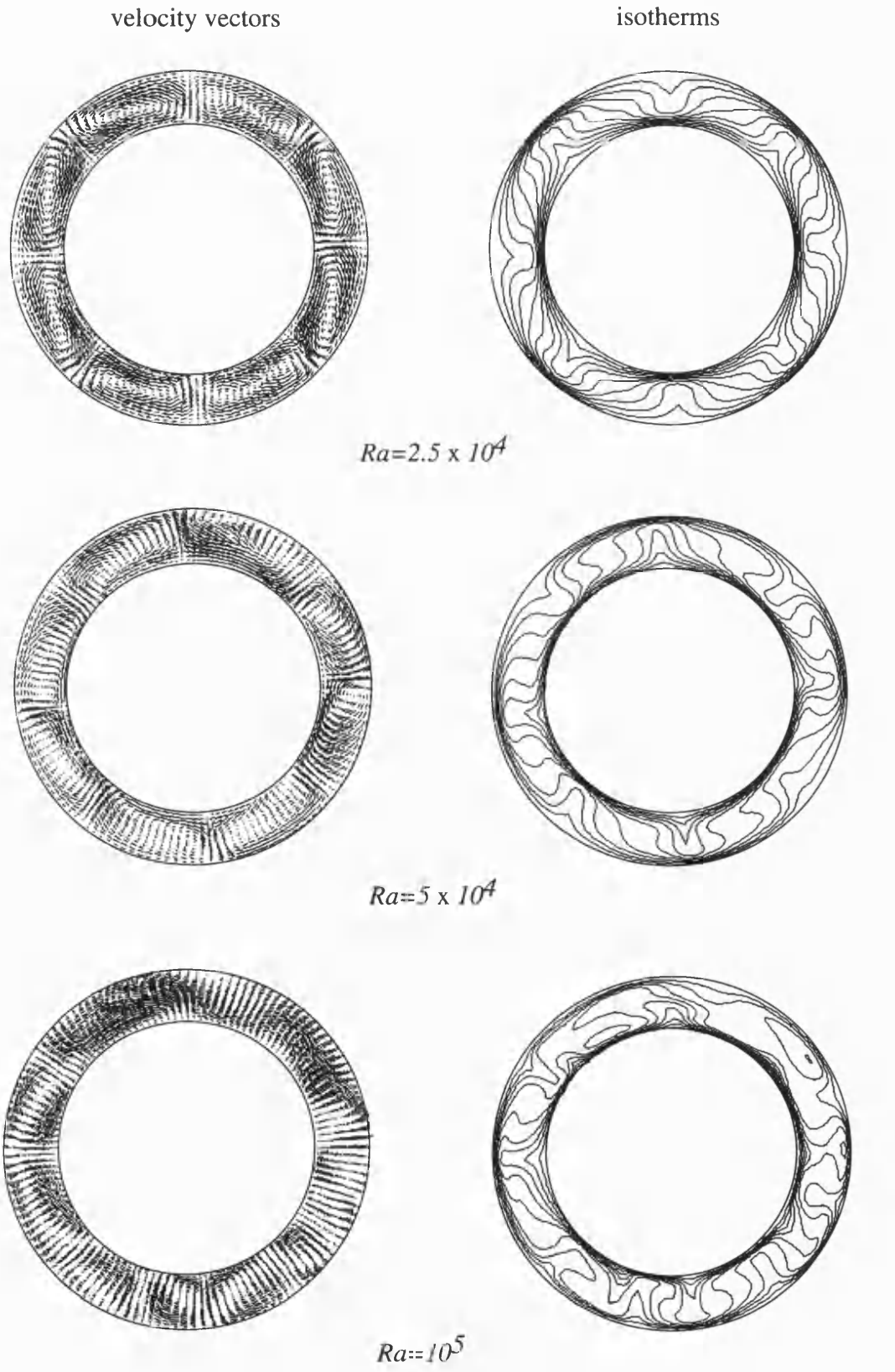

Figure 6.5 Solutions for 3D non–rotating annulus flow (approx. R–B conv) at the mid–axial plane (*s/b=0.25*). The annulus has dimensions of r_o*=1.0*; r_i*=0.7*; *s/b=0.5*.

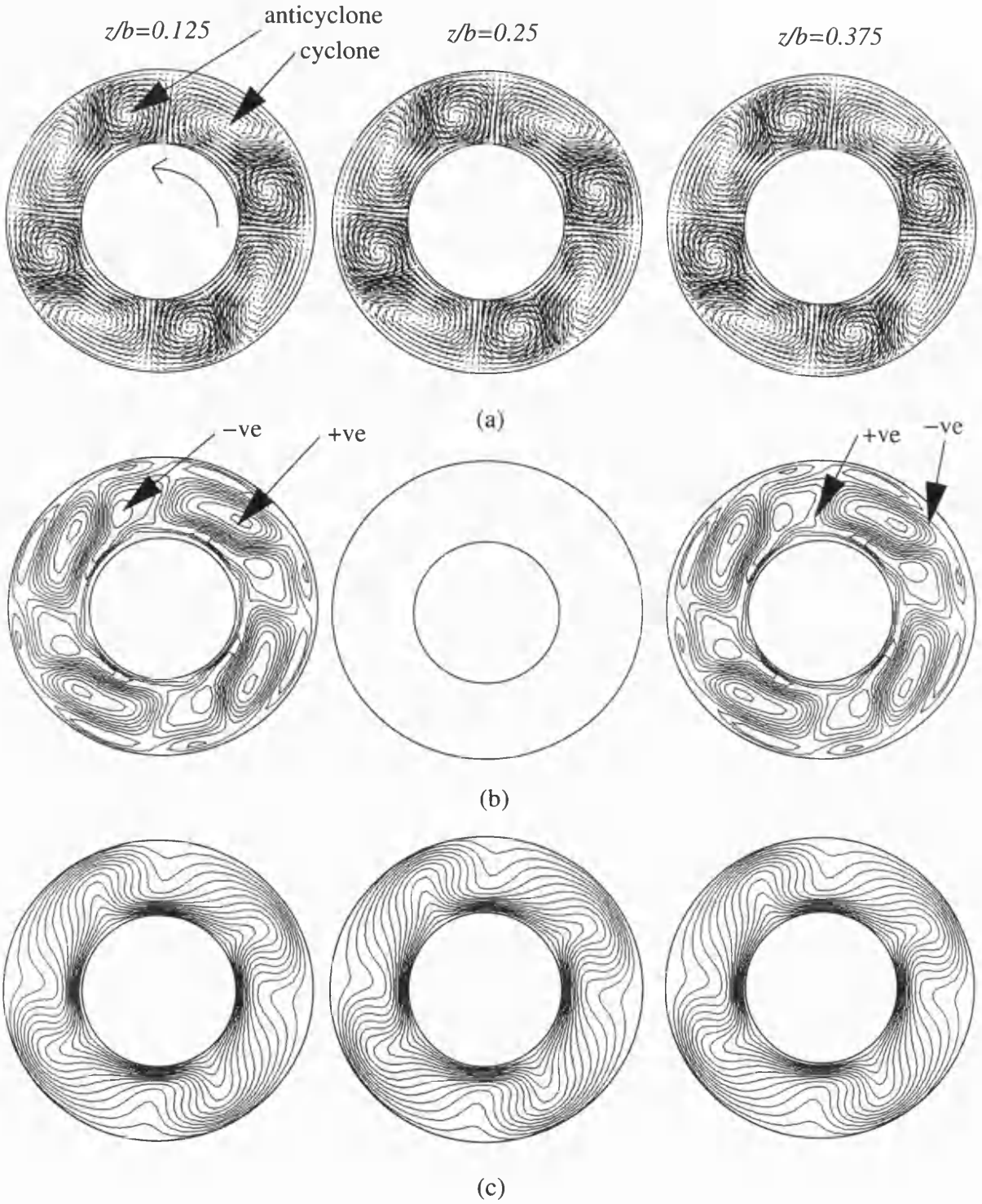

Figure 6.6 Solutions for 3D rotating annulus flow. $Ra_{\phi}=10^{3.9}$, $Re_{\phi}=218$. The annulus has dimensions of $r_O=1.0$, $r_i=0.5$, and $z_{max}=0.5$.

(a) velocity vectors
(b) axial velocity isolines
(c) isotherms

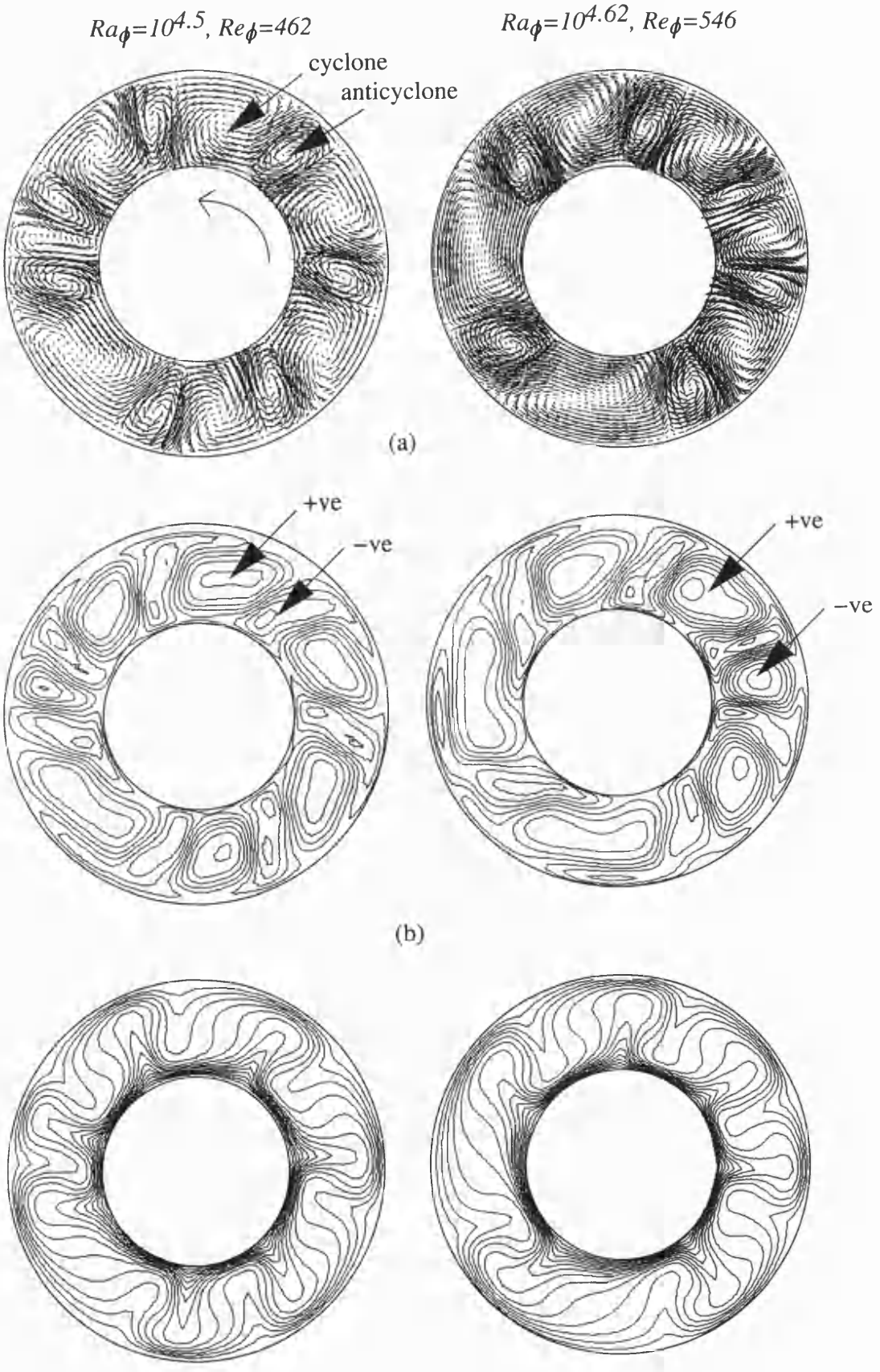

Figure 6.7 Solutions for 3D rotating annulus flow on the $z/b=0.125$ plane. The annulus had dimensions of $r_o=1.0$, $r_i=0.5$, and $z_{max}=0.5$.

(a) velocity vectors
(b) axial velocity isolines
(c) isotherms

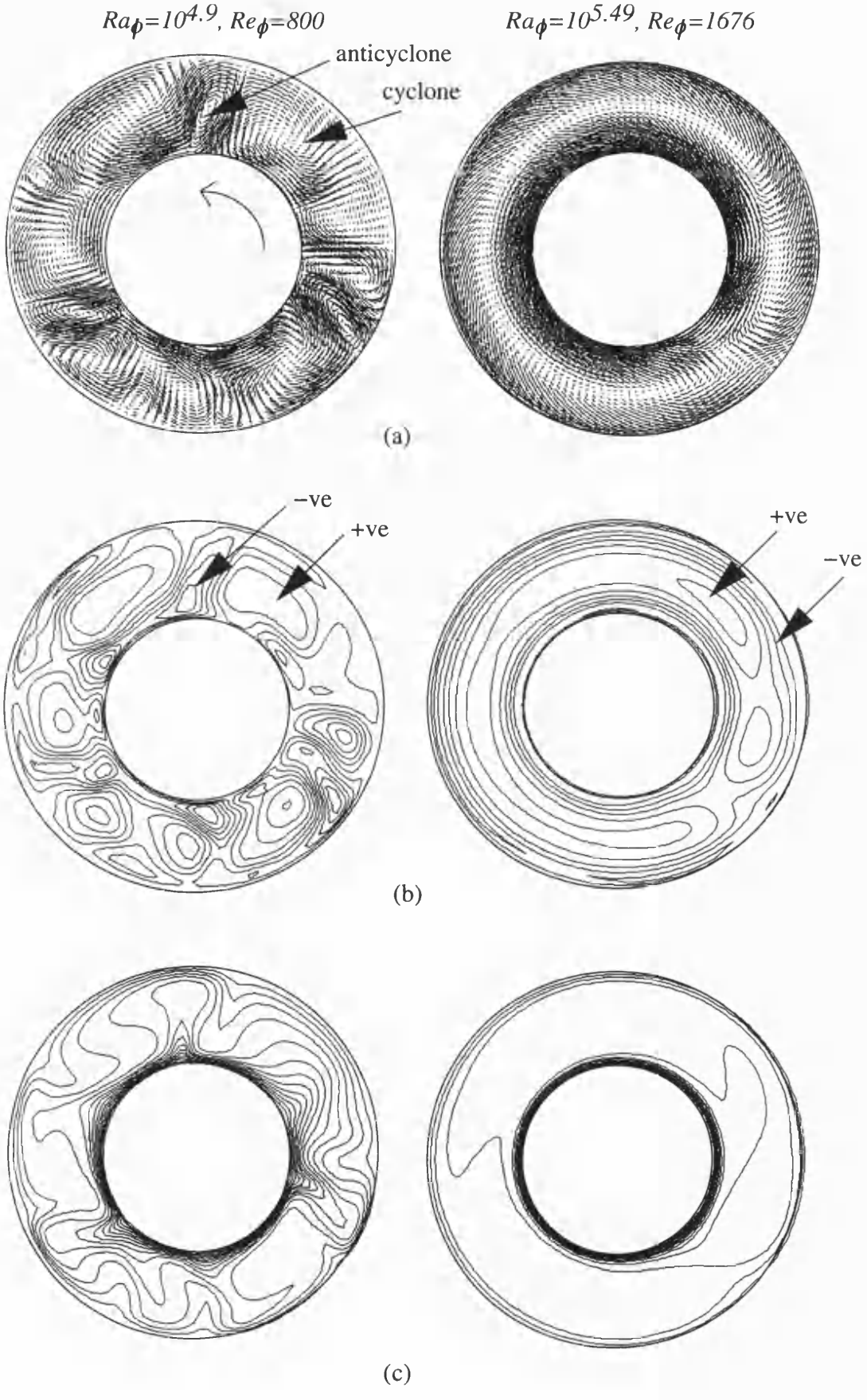

Figure 6.8 Solutions for 3D rotating annulus flow on the $z/b=0.125$ plane. The annulus had dimensions of $r_o=1.0$, $r_i=0.5$, and $z_{max}=0.5$.

(a) velocity vectors
(b) axial velocity isolines
(c) isotherms

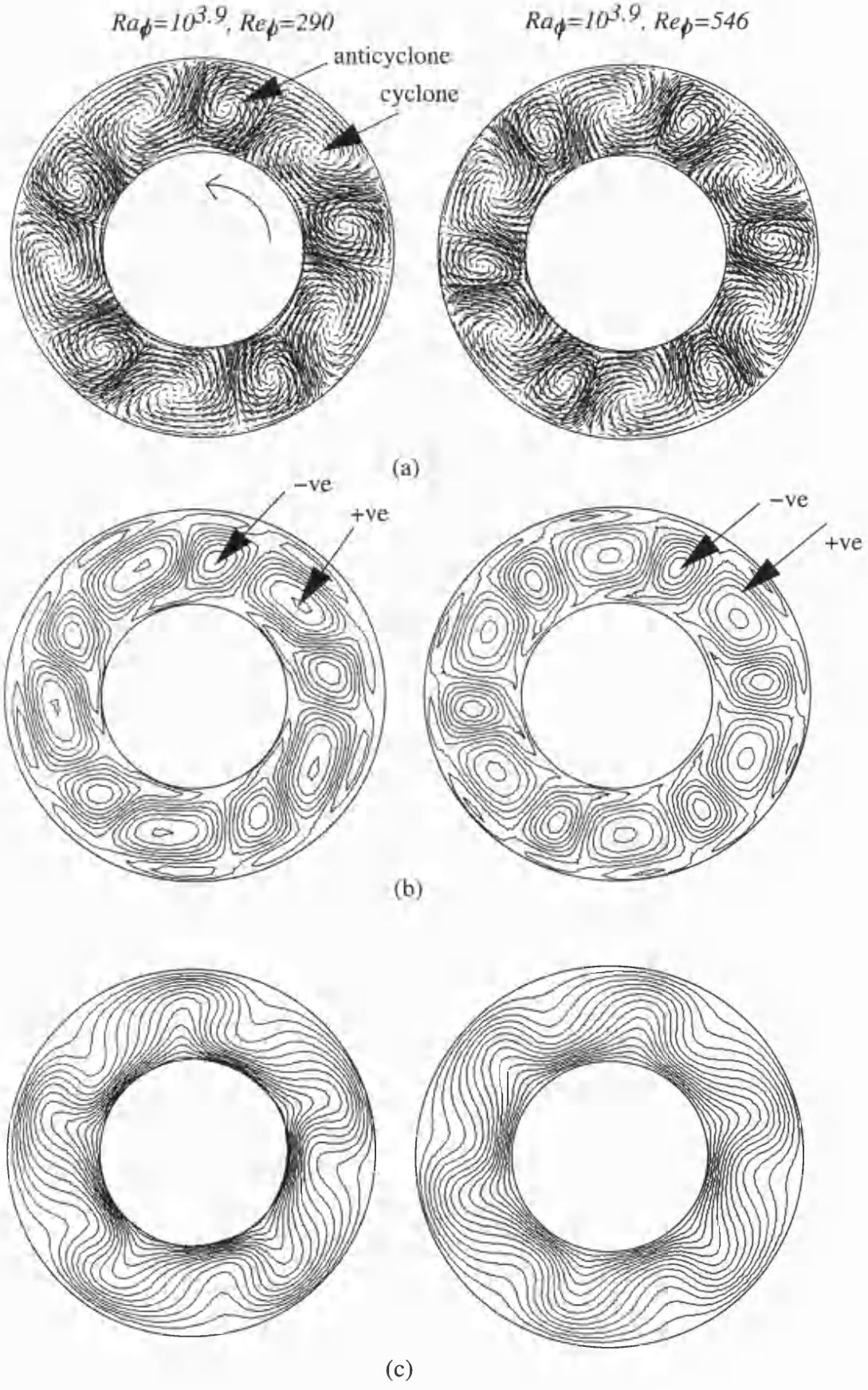

Figure 6.9 Solutions for 3D rotating annulus flow on the $z/b=0.125$ plane. The annulus had dimensions of $r_o=1.0$, $r_i=0.5$, and $z_{max}=0.5$.

(a) velocity vectors
(b) axial velocity isolines
(c) isotherms

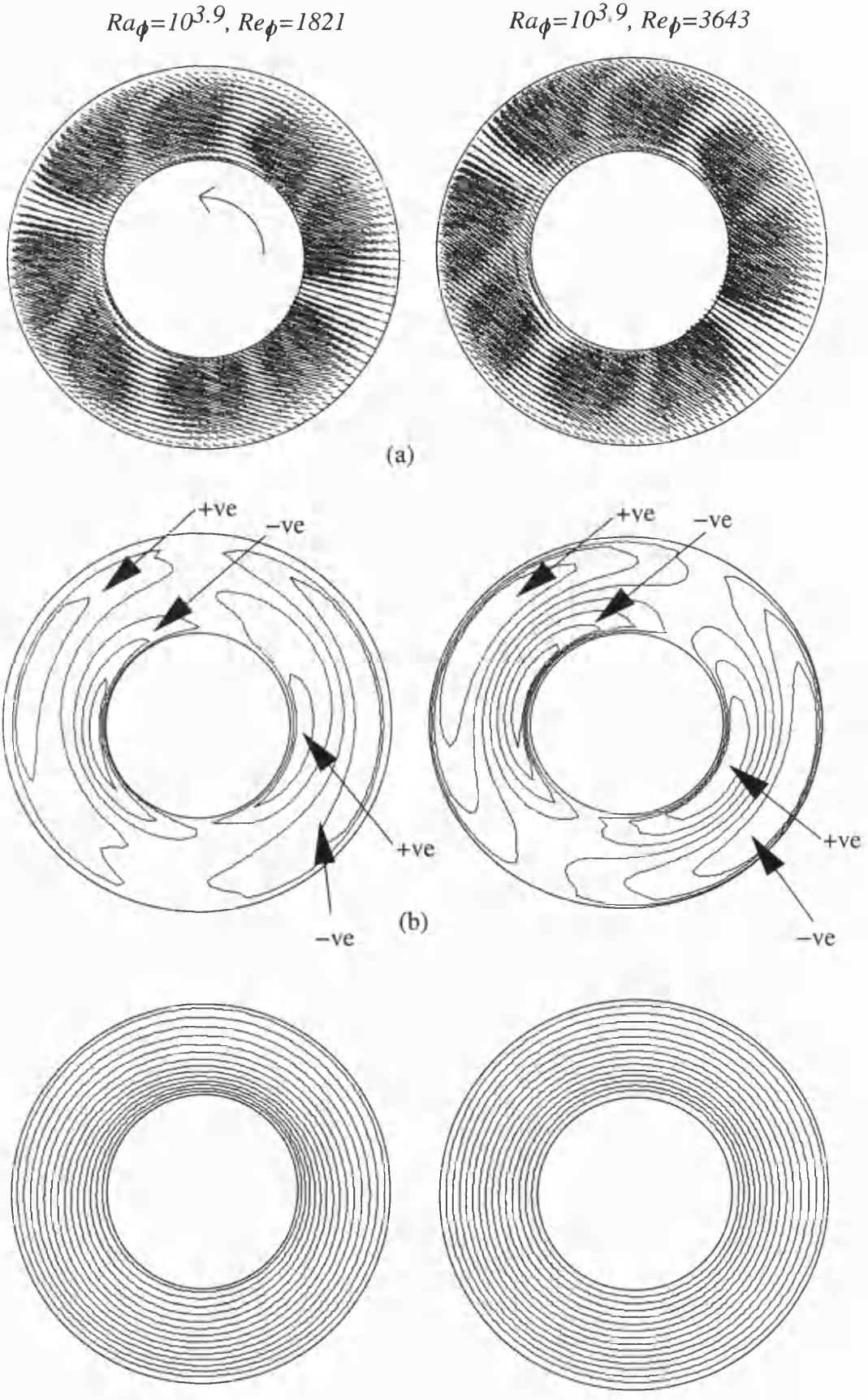

Figure 6.10 Solutions for 3D rotating annulus flow on the $z/b=0.125$ plane. The annulus had dimensions of $r_o=1.0$, $r_i=0.5$, and $z_{max}=0.5$.

(a) velocity vectors
(b) axial velocity isolines
(c) isotherms

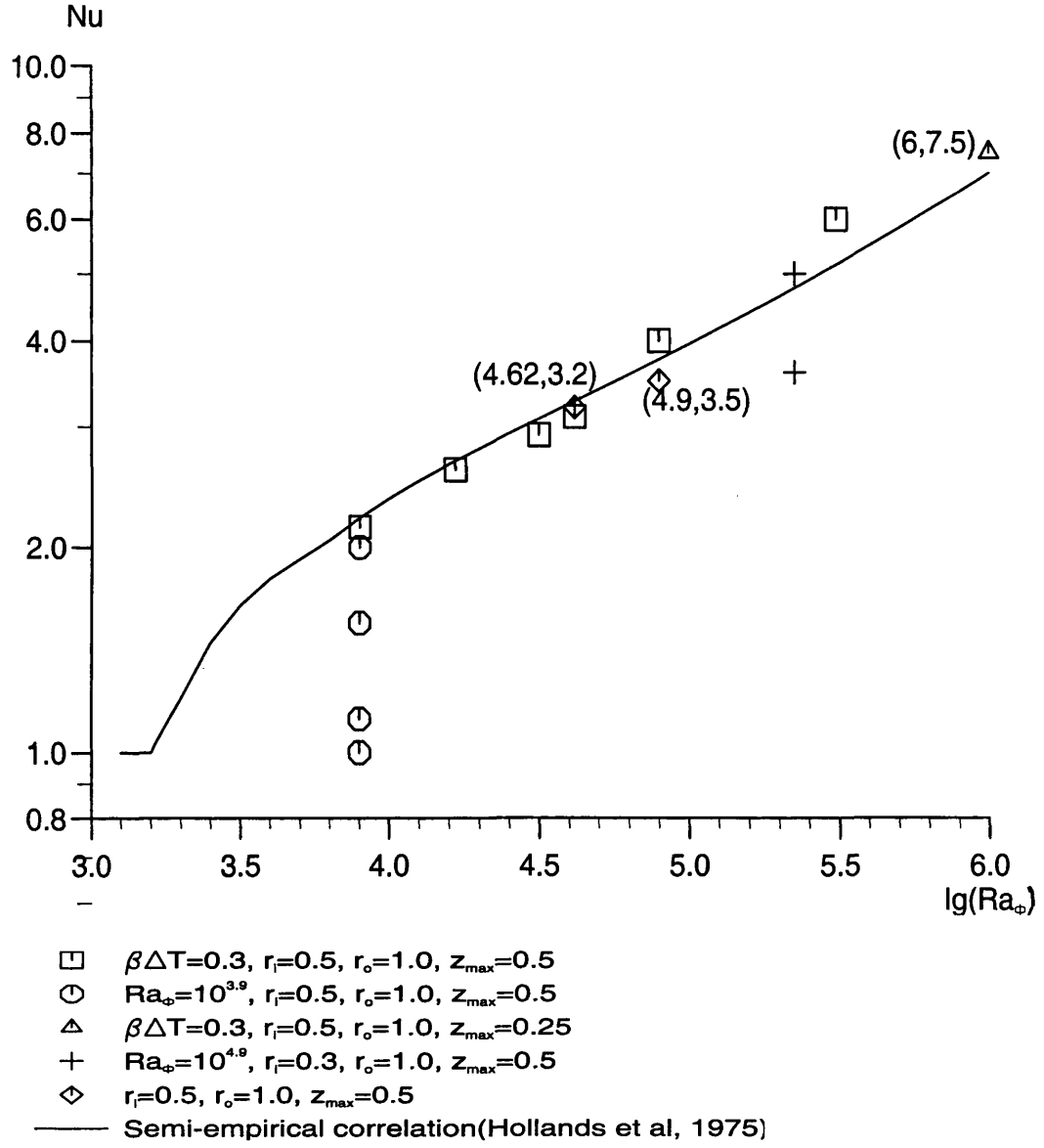

Figure 6.11 Variations of *Nu* with *Ra* for 3D rotating annulus flows. Computed results.

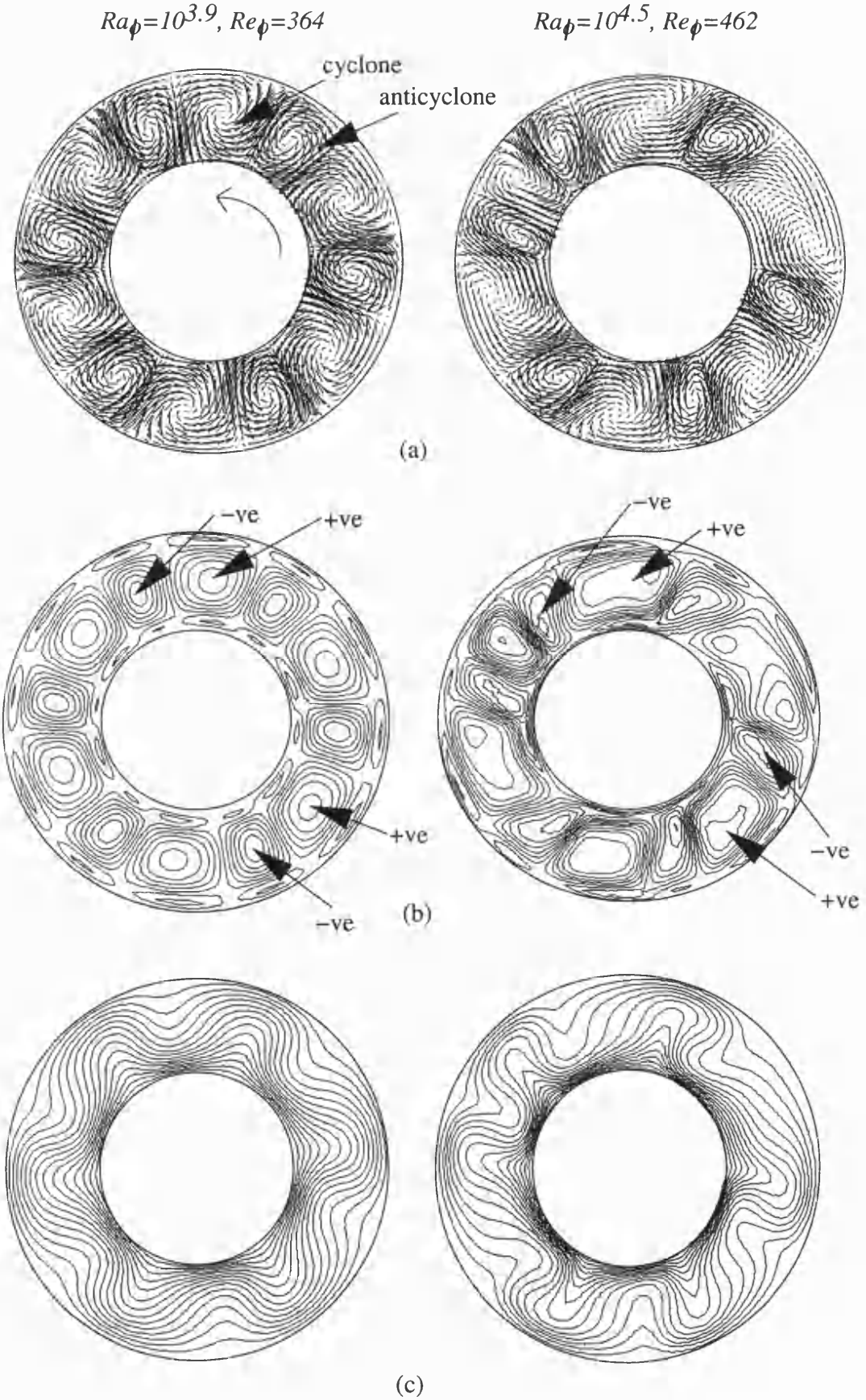

Figure 6.12 Solutions for 3D rotating annulus flow on the $z/b=0.0625$ plane. The annulus had dimensions of $r_o=1.0$, $r_i=0.5$, and $z_{max}=0.25$.

(a) velocity vectors
(b) axial velocity isolines
(c) isotherms

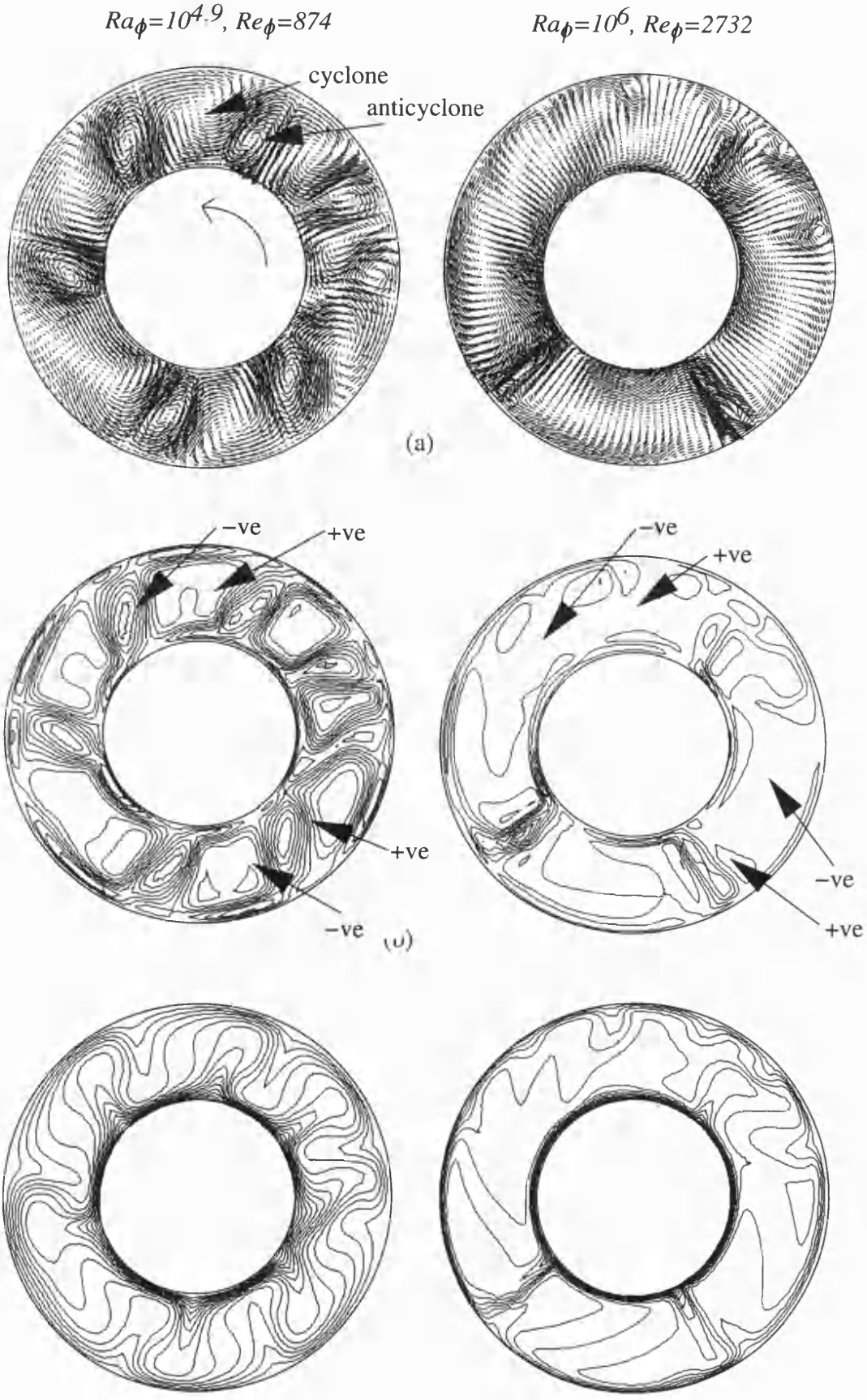

Figure 6.13 Solutions for 3D rotating annulus flow on the $z/b=0.0625$ plane. The annulus had dimensions of $r_o=1.0$, $r_i=0.5$, and $z_{max}=0.25$.

(a) velocity vectors
(b) axial velocity isolines
(c) isotherms

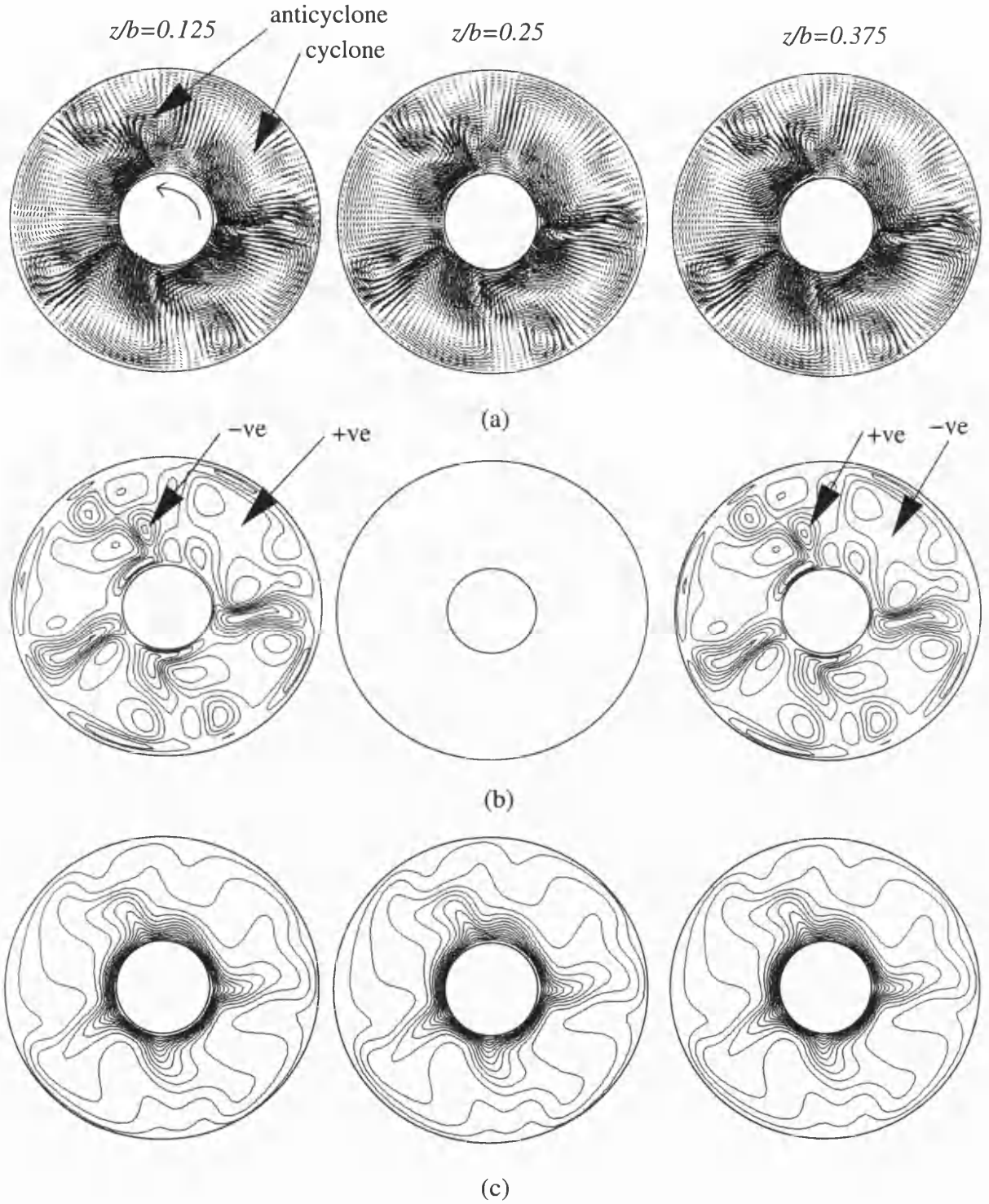

Figure 6.14 Solutions for 3D rotating annulus flow. $Ra_{\phi}=10^{5.35}$, $Re_{\phi}=2283$. The annulus has dimensions of $r_O=1.0$, $r_i=0.3$, and $z_{max}=0.5$.

(a) velocity vectors
(b) axial velocity isolines
(c) isotherms

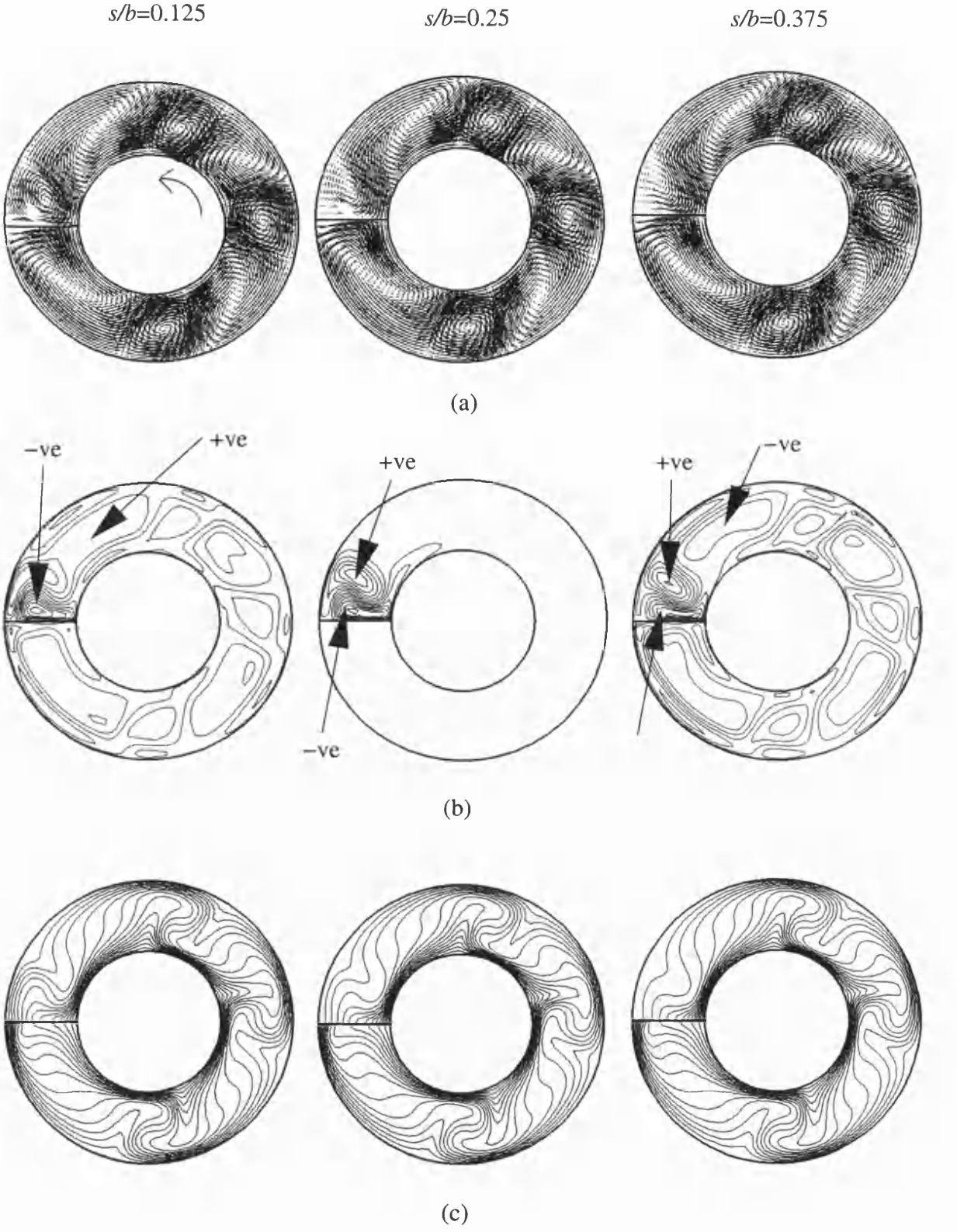

Figure 6.15 Solutions for 3D flow in rotating annulus with an insulating radial barrier. $Ra_\phi=10^{4.6}$, $Re_\phi=546$. The annulus has dimensions of $r_o=1.0$, $r_i=0.5$, $z_{max}=0.5$.
(a) velocity vectors
(b) axial velocity isolines
(c) isotherms

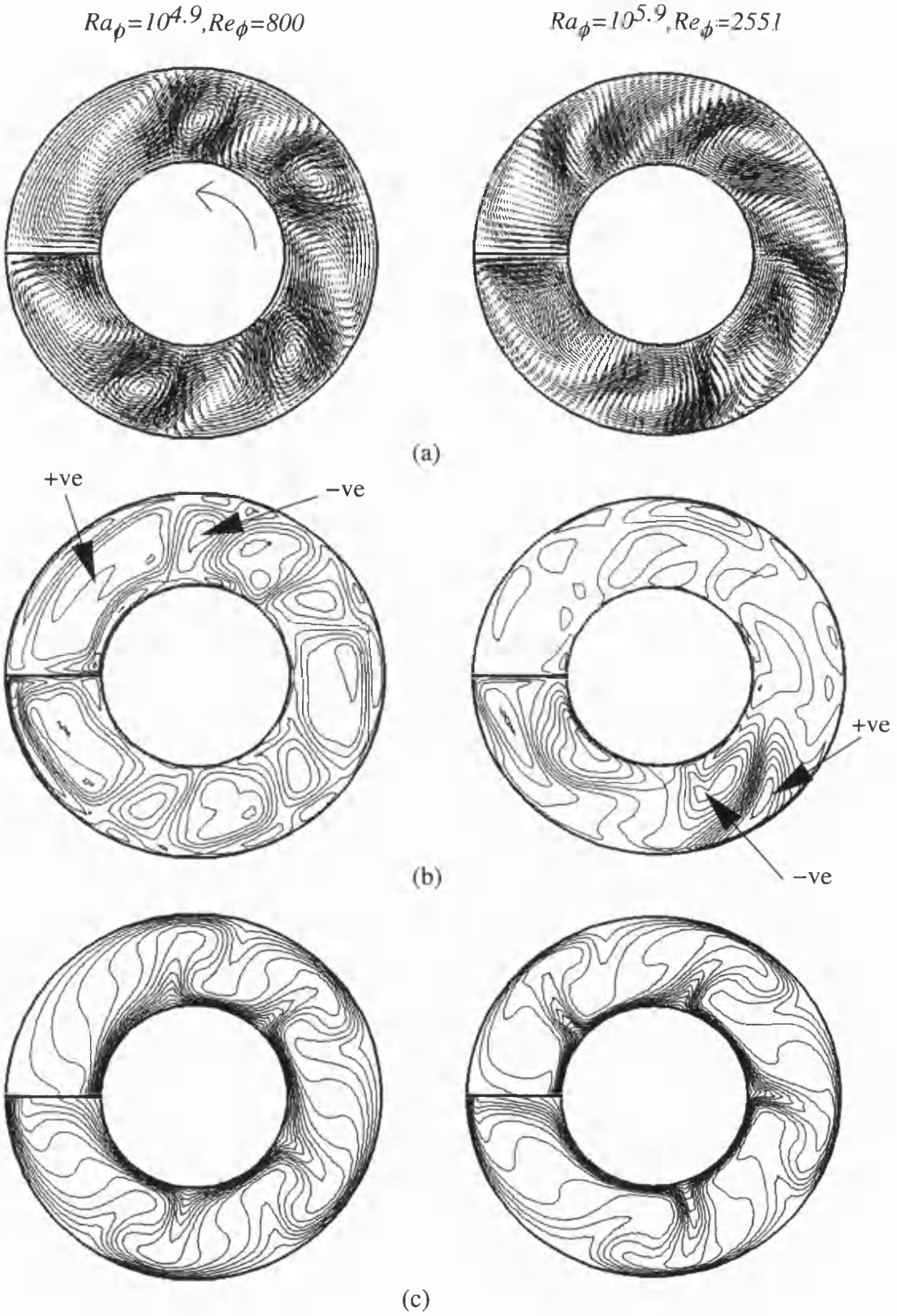

Figure 6.16 Solutions on the $z/b=0.125$ plane for 3D flow in rotating annulus with an insulating radial barrier. $r_o=1.0$, $r_i=0.5$, and $z_{max}=0.5$.

(a) velocity vectors
(b) axial velocity isolines
(c) isotherms

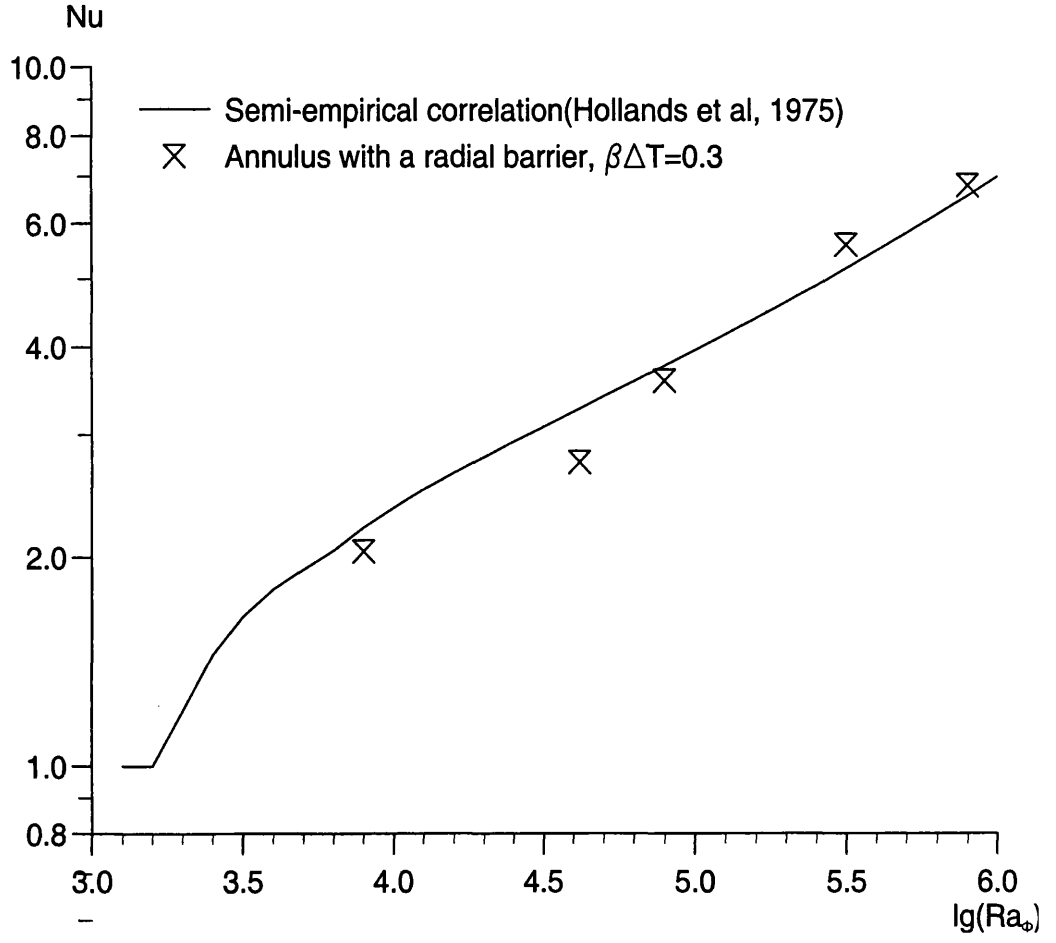

Figure 6.17 Variations of *Nu* with *Ra* for 3D flows in rotating annulus with a radial barrier. r_o=*1.0*, r_i=*0.5*, and z_{max}=*0.5*. Computed results compare to semi–empirical correlation by Hollands et al, 1975.

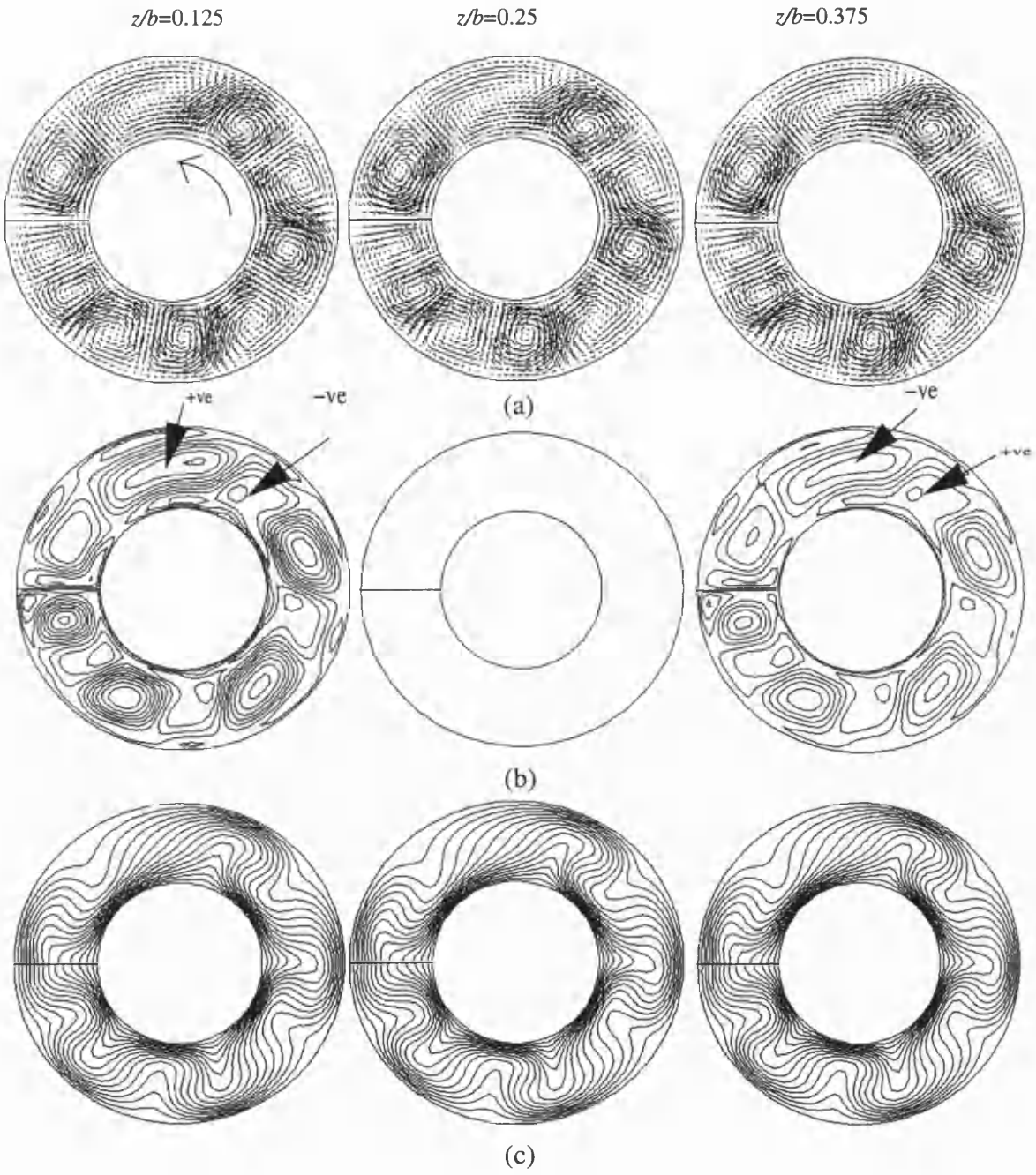

Figure 6.18 Solutions for 3D flow in rotating annulus with a radial barrier
$Ra_\rho=10^{3.9}$, $Re_\rho=218$, $r_o=1.0$, $r_i=0.5$, $z_{max}=0.5$
(a) flow vectors
(b) axial velocity isolines
(c) isotherms

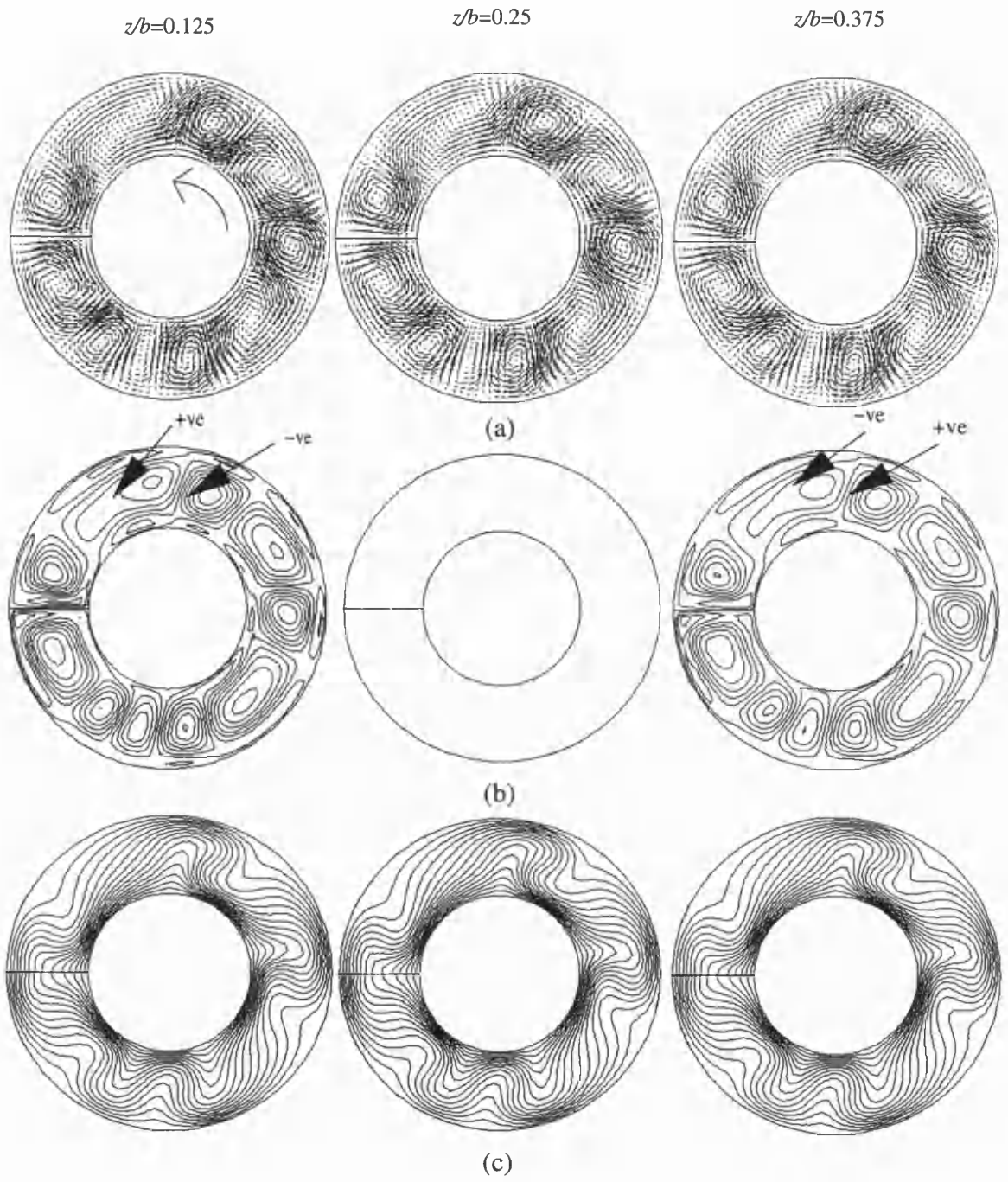

Figure 6.19 Solutions for 3D flow in rotating annulus with a radial barrier
$Ra_{\phi}=10^{3.9}$, $Re_{\phi}=364$, $r_o=1.0$, $r_i=0.5$, $z_{max}=0.5$
(a) flow vectors
(b) axial velocity isolines
(c) isotherms

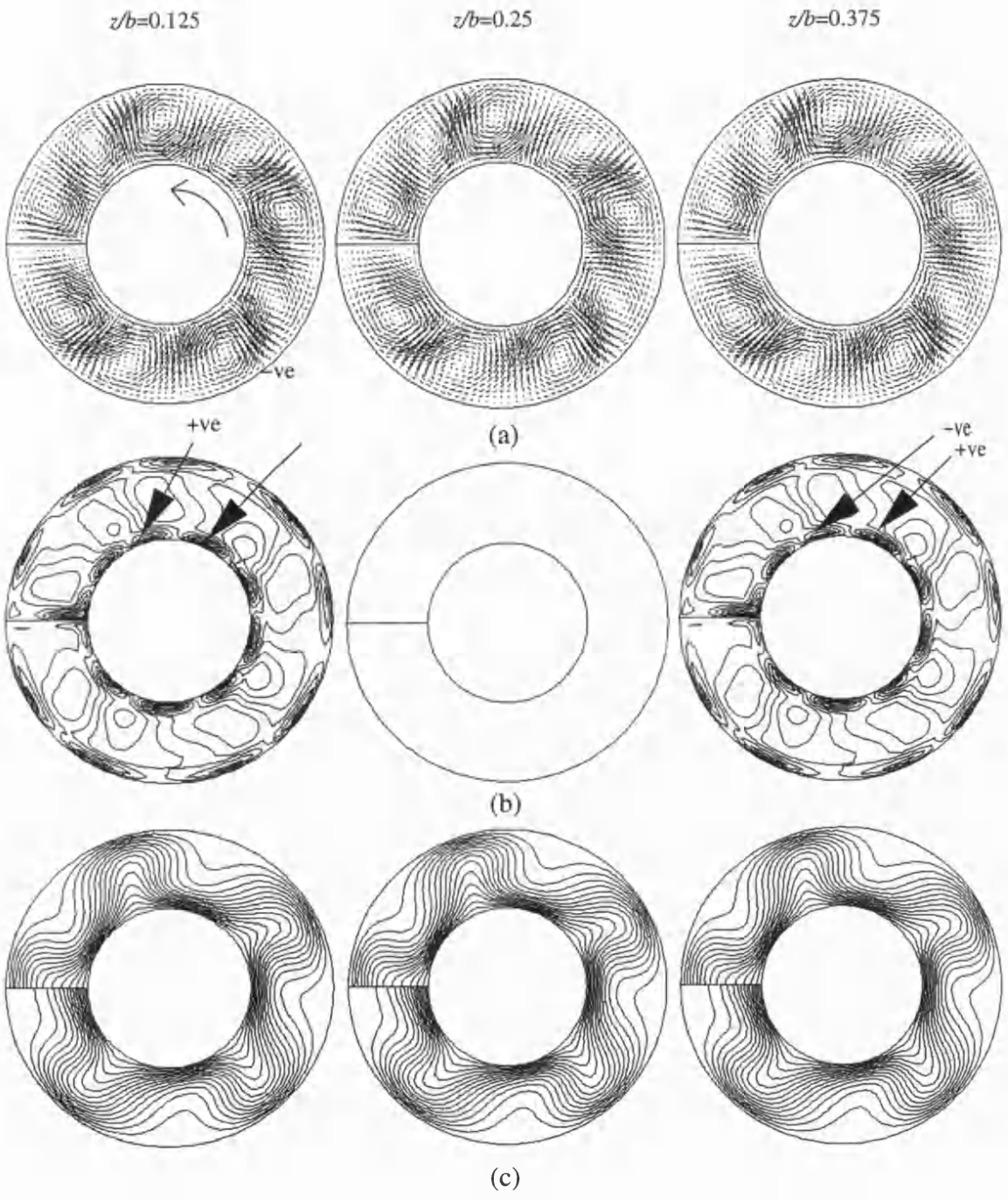

Figure 6.20 Solutions for 3D flow in rotating annulus with a radial barrier
$Ra_{\phi}=10^{3.9}$, $Re_{\phi}=1821$, $r_o=1.0$, $r_i=0.5$, $z_{max}=0.5$
(a) flow vectors
(b) axial velocity isolines
(c) isotherms

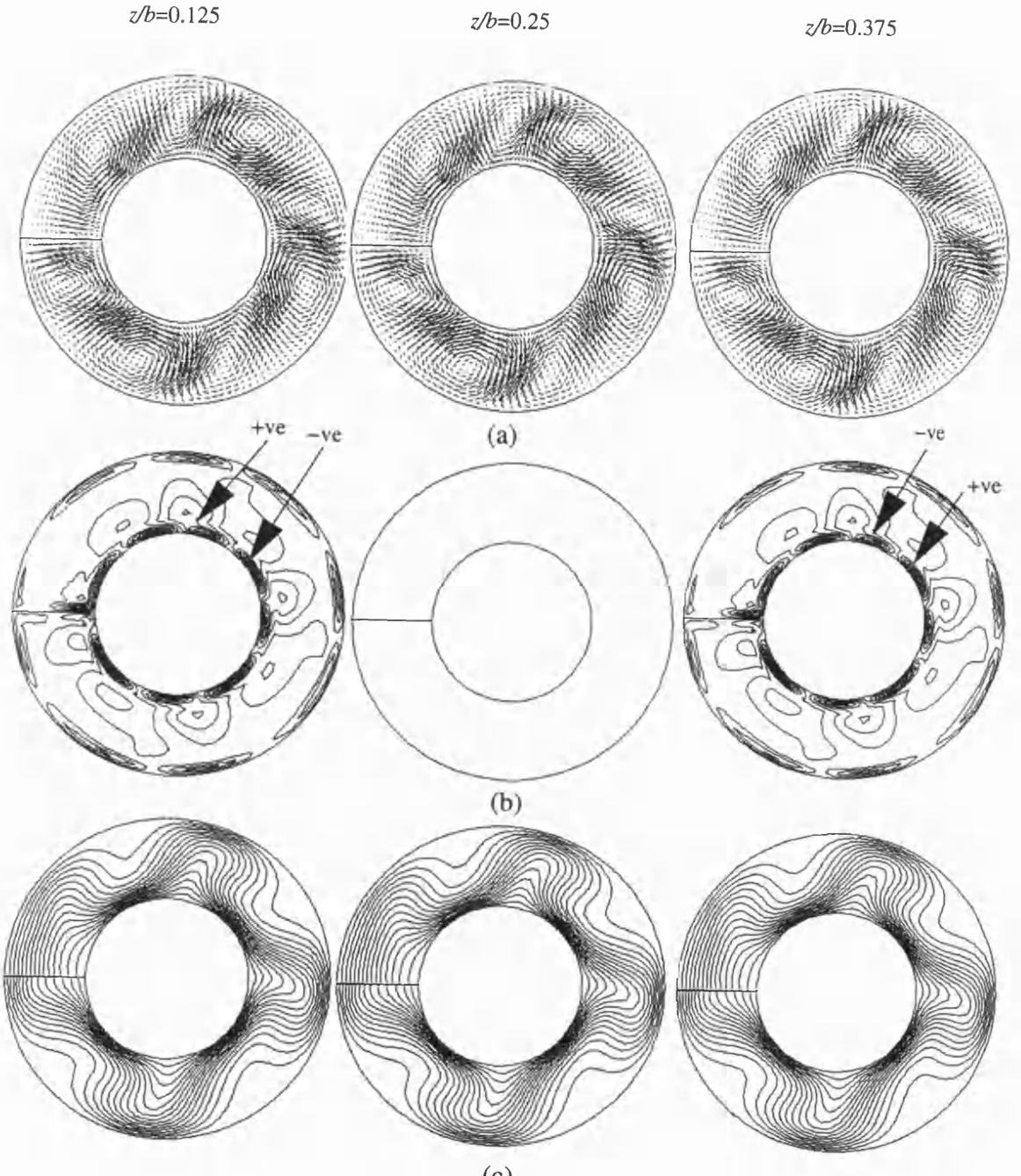

Figure 6.21 Solutions for 3D flow in rotating annulus with a radial barrier
$Ra_{\phi}=10^{3.9}$, $Re_{\phi}=3643$, $r_o=1.0$, $r_i=0.5$, $z_{max}=0.5$
(a) flow vectors
(b) axial velocity isolines
(c) isotherms

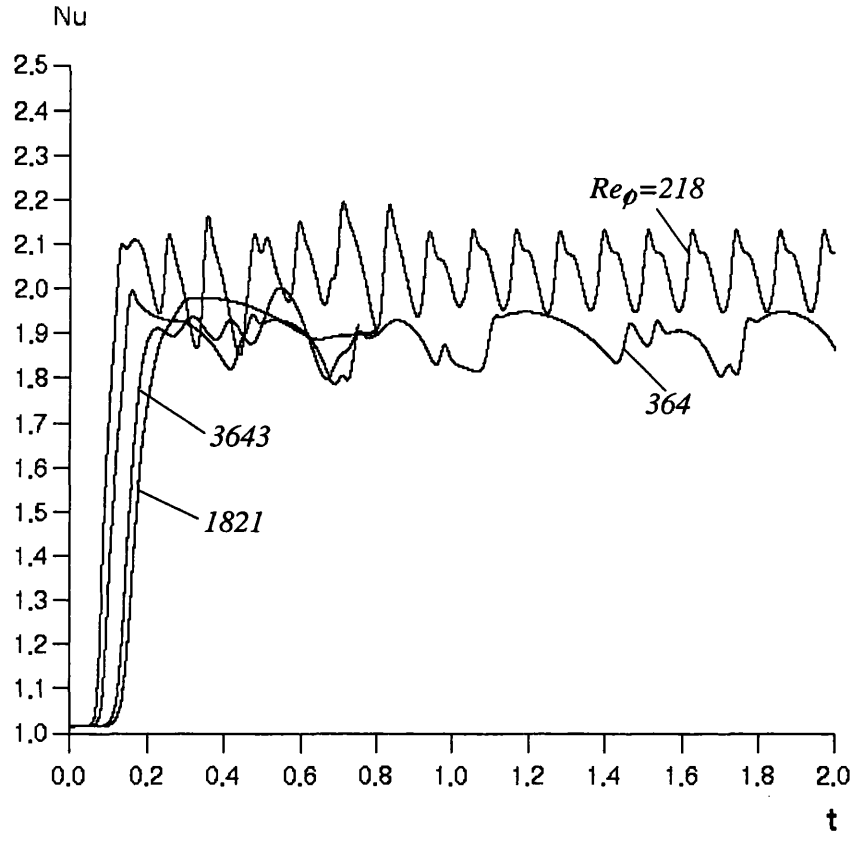

Figure 6.22 Global Nusselt numbers variation with time for rotating annulus with a radial barrier. $Ra_\phi=10^{3.9}$. $r_\phi=1.0$, $r_i=0.5$, $z_{max}=0.5$.

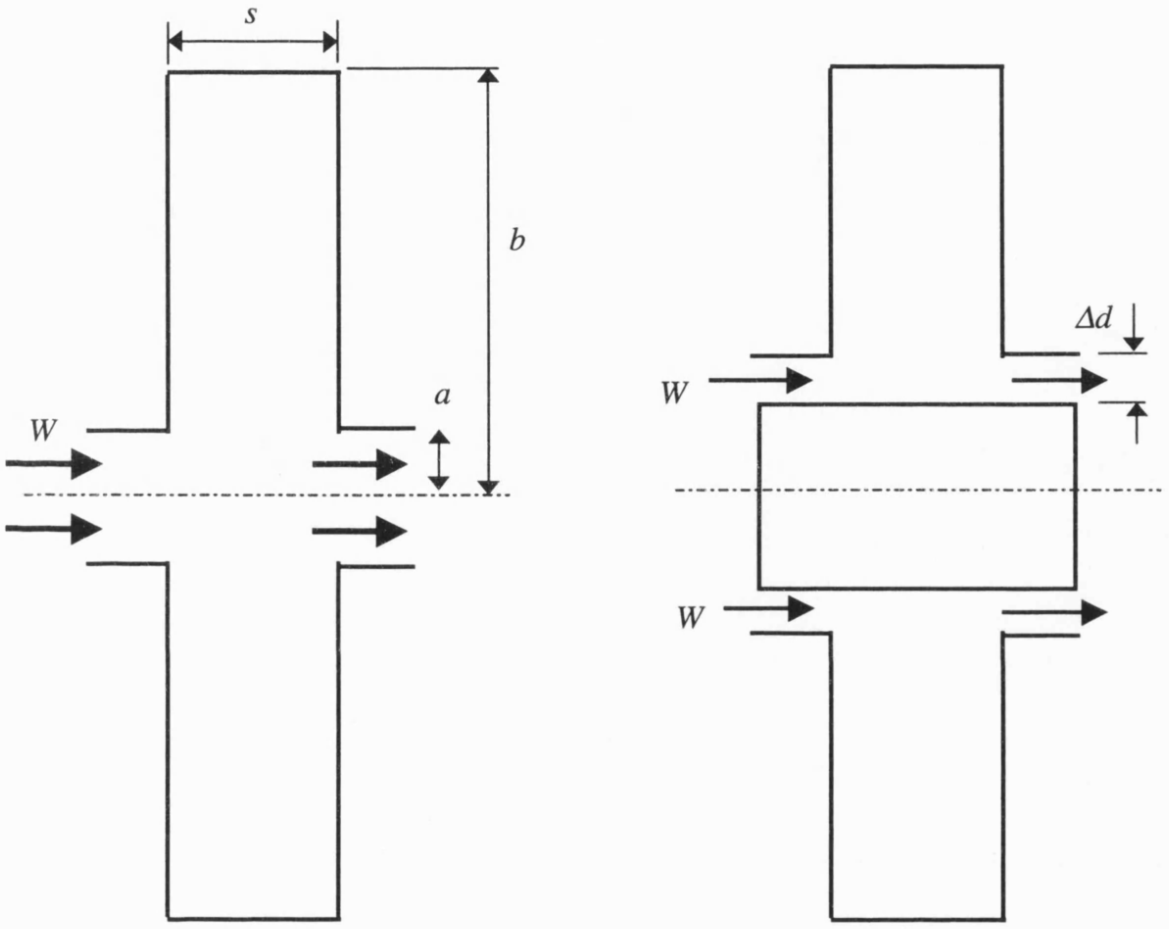

(a) circular inlet

(b) Annular inlet

Figure 7.1 Rotating cavities with axial throughflow

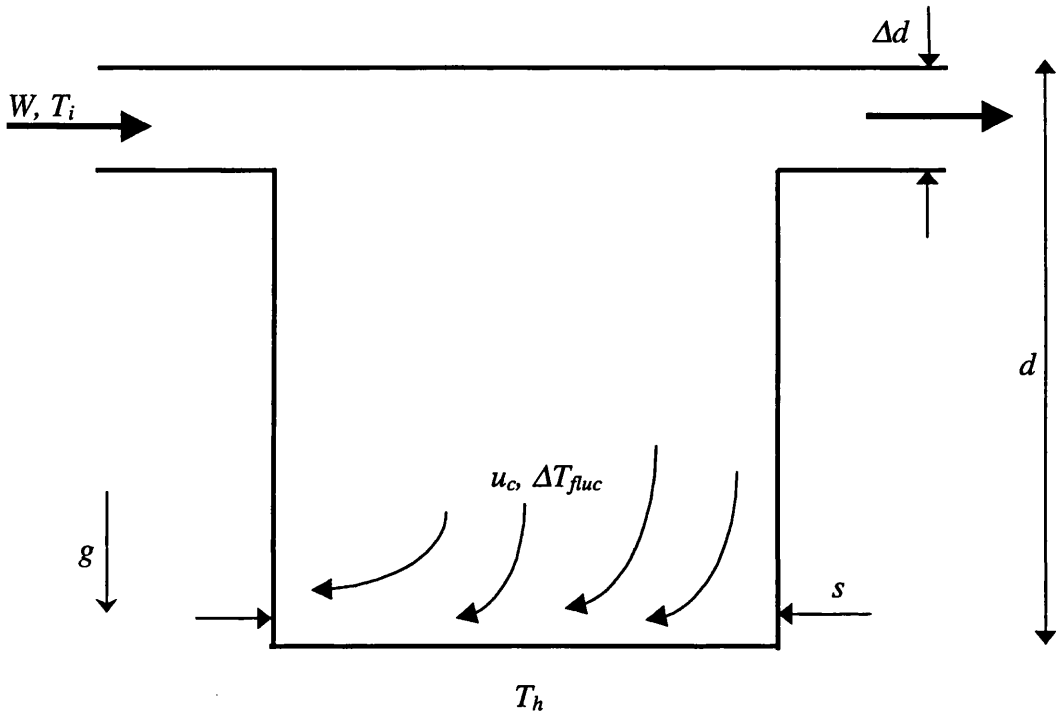

Figure 7.2 A stationary cavity with heating from below and througflow of cooling air.

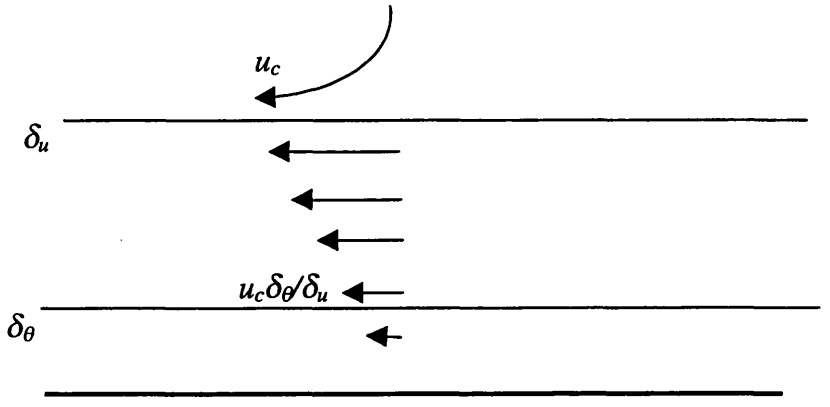

Figure 7.3 Estimating the velocity outside the thermal boundary layer with $u_c\delta_\theta/\delta_u$.

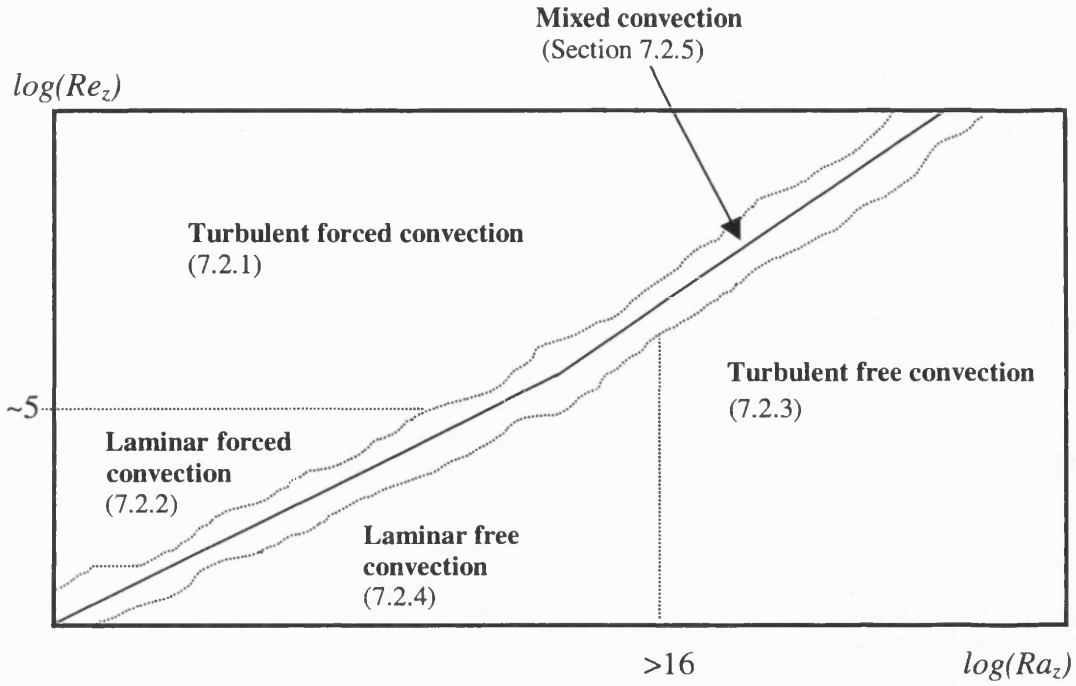

Figure 7.4 Convection regime diagram for cavity with throughflow. $Pr \gtrsim 1$. That for the horizontal or vertical flat plate has similar delineations. There is not enough information for deciding the exact numerical values of Rayleigh and Reynolds numbers at the transitions. The mixed convective line is given by Equations (7.18), (7.19), and (7.20).

Correlations for the different regimes:

Turbulent forced convection: $Nu_z \sim Re_z^{3/4}$
$Nu_z \sim Ra_z^{1/3} Pr^{-2/3}$

Laminar forced convection: $Nu_z \sim Re_z^{1/2}$
$Nu_z \sim Ra_z^{1/5}$

Turbulent free convection: $Nu_z \sim Ra_z^{1/2} Pr^{1/2}$
$Nu_z \sim Re_z^{1/2} Pr^{1/3}$

Laminar free convection: $Nu_z \sim Ra_z^{1/4} Pr^{-1/12}$
$Nu_z \sim Re_z^{1/2} Pr^{1/3}$